



ERNEST ORLANDO LAWRENCE BERKELEY NATIONAL LABORATORY

Novel Nuclear Magnetic Resonance Techniques for Studying Biological Molecules

David D. Laws

Materials Sciences Division

June 2000

Ph.D. Thesis



DISCLAIMER

This document was prepared as an account of work sponsored by the United States Government. While this document is believed to contain correct information, neither the United States Government nor any agency thereof, nor The Regents of the University of California, nor any of their employees, makes any warranty, express or implied, or assumes any legal responsibility for the accuracy, completeness, or usefulness of any information, apparatus, product, or process disclosed, or represents that its use would not infringe privately owned rights. Reference herein to any specific commercial product, process, or service by its trade name, trademark, manufacturer, or otherwise, does not necessarily constitute or imply its endorsement, recommendation, or favoring by the United States Government or any agency thereof, or The Regents of the University of California. The views and opinions of authors expressed herein do not necessarily state or reflect those of the United States Government or any agency thereof, or The Regents of the University of California.

Ernest Orlando Lawrence Berkeley National Laboratory
is an equal opportunity employer.

**Novel Nuclear Magnetic Resonance Techniques
For Studying Biological Molecules**

David Douglas Laws
Ph.D. Thesis

Department of Chemistry
University of California, Berkeley

and

Materials Sciences Division
Ernest Orlando Lawrence Berkeley National Laboratory
University of California
Berkeley, CA 94720

June 2000

This work was supported by the Howard Hughes Medical Institute and by the Director, Office of Science, Office of Basic Energy Sciences, Materials Sciences Division, of the U.S. Department of Energy, under Contract No. DE-AC03-76SF00098.

**Novel Nuclear Magnetic Resonance Techniques
For Studying Biological Molecules**

by

David Douglas Laws

B.S. (University of Illinois, Urbana-Champaign) 1995

a dissertation submitted in partial satisfaction of the

requirements for the degree of

Doctor of Philosophy

in

Chemistry

in the

GRADUATE DIVISION

of the

UNIVERSITY OF CALIFORNIA, BERKELEY

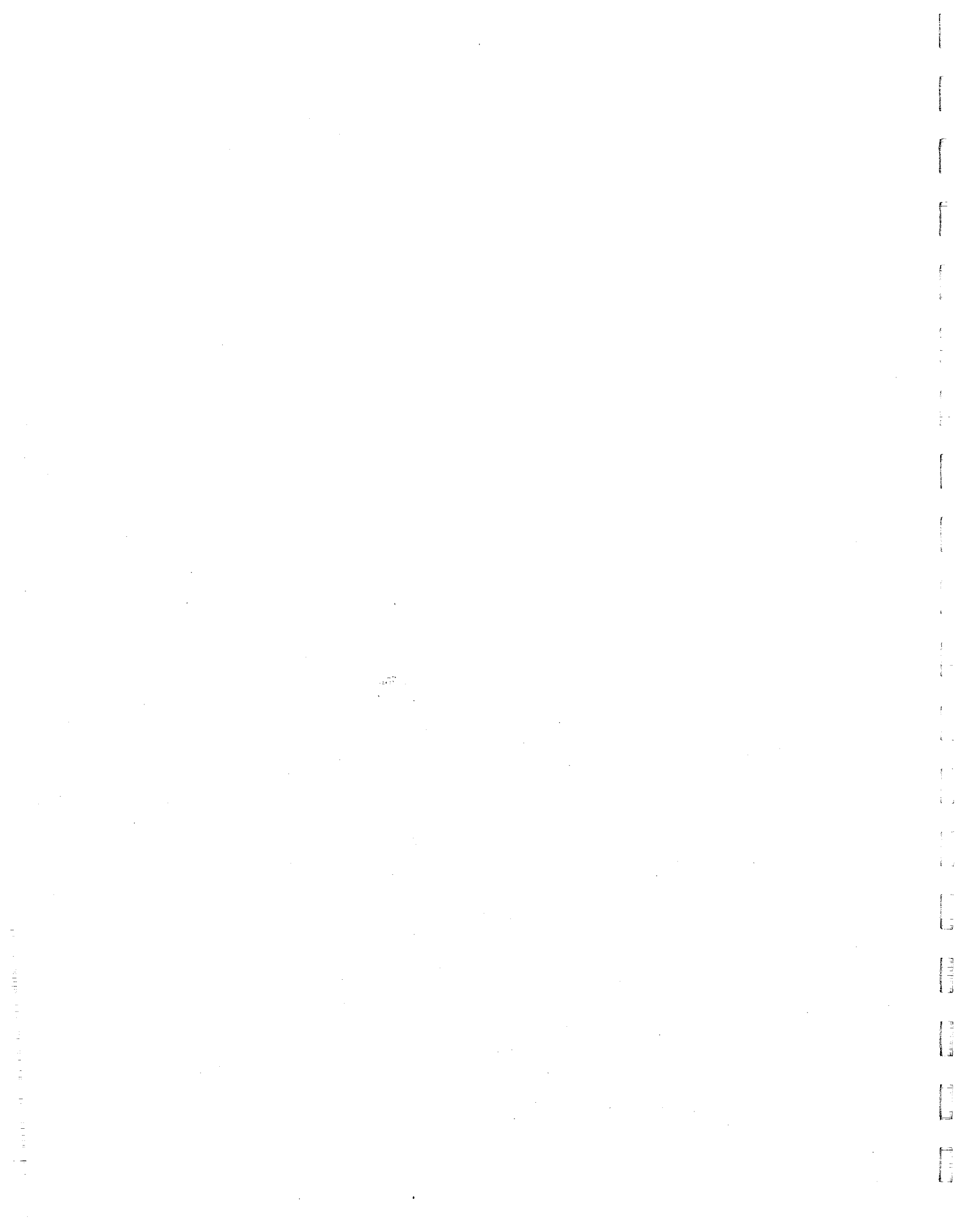
Committee in charge:

Professor Alexander Pines, Chair

Professor Adam Arkin

Professor Jeffrey A. Reimer

Fall 2000



**Novel Nuclear Magnetic Resonance Techniques
For Studying Biological Molecules**

Copyright © 2000

by

David Douglas Laws

The U.S. Department of Energy has the right to use this document
for any purpose whatsoever including the right to reproduce
all or any part thereof

Abstract

Novel Nuclear Magnetic Resonance Techniques For Studying Biological Molecules

by

David Douglas Laws

Doctor of Philosophy in Chemistry

University of California, Berkeley

Professor Alexander Pines, Chair

Over the fifty-five year history of Nuclear Magnetic Resonance (NMR), considerable progress has been made in the development of techniques for studying the structure, function, and dynamics of biological molecules. The majority of this research has involved the development of multi-dimensional NMR experiments for studying molecules in solution, although in recent years a number of groups have begun to explore NMR methods for studying biological systems in the solid-state. Despite this new effort, a need still exists for the development of techniques that improve sensitivity, maximize information, and take advantage of all the NMR interactions available in biological molecules.

In this dissertation, a variety of novel NMR techniques for studying biomolecules are discussed. A method for determining backbone (ϕ/ψ) dihedral angles by comparing experimentally determined $^{13}\text{C}_\alpha$ chemical-shift anisotropies with theoretical calculations is presented, along with a brief description of the theory behind chemical-shift computation in proteins and peptides. The utility of the Spin-Polarization Induced Nuclear Overhauser Effect (SPINOE) to selectively enhance NMR signals in solution is

examined in a variety of systems, as are methods for extracting structural information from cross-relaxation rates that can be measured in SPINOE experiments. Techniques for the production of supercritical and liquid laser-polarized xenon are discussed, as well as the prospects for using optically pumped xenon as a polarizing solvent.

In addition, a detailed study of the structure of PrP 89-143 is presented. PrP 89-143 is a 54 residue fragment of the prion proteins which, upon mutation and aggregation, can induce prion diseases in transgenic mice. Whereas the structure of the wild-type PrP 89-143 is a generally unstructured mixture of α -helical and β -sheet conformers in the solid state, the aggregates formed from the PrP 89-143 mutants appear to be mostly β -sheet.

For Elizabeth, Anne, and James

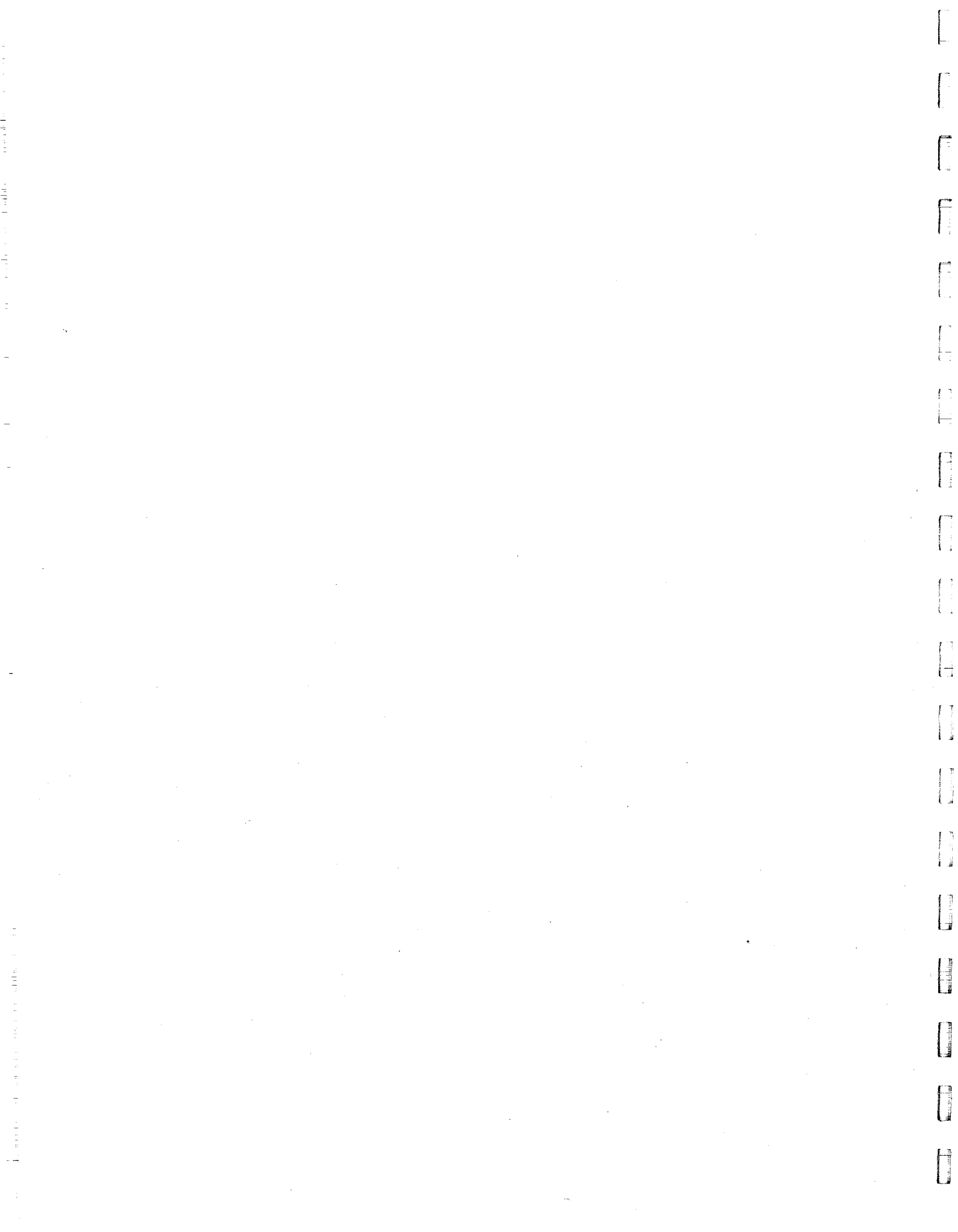


Table of Contents

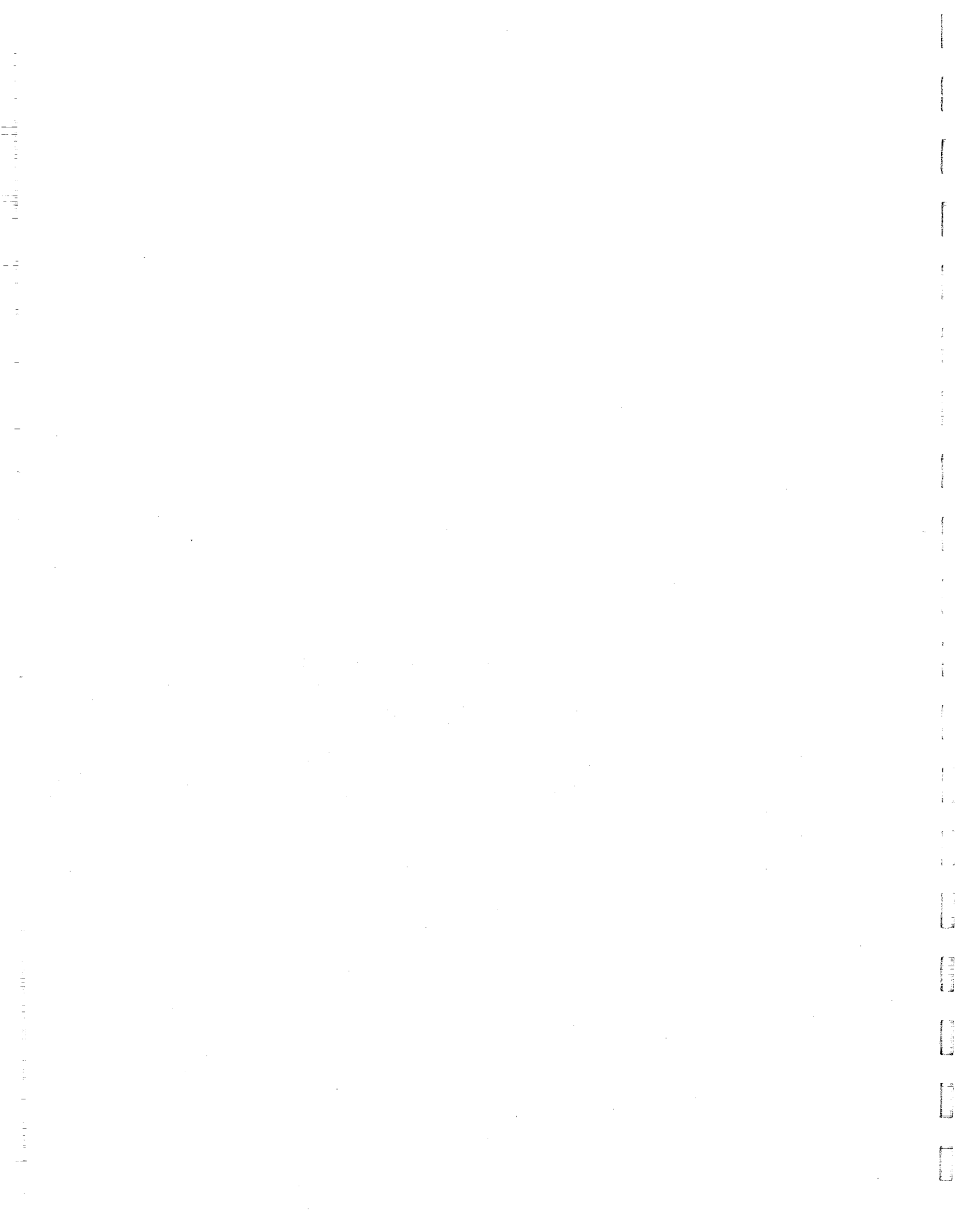
List of Figures.....	vii
List of Tables	ix
Acknowledgements.....	x
I. Introduction.....	1
Chapter 1: Solid-State Nuclear Magnetic Resonance.....	2
1.1. Introduction.....	2
1.1.1. The Zeeman Effect.....	2
1.1.2. Boltzmann Statistics and NMR Sensitivity.....	3
1.1.3. Tensor Notation.....	6
1.2. Fundamental Interactions in Solid-State NMR.....	8
1.2.1. The Chemical Shift.....	10
1.2.2. The Heteronuclear Dipolar Interaction	13
1.2.3. The Homonuclear Dipolar Interaction.....	18
1.2.4. The Quadrupolar Interaction.....	18
1.3. Magic-Angle Sample Spinning.....	22
1.3.1. Theory of NMR in Rotating Solids.....	23
1.3.2. Fast Magic-Angle Spinning	25
1.3.3. Slow Magic-Angle Spinning.....	26
1.4. Cross Polarization.....	26
1.4.1. The Hartmann-Hahn Experiment.....	28
1.4.2. Cross Polarization under Magic-Angle Spinning	32
1.5. Dipolar Recoupling under Magic-Angle Spinning.....	35

1.5.1. Heteronuclear Dipolar Recoupling	37
1.5.2. Homonuclear Dipolar Recoupling	41
1.5.3. Rotational Resonance.....	44
Chapter 2: Chemical-Shift Computation.....	47
2.1. Chemical-Shift Computation: The Early Years	47
2.2. Gauge-Including Atomic Orbitals (GIAO).....	48
2.3. Chemical-Shift Calculations in Peptides and Proteins.....	49
Chapter 3: Laser-Polarization of Xenon-129	53
3.1. Fundamentals of Optical Pumping.....	53
3.2. Experimental Optical Pumping Set-ups.....	57
3.2.1. Batch-Mode Optical Pumping.....	57
3.2.2. Continuous-Flow Optical Pumping.....	60
Chapter 4: Prion Diseases	65
4.1. Description of Prion Diseases	65
4.1.1. The Pathology of Prion Diseases	65
4.1.2. The Protein-Only Hypothesis	68
4.1.3. Sporadic, Familial, and Iatrogenic Prion Diseases	70
4.2. The Prion Protein	71
4.3. PrP 89-143: An Infectious Fragment of the Prion Protein.....	75
II. NMR Technique Development	78
Chapter 5: The CSA/Z Method.....	79
5.1. Introduction.....	79
5.2. Experimental.....	80

5.2.1. Fmoc Protection of ^{13}C -Labeled Amino Acids	81
5.2.2. Peptide Synthesis.....	82
5.2.3. Peptide Crystallization.....	83
5.2.4. Solid-State NMR.....	84
5.3. Computational.....	85
5.4. Results and Discussion.....	86
5.4.1. Correlations between Theory and Experiment.....	87
5.4.2. Predictions of Dihedral Angles in Solid-State Peptides	93
5.5. Conclusions.....	98
Chapter 6: Spin-Polarization Induced Nuclear Overhauser Effect.....	100
6.1. Introduction.....	100
6.2. The Solomon Equations for a Two-Spin System.....	101
6.3. ^{129}Xe to ^1H Polarization Transfer	103
6.4. General Considerations for ^1H - ^{129}Xe Cross-Relaxation Rates	104
6.5. Effects of σ_{HXe} and Intermolecular Interactions on the SPINOE	105
6.5.1. Cross-Relaxation Rates in the Diffusive Coupling Regime	107
6.5.2. Cross-Relaxation Rates in the Binding Regime.....	108
6.5.3. Dependence of σ_{HXe} on the Xe Concentration	109
6.6. The DINOE Sequence	111
Chapter 7: NMR in Liquid and Supercritical Xenon.....	115
7.1. Introduction.....	115
7.2. Experimental.....	116
7.2.1. Design of the High-Pressure NMR Tube.....	116

7.2.2. Production of Polarized Liquid and Supercritical ^{129}Xe	118
7.3. Results and Discussion	120
7.4. Conclusions.....	125
Chapter 8: Double-Quantum MAS NMR of Spin $I = 1$ Nuclei.....	126
8.1. Introduction.....	126
8.2. A Survey of ^{14}N NMR and NQR Techniques	128
8.2.1. Low-Field ^{14}N NMR Techniques.....	128
8.2.2. High-Field ^{14}N NMR Techniques.....	129
8.3 Triple-Resonance Double-Quantum Cross-Polarization	132
III. Applications of NMR to the Study of Macromolecules	135
Chapter 9: Solid-State NMR Studies of PrP 89-143.....	136
9.1. Introduction.....	136
9.2. Experimental.....	137
9.2.1. Peptide Synthesis	138
9.2.2. Conversion of PrP 89-143 to the Aggregated State	138
9.2.3. Solid-State NMR.....	139
9.3. Results and Discussion	139
9.3.1. NMR Studies of the 3AV Mutant of PrP 89-143.....	140
9.3.2. NMR Studies of the P101L Mutant of PrP 89-143.....	143
9.3.3. Comparisons between hPrP 89-143 and mPrP 89-143.....	146
9.4. Conclusions.....	147
Chapter 10: SPINOE Studies of α -Cyclodextrin.....	148
10.1. Introduction.....	148

10.2. Experimental	149
10.3. Results and Discussion	151
10.4. Conclusions	155
Chapter 11: SPINOE Studies of Cryptophane-A.....	156
11.1. Introduction.....	156
11.2. Experimental	158
11.3. Results and Discussion	160
11.4. Conclusions	169
IV. References	170
V. Appendix A: Simulations and Programs	194
A.1. Matlab Script for Calculating CSA Lineshapes.....	195
A.2. REDOR Decay Least-Squares Fitting Function (Matlab)	196
A.3. ^1H - ^{13}C CPMAS Simulation with Build-Up Curve (GAMMA).....	197
A.4. ^1H - ^{13}C CPMAS Matching Profile Simulation (GAMMA).....	201
A.5. ^1H - ^{13}C Static CP Simulation with Build-up Curve (GAMMA).....	204
A.6. ^1H - ^{13}C Static CP Matching Profile Simulation (GAMMA).....	208
A.7. Matlab Script for a Graphical Interface 1D Processing Program.....	211
A.8. Matlab Script Containing 1D NMR Processing Functions.....	217



List of Figures

Figure 1.1. Energy level diagram for a spin $I = \frac{1}{2}$ nucleus.....	3
Figure 1.2. Euler rotation angles.....	7
Figure 1.3. CSA powder patterns.....	14
Figure 1.4. Dipolar Pake pattern.....	17
Figure 1.5. Energy level diagram for a spin $I = 1$ nucleus.....	22
Figure 1.6. Overlapping CSA powder patterns.....	23
Figure 1.7. H_{CS} under magic-angle spinning.....	25
Figure 1.8. ^{13}C glycine spectrum at different MAS speeds.....	27
Figure 1.9. Cross-polarization pulse sequence and build-up curves.....	30
Figure 1.10. ^{13}C NMR spectra of alanyl-histidine.....	31
Figure 1.11. Hartmann-Hahn CP matching profiles (static and MAS).....	34
Figure 1.12. Alternative CPMAS pulse sequences.....	36
Figure 1.13. H_{IS} under magic-angle spinning.....	38
Figure 1.14. REDOR pulse sequence and decay curve.....	39
Figure 1.15. REDOR decay in $1\text{-}^{13}\text{C},^{15}\text{N}$ -glycine.....	41
Figure 1.16. DRAMA pulse sequence.....	43
Figure 1.17. ^{13}C glycine spectrum under rotational resonance.....	46
Figure 1.18. Rotational resonance pulse sequence.....	46
Figure 2.1. Fragments for chemical-shift calculations in proteins.....	50
Figure 2.2. Accuracy of chemical-shift predictions in proteins.....	52
Figure 3.1. Electronic excitation in optical pumping.....	54
Figure 3.2. Transfer of polarization to xenon during optical pumping.....	54
Figure 3.3. Enhancement of ^{129}Xe NMR by optical pumping.....	56
Figure 3.4. Batch-mode optical pumping set-up.....	58
Figure 3.5. Continuous-flow optical pumping set-up.....	61
Figure 3.6. ^{129}Xe NMR of flowing xenon gas.....	63
Figure 4.1. Images of human brains infected with prion diseases.....	67
Figure 4.2. Amino acid sequences for human, Syrian hamster, and mouse PrP.....	72
Figure 4.3. Schematic of the structure of Syrian hamster PrP.....	74

Figure 4.4. Fragments of PrP 89-143.....	76
Figure 5.1. CPMAS spectra of $^{13}\text{C}_\alpha$ -labeled A*AA-hemihydrate.....	89
Figure 5.2. Alanine $^{13}\text{C}_\alpha$ chemical-shift tensor surfaces.....	91
Figure 5.3. Predicted versus experimentally measured $^{13}\text{C}_\alpha$ chemical-shift tensors.....	92
Figure 5.4. Z-surfaces for Boc-VA*L-Aib-VAL-OMe I.....	95
Figure 5.5. The weighted average of a Z-surface prediction.....	97
Figure 6.1. SPINOE enhancement as a function of time and xenon T_1	102
Figure 6.2. Dependence of σ_{HXe} on the correlation time.....	105
Figure 6.3. σ_{HXe} as a function of xenon concentration and binding strength.....	111
Figure 6.4. Variants of the difference SPINOE or “DINOE” pulse sequence.....	113
Figure 7.1. Valve design for a high-pressure NMR tube.....	117
Figure 7.2. Xenon phase diagram.....	119
Figure 7.3. A spectrum of supercritical laser-polarized xenon.....	121
Figure 7.4. ^{129}Xe chemical shift as a function of pressure and density.....	122
Figure 7.5. A better spectrum of supercritical laser-polarized xenon.....	124
Figure 8.1. ^{14}N NQR, overtone, and double-quantum energy level diagrams.....	130
Figure 8.2. Double-quantum cross-polarization.....	131
Figure 8.3. Triple-resonance double-quantum cross-polarization.....	133
Figure 9.1. ^{13}C NMR spectrum of wild-type hPrP 89-143.....	141
Figure 9.2. ^{13}C NMR spectra of wild-type and 3AV (aggregated) hPrP 89-143.....	142
Figure 9.3. ^{13}C NMR spectrum of wild-type mPrP 89-143.....	144
Figure 9.4. ^{13}C NMR spectra of wild-type and P101L (aggregated) mPrP 89-143.....	145
Figure 10.1. Structure of α -cyclodextrin.....	149
Figure 10.2. ^{129}Xe NMR spectrum of xenon in a α -cyclodextrin:DMSO solution.....	150
Figure 10.3. ^1H SPINOE spectrum of α -cyclodextrin in DMSO.....	152
Figure 10.4. Schematic of the possible locations of xenon in α -cyclodextrin.....	154
Figure 11.1. Structure of cryptophane-A.....	157
Figure 11.2. ^{129}Xe NMR spectrum of xenon in a cryptophane-A.....	159
Figure 11.3. Time-evolution of the ^{129}Xe signal in cryptophane-A.....	161

Figure 11.4. ^1H SPINOE spectrum of cryptophane-A in $(\text{CDCl}_2)_2$	162
Figure 11.5. Possible conformations for the linker bridges in cryptophane-A	166

List of Tables

Table 1.1. Elements of the $l = 0, 1,$ and 2 rank spherical tensors.....	9
Table 1.2. Second rank ($l = 2$) reduced Wigner rotation matrix elements.....	9
Table 2.1. Categorization of factors effecting chemical shifts in proteins	50
Table 4.1. Common prion diseases in mammalian species.....	66
Table 4.2. Human prion diseases.....	67
Table 4.3. PrP mutations that cause familial prion diseases	71
Table 5.1. $^{13}\text{C}_\alpha$ -labeled peptides containing alanine, leucine, and valine residues.....	81
Table 5.2. Experimentally measured $^{13}\text{C}_\alpha$ chemical-shift tensors	90
Table 5.3. Summary of dihedral angles predicted using the CSA/Z approach	96
Table 8.1. ^{14}N quadrupolar coupling constants for amino acids	127
Table 9.1. ^{13}C labels used for studying PrP 89-143.....	140
Table 9.2. ^{13}C chemical shifts in wild-type and 3AV hPrP 89-143	141
Table 9.3. ^{13}C chemical shifts in wild-type and P101L mPrP 89-143.....	144
Table 10.1. ^1H - ^{129}Xe cross-relaxation rates and ^1H T_1 's in α -cyclodextrin.....	153
Table 11.1. ^1H - ^{129}Xe cross-relaxation rates and ^1H T_1 's in cryptophane-A.....	161
Table 11.2. Relative H-Xe distances for conformations of cryptophane-A	168



Acknowledgements

The number of people that I need to thank for getting me this far in life is quite long, so I choose to write these acknowledgements in chronological order. First I must thank my parents. Their encouragement and love over the past 27 years has sustained me through far worse than I could possibly imagine. Aside from the literal fact that I could not have come this far without them, I can honestly say that I would not be in the position I am today without their continuous support.

Next I would like to thank my brother, Russell. Sure he beat the snot out of me on numerous occasions when I was younger, but now I look on those times as a growth experience. Besides, it was his desire to compete in absolutely everything that pushed me away from the legal profession and into science.

Next on my list of people to acknowledge are my two high-school chemistry teachers, Jerry Murray and Kate Smirnoff. Whenever I hear people cursing chemistry and saying it was too difficult to understand, I thank God that I had teachers like Mr. Murray and Mrs. Smirnoff who not only made chemistry interesting, but made chemistry fun. This incredible luck with chemistry teachers continued into college with Prof. Steve Zuhmdal, who not only was the best general chemistry teacher a student could ever hope for, but also was instrumental in developing my love of teaching.

I was first introduced to physical chemistry research as a freshman at the University of Illinois by Prof. Eric Oldfield. At the time I was scared to death at the prospect of doing research, since all I had completed was a year of general chemistry. However, with the help of Prof. Oldfield, post-docs Angel de Dios and John Pearson, and others such as Jessica Ballinger and Hongbiao Le, I managed to thrive in the Oldfield

group for over three years. I am eternally grateful to Eric Oldfield for giving me such an opportunity so early on in my undergraduate years, and for pointing me in the right direction after I left the University of Illinois.

For the past five years I have worked in the Pines group at the University of California, Berkeley. I owe any success I have had here in research and teaching to Prof. Alexander Pines. I could not begin to list all of the things that I have learned from Alex over the past few years, and I am forever grateful for the opportunities he has given me. I am also grateful to Hans-Marcus Ludwig Bitter, Boyd Goodson, Marco Tomaselli, Thomas Meersmann, Jonathan Heller, Mathias Haake, Yi-Qiao Song and Prof. David Wemmer for their help, friendship, and criticism (when necessary). Finally, I would like to thank the Pinenuts, past and present, for providing a stimulating environment for me to work in, especially Matt Augustine, Matthias Ernst, Fred Salsbury, Annjoe Wong-Foy, Dione Carmichael, Michel Luhmer, Eike Brunner, Rebecca Taylor, Yung-ya Lin, Megan Spence, Malgorzata Marjanska, and Susan DePaul. I would also like to thank our collaborators, including Haydn Ball, David King, Stanley Prusiner, Lori Sanders, and Joshua Grimley. I also gratefully acknowledge the Howard Hughes Medical Institute for my pre-doctoral fellowship.

Finally, I would like to thank my wife, Elizabeth. Her love and support have been instrumental in my surviving the last 4 years of my graduate career.

I. Introduction

Chapter 1: Solid-State Nuclear Magnetic Resonance

1.1. Introduction

The primary focus of this dissertation regards the development and implementation of novel techniques in NMR for studying biological molecules in both the liquid and solid state. Therefore, a reasonable place to begin is with a basic description of the quantum mechanics behind the NMR experiments that will be discussed.

1.1.1. The Zeeman Effect

Most nuclei have spin, and so possess an intrinsic magnetic moment that is directly proportional to the spin of the nucleus. This relationship can be seen in eq. (1.1),

$$(1.1) \quad \vec{\mu} = \gamma \vec{I},$$

where $\vec{\mu}$ is the magnetic moment operator, γ is the magnetogyric ratio and \vec{I} is the nuclear angular-momentum operator. In the presence of an external magnetic field, \vec{B} , the energy of a nucleus becomes dependent on its spin, giving rise to the Zeeman effect, which is described by the Hamiltonian

$$(1.2) \quad \begin{aligned} H_Z &= \vec{\mu} \cdot \vec{B} \\ &= \gamma \vec{I} \cdot \vec{B}, \end{aligned}$$

where H_Z is referred to as the Zeeman Hamiltonian. If the external field is taken to be along the z-axis such that $B_0 = B_z$, eq. (1.2) can be rewritten as

$$(1.3) \quad H_Z = \gamma B_0 I_z.$$

The energy of a nucleus with a spin state $|I, m\rangle$ in a magnetic field B_0 can be determined by operating on $|I, m\rangle$ with H_Z :

$$(1.4) \quad E_m = \langle I, m | H_Z | I, m \rangle = \gamma B_0 \langle I, m | I_z | I, m \rangle = \gamma B_0 \hbar m.$$

For a spin $I = 1/2$ nucleus, this leads to a splitting of the normally degenerate $m = +1/2$ and $-1/2$ energy levels, with $\Delta E_Z = \gamma B_0 \hbar$ (fig. 1.1). The resonance frequency that corresponds to this splitting is commonly known as the Larmour frequency, ω_0 , where

$$(1.5) \quad \omega_0 = 2\pi\nu_0 = \frac{\Delta E_Z}{\hbar} = \gamma B_0.$$

The fact that ω_0 does not depend on \hbar explains why the Zeeman effect in NMR can be explained in purely classical terms[1].

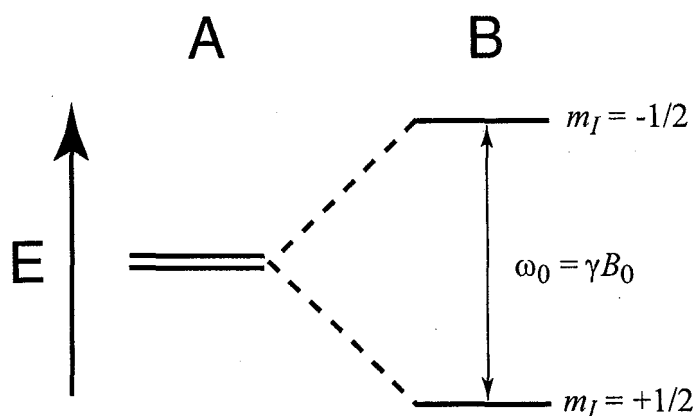


Figure 1.1. Energy levels of a spin $I = 1/2$ nucleus both with and without the presence of an external magnetic field. (A) Without the presence of a magnetic field, the $m = +1/2$ and $m = -1/2$ spin states have degenerate energies. (B) In the presence of an external field, the two states are split by $\gamma \hbar B_0$.

1.1.2. Boltzmann Statistics and NMR Sensitivity

Although it is often convenient to think of nuclear magnetic resonance in terms of one or two spins, NMR is fundamentally a bulk effect. The magnetic moments of

individual nuclei are far too small to be detected alone; rather the fluctuating magnetic field detected in the coil of an NMR probe is the product of a coherent precession of many spins, each contributing its small magnetic moment to the detected signal. Thus to properly describe an NMR experiment, the sample must be considered an ensemble of spins, whose behavior can be described using Boltzmann statistics.

In an ensemble of spin $I = 1/2$ nuclei, if N_{\uparrow} is taken to be the total number of nuclei with $m = +1/2$, and N_{\downarrow} is the total number of nuclei with $m = -1/2$, then the fractional populations of the two spin orientations, W_{\uparrow} and W_{\downarrow} , are given by

$$(1.6) \quad W_{\uparrow} = \frac{N_{\uparrow}}{N_{\uparrow} + N_{\downarrow}} \quad \text{and} \quad W_{\downarrow} = \frac{N_{\downarrow}}{N_{\uparrow} + N_{\downarrow}}.$$

The total polarization of the sample can then be written as

$$(1.7) \quad P = W_{\uparrow} - W_{\downarrow},$$

where $P = 1$ denotes that all spins are in the $m = +1/2$ orientation and $P = -1$ denotes that all spins are in the $m = -1/2$ orientation. The values of W_{\uparrow} and W_{\downarrow} can be found using the Boltzmann equation,

$$(1.8) \quad W_{\uparrow} = \frac{\exp\left(\frac{-E_{\uparrow}}{kT}\right)}{\exp\left(\frac{-E_{\uparrow}}{kT}\right) + \exp\left(\frac{-E_{\downarrow}}{kT}\right)} \quad \text{and} \quad W_{\downarrow} = \frac{\exp\left(\frac{-E_{\downarrow}}{kT}\right)}{\exp\left(\frac{-E_{\uparrow}}{kT}\right) + \exp\left(\frac{-E_{\downarrow}}{kT}\right)}.$$

Thus the polarization of a sample of spin $I = 1/2$ nuclei is just

$$(1.9) \quad P = \frac{\exp\left(\frac{\gamma\hbar B_0}{2kT}\right) - \exp\left(\frac{-\gamma\hbar B_0}{2kT}\right)}{\exp\left(\frac{\gamma\hbar B_0}{2kT}\right) + \exp\left(\frac{-\gamma\hbar B_0}{2kT}\right)}.$$

Since most NMR experiments are performed at or around room temperature, kT is almost always much larger than $\gamma\hbar B_0$. Therefore, each exponent can be expanded in a Taylor series to obtain

$$(1.10) \quad P \approx \frac{\left[1 + \frac{\gamma\hbar B_0}{2kT}\right] - \left[1 - \frac{\gamma\hbar B_0}{2kT}\right]}{\left[1 + \frac{\gamma\hbar B_0}{2kT}\right] + \left[1 - \frac{\gamma\hbar B_0}{2kT}\right]} = \frac{\gamma\hbar B_0}{2kT}.$$

For protons in a field of 11.72 T, corresponding to a Larmour frequency of ~ 500 MHz, the value of P is 6.76×10^{-6} . This explains why NMR spectroscopy is notoriously insensitive. The magnetization measured in an NMR experiment is proportional to the polarization, which measures the number of spins that are preferentially aligned with the external magnetic field. At 11.72 T, only ~ 7 out of every 1×10^6 ^1H nuclei are preferentially oriented along B_0 . Therefore, in a sample containing 1×10^{18} ^1H nuclei, the magnetic moments of only $\sim 7 \times 10^{12}$ spins are actually detected. There are two simple ways to enhance the polarization of a sample that are evident from eq. (1.9); the strength of the external field, B_0 , can be increased, or the temperature can be decreased. Unfortunately, there are technical limitations that should soon slow the growth of magnetic fields, and practical reasons why it is often undesirable to work at very low temperatures. However, there are techniques such as cross-polarization and optical pumping that allow the polarization of a sample to be increased. Both of these techniques will be discussed later.

1.1.3. Tensor Notation

Hamiltonians in NMR involve interactions between a nuclear spin and its environment. That environment can consist of an external field (chemical shift and Zeeman Hamiltonians), another spin (dipolar couplings), the lattice (relaxation), or an electric field gradient (quadrupolar Hamiltonian). However, despite the differences in their origin, almost NMR Hamiltonians can be written in a similar form,

$$(1.11) \quad H = \vec{X} \cdot \hat{A} \cdot \vec{Y},$$

where \vec{X} is a spin vector, \vec{Y} is either a second spin vector or a vector describing an external field, and \hat{A} is a 2nd rank Cartesian tensor that relates the both magnitude and orientational dependence of the Hamiltonian. Written in matrix form, the Hamiltonian in eq. (1.11) is simply

$$(1.12) \quad H = \begin{bmatrix} X_x & X_y & X_z \end{bmatrix} \begin{bmatrix} A_{xx} & A_{xy} & A_{xz} \\ A_{yx} & A_{yy} & A_{yz} \\ A_{zx} & A_{zy} & A_{zz} \end{bmatrix} \begin{bmatrix} Y_x \\ Y_y \\ Y_z \end{bmatrix},$$

or

$$(1.13) \quad H = \sum_{i,y=x,y,z} X_i A_{ij} Y_j.$$

For example, in the Zeeman Hamiltonian, $\vec{X} = [I_x \ I_y \ I_z]$, $\vec{Y} = [0 \ 0 \ B_0]$, and since the Zeeman splitting is invariant to rotation, $\hat{A} = \gamma \hat{1}$, giving

$$(1.14) \quad H_Z = \begin{bmatrix} I_x & I_y & I_z \end{bmatrix} \begin{bmatrix} \gamma & 0 & 0 \\ 0 & \gamma & 0 \\ 0 & 0 & \gamma \end{bmatrix} \begin{bmatrix} 0 \\ 0 \\ B_0 \end{bmatrix} = \gamma B_0 I_z,$$

which is the same result obtained in eq. (1.3). The magnitude of the Hamiltonian in any frame is obtained through a unitary rotation of the spatial Cartesian matrix. This can be

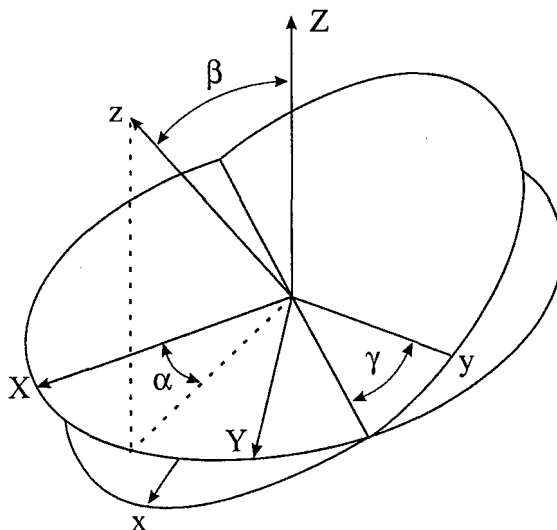


Figure 1.2. Definition of the Euler angles, α , β , and γ . These three angles allow the transformation of a tensor from a coordinate system defined by axes X, Y, and Z (\hat{A}) to one defined by x, y, and z (\hat{a}). Taken from Ref. [2].

accomplished by rotations about the three Euler angles, α , β , and γ , as defined in fig. 1.2 such that

$$(1.15) \quad \hat{a} = \hat{R}(\alpha, \beta, \gamma) \cdot \hat{A} \cdot \hat{R}^{-1}(\alpha, \beta, \gamma).$$

It should be noted that because the rotation is unitary, the value of $Tr\{\hat{A}\}$, which corresponds to the isotropic component of \hat{A} , does not change.

Although it is possible to describe all NMR Hamiltonians in the manner expressed in eq. (1.11), it is often undesirable to utilize Cartesian coordinates when working with NMR Hamiltonians, especially when sample spinning is considered. It is instead preferable to transform the Hamiltonian into a spherical coordinate system, where actions such as sample spinning can be written as a function of one polar angle as opposed to

three Cartesian coordinates. Since X_i , Y_i , and A_{ij} are scalar quantities, eq. (1.13) can be rewritten in the form

$$(1.16) \quad H = \sum_{i,j=x,y,z} A_{ij} X_i Y_j,$$

whose analog in spherical coordinates is

$$(1.17) \quad H = \sum_{l=0}^2 \sum_{q=-2}^2 (-1)^q A_{lq} T_{l-q},$$

where \hat{A} is the spherical tensor corresponding to the spatial part of the Hamiltonian and \hat{T} (a direct product of \vec{Y} and \vec{X}) is the spherical tensor corresponding to the spin part of the Hamiltonian. Just as polar coordinates result from combinations of Cartesian coordinates, the components of the spherical tensor are simply linear combinations of the terms of the Cartesian tensor, as shown in table 1.1. Rotation of a spherical tensor can be accomplished using the expression

$$(1.18) \quad \begin{aligned} a_{lq} &= \sum_{k=-l}^l A_{lk} D_{kq}^{(l)}(\alpha, \beta, \gamma) \\ &= \sum_{k=-l}^l A_{lk} \exp[-i\alpha k] d_{kq}^{(l)}(\beta) \exp[-i\gamma q], \end{aligned}$$

where $\hat{D}^{(l)}$ is the l^{th} rank Wigner rotation matrix and the $d_{kq}^{(l)}(\beta)$'s are elements of the reduced Wigner rotation matrix (shown in table 1.2 for $l = 2$).

1.2. Fundamental Interactions in Solid-State NMR

In high-field nuclear magnetic resonance, the Zeeman interaction dominates the resonant frequency of nuclei, as it is typically at least three orders of magnitude larger than any other interaction (with the exception of quadrupolar nuclei, where the quadrupolar coupling can in some cases exceed 20 MHz). Therefore, it is possible to

Table 1.1. Elements of the $l = 0, 1,$ and 2 rank spherical tensors for spin and space.

	l, m	Spin, T_{lm}	Space, A_{lm}
Scalar:	0,0	$-\left(\frac{1}{\sqrt{3}}\right)[I_x S_x + I_y S_y + I_z S_z]$	$-\left(\frac{1}{\sqrt{3}}\right)[A_{xx} + A_{yy} + A_{zz}]$
Antisymmetric:	1,0	$-\left(\frac{1}{\sqrt{2}}\right)[I_x S_y - I_y S_x]$	$-\left(\frac{1}{\sqrt{2}}\right)[A_{xy} - A_{yx}]$
	1, ± 1	$\frac{1}{2}[I_z S_x - I_x S_z \pm i(I_z S_y - I_y S_z)]$	$\frac{1}{2}[A_{zx} - A_{xz} \pm i(A_{zy} - A_{yz})]$
Symmetric:	2,0	$\left(\frac{1}{\sqrt{6}}\right)[2I_z S_z - I_x S_x - I_y S_y]$	$\left(\frac{1}{\sqrt{6}}\right)[2A_{zz} - A_{xx} - A_{yy}]$
	2, ± 1	$\mp \frac{1}{2}[I_x S_z + I_z S_x \pm i(I_y S_z + I_z S_y)]$	$\mp \frac{1}{2}[A_{xz} + A_{zx} \pm i(A_{yz} + A_{zy})]$
	2, ± 2	$\frac{1}{2}[I_x S_x - I_y S_y \pm (I_x S_y + I_y S_x)]$	$\frac{1}{2}[A_{xx} - A_{yy} \pm (A_{xy} + A_{yx})]$

Table 1.2. Second rank ($l = 2$) reduced Wigner rotation matrix elements, $d_{kq}^{(2)}(\beta)$.

$k \setminus q$	2	1	0	-1	-2
2	$\left(\frac{1 + \cos \beta}{2}\right)^2$	$-\frac{1 + \cos \beta}{2} \sin \beta$	$\sqrt{\frac{3}{8}} \sin^2 \beta$	$-\frac{1 - \cos \beta}{2} \sin \beta$	$\left(\frac{1 - \cos \beta}{2}\right)^2$
1	$\frac{1 + \cos \beta}{2} \sin \beta$	$\cos^2 \beta - \frac{1 - \cos \beta}{2}$	$-\sqrt{\frac{3}{8}} \sin 2\beta$	$\frac{1 + \cos \beta}{2} - \cos^2 \beta$	$-\frac{1 - \cos \beta}{2} \sin \beta$
0	$\sqrt{\frac{3}{8}} \sin^2 \beta$	$\sqrt{\frac{3}{8}} \sin 2\beta$	$\frac{3 \cos^2 \beta - 1}{2}$	$-\sqrt{\frac{3}{8}} \sin 2\beta$	$\sqrt{\frac{3}{8}} \sin^2 \beta$
-1	$\frac{1 - \cos \beta}{2} \sin \beta$	$\frac{1 + \cos \beta}{2} - \cos^2 \beta$	$\sqrt{\frac{3}{8}} \sin 2\beta$	$\cos^2 \beta - \frac{1 - \cos \beta}{2}$	$-\frac{1 + \cos \beta}{2} \sin \beta$
-2	$\left(\frac{1 - \cos \beta}{2}\right)^2$	$\frac{1 - \cos \beta}{2} \sin \beta$	$\sqrt{\frac{3}{8}} \sin^2 \beta$	$\frac{1 + \cos \beta}{2} \sin \beta$	$\left(\frac{1 + \cos \beta}{2}\right)^2$

consider the other principle interactions in solid-state NMR (the chemical shift, dipolar couplings, and the quadrupolar interaction) to be perturbations to the energy splitting produced by the Zeeman effect. Thus, for any nuclear spin state $|I, m\rangle$, one can calculate first- and second-order corrections to the Zeeman energy splitting by using time-independent perturbation theory, where the first-order correction to the energy, $E_m^{(1)}$, is

$$(1.19) \quad E_m^{(1)} = \langle I, m | H_{pert} | I, m \rangle,$$

and the second order correction, $E_m^{(2)}$, is

$$(1.20) \quad E_m^{(2)} = \sum_{m \neq n} \frac{\langle I, m | H_{pert} | I, n \rangle \langle I, n | H_{pert} | I, m \rangle}{E_m - E_n}.$$

Since the energy E_m is just the unperturbed Zeeman energy, eq. (1.20) can be simplified to

$$(1.21) \quad E_m^{(2)} = \frac{1}{\hbar\omega_0} \sum_{m \neq n} \frac{\langle I, m | H_{pert} | I, n \rangle \langle I, n | H_{pert} | I, m \rangle}{m - n},$$

where ω_0 is the Larmour frequency. In the limit of high-field, the second-order correction to the energy is rarely necessary, except when dealing with the quadrupolar interaction, whose strength can be on the order of the Zeeman splitting.

1.2.1. The Chemical Shift

The chemical shift (or chemical shielding), like the Zeeman interaction, results from the application of an external magnetic field to a molecule. Whereas the Zeeman effect is due to a coupling of a nucleus with the external field, the chemical shift arises from a coupling of the surrounding electrons to the external field that produces secondary magnetic fields that can add to or subtract from the total magnetic field felt by the

nucleus. Classically, the induced magnetic fields produced by the electrons, B_e , can be written as

$$(1.22) \quad B_e = -\sigma B_0,$$

where σ is known as the nuclear-shielding factor, and is typically on the order of 1×10^{-6} .

In quantum mechanics, the chemical-shift Hamiltonian can be written as

$$(1.23) \quad H_{cs} = -\gamma B_e = -\gamma\sigma B_0.$$

In actuality, the chemical shift of a nucleus is dependent on its orientation with respect to the external field, and so σ is more appropriately written as the chemical-shift tensor, $\hat{\sigma}$, such that the Cartesian chemical-shift Hamiltonian becomes

$$(1.24) \quad H_{cs} = \vec{I} \cdot \hat{\sigma} \cdot \vec{B}.$$

In spherical coordinates, the spin part of the chemical-shift Hamiltonian involves the direct product of the spin vector, $\vec{I} = [I_x \ I_y \ I_z]$, and the external field vector, $\vec{B} = [0 \ 0 \ B_0]$, so the non-zero elements of \hat{T} are

$$(1.25) \quad \begin{aligned} T_{00} &= -\frac{1}{\sqrt{3}} I_z B_0 \\ T_{1\pm 1} &= -\frac{1}{2} [I_x B_0 \pm I_y B_0] \\ T_{20} &= \frac{1}{\sqrt{6}} I_z B_0 \\ T_{2\pm 1} &= \mp \frac{1}{2} [I_x B_0 \pm i I_y B_0] \\ T_{2\pm 2} &= 0. \end{aligned}$$

The spatial part of the chemical-shift Hamiltonian can be decomposed into a symmetric matrix and an antisymmetric matrix, and since the antisymmetric matrix does not affect the spectrum to first order, it can be ignored. So assuming \hat{A} to be purely symmetric, the relevant spatial elements of the chemical-shift Hamiltonian are

$$\begin{aligned}
(1.26) \quad A_{00} &= \gamma \frac{1}{\sqrt{3}} [\sigma_{xx} + \sigma_{yy} + \sigma_{zz}] \\
A_{20} &= -\gamma \frac{1}{\sqrt{6}} [2\sigma_{zz} - \sigma_{xx} - \sigma_{yy}] \\
A_{2\pm 1} &= \pm \gamma [\sigma_{xz} \pm i\sigma_{yz}].
\end{aligned}$$

Thus, the complete form of the chemical-shift Hamiltonian is

$$(1.27) \quad H_{cs} = A_{00}T_{00} + A_{20}T_{20} + A_{21}T_{2-1} + A_{2-1}T_{21}.$$

This can be further simplified by using the secular approximation, which states that to 1st-order, the $A_{21}T_{2-1}$ and $A_{2-1}T_{21}$ terms are zero, since $\langle I, m | I_x | I, m \rangle = \langle I, m | I_y | I, m \rangle = 0$.

Therefore, all that remains is

$$(1.28) \quad H_{cs} = A_{00}T_{00} + A_{20}T_{20}.$$

The $A_{00}T_{00}$ term is scalar, and so produces an isotropic shift in the resonance frequency of a nucleus. The $A_{20}T_{20}$ term is orientationally dependent, and thus produces an anisotropy in the NMR spectrum.

Any Cartesian spatial tensor can be transformed by rotations into a reference frame in which the tensor is purely diagonal. This frame is referred to as the principle-axis system, or PAS. The chemical-shift Hamiltonian in the PAS using spherical tensors is given by

$$\begin{aligned}
(1.29) \quad {}^{PAS}H_{cs} &= \rho_{00}T_{00} + T_{20} \sum_{k=-2}^2 D_{m0}^{(2)}(\Omega_{PAS}) \rho_{2k} \\
&= \rho_{00}T_{00} + T_{20} \sum_{k=-2}^2 d_{k0}^{(2)}(\beta) \exp[-i\gamma k] \rho_{2k},
\end{aligned}$$

where β and γ are two of the Euler rotation angles, and $\hat{\rho}$ is the spatial tensor in the PAS frame. Since only the ρ_{20} and $\rho_{2\pm 2}$ terms are non-zero ($\hat{\sigma}$ has no off-diagonal terms in the PAS), the chemical-shift Hamiltonian in the PAS is given by

$$(1.30) \quad \begin{aligned} {}^{PAS}H_{cs} &= \rho_{00}T_{00} + T_{20} \left[\frac{1}{2}(3\cos^2\beta - 1)\rho_{20} + \sqrt{\frac{3}{2}}(\sin^2\beta \cos 2\gamma)\rho_{2\pm 2} \right] \\ &= \sigma_{iso}I_z B_0 + \frac{1}{2}\sigma_{csa}I_z B_0 [3\cos^2\beta - 1 - \eta_{csa} \sin^2\beta \cos 2\gamma] \end{aligned}$$

where

$$(1.31) \quad \sigma_{iso} = \frac{\sigma_{xx} + \sigma_{yy} + \sigma_{zz}}{3}, \quad \sigma_{csa} = \sigma_{zz} - \sigma_{iso}, \quad \text{and} \quad \eta_{csa} = \frac{\sigma_{xx} - \sigma_{yy}}{\sigma_{csa}}.$$

The value σ_{iso} is just the isotropic chemical shift and is what is observed in liquid-state NMR where sample rotation completely removes the anisotropic component of the chemical shift. The parameters σ_{csa} and η_{csa} are often referred to as the width and the anisotropy, and describe the shape of the distorted electron density. The effect that H_{cs} has on the resonance frequency of a particular crystallite can be found using 1st-order perturbation theory, which gives a correction (ΔE_{cs}) to the Zeeman energy splitting (ΔE_Z),

$$(1.32) \quad \Delta E_{cs} = \sigma_{iso}B_0 + \frac{1}{2}\sigma_{csa}B_0 [3\cos^2\beta - 1 - \eta_{csa} \sin^2\beta \cos 2\gamma].$$

Figure 1.3 shows a series of CSA lineshapes for different values of η_{csa} . When $\eta_{csa} = 0.0$, $\sigma_{xx} = \sigma_{yy}$ and the lineshape shown in fig. 1.3a results. For $\eta_{csa} = 1.0$, $\sigma_{xx} - \sigma_{yy} = \sigma_{yy} - \sigma_{zz}$ and the lineshape shown in fig. 1.3c results.

1.2.2. The Heteronuclear Dipolar Interaction

The heteronuclear dipolar coupling arises from an interaction between the nuclear magnetic moments of two different nuclei, which for simplicity will be designated I and S. In the presence of an external magnetic field, the I spin will align itself either parallel or antiparallel with respect to the external field, B_0 , as will spin S. Since each spin is a

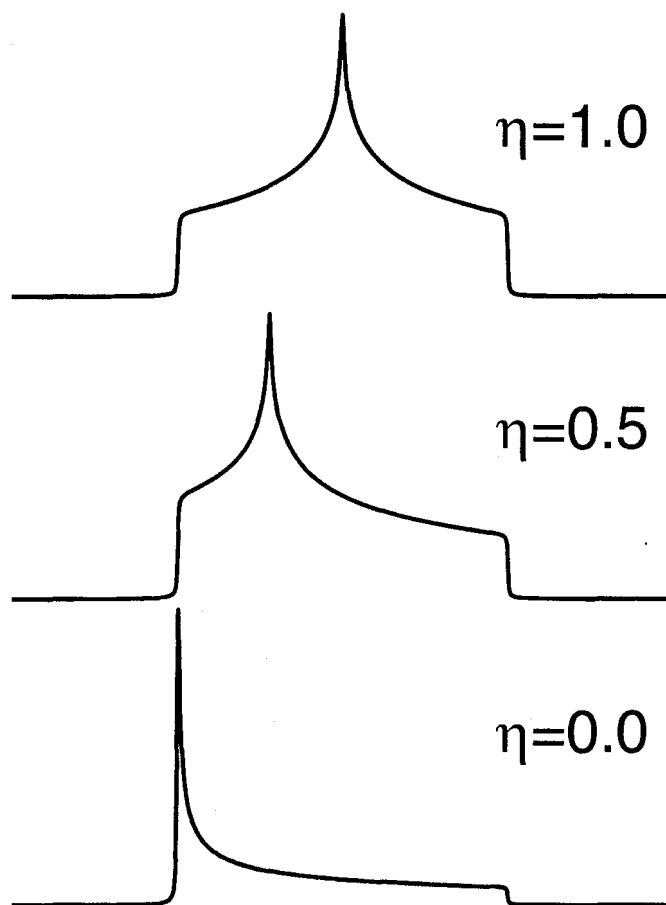


Figure 1.3. Simulated chemical shift-anisotropy lineshapes for different values of η_{csa} .

nuclear magnetic moment that produces a small magnetic field, when the two spins I and S are within a reasonable proximity ($<10 \text{ \AA}$), the S spin will feel the magnetic field produced by the I spin and vice versa. This magnetic field produced by the I-spin will either add to or subtract from the external field felt by the S-spin (depending on the orientation of the I-spin), thus increasing or decreasing the effective magnetic field and changing the resonant frequency of spin S.

The degree to which spin-I affects the magnetic field felt by spin-S is characterized by the heteronuclear dipolar coupling Hamiltonian,

$$(1.33) \quad H_{IS} = \vec{I} \cdot \hat{D}_{IS} \cdot \vec{S},$$

where \vec{I} and \vec{S} are the I-spin and S-spin vectors, respectively, and \hat{D}_{IS} describes the orientational dependence of dipolar coupling with respect to B_0 . Because the dipolar coupling results only in a splitting (as opposed to an isotropic shift), \hat{D}_{IS} must be traceless. In addition, since the dipolar coupling between two nuclei is projected along a vector, \hat{D}_{IS} must be axially symmetric. These two properties can be seen most easily by examining \hat{D}_{IS} in the PAS,

$$(1.34) \quad {}^{PAS} \hat{D}_{IS} = \begin{pmatrix} \frac{-d}{2} & 0 & 0 \\ 0 & \frac{-d}{2} & 0 \\ 0 & 0 & d \end{pmatrix}.$$

The magnitude of the dipolar coupling in eq. (1.34) is given by the dipolar coupling constant, d ,

$$(1.35) \quad d = \frac{\hbar \gamma_I \gamma_S}{r_{IS}^3}$$

where γ_I and γ_S are the I- and S-spin magnetogyric ratios and r_{IS} is the internuclear distance. Because \hat{D}_{IS} is both symmetric and traceless, both the scalar and anti-symmetric elements are zero in spherical tensor notation, and so all that remains is

$$(1.36) \quad \begin{aligned} A_{20} &= \frac{1}{\sqrt{6}} [2D_{zz} - D_{xx} - D_{yy}] \\ A_{2\pm 1} &= \mp [D_{xz} \pm iD_{yz}] \\ A_{2\pm 2} &= \frac{1}{2} [D_{xx} - D_{yy} \pm 2D_{xy}] \end{aligned}$$

and the corresponding spatial tensor elements

$$\begin{aligned}
(1.37) \quad T_{20} &= \frac{1}{\sqrt{6}} [3I_z S_z - \vec{I} \cdot \vec{S}] \\
T_{2\pm 1} &= \mp \frac{1}{2} [I_x S_z + I_z S_x \pm i(I_y S_z + I_z S_y)] \\
T_{2\pm 2} &= \frac{1}{2} [I_x S_x - I_y S_y \pm i(I_x S_y + I_y S_x)].
\end{aligned}$$

Thus, without invoking the secular approximation, the heteronuclear dipolar Hamiltonian can be written as

$$(1.38) \quad H_{IS} = A_{20}T_{20} - A_{21}T_{2-1} - A_{2-1}T_{21} + A_{22}T_{2-2} + A_{2-2}T_{22}.$$

However, by rewriting the $T_{2\pm 1}$ and $T_{2\pm 2}$ spin elements in terms of raising and lowering operators,

$$(1.39) \quad T_{2\pm 1} = \mp \frac{1}{2} (I_z S_{\pm} + S_z I_{\pm}) \quad \text{and} \quad T_{2\pm 2} = \frac{1}{2} I_{\pm} S_{\pm}$$

it becomes clear that both terms are zero since to first order raising or lowering operators do not commute with the Zeeman Hamiltonian. Thus, all that remains of H_{IS} under the secular approximation is the $A_{20}T_{20}$ term. To derive the heteronuclear dipolar Hamiltonian in the PAS, it is only necessary to perform only a single rotation about β :

$$\begin{aligned}
(1.40) \quad {}^{PAS}H_{IS} &= \rho_{20} T_{20} d_{20}^{(2)}(\beta) \\
&= \frac{1}{6} (1 - 3 \cos^2 \beta) [2D_{zz} - D_{xx} - D_{yy}] [3I_z S_z - \vec{I} \cdot \vec{S}].
\end{aligned}$$

If the resonance frequencies of the I- and S- spins are sufficiently different (as they are for most heteronuclear species), the $3I_z S_z - \vec{I} \cdot \vec{S}$ term reduces to $2I_z S_z$. Furthermore, according to eq. (1.34), $2D_{zz} - D_{xx} - D_{yy} = 2d$ in the PAS. Therefore, the final simplified version of the heteronuclear dipolar coupling Hamiltonian is

$$(1.41) \quad H_{IS} = \frac{\hbar \gamma_I \gamma_S}{r_{IS}^3} (1 - 3 \cos^2 \beta) I_z S_z.$$

The $(1 - 3\cos^2\beta)$ orientational dependence of H_{IS} gives rise to the famous “Pake doublet” shown in fig. 1.4. For the large number of I-S internuclear vectors oriented such that $\beta = 90^\circ$, the value of H_{IS} according to eq. (1.41) is $-\frac{d}{2}$, so the frequency splitting between the highest points of the Pake pattern gives the magnitude of the heteronuclear dipolar coupling, d .

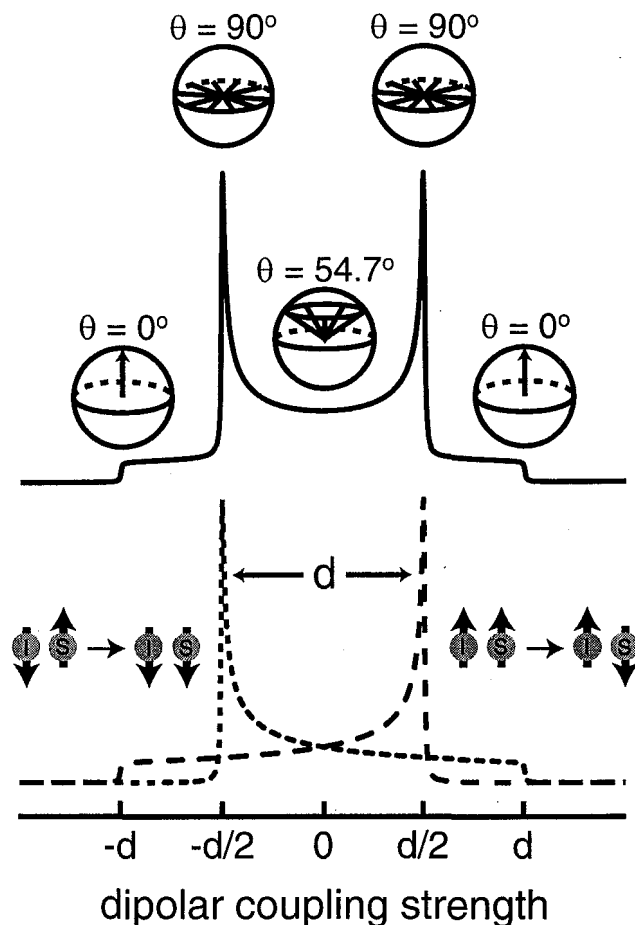


Figure 1.4. A representation of the dipolar Pake pattern or “Pake doublet”. The highest points of the spectrum are due to the geometrically abundant internuclear vectors that point perpendicular to B_0 . The lowest points of the spectrum are due to the relatively few internuclear vectors that point along B_0 . The trace on the bottom shows the two components of the Pake doublet that arise from the S-spin transition in the presence of the two possible I-spin orientations.

1.2.3. The Homonuclear Dipolar Interaction

The homonuclear dipolar coupling arises from an interaction between the nuclear magnetic moments of two nuclei of the same type, which are designated I_1 and I_2 . The form of the homonuclear dipolar coupling Hamiltonian, H_{II} , is identical to that of H_{IS} , with one notable exception. When the chemical shifts of two coupled spins are close enough that their lineshapes overlap, it is possible for the two nuclei to exchange angular momentum through an energy conserving transition, often referred to as a “flip-flop” transition. With the inclusion of the “flip-flop” term, the homonuclear dipolar coupling can be written as

$$(1.42) \quad {}^{PAS}H_{II} = \frac{\hbar\gamma_I^2}{r_{II}^3} (1 - 3\cos^2\beta) \left[2I_{1z}I_{2z} - \frac{1}{2}(I_1^+I_2^- + I_2^+I_1^-) \right].$$

The orientational dependence of H_{II} is identical to that of H_{IS} and so will also result in a dipolar Pake pattern like the one shown in fig. 1.4. However, because of the addition of the “flip-flop” term, the value of H_{II} at $\beta = 90^\circ$ is $0.75d$, so the splitting between the two highest peaks is $1.5d$. It should be noted that only when the flip-flop transition is energy conserving do the $I_1^+I_2^-$ and $I_2^+I_1^-$ terms commute with H_Z . When the resonance frequencies of the I_1 and I_2 spins do not overlap, H_{II} reduces to the exact same form as H_{IS} .

1.2.4. The Quadrupolar Interaction

Unlike spin $I = \frac{1}{2}$ nuclei, spin $I > 1$ nuclei, also referred to as quadrupolar nuclei, possess a non-spherical nuclear charge distribution. As a result, quadrupolar nuclei will couple to electric field gradients present at the nucleus through the quadrupolar interaction. In contrast to the other spin interactions that have been discussed in this

section that are typically orders of magnitude smaller than the Zeeman Hamiltonian, the quadrupolar Hamiltonian can easily exceed 1 MHz. When the quadrupolar coupling does become this large, it is no longer sufficient to describe the quadrupolar Hamiltonian in terms of 1st-order perturbation theory. Rather, the quadrupolar Hamiltonian (H_Q) is often written as a sum of 1st-order ($H_Q^{(1)}$) and 2nd-order ($H_Q^{(2)}$) terms.

As with all other NMR Hamiltonians, H_Q can be written as a products of spin vectors and a spatial tensor,

$$(1.43) \quad H_Q = \vec{I} \cdot \hat{Q} \cdot \vec{I},$$

where both \vec{I} 's refer to the same nucleus. The tensor \hat{Q} describes the magnitude and orientation of the quadrupolar interaction with respect to the external magnetic field. It is often convenient to write \hat{Q} as

$$(1.44) \quad \hat{Q} = q_c \cdot \hat{V},$$

where q_c is a constant, and \hat{V} describes the orientation of the electric field gradient felt at the nucleus with respect to the external magnetic field. As was the case with the dipolar coupling, \hat{V} is traceless and symmetric, and so produces an orientationally dependent splitting of the resonance frequency to 1st-order. However, whereas $D_{xx} = D_{yy}$ for the dipolar coupling, V_{xx} need not equal V_{yy} for the quadrupolar coupling. The constant q_c has the form

$$(1.45) \quad q_c = \frac{3eQ}{2I(2I+1)\hbar},$$

where e is the charge of an electron and Q is the nuclear electric quadrupolar moment, which dictates how strongly a particular nucleus will couple to an electric field gradient.

In spherical coordinates, the spin vectors of the quadrupolar Hamiltonian merge to form the following non-zero terms of the spin tensor, \hat{T} :

$$(1.46) \quad \begin{aligned} T_{20} &= \frac{1}{\sqrt{6}} [3I_z^2 - \bar{I}^2] \\ T_{2\pm 1} &= \mp \frac{1}{2} [I_{\pm} I_z + I_z I_{\pm}] \\ T_{2\pm 2} &= \frac{1}{2} [I_{\pm} I_{\pm}]. \end{aligned}$$

The non-zero spatial components of H_Q in spherical coordinates are

$$(1.47) \quad \begin{aligned} A_{20} &= \left(\sqrt{\frac{3}{2}} \right) [V_{zz}] \\ A_{2\pm 1} &= \mp [V_{xz} + iV_{yz}] \\ A_{2\pm 2} &= \frac{1}{2} [V_{xx} - V_{yy}]. \end{aligned}$$

Therefore, the full quadrupolar Hamiltonian can be written as

$$(1.48) \quad H_Q = q_c [A_{20}T_{20} - A_{21}T_{2-1} - A_{2-1}T_{21} + A_{22}T_{2-2} + A_{2-2}T_{22}].$$

Normally at this stage, one might invoke the secular approximation and throw away all but the $A_{20}T_{20}$ term. Indeed, it is through this simplification that one arrives at the form of the 1st-order quadrupolar Hamiltonian,

$$(1.49) \quad H_Q^{(1)} = q_c A_{20} T_{20}.$$

However, as one may recall from eq. (1.21), the 2nd-order correction to the energy of a spin state involves terms that go as $\langle I, m | H | I, m' \rangle$, where $m \neq m'$. For such an integral to be non-zero, each term in H would have to possess either raising or lowering operators. Thus, all of the remaining terms of \hat{A} and \hat{T} comprise the 2nd-order quadrupolar Hamiltonian,

$$(1.50) \quad H_Q^{(2)} = q_c [A_{22}T_{2-2} + A_{2-2}T_{22} - A_{21}T_{2-1} - A_{2-1}T_{21}].$$

The derivation of the orientational dependence of the 2nd-order quadrupolar Hamiltonian is outside the scope of this thesis, and can be found elsewhere[3]. The orientational dependence of the 1st-order quadrupolar Hamiltonian can be derived through a rotation about two angles, β and γ , into the PAS,

$$\begin{aligned}
 {}^{PAS}H_Q^{(1)} &= q_c T_{20} \sum_{m=-2}^2 \rho_{2m} d_{0m}^{(2)}(\beta) \exp(-im\gamma) \\
 (1.51) \quad &= q_c T_{20} \sum_{m=-2}^2 \rho_{2m} d_{0m}^{(2)}(\beta) \exp(-im\gamma) \\
 &= q_c T_{20} \left[\frac{1}{2} (3 \cos^2 \beta - 1) \rho_{20} + \sqrt{\frac{3}{2}} (\sin^2 \beta \cos 2\gamma) \rho_{2\pm 2} \right].
 \end{aligned}$$

By using the parameter η_Q to relate the anisotropy of the quadrupolar interaction,

$$(1.52) \quad \eta_Q = \frac{V_{xx} - V_{yy}}{V_{zz}},$$

and by taking the z-component of the electric field gradient to be eq , $H_Q^{(1)}$ can be further simplified to

$$(1.53) \quad {}^{PAS}H_Q^{(1)} = \frac{3e^2qQ}{2I(I+1)\hbar} \left[3 \cos^2 \beta - 1 - \eta_Q \sin^2 \beta \cos 2\gamma \right] (2I_z^2 - \bar{I}^2).$$

Note that for $\eta_Q = 0$, the orientational dependence of the 1st-order quadrupolar coupling is identical to that of the homo- and heteronuclear dipolar coupling Hamiltonians. It is for this reason that the static 1st-order quadrupolar lineshape produced by a spin $I = 1$ nucleus takes the form of a Pake doublet.

The effect of the quadrupolar interaction on the energy levels of a spin $I = 1$ nucleus is summarized in fig. 1.5[4]. Note that the double-quantum $m = -1$ to $m = +1$ is unaffected to first order. This fact will be utilized in chapter 8 to propose a technique for performing ^{14}N NMR experiments in the solid state.

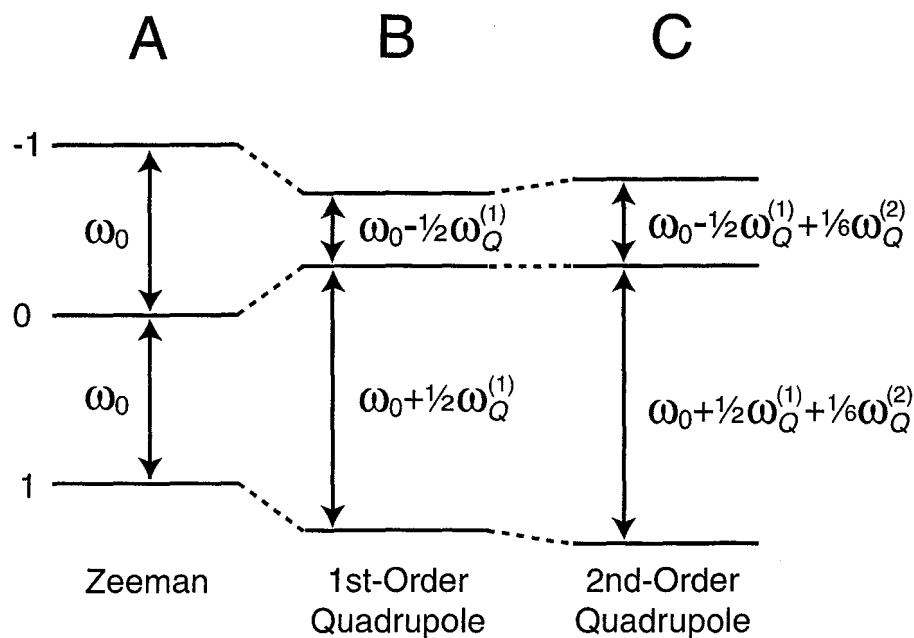


Figure 1.5. Spin $I=1$ energy level diagram for nuclei subject to the Zeeman Hamiltonian (A), to both the Zeeman Hamiltonian and 1st-order quadrupolar Hamiltonian (B), and to the Zeeman, 1st-order quadrupolar, and 2nd-order quadrupolar Hamiltonians (C).

1.3. Magic-Angle Sample Spinning

Thus far, all the spectra that have presented are of static powdered samples, and thus possess inherently low resolution and sensitivity. Although the information available through analysis of these powder lineshapes is considerable, the information is often unattainable when powder patterns from nuclei in different sites overlap, as seen in fig. 1.6. To improve resolution and sensitivity, it is often desirable to suppress dipolar couplings and the chemical-shift anisotropy leaving a spectrum with relatively sharp

lines. The most commonly used method for achieving such a spectral averaging is magic-angle sample spinning.

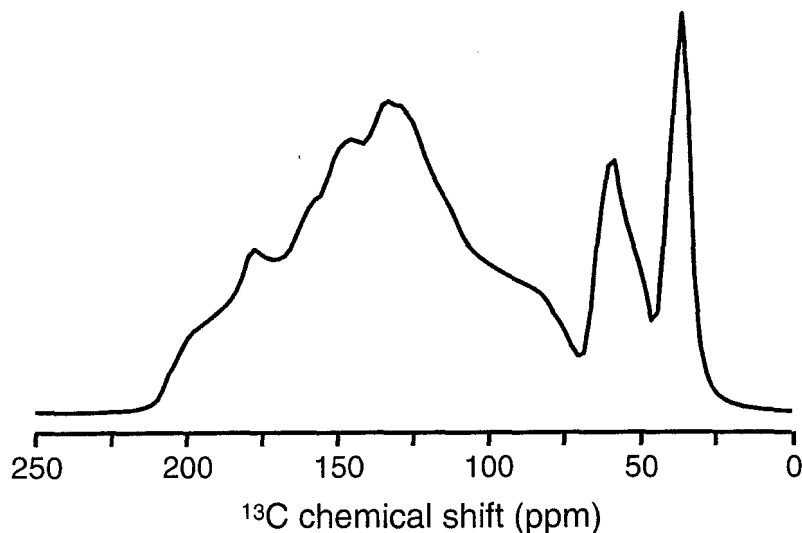


Figure 1.6. Simulated spectrum for three chemically different spin $I = \frac{1}{2}$ sites in a static powder sample. Each site has a different value of the isotropic chemical shift and different anisotropy parameters. Taken from Ref. [2].

1.3.1. Theory of NMR in Rotating Solids

Magic-angle spinning is a technique through which spectral simplification is achieved by averaging away the anisotropic components of the dipolar, chemical shift, and first-order quadrupolar Hamiltonians. As a precursor to the discussion of magic-angle spinning and its general applications, an overview of the effect of sample spinning about a single axis on the chemical shift Hamiltonian is presented.

As seen in eq. (1.28), the truncated chemical-shift Hamiltonian consists of two terms: an isotropic term, $A_{00}T_{00}$, and an anisotropic (orientationally dependent) term, $A_{20}T_{20}$. By transforming the tensor \hat{A} into a new frame defined by the tensor \hat{a} that is

tilted by an angle θ away from the z-axis (along which the external magnetic field lies) and that rotates at a speed ω_r around this new axis, the chemical-shift Hamiltonian under sample spinning becomes time dependent and takes on the form:

$$(1.54) \quad {}^{SS}H_{cs} = a_{00}T_{00} + T_{20} \sum_{q=-2}^2 D_{q0}^{(2)}(\Omega_{rotor}(t))a_{2q},$$

where the rotor frame, $\Omega_{rotor} = (0, \theta, \phi)$, and $\phi = \omega_r t$. The explicit rotor phase at any time t can be written as $\phi(t)$, where $\phi(t) = \omega_r t + \phi_0$, and ϕ_0 is the initial rotor phase. Since

$$(1.55) \quad D_{m'm}^{(l)}(\Psi, \Theta, \Phi) = \exp[-i\Psi m'] d_{m'm}^{(l)}(\Theta) \exp[-i\Phi m'],$$

and $\Psi = 0$, H_{cs} reduces to:

$$(1.56) \quad {}^{SS}H_{cs} = a_{00}T_{00} + T_{20} \sum_{q=-2}^2 d_{q0}^{(2)}(\theta) \exp[-i\phi(t)q] a_{2q}.$$

A second coordinate rotation, $\Omega_{pas} = (\alpha, \beta, \gamma)$, can be used to move the Hamiltonian into the principle-axis system of an individual crystallite, such that

$$(1.57) \quad \rho_{lq} = \sum_{k=-2}^2 D_{kq}^{(l)}(\Omega_{pas}(t)) a_{2k}.$$

When eq. (1.56) is combined with eq. (1.57), the chemical-shift Hamiltonian becomes

$$(1.58) \quad {}^{SS}H_{cs} = \rho_{00}T_{00} + T_{20} \sum_{q=-2}^2 d_{q0}^{(2)}(\theta) \exp[-i\phi(t)q] \sum_{k=-2}^2 D_{kq}^{(l)}(\Omega_{pas}) \rho_{2k},$$

which when expanded is

$$(1.59) \quad {}^{SS}H_{cs} = \rho_{00}T_{00} + T_{20} \sum_{q=-2}^2 d_{q0}^{(2)}(\theta) \exp[-i\phi(t)q] \sum_{k=-2}^2 \exp[-iq\alpha] d_{kq}^{(2)}(\beta) \exp[-ik\gamma] \rho_{2k}.$$

Remembering that the $\rho_{2\pm 1}$ terms are zero in the PAS, the chemical-shift Hamiltonian under sample spinning becomes

$$\begin{aligned}
{}^{SS}H_{cs} = & \rho_{00}T_{00} + \frac{1}{4}(1-3\cos^2\theta)(1-3\cos\beta)\rho_{20}T_{20} + \\
& \sqrt{\frac{3}{8}}(1-3\cos^2\theta)(\sin^2\beta)(\cos 2\gamma)\rho_{2\pm 2}T_{20} + \\
& \frac{1}{2}(\sin 2\theta)[\cos(\phi(t)+\alpha)](\sin 2\beta)\rho_{20}T_{20} + \\
(1.60) \quad & \sqrt{\frac{3}{8}}(\sin 2\theta)[\sin(\phi(t)+\alpha+2\gamma)](\sin\beta+\sin\beta\cos\beta)\rho_{2\pm 2}T_{20} + \\
& \sqrt{\frac{3}{8}}(\sin 2\theta)[\sin(\phi(t)+\alpha-2\gamma)](\sin\beta-\sin\beta\cos\beta)\rho_{2\pm 2}T_{20} + \\
& \frac{1}{2}(\sin^2\theta)[\cos(2\phi(t)+2\alpha)](\sin^2\beta)\rho_{20}T_{20} + \\
& \sqrt{\frac{3}{8}}(\sin^2\theta)[\cos(2\phi(t)+2\alpha)](1+\cos\beta)^2(\cos 2\gamma)\rho_{2\pm 2}T_{20}.
\end{aligned}$$

1.3.2. Fast Magic-Angle Spinning

Spinning a rotor at high speeds around the magic angle has two effects on the Hamiltonian in eq. (1.60). First, at $\theta = 54.74^\circ$, all the terms in eq. (1.60) containing $(1-3\cos^2\theta)$ are made zero. Second, all of the other terms (accept the scalar term) become time dependent and oscillate at frequencies of $\phi(t)$ and $2\phi(t)$. Figure 1.7 shows the evolution of the time-dependent portion of ${}^{MAS}H_{cs}$ as a function of the rotor evolution, $\phi(t)$. When the spinning speed is made much larger than the width of the CSA, the time-dependent terms average to zero and all that remains is the isotropic component of the chemical shift. When the spinning speed is smaller than the width of the CSA, the evolution of the CSA interferes with the averaging produced by the spinning rotor, resulting in the formation of spinning sidebands at integer multiples of the spinning speed.

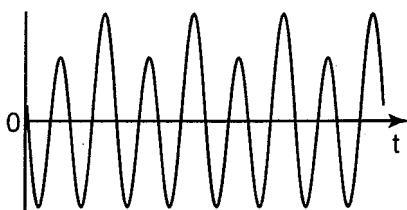


Figure 1.7. Evolution of the anisotropic component of the chemical-shift Hamiltonian under MAS. Over a single rotor period, the average value of H_{cs} is zero.

1.3.3. Slow Magic-Angle Spinning

Although in most circumstances it is desirable to spin at as high a speed as is mechanically possible, there are advantages to spinning at slow speeds, such that the vast majority of the powder pattern has been removed and all that remains is the isotropic peak surrounded by a few spinning sidebands. In this way, the resolution and sensitivity of the spectrum can be greatly enhanced without completely discarding all of the anisotropic information. For example, in systems of rare spin $I = \frac{1}{2}$ nuclei, where heteronuclear dipolar couplings can be effectively removed by broadband decoupling, the principle values of the CSA are routinely determined by fitting spinning sideband spectra to theoretical simulations[5-7]. Figures 1.8b-e show a series of CPMAS spectra of uniformly 10% ^{13}C -labeled glycine acquired at different spinning speeds. The chemical-shift anisotropy of each site was determined by fitting the sidebands of the three slow-MAS spectra (b-d) using the Herzfeld-Berger method[5]. Using the experimentally determined chemical-shift tensor values, a simulated static spectrum of natural abundance ^{13}C -labeled glycine was created (fig. 1.8e) using the fitting program in Appendix A.1.

1.4. Cross Polarization

Compared to other forms of spectroscopy, NMR is inherently insensitive, owing to the small splitting of the nuclear energy levels by the external magnetic field resulting in only a small difference in the spin populations. This is especially the case for NMR of rare spins, such as ^{13}C , where the magnetogyric ratio is one-fourth that of protons, and the isotopic abundance is often very low. Fortunately, a variety of techniques exist for

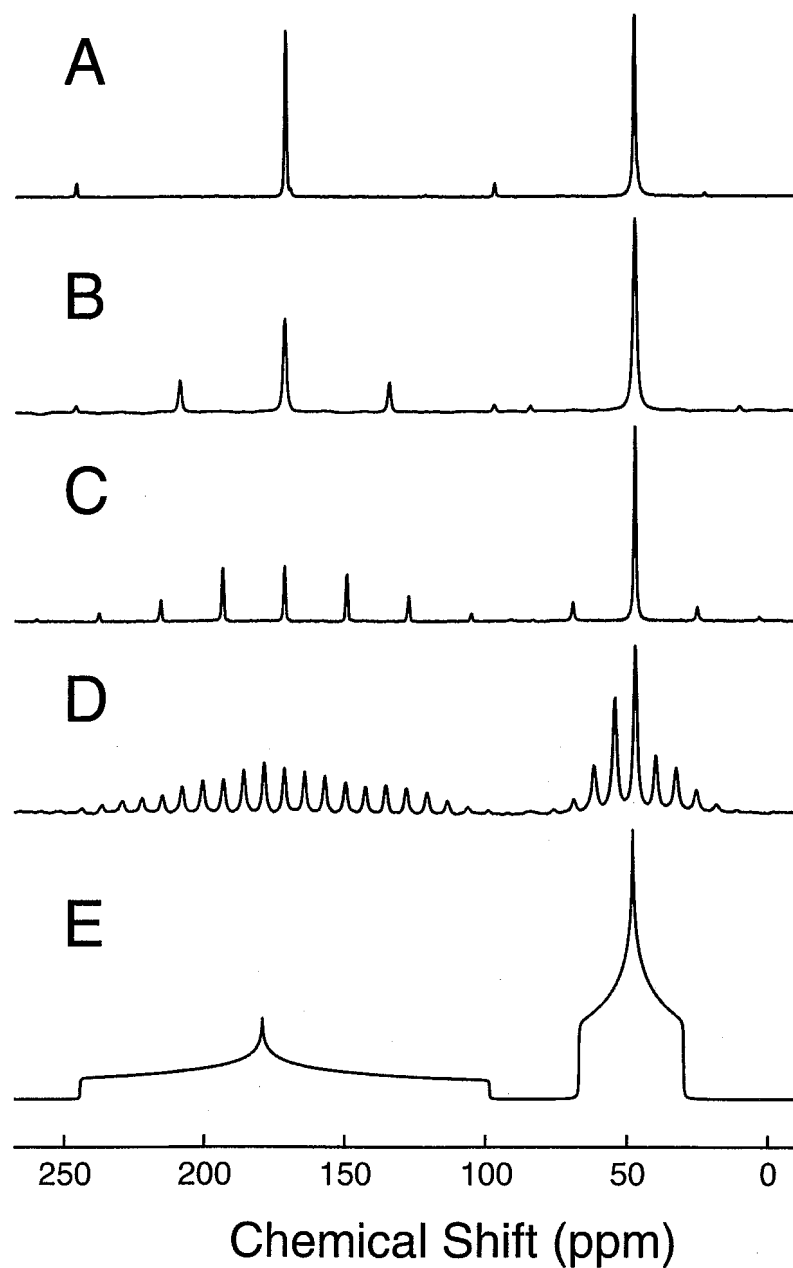


Figure 1.8. 125 MHz solid-state ^{13}C NMR spectra of 10% uniformly ^{13}C labeled glycine powder acquired under continuous-wave ^1H decoupling and magic-angle spinning. The top four spectra correspond to spinning speeds of 10 kHz (A), 5 kHz (B), 2 kHz (C), and 1 kHz (D). As the spinning speed decreases the envelope of spinning sidebands begins to resemble the simulated static NMR spectrum shown in (E).

increasing the spin polarization of nuclei. One such technique, optical pumping, allows the direct manipulation of the nuclear spin populations, and will be discussed at length in later chapters. Another technique, cross polarization, utilizes the existence of abundant (usually high- γ) spins, such as protons, to provide a source of magnetization for polarizing rare spins.

1.4.1. The Hartmann-Hahn Experiment

To enhance the signal of rare spins, such as ^{13}C and ^{15}N nuclei, many solid-state NMR experiments involve the transfer of polarization from abundant spins (usually ^1H nuclei) to rare spins using a technique called Cross-Polarization or CP[8]. CP occurs through the natural entropic tendency for magnetization from highly-polarized nuclei to flow to nuclei with lower polarizations when the two are coupled in some manner. This flow of magnetization is analogous to the flow of heat from a hot object to a cold object when the two are in thermal contact. Unfortunately, magnetization is exchanged between nuclei through mutual, energy conserving spin flips, and for heteronuclei such as ^1H and ^{13}C , such spin flips are only energy conserving at very low fields[9]. Therefore, the exchange of magnetization must be driven externally by the application of RF fields. Although there are many techniques for establishing a dipolar connection between two different spin systems, I and S, perhaps the most effective method was developed by Erwin Hahn and Sven Hartmann in 1962[10].

The Hartmann-Hahn method for cross-polarization requires the simultaneous application of two continuous RF fields, one at the I-spin Larmour frequency and the other at the S-spin Larmour frequency. The effect of any RF field is to rotate the

magnetization about the axis of the applied field. The rotation or "nutaton" rate depends on two factors: the strength and the frequency of the RF field. The nutation rate increases with increasing field strength, and decreases as the frequency of the field moves further from the Larmour frequency. Therefore, an RF field oscillating at the I-spin frequency, say 500 MHz, would have almost no affect on S-spins with a frequency of 125 MHz. Likewise, an RF field tuned to the S-spin resonance frequency would have almost no affect on the I-spins. By applying two RF fields, one tuned to the I-spins the other to the S-spins, both the I-spins and S-spins can be rotated independently around a particular axis at rates dependent on the strengths of the two applied fields. Hartmann and Hahn found that when the nutation frequencies of the I and S spins were equal,

$$(1.61) \quad \Omega_I = \Omega_S,$$

an artificial, energy-conserving dipolar connection between the two spin systems is created with the differences in energy being supplied by the RF fields. It is through this dipolar connection that polarization is transferred between the I- and S-spins.

The experimental implementation of this concept is shown in fig. 1.9a. First, the proton magnetization is pulsed down along the x-axis. RF fields are then applied to the I- and S-spins for a time τ_{mix} , causing the magnetization to be exchanged from the I-spins to the S-spins. Finally, the S-spins are detected while the I-spins are decoupled. The growth of S-spin magnetization during the CP mixing period, τ_{mix} , is dependent on the strength of the I-S dipolar coupling, as shown in fig 1.9b for ^1H - ^{13}C CP in 10% uniformly ^{13}C -labeled glycine. The build-up of polarization in the unprotonated carbonyl carbon requires a longer mixing time than the α -carbon, which is quickly polarized by its bonded protons. Typical mixing times in CP range from between 100 μs to 10 ms.

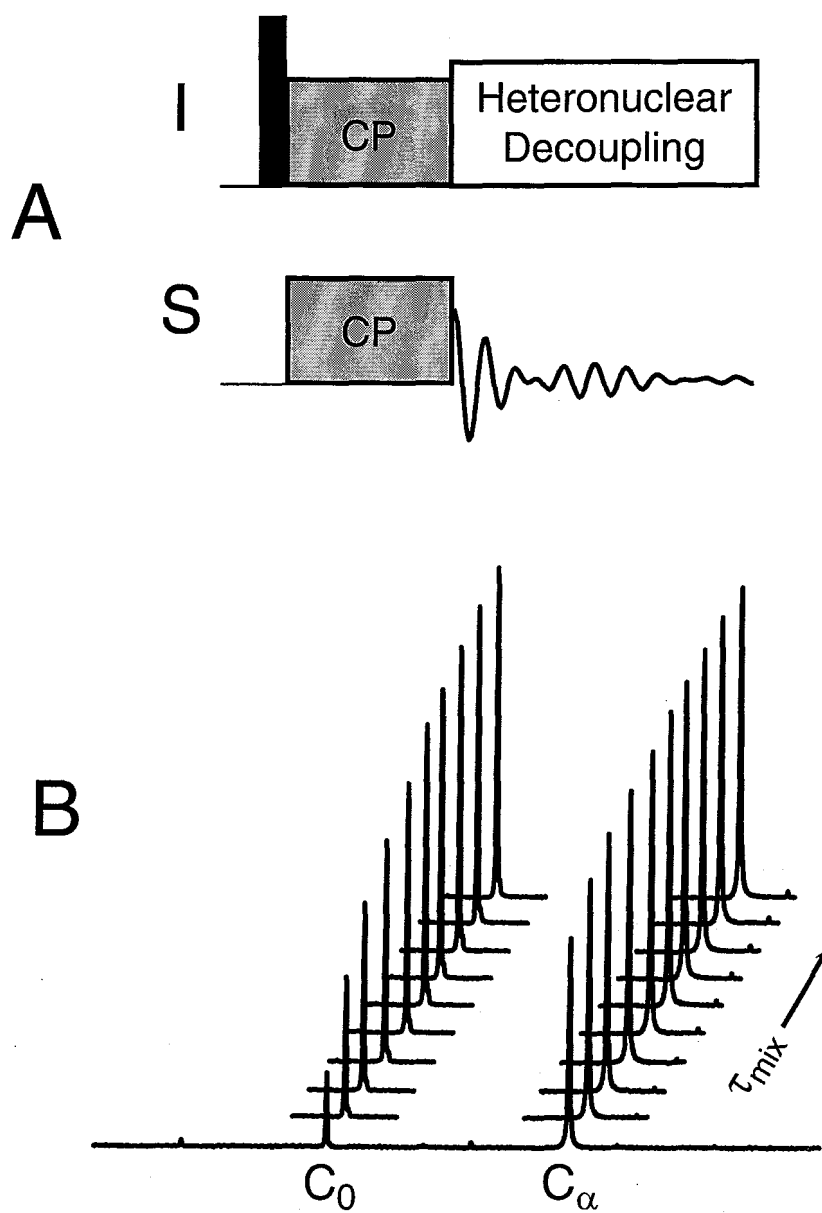


Figure 1.9. Hartmann-Hahn cross polarization. (A) Pulse sequence for the cross-polarization of ^{13}C nuclei from protons with detection of the ^{13}C magnetization. (B) 125 MHz solid-state ^{13}C NMR spectra of 10% uniformly ^{13}C labeled glycine powder acquired using the pulse sequence in (A) as a function of the cross-polarization time, τ_{mix} . Because of the directly bonded H_α protons, the $^{13}\text{C}_\alpha$ nuclei are polarized much faster than the unprotonated carbonyl carbons.

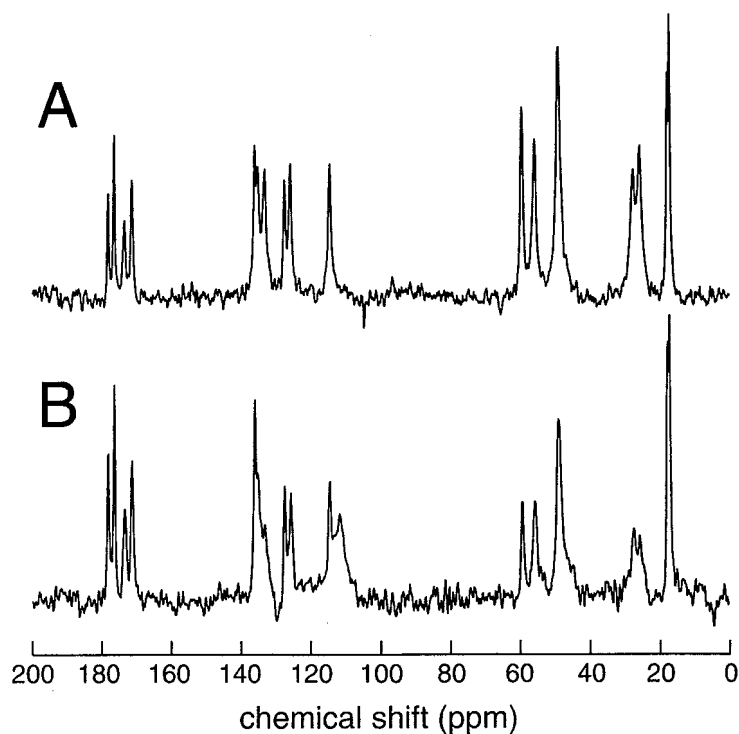


Figure 1.10. 125 MHz solid-state ^{13}C NMR spectra of unlabeled alanyl-histidine powder acquired using cross-polarization from protons (A), and using a standard 1-pulse experiment (B). Both spectra were recorded under MAS at a speed of 12 kHz and using CW ^1H decoupling. The recycle delay for the spectrum in (A) was 2 s. The recycle delay for the spectrum in (B) was 90 s, owing to the long ^{13}C T_1 relaxation time (~ 20 s for this sample).

The maximum theoretical enhancement using the Hartmann-Hahn method of cross-polarization is $\frac{1}{2} \frac{\gamma_I}{\gamma_S}$ (where γ_I and γ_S are the magnetogyric ratios of spins I and S), although this degree of enhancement is rarely attainable. It should be noted, however, that this theoretical enhancement is merely a thermodynamic argument, and does not

account for the practical advantages of using cross-polarization. In most NMR experiments, the acquisition or sampling rate is dictated by the relaxation time (T_1) of the detected nuclei. In CP, the sampling rate depends on the relaxation time of the nuclei from which the magnetization is transferred. Since protons in the solid state have a far shorter relaxation time than most other spin $I = \frac{1}{2}$ nuclei, CP experimental times are usually far shorter than those of simple one-pulse experiments. To illustrate this point, fig. 1.10 shows a natural abundance solid-state ^{13}C spectrum of alanyl-histidine both with and without CP from the protons. Although the signal to noise ratios of the two spectra in figs. 1.10a and 1.10b are comparable ($\sim 1.7:1$) the acquisition time of the non-CP spectrum was 45 times longer than the CP spectrum, owing to the ~ 18 s T_1 of the carbon nuclei.

1.4.2. Cross Polarization under Magic-Angle Spinning

In the previous two subsections, the utility of cross-polarization as a tool for both increasing the polarization of rare or low- γ nuclei and for increasing the acquisition rate was established. However, a problem exists when one wishes to incorporate magic-angle sample spinning into an experiment involving cross polarization, since as was seen in section 1.3.1, the heteronuclear dipolar coupling under MAS is effectively averaged to zero when $\omega_r \gg d$. This raises an interesting question: without a dipolar connection between the two Zeeman reservoirs, how can there be a transfer of polarization? The answer can be found by examining the time-dependent modulation of the heteronuclear dipolar coupling under MAS.

Since the dipolar coupling is traceless and symmetric, the truncated dipolar Hamiltonian for a pair of non-identical spins is simply

$$(1.62) \quad H_{IS} = a_{20}T_{20},$$

which is essentially the same as the chemical shift Hamiltonian, minus the isotropic term.

Under magic-angle spinning, the dipolar Hamiltonian becomes time-dependent, taking on the form[11]

$$(1.63) \quad \begin{aligned} {}^{MAS}H_{IS} &= T_{20} \sum_{m=-2}^2 D_{m0}^{(2)}(\Omega_{rotor}(t)) a_{2m} \\ &= T_{20} \sum_{m=-2}^2 d_{m0}^{(2)}(\theta_M) a_{2m} \exp[-i\phi(t)m] \end{aligned}$$

where $\phi(t)$ is the time-dependent angle carved out by the sample rotation and θ_M is the magic angle. Thus the total heteronuclear dipolar Hamiltonian under MAS is

$$(1.64) \quad \begin{aligned} {}^{MAS}H_{IS} &= \frac{1}{2} a_{20} T_{20} (3 \cos^2 \theta_M - 1) + \\ &\quad \sqrt{\frac{3}{2}} a_{21} T_{20} \sin \theta_M \cos \theta_M \exp[i\phi(t)] + \\ &\quad \sqrt{\frac{3}{2}} a_{2,-1} T_{20} \sin \theta_M \cos \theta_M \exp[-i\phi(t)] + \\ &\quad \sqrt{\frac{3}{8}} a_{22} T_{20} \sin^2 \theta_M \exp[2i\phi(t)] + \\ &\quad \sqrt{\frac{3}{8}} a_{2,-2} T_{20} \sin^2 \theta_M \exp[-2i\phi(t)]. \end{aligned}$$

The first term of ${}^{MAS}H_{IS}$ is zero, and the other four terms oscillate at frequencies of $\pm\omega_r$ and $\pm 2\omega_r$, such that over one complete rotor cycle, the average value of each term is zero.

However it is possible to interfere with this averaging by adjusting the Hartmann-Hahn matching condition such that $\Omega_I = \Omega_S \pm \omega_r$ or $\Omega_I = \Omega_S \pm 2\omega_r$. Under these conditions, the heteronuclear dipolar coupling is essentially “recoupled” and CP is again possible.

Figure 1.11 shows both the static and MAS CP matching profiles for a two-spin system. In normal samples, matching profiles such as the ones in fig. 1.11 are rarely

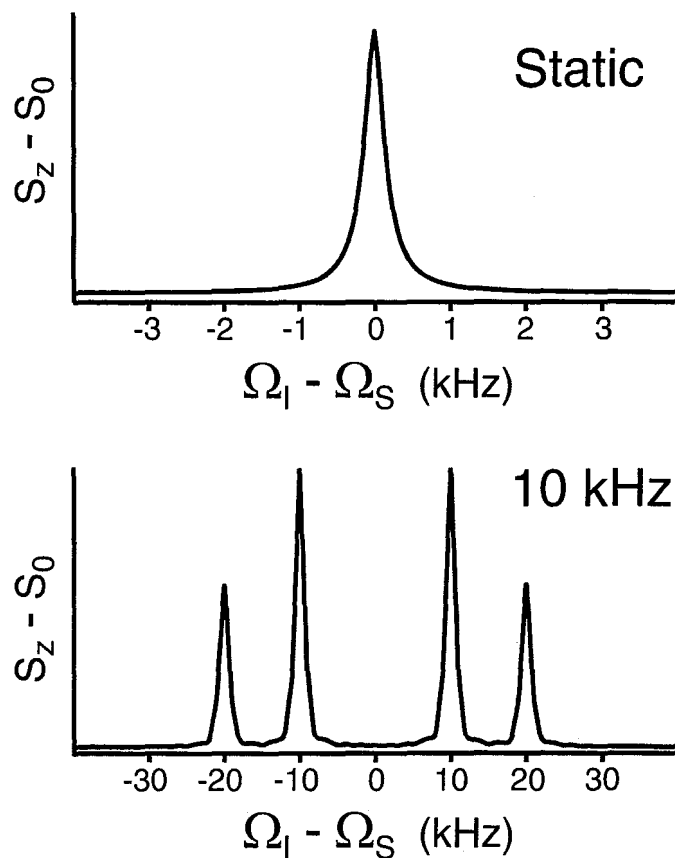


Figure 1.11. S -spin polarization plotted as a function of the Hartmann-Hahn mismatch ($\Omega_I - \Omega_S$) of the S -spin nutation frequency. For static samples, maximum polarization transfer occurs when the I -spin and S -spin nutation frequencies exactly match (A). In spinning samples, the Hartmann-Hahn condition is manifest in four sidebands spaced around $\Omega_I - \Omega_S = 0$ at integer multiples of the spinning speed (B). The four peaks correspond to matching the $a_{2,-2}$, $a_{2,-1}$, $a_{2,1}$, and $a_{2,2}$ terms of the time-dependent I - S dipolar coupling (eq. 1.64).

seen, owing to the inherent broadening of the match condition whenever a system of more than two spins exists[12]. However as spinning speeds increase beyond 10 kHz, problems do arise from the fact that the match condition is often very narrow, and

fluctuations in either the spinning speed or the RF amplitude, as well as the inhomogeneity of the RF field, can lead to little or no polarization being transferred. This is especially true in the case of CP between two rare spins, such as ^{13}C and ^{15}N , where the experiment may indeed involve an isolated spin pair. In such a circumstance, simply locating the extremely narrow matching sidebands can be very difficult. Fortunately, many techniques have been developed to make cross polarization in systems with narrow match conditions more robust. Figure 1.12 shows two of the more simple (yet very effective) methods for decreasing the sensitivity of cross-polarization efficiency to RF inhomogeneity and power fluctuations. These techniques involve modulating the amplitude of one of the spin-locking fields with either a linearly ramped or hyperbolic tangent pulse[13-16]. Although the RF amplitude sweep can be made very broad (and often very long), implementation typically takes the form of a short sweep through one of the four matching sidebands. In addition, there exist other techniques involving combinations of phase, frequency, and/or amplitude modulations that serve to broaden the entire matching profile in order to make it less susceptible to spinning speed and RF fluctuations[13,14,17-19] as well as chemical-shift differences[20].

1.5. Dipolar Recoupling under Magic-Angle Spinning

Although the removal of the chemical-shift anisotropy and dipolar coupling via magic-angle sample spinning is usually necessary to obtain high-resolution spectra in solid-state NMR, it is often desirable to re-introduce either the homo- or heteronuclear dipolar coupling under MAS. A perfect example of such a situation was provided in

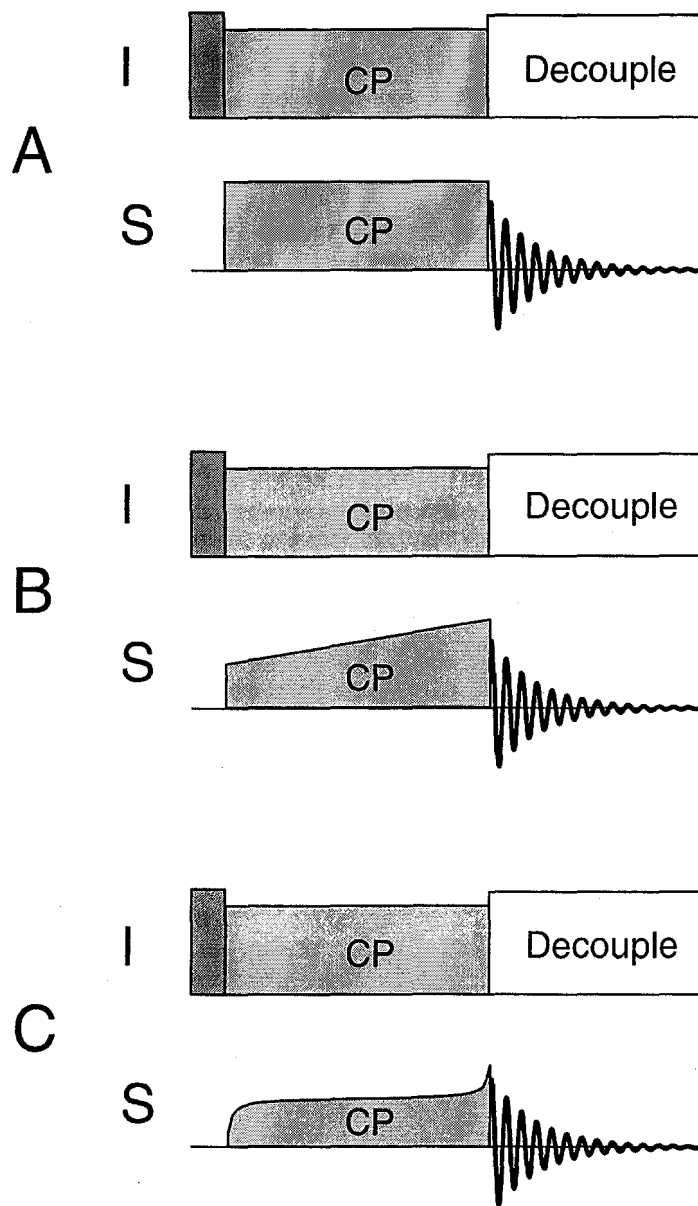


Figure 1.12. Pulse sequences for heteronuclear CPMAS. (A) Typical CPMAS experiment with constant-amplitude RF irradiation on both the I and S spins during the CP mixing period. (B) Ramped-CP experiment in which the RF amplitude is ramped linearly through one (or more) of the sidebands shown in fig. 1.11b. (C) APHH-CP experiment in which the RF amplitude is adiabatically swept through the matching condition by using a long tangential pulse.

subsection 1.4.2, where it was shown that one must “recouple” the heteronuclear dipolar coupling in order to achieve cross polarization under MAS. Another reason for reintroducing the homo- or heteronuclear dipolar Hamiltonian would be for structure determination in solids, where the $\frac{1}{r^3}$ distance dependence of the dipolar coupling can be exploited to measure internuclear distances. In this section, the general theory behind dipolar recoupling under magic-angle sample spinning is presented, followed by examples of both heteronuclear and homonuclear dipolar recoupling experiments.

1.5.1. Heteronuclear Dipolar Recoupling

In all recoupling experiments, the general idea is to interfere with the coherent averaging of the dipolar Hamiltonian such that its overall value is non-zero. In the case of heteronuclear dipolar recoupling, creating such an interference is relatively simple.

Consider the dipolar coupling between two rare spin $I = \frac{1}{2}$ nuclei, such as ^{13}C and ^{15}N . Close inspection of the evolution of a single I-S spin pair under the Hamiltonian in eq. (1.64) reveals that the time integral of H_{IS} over one rotor cycle is zero, as shown in fig. 1.13a. Therefore, if the spinning speed is fast enough, the spatial part of the Hamiltonian is averaged to zero and the dipolar coupling is essentially removed. However by manipulating the *spin* portion of the Hamiltonian, it is possible to interfere with the averaging produced by MAS, and make the value $\langle H_{IS} \rangle$ non-zero. One way to accomplish this is to apply a series of rotor synchronized π -pulses to one of the two spins. Since every π -pulse has the effect of changing the sign of H_{IS} , if two pulses are applied

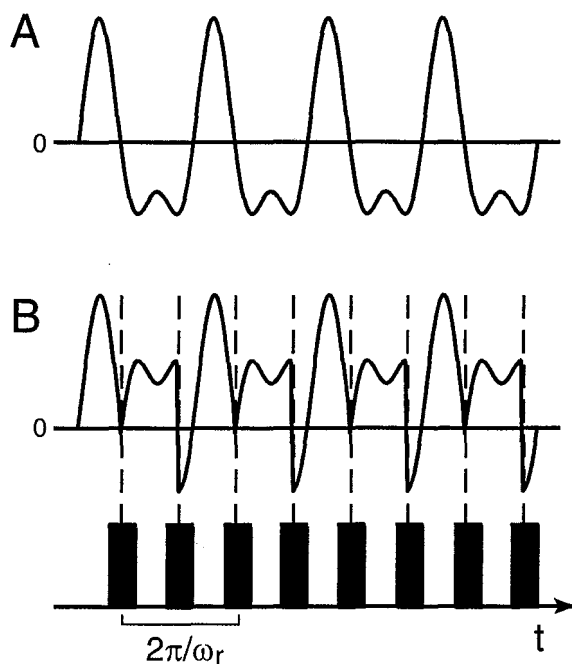


Figure 1.13. Time-dependent behavior of the heteronuclear dipolar coupling. (A) The time-dependent evolution of the heteronuclear dipolar Hamiltonian, H_{IS} , under MAS. Since the integral of the dipolar coupling over a single rotor cycle is zero, the dipolar coupling is effectively removed if the spinning speed is sufficiently high. (B) The time-dependent evolution of H_{IS} under MAS with two π -pulses on the S-spin per rotor cycle. Each π -pulse reverses the sign of the dipolar coupling Hamiltonian, creating a time evolution of H_{IS} that no longer averages to zero.

per rotor cycle, the integral of H_{IS} over one rotor cycle becomes non-zero, as seen in fig. 1.13b. This technique, known as Rotational-Echo Double Resonance (REDOR)[21] is shown in fig. 1.14a for ^{13}C - ^{15}N dipolar recoupling. After cross-polarization from protons (which is optional) the ^{13}C magnetization is allowed to evolve under the ^{13}C - ^{15}N dipolar coupling, which is reintroduced via a series of rotor-synchronized π -pulses on the ^{15}N channel. A π -pulse at time $\frac{t}{2}$ serves to refocus the ^{13}C chemical shift at the end of the

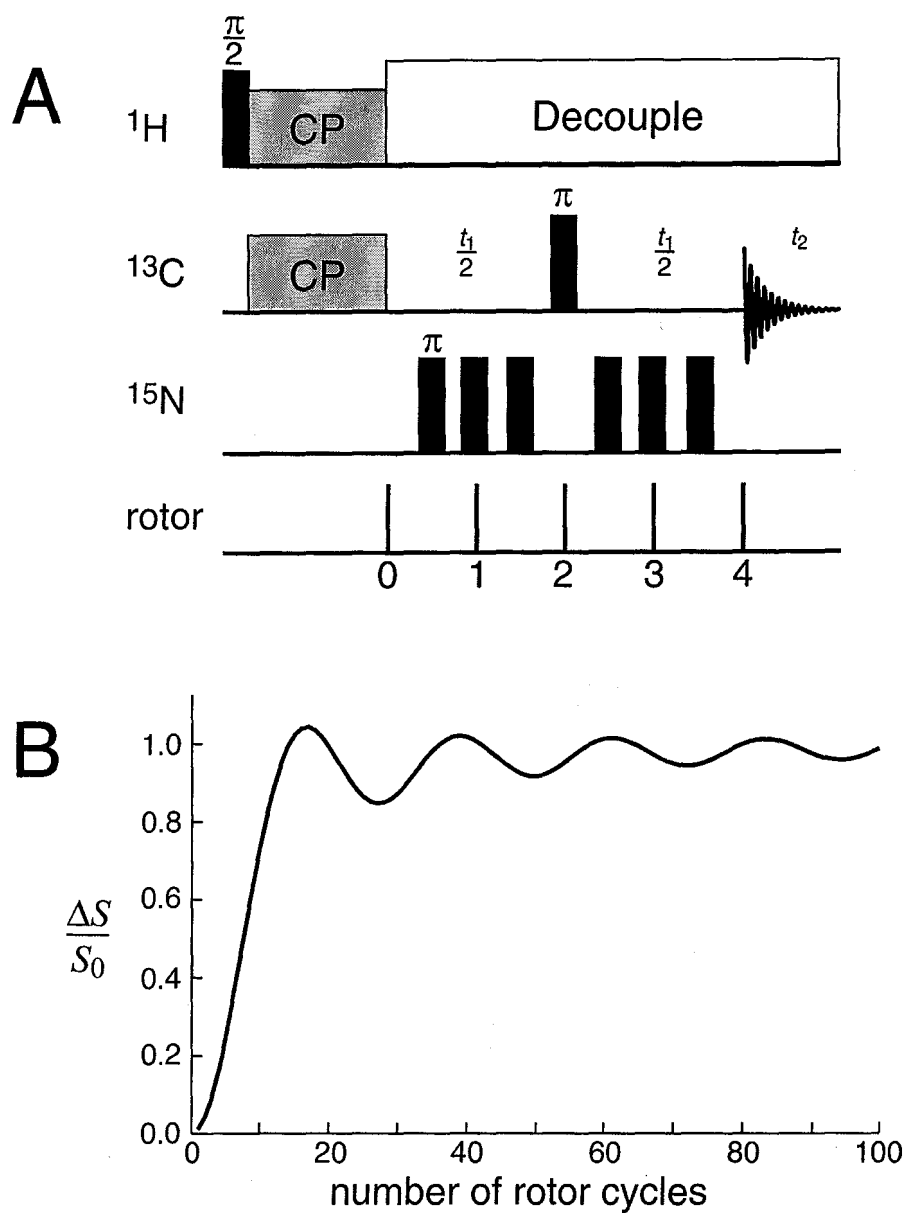


Figure 1.14. (A) REDOR pulse sequence. Cross-polarization of the ^{13}C nuclei is followed by a period t_1 in which the ^{13}C magnetization is dephased by the application of a series of pulses on the ^{15}N magnetization. (B) Decay of the ^{13}C magnetization as a function of the length of the dephasing period, t_1 . The quantity $\Delta S/S$ (known as the REDOR difference) is the normalized difference between the ^{13}C signals with and without the ^{15}N pulses.

dephasing time t_1 . With H_{IS} reintroduced, the ^{13}C magnetization decays with a frequency characterized by the scaled (average) dipolar coupling.

The standard means for determining the heteronuclear dipolar coupling with REDOR is to perform the REDOR experiment with a series of different dephasing times, t_1 , and then to repeat all the experiments with the dephasing pulses removed. This allows the calculation of a normalized “REDOR difference” magnetization, $\frac{\Delta S}{S_0} = \frac{S_0 - S_{REDOR}}{S_0}$, that is characteristic of the dephasing of the observed magnetization due only to the heteronuclear dipolar coupling, with the contributions from all other T_2 relaxation mechanisms removed. The behavior of $\frac{\Delta S}{S_0}$ is governed by the equation[22]:

$$(1.65) \quad \frac{\Delta S}{S_0} = 1 - \frac{\pi\sqrt{2}}{4} X_{0.25}\left(\frac{d}{4} \cdot t_1\right) X_{-0.25}\left(\frac{d}{4} \cdot t_1\right),$$

where X is a Bessel function and d is the dipolar coupling constant from eq. (1.35). A plot of $\frac{\Delta S}{S_0}$ versus the number of rotor cycles for a strongly coupled spin pair is shown in fig. 1.14b. In contrast, fig. 1.15 shows a plot of the experimentally determined REDOR difference versus time for 1- ^{13}C , ^{15}N -glycine, where the ^{13}C - ^{15}N dipolar coupling is 207 Hz (corresponding to a distance of 2.46 Å). Using a least-squares fit, the experimentally determined dipolar coupling was found to be 206 Hz. The code for a Matlab function for fitting REDOR data can be found in Appendix A.2.

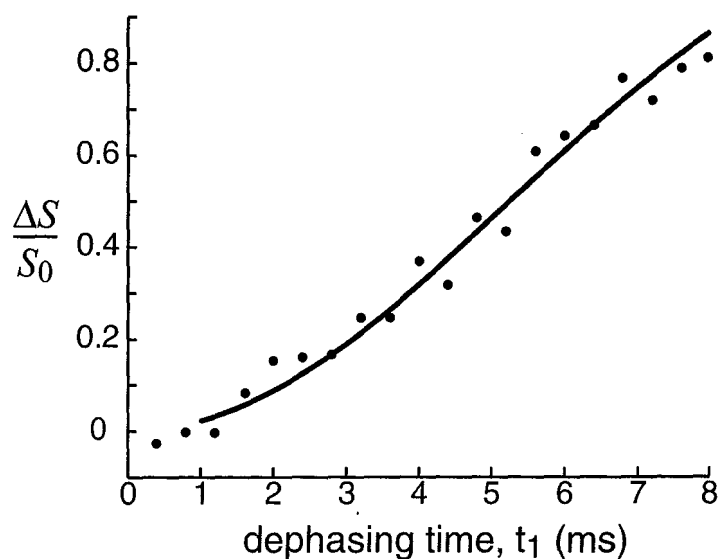


Figure 1.15. Decay of the ^{13}C magnetization in 1- ^{13}C , ^{15}N -labeled glycine as a function of the length of the dephasing period, t_1 . The quantity $\Delta S/S$ (known as the REDOR difference) is the normalized difference between the ^{13}C signal with and without the ^{15}N pulses. By fitting the decay of the ^{13}C magnetization, the ^{13}C - ^{15}N dipolar coupling was determined to be 206 Hz.

1.5.2. Homonuclear Dipolar Recoupling

Homonuclear dipolar recoupling can be accomplished in much the same way as heteronuclear dipolar recoupling—by manipulating the spin component of the dipolar Hamiltonian, one can interfere with the motional averaging produced by the spinning rotor. The principle difference between heteronuclear and homonuclear dipolar recoupling lies in the impossibility of individually addressing different homonuclear spins. In REDOR, one can repeatedly alternate the sign of H_{IS} by applying pulses to either the I- or the S-spin. Unfortunately, for a homonuclear I_1I_2 -spin system, the I_1 - and I_2 -spins have very similar (and some times even the same) resonant frequencies, and so

any π -pulse intended to change the sign of I_{1z} , will also result in changing the sign of I_{2z} .

Thus, the value of H_{II} is unaffected by the application of a π -pulse.

One alternative to using π -pulses is to use $\frac{\pi}{2}$ -pulses, which instead change the *direction* of the dipolar coupling. In fig. 1.13a, it was shown that over a single rotor period, the spatial evolution of the dipolar Hamiltonian is such that its value is zero. This is true regardless of whether the spin component of the dipolar Hamiltonian, T_{II} , is equal to T_{xx} , T_{yy} , or T_{zz} , where

$$(1.66) \quad \begin{aligned} T_{xx} &= 3I_{1x}I_{2x} - \vec{I}_1 \cdot \vec{I}_2 \\ T_{yy} &= 3I_{1y}I_{2y} - \vec{I}_1 \cdot \vec{I}_2 \\ T_{zz} &= 3I_{1z}I_{2z} - \vec{I}_1 \cdot \vec{I}_2. \end{aligned}$$

However, by toggling between one or more of these spin states during the rotor period by the application of $\frac{\pi}{2}$ -pulses, the averaging produced by the MAS rotor can be interrupted.

One technique that makes use of $\frac{\pi}{2}$ -pulses to toggle between different spin states is DRAMA, which stands for Dipolar Recovery At the Magic Angle[23]. During the DRAMA pulse sequence, shown in fig. 1.16a, two $\frac{\pi}{2}$ -pulses per rotor period toggle the magnetization from the z -axis to the y -axis and back again. When optimized such that the magnetization spends half of the rotor period along the z -axis and half of the rotor period along the y -axis (i.e. $\tau = \frac{\tau_r}{2}$), DRAMA is capable of recoupling up to 45% of the homonuclear dipolar coupling. Unfortunately, the two-pulse per rotor period sequence also interrupts the averaging of the chemical-shift anisotropy under

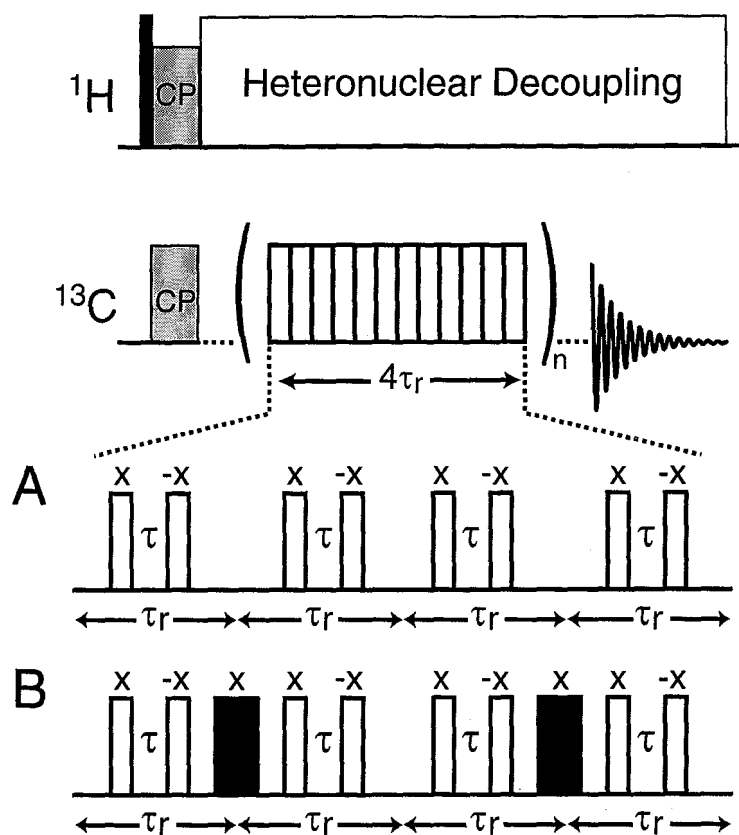


Figure 1.16. (A) Pulse sequence for one cycle of the DRAMA homonuclear dipolar recoupling sequence. The partial recoupling of the CSA that occurs under the sequence in (A) can be removed applying a π -pulse at the end of each rotor cycle, as shown in (B).

MAS, and so a better implementation of the DRAMA sequence also includes an occasional π -pulse, as shown in fig. 1.16b, to remove the CSA.

Distance determination via DRAMA is carried out in generally the same way as REDOR. During the mixing period, τ_m , the magnetization of the recoupled nuclei will decay due to the dephasing effects of the homonuclear dipolar coupling. By measuring

the decay of the magnetization as a function of τ_m , it is possible to determine homonuclear dipolar couplings and internuclear distances.

In addition to DRAMA, a plethora of multi-pulse homonuclear recoupling sequences have been developed, including HORROR[24], DRAWS[25], MELODRAMA[26], RFDR[27], and C7[28]. Aside from the potential for more robust recoupling, each of these sequences possess certain advantages and disadvantages when compared to DRAMA. Although a comparison of these techniques will not be given in this thesis, a detailed evaluation of homonuclear recoupling techniques can be found elsewhere[29].

1.5.3. Rotational Resonance

Another commonly used method for recoupling homonuclear dipolar couplings under MAS is rotational resonance or R²[30]. Unlike DRAMA, rotational resonance does not require the application of multiple pulses to interrupt the effect of the spinning rotor—in fact, rotational resonance utilizes the spinning rotor to recouple two spins. Recall from eq. (1.42) that the spin component of the homonuclear dipolar coupling contains two terms, one proportional to $I_{1z}I_{2z}$ and the other containing the $(I_1^+I_2^- + I_1^-I_2^+)$ or “flip-flop” term. When the chemical shifts of two nuclei differ enough that their NMR lineshapes do not overlap, the “flip-flop” term disappears since it is no longer possible for the spins to undergo an energy conserving transfer of angular momentum. However, when the frequency of the MAS rotor, ω_r , is set such that it is equal to a multiple of the splitting between the isotropic of the two nuclei, ω_{iso} ,

$$(1.67) \quad \Delta\omega_{iso} = n\omega_r,$$

the homonuclear dipolar coupling is effectively recoupled. Although the origin of this recoupling is complex, it can generally be understood by considering the rotor to be an additional source of energy for the system to bridge the energy gap between the nuclear transitions. Only when the rotor spins at one of the rotational resonance conditions dictated by eq. (1.67) are the nuclei recoupled. Figure 1.17 shows a ^{13}C CPMAS spectrum of glycine taken on the rotational resonance condition. The splitting is a result of the interaction between the nuclei, and is indicative of the coupling strength.

Distance measurement using R^2 is accomplished in a somewhat different manner than other recoupling techniques, as shown in fig. 1.18 for ^{13}C - ^{13}C dipolar recoupling. After polarization by CP, the ^{13}C magnetization is returned to the z-axis, at which point the magnetization from one of the ^{13}C resonances is inverted using a long, low-power pulse. Absent any dipolar recoupling, the magnetization of the inverted ^{13}C spins should slowly relax back to equilibrium. However, when at the R^2 condition, the flip-flop term is recoupled and the nuclei will exchange magnetization. This effect is manifest in a decrease in the intensity of both resonances once the magnetization is detected using a $\frac{\pi}{2}$ -pulse. As the mixing time, τ_m , is increased, the spins have more time to exchange magnetization and their intensity in the spectrum decreases. By plotting the absolute value of the integrated intensities of the two peaks as a function of τ_m , one obtains a decay curve that can be fitted to determine the strength of the dipolar coupling and hence the internuclear distance.

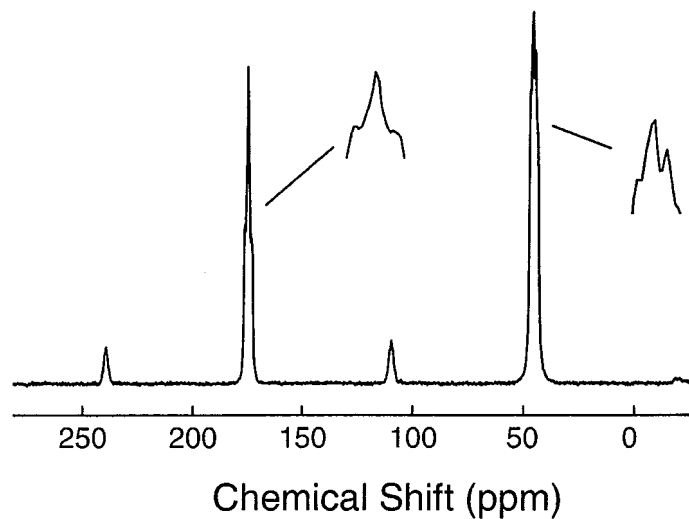


Figure 1.17. 125 MHz CPMAS spectra of 10% uniformly ^{13}C labeled glycine powder acquired while spinning on the rotational resonance condition. The 8.3 kHz spinning speed corresponds to the $n = 1$ rotational resonance condition of eq. (1.67). The distorted lineshapes are a result of the recoupling of H_{II} .

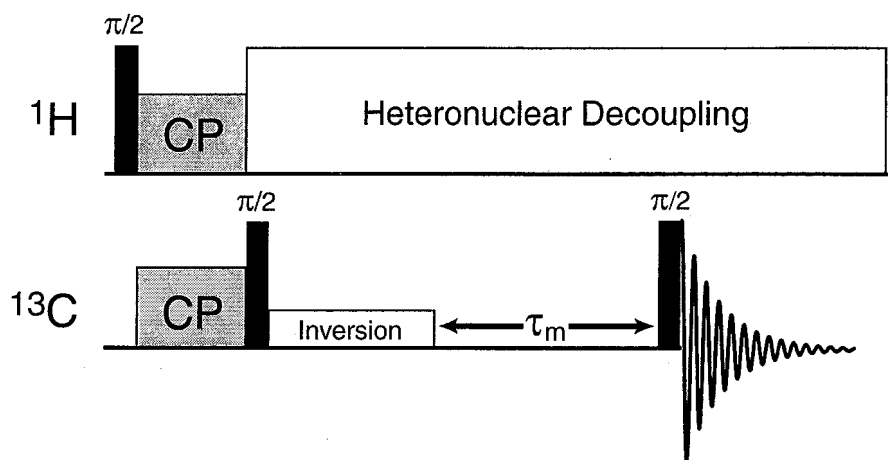


Figure 1.18. Pulse sequence for rotational resonance. Following CP from protons, the ^{13}C magnetization is stored along the z-axis, and one of the resonances is inverted. The magnetization then decays for a period τ_m , before it is returned to the x-y plane for detection.

Chapter 2: Chemical-Shift Computation

The chemical shift in NMR is due to an interaction between a nucleus and small magnetic fields produced by the electrons surrounding the nucleus. These magnetic fields are induced by the presence of the external magnetic field, and their strength is strongly dependent on the shape and density of the electron cloud. Because the size and shape of the electron density around a nucleus is strongly dependent on the surrounding molecular environment, the chemical-shift anisotropy of a nucleus contains a wealth of information about local structure. Unfortunately, except for empirical observations of the behavior of the CSA in certain molecular environments, it is relatively difficult to draw direct conclusions about the local structure of a molecule based only on chemical shifts. However, the chemical shift can be used to study structure indirectly, by correlating observed chemical shifts or chemical-shift tensors with chemical-shift values obtained from quantum chemical calculations on hypothetical structures.

2.1. Chemical-Shift Computation: The Early Years

The first attempts at calculating chemical shifts were made in the 1950's by Ramsey[31], who proposed that the chemical-shift tensor, $\hat{\sigma}$, can be divided into a diamagnetic and a paramagnetic contribution, with elements

$$(2.1) \quad \sigma_{ij} = \sigma_{ij}^d + \sigma_{ij}^p.$$

Ramsey showed that the diamagnetic contribution, σ_{ij}^d , could be calculated based only on the ground electronic state of a molecule, whereas the paramagnetic contribution, σ_{ij}^p , must be calculated from the excited electronic states of a molecule. When performing

calculations of the chemical shift, the external magnetic field, B_0 , is taken to be a vector potential, and the values of σ_{ij}^d and σ_{ij}^p depend heavily on the origin of this vector potential (known as the gauge origin)[32]. However, the chemical shift of a nucleus cannot be dependent on an arbitrary choice of the gauge origin; indeed, as the gauge origin is moved, the values of σ_{ij}^d and σ_{ij}^p change by equal and opposite amounts so that the total chemical shift remains independent of gauge origin. This causes a major problem for the calculation of chemical shifts; since it is much easier to calculate the ground electronic state of a molecule than it is to calculate excited states, the accuracy of σ_{ij}^d will always be higher than that of σ_{ij}^p . Thus, when a choice of gauge origin makes the values of σ_{ij}^d and σ_{ij}^p very large, there are problems with incomplete cancellation and the chemical shift becomes dependent on the gauge origin[32].

2.2. Gauge-Including Atomic Orbitals (GIAO)

Until recently, almost all chemical-shift computation techniques utilized self-consistent field Hartree-Fock methods to obtain the ground and excited state electronic wave functions necessary to calculate the chemical shift of a nucleus. Such calculations usually use basis sets comprised of Gaussian functions to represent the various atomic orbitals, and the larger the basis sets used, the greater the accuracy of the computations. This helps minimize cancellation errors between σ_{ij}^d and σ_{ij}^p that arise from the choice of gauge origin, although not entirely. However, the use of very large basis sets is computationally demanding, and as it turns out, unnecessary. In 1972, a solution to the gauge problem was proposed by Ditchfield in the form of gauge-including atomic orbitals

or GIAO's[33]. Ditchfield's solution was to place a local gauge origin at the center of each atomic orbital, so that any computation performed with these "GIAO's" would be independent of gauge. This has the effect of greatly increasing the accuracy of both σ_{ij}^d and σ_{ij}^p , leading to excellent agreements between theory and experiment[34].

2.3. Chemical-Shift Calculations in Peptides and Proteins

In 1991, Wolinski *et al.* incorporated the GIAO method into a program called TEXAS-90[35]. Using the TEXAS-90 program, de Dios and Oldfield showed that it was possible to reproduce experimentally measured ^{19}F chemical-shift tensors in a variety of fluorobenzene molecules[36]. However, calculating chemical shifts in a 7 to 12 atom molecule is a far simpler task than calculating chemical shifts in a proteins of thousands of atoms. Indeed, to calculate the chemical shift of one α -carbon while taking into account all the other atoms in the protein, would require over a century of computational time and more disk space than is currently available on earth. Fortunately, the chemical shift is a local phenomenon, and can be treated as such. For instance, Jameson *et al.* showed that it was possible to separate the chemical shift into contributions from short (σ_s), medium (σ_m), and long (σ_l) range interactions[37],

$$(2.2) \quad \sigma = \sigma_s + \sigma_m + \sigma_l.$$

Exactly what interactions fall into each category depends largely on the sample and the nucleus in question, although an attempt is made in table 2.1 to classify the common protein interactions according to eq. (2.2). For sp^3 -hybridized atoms like aliphatic carbon atoms in proteins and peptides, the major contribution to σ is σ_s . Therefore, given the

Table 2.1. A survey of common contributions to σ_s , σ_m , and σ_l in proteins. The effect of each interaction as well as its classification can vary in different samples.

σ_s	σ_m	σ_l
Bond Lengths	H-Bonding	Surface Charges
Bond Angles	Ring Currents	Electric Fields
Dihedral Angles	Charged Residues	Charged Residues

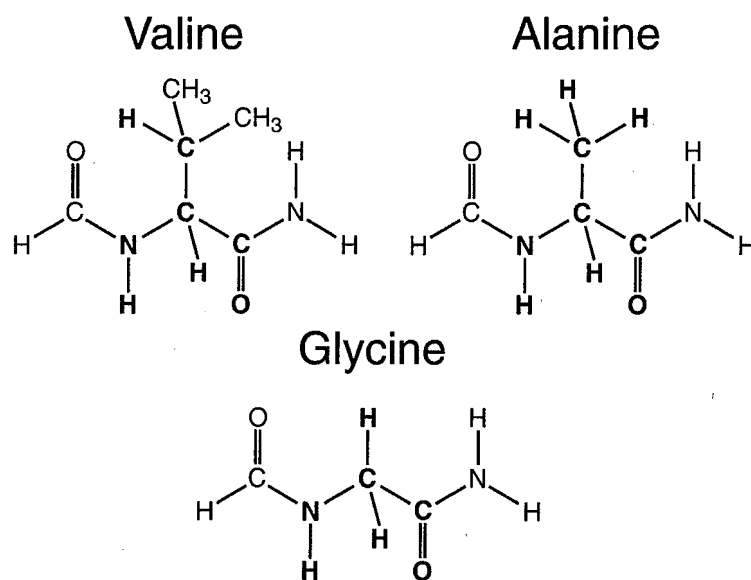


Figure 2.1. Fragments used for *ab initio* chemical-shift computations of glycine, alanine, and valine residues in peptides and proteins. In calculations using a “locally-dense” basis set, the central atoms in bold receive larger basis sets than the unbolded outer atoms.

correct description of the local environment, it is possible to calculate the chemical shifts of aliphatic carbons in a protein.

Figure 2.1 shows fragments used to calculate chemical shifts in glycine, alanine, and valine[38]. Because the major variables in the local structure of a protein backbone are the dihedral angles, each fragment consists of an N-terminal *N*-formyl group and a C-terminal amide group. This provides the necessary atoms to completely describe the C'-N-C_α-C' or ϕ dihedral angle and the N-C_α-C'-N or ψ dihedral angle. To minimize the size of the basis set used, a "locally-dense" basis set is utilized that places larger basis sets on the central atoms (which are bold in fig. 2.1) and smaller basis sets on the outer atoms. It has been shown that calculations performed with the TEXAS-90 program using the fragments in fig. 2.1 and locally-dense basis sets are capable of reproducing experimental chemical shifts in certain amino acid residues of proteins. Figure 2.2 shows a comparison between experimentally measured ¹³C_α isotropic chemical shifts in the glycine, alanine, and valine residues of two proteins, *Drosophila* calmodulin[39] and *Staphylococcal* nuclease[40], versus theoretical calculations based on local dihedral angles. As is clear in fig. 2.2, it is possible to accurately calculate isotropic chemical shifts in proteins using *ab initio* methods. In chapter 5, comparisons of theory versus experiment will be extended to include calculations of chemical-shift tensors in peptides. In addition, a technique for determining local dihedral angles from experimentally measured ¹³C_α chemical-shift tensors will be presented.

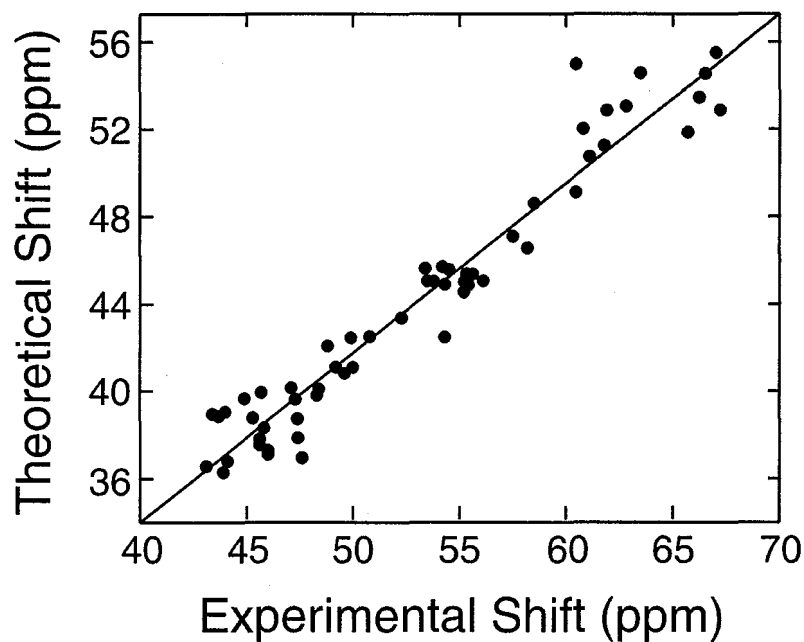


Figure 2.2. Experimental chemical shifts versus theoretical chemical shifts for C_{α} sites in glycine, alanine, and valine residues in *Drosophila* calmodulin and *Staphylococcal* nuclease. The slope of the trend line is 0.75, and the y-intercept is 3.5 ppm. Calculations were performed with the TEXAS-90 program of Wolinski *et al.*, using locally dense basis and the fragments shown in fig. 2.1. Taken from Ref. [38].

Chapter 3: Laser Polarization of Xenon-129

3.1. Fundamentals of Optical Pumping

Nuclear magnetic resonance is an inherently insensitive form of spectroscopy because, as discussed in subsection 1.1.2, nuclear polarizations in NMR are very small for low- γ nuclei like ^{15}N , ^{13}C , and ^{129}Xe . Therefore, it is not surprising that many techniques have been developed to enhance the polarizations of certain nuclei through a transfer of magnetization from spins with higher polarizations. Among the more successful techniques are INEPT in liquid-state NMR[41], cross-polarization in solid-state NMR (subsection 1.4), and Dynamic Nuclear Polarization or DNP[42]. However, in each of these techniques, the degree to which the polarization of a nucleus can be enhanced is still limited by Boltzmann statistics, since the source of polarization is always another group of spins that possess a Boltzmann spin distribution.

Optical pumping (OP) differs from standard methods of enhancing spin polarizations because of its ability to create *non-Boltzmann* spin populations through the transfer of angular momentum from photons to electrons and then to nuclei. The first demonstrations of optical pumping were performed in the 1950's by Kastler[43], who found that it was possible to pump the unpaired valence electrons of alkali metal vapors using circularly-polarized laser light tuned to the correct excitation wavelength. The general principle behind the pumping of electronic spins in alkali metal vapors is shown in fig. 3.1. For an unpaired "s"-electron in the ground state, the energy levels of the $m_J = 1/2$ and $m_J = -1/2$ states are degenerate, and so in an ensemble of "s"-electrons, the $m_J = 1/2$ and $m_J = -1/2$ spin states will be equally populated. If the D_1 transition of the alkali metal is irradiated with linearly polarized light (fig. 3.1a), the $m_J = 1/2$ and $m_J = -1/2$

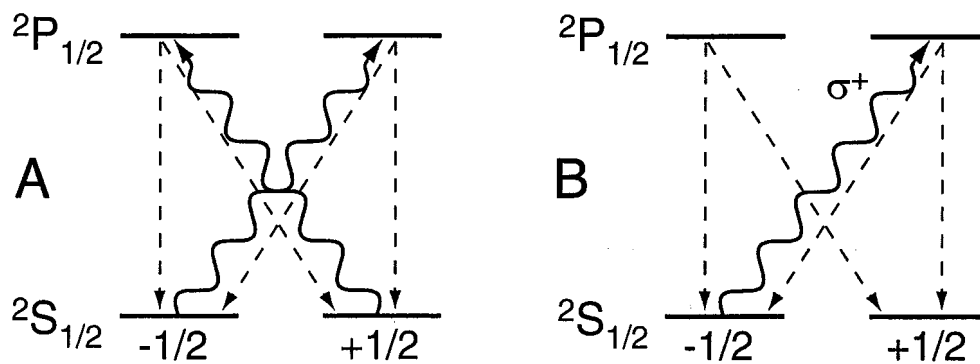


Figure 3.1. Energy level diagram describing the optical pumping of electrons with circularly polarized light. (A) With linearly polarized light, which is a superposition of right and left-handed circularly polarized light, the $m_J = 1/2$ and $m_J = -1/2$ electronic spin states are equally depleted. (B) With σ^+ circularly polarized light, only the $m_J = 1/2$ state is depleted.

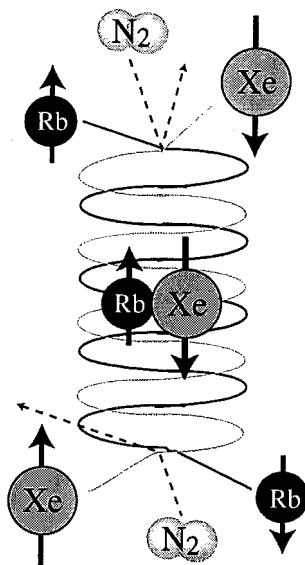


Figure 3.2. Polarization is exchanged between pumped Rb electrons and ^{129}Xe nuclei through a Fermi contact interaction that is facilitated by short-lived van der Waals complexes. $\text{N}_2(\text{g})$ is present to quench the fluorescence of the Rb electrons, which would deplete the electronic polarization. Figure courtesy of Boyd M. Goodson.

excited spin states will become equally populated. However, since σ^+ circularly polarized light carries with it an angular momentum of $+\hbar$, by pumping the D_1 transition with σ^+ circularly polarized light, electrons can be pushed from the $m_J = -1/2$ ground state to the $m_J = 1/2$ excited state (fig. 3.1b). Even though the excited $m_J = 1/2$ state is equally likely to decay to the $m_J = 1/2$ or $m_J = -1/2$ ground states because of collisional mixing, the $m_J = -1/2$ ground state is still depleted since it is the only source of excited electrons.

The next step in the evolution of OP in NMR was made by Bouchiat *et al.*[44], who realized that if noble gases were introduced into the optical pumping apparatus during pumping, then the polarized electrons in the alkali metal atoms would polarize the noble gas nuclei. This polarization transfer occurs through a Fermi contact interaction between the polarized electrons and the noble gas nuclei, mediated in some noble-gas/alkali metal mixtures by short-lived van der Waals complexes that form between the metal atoms and the noble gas atoms. This is shown pictorially in fig. 3.2. The nitrogen gas molecules shown in fig. 3.2 are present in very low concentrations, and are necessary for pumping to occur because they quench the fluorescence of the excited electrons. Without the presence of the nitrogen, the decay of the pumped electron spin polarization would be too rapid for a transfer of polarization to occur efficiently.

In the 1980's the use of optical pumping or "laser-polarization" for the enhancement of ^{129}Xe NMR was explored in great detail by both the Happer[45,46] and Pines[47] groups. Using rubidium metal vapor (whose D_1 transition frequency of 794.7 nm lies in the infrared region) as the alkali metal, Raftery *et al.* showed that it was possible to pump enriched ^{129}Xe gas to a polarization of $\sim .01$ -.1. Given that in a 9.4 T

^{129}Xe polarization of $\sim 1\text{-}5\%$. Once pumping is complete, the cell is cooled to below $\sim 35\text{ }^\circ\text{C}$ to condense the rubidium vapor, after which, the xenon is cryopumped into a sidearm attached to the sample tube. Once frozen in the sidearm, the polarized xenon can be stored for many hours without significant relaxation, so long as a sufficient magnetic field ($> 500\text{ G}$) is present[58]. For our experiments this field was produced by a pair of 1-T bar magnets placed inside a dewar of liquid N_2 . The sample tube can then be detached from the pumping cell and walked to the magnet, where the xenon is warmed and shaken into the liquid sample for experimentation.

Batch-mode optical pumping is primarily used for preparing very small quantities of laser-polarized xenon at low pressures. Under optimized conditions, polarizations in excess of 70% can be obtained using a batch mode set-up similar to the one described in this subsection[59]. In addition, because all pumping and xenon transfer occurs within a closed system, it is relatively simple to keep a batch-mode setup free of oxygen, which can quickly relax the ^{129}Xe polarization[60].

3.2.2. Continuous-Flow Optical Pumping

Although there are definite advantages to using a batch-mode optical pumping setup, there is one large disadvantage. With such a small pumping cell, it is very difficult to produce large quantities of laser-polarized noble gases. For experiments involving liquid or supercritical xenon, this means that the sample tube volume has to be extremely small in order raise the xenon pressure from $\sim 400\text{ torr}$ to $\sim 60\text{ atm}$ [61]. One alternative to a batch-mode OP setup, where small quantities of xenon are pumped for long periods of

time, is to use a continuous-flow OP setup in which large quantities of xenon can be optically pumped with a high-power laser in a relatively short period of time.

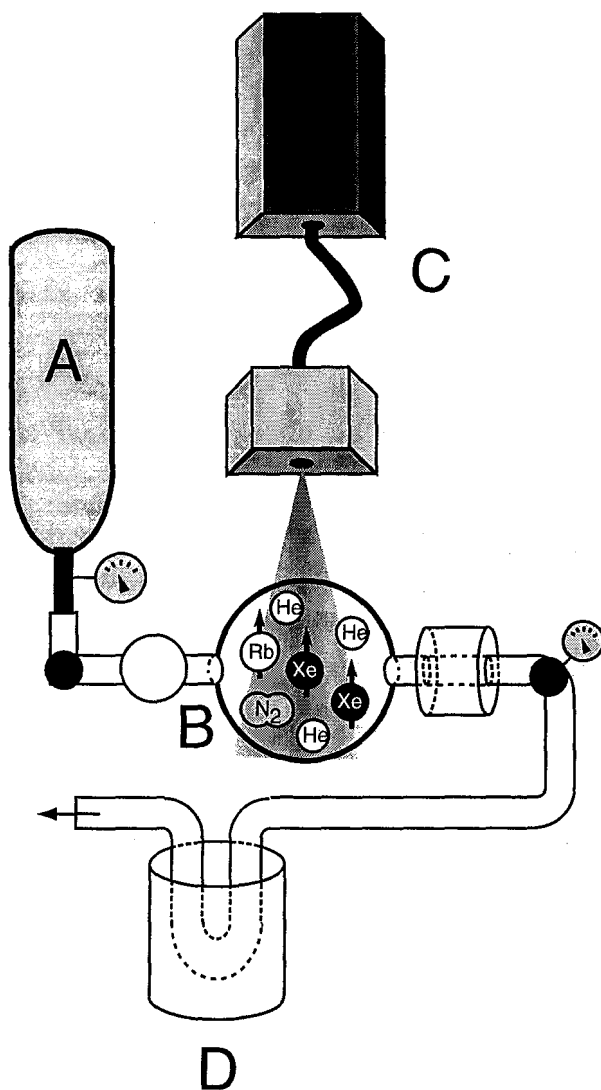


Figure 3.5. Continuous flow optical pumping apparatus. A high pressure mixture of He, Xe, and N_2 pass from a storage cylinder (A) into the pumping cell (B). There, the gases mix with Rb vapor, which is optically pumped by a 120 W diode laser (C). Once the Xe/He/ N_2 /Rb mixture exits the cell, the Rb vapor is removed by a condenser and the xenon is collected in a U-tube (D). Figure courtesy of Boyd M. Goodson.

Figure 3.5 shows a diagram of the continuous-flow optical pumping (CFOP) apparatus used for some of the liquid and supercritical xenon experiments that will be discussed in chapter 7. The xenon gas originates from a ~10 L gas cylinder (fig. 3.5a) that contains He gas at ~10 atm with ~1-3% xenon added as well as ~0.5-1.5% N₂. After exiting the cylinder under pressure, the gas mixture passes through a heated getter and into the pumping cell (fig. 3.5b). The pumping cell in our CFOP setup consists of a two-chamber design that resides inside a small oven. The first chamber contains Rb metal, which is partially vaporized by a stream of hot air and is carried with the flowing gas mixture into the second chamber. The second chamber is where the laser light is focused and the optical pumping occurs. Unlike the batch-mode OP cell, the cell in the CFOP setup is made spherical to decrease (although not eliminate) the chances of explosion. Once the Xe/He/Rb/N₂ mixture exits the pumping cell, it is passed through a condenser to remove the Rb. Using a restriction valve at the end of the condenser, the pressure in the pumping cell is kept near 10 atm, whereas after the valve, the pressure decreases to ~850 torr.

The laser source for the CFOP setup is a 120 W diode array laser (Opto Power Corporation, Tucson, AZ), which produces a beam ~2 cm in diameter at a wavelength of 794.7 ± 2 nm (fig. 3.5c). Because of the wide bandwidth of the diode array laser, the Rb absorption line must be broadened in order to maximize pumping efficiency. This is accomplished through the presence of a high-pressure buffer gas (in our experiments He) and by heating the pumping cell to between 120 and 180 °C. To obtain the ~50 G magnetic field required for optical pumping, the entire CFOP setup was located next to an 11.72 T superconducting magnet. The cell was located so that the stray field of the

magnet was exactly parallel to the incoming laser beam, and at a distance that matched the desired field of ~ 50 G.

Once the ^{129}Xe has been polarized and exits the condenser, the flow can either be directed straight to a magnet for continuous-flow experiments, or can be collected in a U-tube immersed in liquid N_2 (fig. 3.5d). Figure 3.6 shows a plot of the ^{129}Xe signal observed for a continuous-flow experiment as a function of time. Once an equilibrium is reached (~ 75 s after the valve leading from the pumping cell is first opened), the ^{129}Xe polarization is relatively consistent over long periods of time.

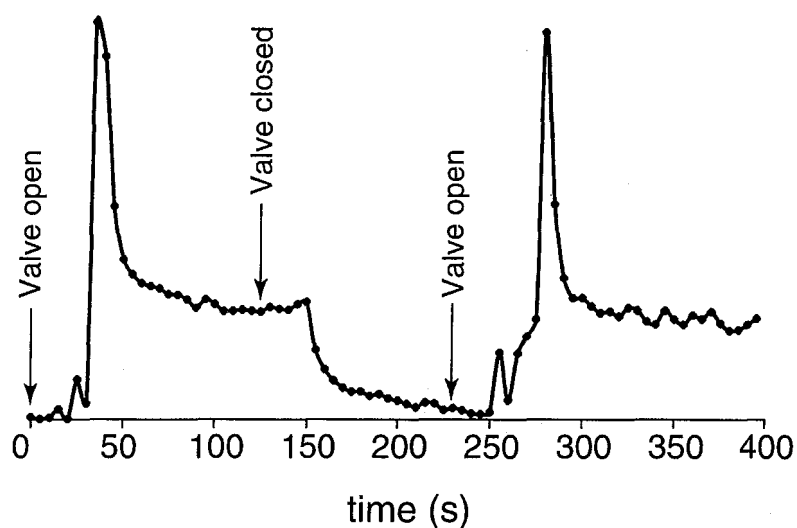


Figure 3.6. ^{129}Xe NMR signal as a function of time in a continuous-flow optical pumping experiment. At $t = 0$, the valve at the exit of the pumping cell is opened and xenon begins to flow through a hose into an NMR tube. Signal is observed ~ 30 s after the valve is opened. The large spike in signal is due to the highly polarized xenon that was held in the pumping cell before the valve was opened. At ~ 125 s, the valve was closed, causing a significant drop in signal at ~ 155 s. The valve was re-opened at ~ 230 s.

For all of the CFOP experiments discussed in this thesis, the gas mixture was passed through a U-tube immersed in liquid N₂ in order to collect the polarized ¹²⁹Xe. The U-tube was located as close to the superconducting magnet as possible, so that the polarization would be maintained over the entire collection process. In a ~20 minute period, with a flow rate of 0.6-0.8 ft³/min, ~0.20 grams of polarized xenon can be accumulated. By warming the U-tube and then freezing the xenon into a smaller volume, it is relatively straightforward to produce either liquid or supercritical xenon, depending on the amount of xenon used and the temperature.

Chapter 4: Prion Diseases

4.1. Description of Prion Diseases

Up until the 1980's it was thought that all infectious or transmissible diseases were caused by either viruses or bacteria. This was because only these pathogens carry with them the genetic information necessary to replicate in vast numbers. However, there were certain cases of neurological disorders, such as Creutzfeld-Jakob disease (CJD) in humans, that seemed to contradict the notion that only viruses and bacteria could cause infectious diseases. Since 1954, it has been known that it is possible to transmit a neurological disease in sheep called "scrapie" to healthy sheep via an intracerebral injection of brain matter taken from diseased sheep[62]. In 1966, Alper *et al.* showed that even after the brain matter taken from scrapie sheep had been irradiated with UV and ionizing radiation, the scrapie brain matter remained infectious[63]. This seemed to contradict the idea that this infectious disease was caused by a virus or bacterium, since DNA and RNA molecules that are irradiated in this way typically degrade to the point that they are no longer functional. Therefore, it appeared that these diseases were caused by an unknown pathogen.

4.1.1. The Pathology of Prion Diseases

Transmissible neurological diseases like scrapie are found in a wide variety of mammalian species, as shown in table 4.1. The pathology of these infectious neurological disorders (now referred to as prion diseases) is relatively similar for all of these mammalian species, both in the physiological effects caused by the disease and the outward symptoms of the disease. The two major symptoms of prion diseases in all

Table 4.1. Common prion diseases in mammalian species.

Mammalian Species	Prion Disease
Sheep	Scrapie
Cows	Bovine Spongiform Encephalopathy
Minks	Transmissible Mink Encephalopathy
Mule Deer and Elk	Chronic Wasting Disease
Cats	Feline Spongiform Encephalopathy
Nyala and Oryx	Exotic Ungulate Encephalopathy

mammals are ataxia, which is a loss of coordination or motor control, and dementia, which is characterized by a deterioration in mental faculties. In addition to these two symptoms, a variety of other symptoms commonly appear depending on the strain of prion disease and on the species of mammal it is affecting. For instance, the initial signs of fatal familial insomnia (FFI) in humans are a loss of sleep followed by chronic insomnia. For sheep, one of the telling signs of the onset of a prion disease is an intense itching that sheep try to suppress by scraping their bodies against fences and trees (hence the term “scrapie”). Table 4.2 lists all of the known human prion diseases along with their common symptoms and methods of transmission. Listings of common symptoms in other mammalian species can be found elsewhere[64-66].

The symptoms of ataxia and dementia that are characteristic of prion diseases arise from a slow deterioration of the brain of a mammal infected with a prion disease. This deterioration occurs in many ways, with four features present in almost all prion diseased brains. These four features are spongiform degeneration, amyloid plaque formation, vacuolation, and gliosis[67]. Spongiform degeneration occurs through a loss of nerve cells in the brain, resulting in the formation of amyloid plaques that consist of dead cellular

Table 4.2. Human prion diseases, their symptoms, and routes of infection.

Disease	Symptoms	Routes of Acquisition
Kuru	Ataxia followed by dementia	Infection by ritualistic cannibalism
Creutzfeld-Jacob Disease (CJD)	Dementia followed by ataxia	Inheritance, infection from procedures, BSE beef?
Gersmann-Sträussler-Sheinker Disease (GSS)	Ataxia followed by dementia	Inheritance
Fatal Familial Insomnia (FFI)	Insomnia followed by dementia	Inheritance

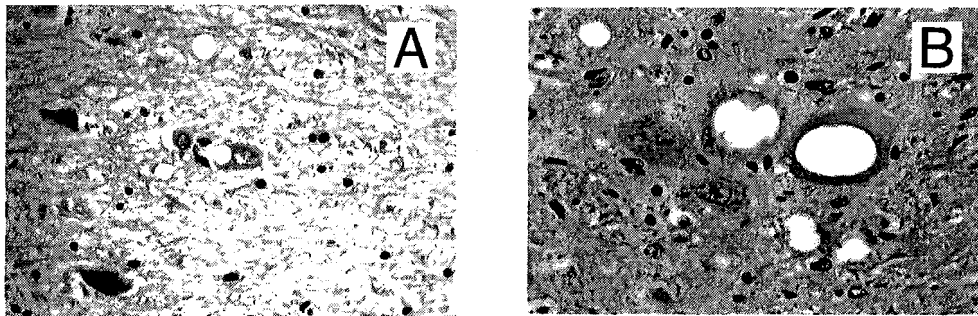


Figure 4.1. Stained section of the frontal cortex of human brains. (A) Brain sample taken from a patient with Creutzfeldt-Jacob disease. (B) Brain sample taken from a patient with Kuru. Photographs courtesy of Dr. Thomas Parsons.

material and aggregated protein fibrils. Vacuolation is the formation of large vacuoles inside the cytoplasm of nerve cells, pushing the cell nucleus and other vital cell components against the cell membrane. Figure 4.1 shows magnified images of two brain samples, one from a brain affected by Kuru, the other by CJD. The stained black spots present in both pictures are the vacuoles that form as a result of the prion disease. Finally, gliosis is characterized by the production of dense fibrous networks of glial cells, which normally form the backbone of nerve cells in the brain and spinal cord.

Although the pathology of prion diseases has been documented for over 70 years, only in the last 20 years has there been a clear picture of the cause of prion diseases. As far back as the 1960's, evidence suggested the presence of a pathogen other than a virus or bacterium. However, the identity of this pathogen remained elusive until the work of Dr. Stanley Prusiner and others in the 1980's.

4.1.2. The Protein-Only Hypothesis

In 1982, Prusiner put forth the hypothesis that prion diseases were caused by an infectious particle that possesses no genetic material[68]. This particle, dubbed a "prion" for "*proteinaceous infectious*" was thought to be a protein that undergoes a structural transformation to a folded conformation that helps catalyze this transformation in other proteins. However, this hypothesis was met with enormous resistance and skepticism from the scientific community. At the time that Prusiner set forth his prion hypothesis, the evidence supporting proteins being responsible for these infectious neurological disorders was still circumstantial. It was known that a result of these diseases was the formation of amyloid plaques in the brain, and that these plaques contained large

quantities of protein. However, other constituents of the plaques could also be responsible for the disease—maybe even a small resistant virus that could have gone undetected.

In 1982, Prusiner *et al.* isolated from the brains of infected Syrian hamsters, an insoluble, protease resistant 27-30 kDa protein that became known as PrP 27-30[69]. In 1986, a soluble form of the prion protein was discovered in healthy cells and was designated PrP^c or PrP-“cellular”[70]. This non-infectious form of the prion protein has a molecular weight of 33-35 kDa, which led researchers to search for a similar length infectious protein in infected brains. It was later discovered that PrP 27-30 was just a cleaved version of a larger infectious protein, dubbed PrP^{Sc} or PrP-“scrapie”[71].

Three discoveries helped bolster the hypothesis that prion diseases are caused only by proteins. First, it was found that intracerebral injections of purified PrP^{Sc} are capable of inducing prion diseases in animals, whereas injections of PrP^c does not[72]. This all but eliminates the possibility that a small virus could be lurking in the amyloid plaque material. Second, transgenic mice that were genetically altered to remove the PrP gene grew up healthy and *completely resistant* to inoculations of PrP^{Sc}[73]. This eliminates the possibility that PrP^{Sc} triggers the activity of a dormant virus that causes the prion disease. Finally, it has been recently shown that a synthetic fragment of PrP, when converted to what is believed to be a scrapie-like conformation, is capable of inducing infectivity in transgenic mice[74]. This last discovery will be discussed in greater detail in section 4.3 and in chapter 9.

4.1.3. Sporadic, Familial, and Iatrogenic Prion Diseases

Given that prion diseases are caused by a protein (PrP^{Sc}) that can catalyze the transformation of PrP^{C} to PrP^{Sc} , it is not surprising that prion diseases appear infectious. Just as injecting a virus into an unwitting host will induce sickness, injection of PrP^{Sc} into the brain of a healthy animal will induce a prion disease. However, not all prion diseases are caused by a transmission of the scrapie pathogen. In fact, there are three different classes of prion diseases, each based on the method of infection. The first class of diseases are iatrogenic prion diseases, and are caused by the direct transmission of PrP^{Sc} . For instance, the onset of bovine spongiform encephalopathy (BSE or mad cow's disease) in British cattle was traced to the practice of feeding ground-up sheep (some infected with scrapie) to the cattle[75]. This practice led to the death of over 200,000 cows in a period of ~15 years. There is some concern now that humans may be contracting an iatrogenic prion disease by eating beef from BSE cattle[76]. Humans have also been infected with iatrogenic prion diseases through corneal implants, derma grafts, and injections of human growth factor, all taken from CJD patients[77-79].

The second class of prion diseases are genetically induced, hence the name familial prion diseases. In all, about 10 to 15% of all prion diseases in humans are caused by the ~20 genetic mutations in the sequence of PrP^{C} that are believed to destabilize the protein in favor of formation of PrP^{Sc} . The mutations that are known to cause or contribute to the onset of prion diseases are shown in table 4.3. Familial prion diseases typically have very long incubation periods (>60 years), which is why they can be passed on from generation to generation.

Table 4.3. Mutations in the PrP sequence that are known to either cause or contribute to the onset of a familial prion disease in humans and mice.

Mutation	Species	Mutation	Species
P101L	Both	T189V	Mouse
P104L	Both	F197S	Both
L108F	Mouse	E199K	Both
A117V	Both	R207H	Both
M128V	Human	V209I	Both
N170S	Human	Q216R	Both
D177N	Both	E218K	Human
V179I	Both	M231R	Human
T182A	Both		

The final class of prion diseases corresponds to those cases that are lumped under the name “sporadic”. Put simply, these are cases of prion diseases where it is unclear what causes the onset of the disease. Whereas sporadic occurrences of GSS and FFI in humans rarely occur, nearly 80% of all cases of CJD are classified as sporadic.

4.2. The Prion Protein

In humans, the prion protein, PrP, is a 253 amino acid protein (fig. 4.2) that is reduced to a 208 amino acid protein after the N-terminus and C-terminus are cleaved by post-translational modifications[80]. In the N-terminal region of PrP, there are a number of repetitive GGWGQPHG octarepeats that are thought to bind one or two copper ions[81]. A disulfide bond links the C178 and C213 residues of PrP, and two oligosaccharides are attached to the protein at N180 and N196. In its cellular state, PrP spends most of the time attached to the cell surface by a glycosyl phosphatidylinositol (GPI) anchor coupled to S231.

		1	2	3	4	5
	012345678901234567890123456789012345678901234567890					
Human	MANLGCWMLVLFVATWSDLGLCKKRPKPGGWNTGGSRYPGQGSPGGNRYPP					
MouseY·L·A···TM·T·V··········					
S.Hamst.SY·L·A···M·T·V··········					
		6	7	8	9	10
	12345678901234567890123456789012345678901234567890					
Human	QGGGGWGQPHGGGWGQPHGGGWGQPHGGGWGQPHGGGWGQGGGTHSQWNK					
Mouse-T··········S········S········N····					
S.HamsterT··········N····					
		11	12	13	14	15
	12345678901234567890123456789012345678901234567890					
Human	PSKPKTNMKHMAGAAAAGAVVGGGLGGYMLGSAMSRPIIHFGSDYEDRYR					
MouseL·V··········M····N·W····					
S.HamsterMM····N·W····					
		16	17	18	19	20
	12345678901234567890123456789012345678901234567890					
Human	ENMHRYPNQVYYRPMDEYNNQNNFVHDCVNITIKQHTVTTTTKGENFTET					
Mouse	...Y········V·Q··········					
S.Hamster	...N········V·Q·N········					
		21	22	23	24	
	12345678901234567890123456--789012345678901234567					
Human	DVKMMERVVEQMCITQYERESQAYYQ--RGSSMVLFSPPVILLISFLIF					
MouseV···QK·····DGR·S··T········					
S.Hamster	·I·I······T···QK·····DGR·--·A······					
		25				
	8901					
Human	LIVG					
Mouse					
S.Hamster	·M··					

Figure 4.2. Amino acid sequences for the human, mouse, and golden Syrian hamster variants of the prion protein, PrP. Although the numbering is done according to the human sequence, it was begun at zero to reflect the numbering of the mouse sequence.

As is the case with all proteins, the structure of PrP is critical to its functionality. Even though the amino acid sequences of PrP^c and PrP^{sc} are identical, the differences in their structures make one a harmless, soluble protein and the other a deadly, insoluble pathogen. Thus, to understand how prion proteins cause the onset of neurological diseases, it is important to know what structural changes lead PrP^c to form PrP^{sc}. Unfortunately, this is easier said than done. PrP^c is a soluble protein, and so its structure can be studied via liquid-state NMR. Indeed, the structure of mouse PrP^c has already been solved by Wütrich and coworkers[82] and the structure of Syrian hamster PrP^c has been solved by James and coworkers[83]. Figure 4.3 shows a schematic of the structure of Syrian hamster PrP^c 90-231. The structure of PrP^c is predominantly α -helical, with only 2 short regions of β -sheet, each ~5 residues long. The first 105 amino acid residues (where the octarepeats reside) form an unstructured region of the protein that may become structured upon binding to copper.

In contrast to PrP^c, PrP^{sc} is insoluble, and attempts to solubilize it in various detergents have met with little success. Furthermore, PrP^{sc} forms aggregates that cannot be crystallized for study by x-ray crystallography. Therefore, little is known about the structure of PrP^{sc}, other than the fact that it appears from circular dichroism (CD) studies to be predominantly β -sheet[84]. One possible means of performing structural studies of PrP^{sc} is to use solid-state NMR, since there are no requirements of solubility or long range order. However, solid-state NMR is not yet sufficiently advanced to determine the full structure of an amorphous protein sample when the protein is much larger than ~30 residues[85].

To date, not much is known about the structural conversion from PrP^c to PrP^{sc}, other than the fact that it involves at least a partial conversion to β -sheet. It is believed that an exposed region of β -sheet in the protein may serve as an active site for the binding

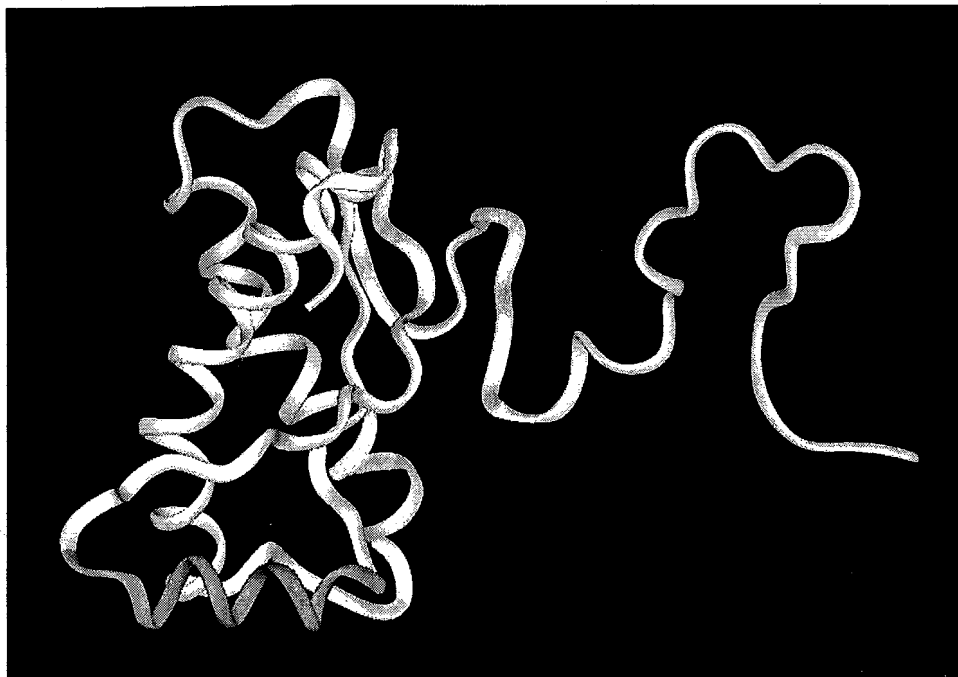
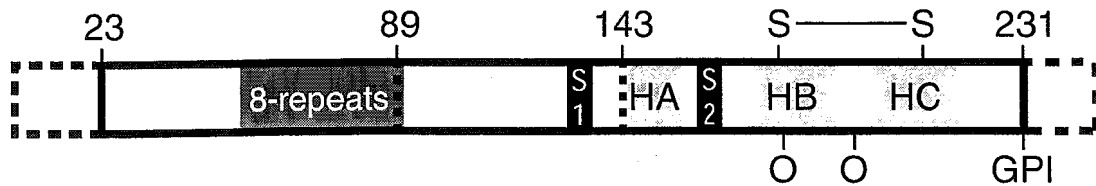


Figure 4.3. Structure of the prion protein, PrP^c. The schematic on top shows a structural layout of the complete PrP^c sequence. HA, HB, and HC are the common designations for the three helices in PrP^c, and S1 and S2 are the two sheets. The two “O’s” refer to the locations of PrP^c where the two oligosaccharides are attached. Below the schematic is a three-dimensional picture of the structure of Syrian Hamster PrP^c 89-231[83].

of PrP^c. The bound PrP^c then undergoes a structural transformation to PrP^{sc}, providing an active site for the next PrP^c monomer. There is relatively strong evidence that another protein, dubbed protein X, helps mediate the conversion of PrP^c to PrP^{sc}, although no protein has been identified thus far[86].

4.3. PrP 89-143: An Infectious Fragment of the Prion Protein

A significant barrier to structural studies of PrP^{sc} has been the inability to carry out an *in vitro* conversion of PrP^c to PrP^{sc}, preventing isotopic labeling for NMR studies. However, in 1999, it was discovered by Kaneko *et al.*[74] that a synthetic 54 amino acid fragment of the prion protein, PrP 89-143, can form an aggregate that may indeed mimic the aggregation of PrP^{sc}. More importantly, they found that the aggregated forms of some mutants of PrP 89-143 were infectious in transgenic mice, whereas the unaggregated forms were not.

The fragment PrP 89-143 spans an unstructured globular region of PrP^c as well as first sheet (fig. 4.4). Despite being in a mostly unstructured region of the soluble protein, many have long held that within this region of the prion protein is the key to its conversion from PrP^c to PrP^{sc}. The reason for this belief lies two fold. First, early computer models of the prion protein suggested that this region had almost an equal propensity to form either an α -helical or β -sheet structure. Indeed, solid-state NMR studies of the 14 amino acid fragment PrP 108-121 demonstrated this helix/sheet duality[87]. The fact that this region of the protein is unstructured in the cellular form only partially conflicts with this model since PrP 89-143 may very well be predominantly β -sheet in the scrapie form. The second reason why 89-143 region of PrP is believed to

II. NMR Technique Development

Chapter 5: The CSA/Z Method

5.1. Introduction

Over the past twenty-five years, an enormous amount of research has focused on the development of liquid-state NMR techniques for determining protein structures. As a result, a plethora of experiments exist that make finding the structure of a protein in solution relatively straightforward, albeit time-consuming. The development of solid-state NMR techniques for studying protein structures is far less advanced, due in part to the fact that only recently has there been widespread interest in the field, but due mostly to the difficulties inherent in examining many-spin systems in the solid-state. Whereas in liquids, rapid molecular tumbling serves to average nearly all anisotropic interactions leaving extremely sharp spectra, the presence of strong proton-proton dipolar couplings in solids, as well as anisotropies in both the chemical shift and bulk magnetic susceptibility, results in linewidths that are rarely less than $\sim 1-2$ ppm. This effectively eliminates the possibility of performing experiments on fully ^{13}C and ^{15}N labeled protein samples (as is routinely done in liquids) unless they are either polycrystalline or the protein is relatively small (< 30 residues)[85].

Without the ability to study a fully labeled protein via solid-state NMR, many solid-state NMR techniques have recently been developed that rely on selective ^{13}C and ^{15}N labeling to measure both distances[21,23,30,88] and dihedral angles[89-93] in solids. One possible means for augmenting the information available from these experiments is to use *ab initio* chemical-shielding computations to gain insight into the backbone structure of a protein. In such methods, the chemical shielding is calculated as a function of the backbone and side-chain torsion angles. Correlations between isotropic chemical

stirring for 24 hours, at which point the acetone was removed by rotary evaporation. Citric acid (1 M) was used to precipitate the Fmoc- amino acids from the aqueous solution. Ethyl acetate (EtOAc) (150 mL) was added to redissolve the precipitate. The mixture was transferred to a separatory funnel and the layers were separated. The aqueous layer was washed with EtOAc (100 mL). The combined organic layers were then washed with H₂O (2×100 mL) and saturated NaCl (2×100 mL). The organic layers were dried over magnesium sulfate and the solvent was removed by rotary evaporation. The product was used for solid-phase peptide synthesis without further purification.

5.2.2. Peptide Synthesis

G*AV, A*AA, L*LVY-OMe, and LL*VY-OMe were synthesized using N-Fmoc protected amino acids on an Applied Biosystems 431A (Perkin Elmer-Perceptive Biosystems, Foster City, CA) peptide synthesizer. The peptides were cleaved from the resin and deprotected by stirring for 3 hours in a 95% (v/v) trifluoroacetic acid (TFA)/H₂O solution. The mixture was filtered to remove the resin. TFA was removed by rotary evaporation, followed by lyophilization. The cleaved A*AA was then redissolved in H₂O and purified by reversed-phase HPLC on a Vydac C-18 column. Purity and identity of all of these samples were checked by electrospray-ionization mass spectrometry (Hewlett-Packard 5989A).

Boc-V*AL-Aib-*VAL-OMe and Boc-VA*L-Aib-VAL-OMe were synthesized using optimized Fmoc chemistry on an Applied Biosystems 433 peptide synthesizer. Fmoc amino acid derivatives were pre-activated by reaction with 2-(¹H-benzotriazol-1-yl)-1,1,3,3-tetramethyluronium hexafluorophosphate (HBTU) and diisopropylethylamine

(DIEA). After the coupling of each amino acid, a capping step was performed using N-(2-chlorobenzylloxycarbonyloxy) succinimide (Novabiochem, La Jolla, CA). Labeled residues were coupled manually using a 1.5 fold excess of amino acid and coupling efficiency was monitored using the quantitative ninhydrin test. The last residue was coupled as the Boc derivatized amino acid. Peptides were cleaved from the resin with 1% TFA in dichloromethane (CH_2Cl_2), and the cleaved peptide solution was collected in a round-bottomed flask containing pyridine. The peptidyl-resin was treated with additional aliquots of cleavage mixture and the filtrates were combined. CH_2Cl_2 was eliminated using a rotary evaporator and the residue taken up in 20% acetic acid. The crude peptides were purified by reversed-phase HPLC on a Rainin (Emeryville, CA) liquid chromatography system using a Vydac C-18 semi-preparative column (250×10 mm). The identity of the purified peptides was confirmed by electrospray mass spectrometry using a Perkin Elmer-Sciex API-300 instrument.

5.2.3. Peptide Crystallization

Peptides were crystallized following the protocols from the references listed in table 5.1, with slight modifications made in order to crystallize larger quantities. In all cases, small crystal clusters were obtained; large single crystals are not necessary in this approach. GAV[106] was dissolved in a minimal volume of warm H_2O and the solution was placed in a Petri dish. The dish was then placed into a sealed container over a reservoir of methanol. Due to vapor diffusion, small crystals formed quickly and crystallization was complete within a day. AAA was crystallized in two crystal forms. The first crystal form of AAA (hence referred to as AAA I) was formed by dissolving the

tripeptide in a solution of 60% (v/v) *N,N'*-dimethylformamide (DMF) in water and placing the solution in a glass Petri dish. The solvent was allowed to evaporate slowly. The second crystal form, AAA-hemihydrate (hence referred to as AAA II), was formed by a similar procedure, except that the concentration of DMF was 20% (v/v). The two crystal forms were visually distinguishable, with AAA I forming plates and AAA II forming needles.

Boc-VAL-Aib-VAL-OMe crystals were grown in sample vials with a slow flow of nitrogen gas blowing over the solution. As with AAA, the Boc-VAL-Aib-VAL-OMe peptides crystallize in two forms, depending on the solvent. The first crystal form, Boc-VAL-Aib-VAL-OMe I, was obtained through slow evaporation of the peptide from a 50:50 methanol:water solution. The second crystal form, Boc-VAL-Aib-VAL-OMe II, was obtained through slow evaporation of the peptide from a 50:50 isopropanol:DMSO solution. Unfortunately, only the leucine $^{13}\text{C}_\alpha$ -labeled peptide produced useable crystals in the second form, due presumably due to contamination in the alanine/valine labeled Boc compound. Low-angle x-ray powder diffraction profiles using $\text{CuK}\alpha$ radiation were taken to confirm crystallinity (Inel, Inc. CPS120 Powder Diffraction System, Idaho Falls, ID).

The LLVY-OMe peptides were crystallized from water and DMF. The peptides were first suspended in ~200 μL of water. The suspension was then heated in an oil bath to 70°C and DMF was added in 1 μL aliquots until the peptides completely dissolved. Upon slow cooling, small crystals formed. The remaining solution was removed by slow evaporation.

5.2.4. Solid-State NMR

All GAV and AAA ^{13}C NMR spectra as well as some Boc-VAL-Aib-VAL-OMe ^{13}C NMR spectra were obtained at 7.07 Tesla (corresponding to a ^{13}C Larmor frequency of

75.74 MHz) on a home-built spectrometer based on a Tecmag (Houston, Texas) pulse programmer. A Chemagnetics (Fort Collins, CO) 4-mm double-resonance MAS probe was used for all experiments. Spinning speeds were controlled to ± 1 Hz using a home-built spinning-speed controller. The CP contact time was 2.5 ms, the ^1H decoupling field strength was 108 kHz, and the recycle delay was 1.5 seconds. The remaining Boc-VAL-Aib-VAL-OMe and the LLVY-OMe ^{13}C NMR spectra were obtained at 11.72 Tesla (corresponding to a ^{13}C Larmor frequency of 125.75 MHz) on a triple-resonance Varian/Chemagnetics Infinity spectrometer with a 4-mm T3 triple-resonance MAS probe. Spinning speeds were controlled to within ± 3 Hz using a Chemagnetics spinning-speed controller. The CP contact time was 2.0 ms, the ^1H decoupling field strength was 104 kHz, and the recycle delay was 2 seconds. The experimental data was fitted using the Herzfeld-Berger method[5]. An average of the CSA values derived from each spinning speed was taken and used to compare with theoretically calculated values. Isotropic shift values were measured relative to the carbonyl carbon of glycine at 176.04 ppm.

5.3. Computational

The alanine shielding calculations were performed using the TEXAS-90 program[35] which utilizes the gauge-including-atomic-orbital (GIAO) method[33,113]. The leucine and valine calculations were performed using the GIAO package in Gaussian-98 (Gaussian, Inc., Carnegie, PA). All calculations were done on *N*-formyl-L-[amino acid] amide fragments extensively minimized at the helical geometry. A "locally-dense" basis set was employed consisting of 6-311++G(2d,2p) basis functions on the central residue and 6-31G basis functions on the formyl and amide groups (see fig. 2.1).

Computations were performed on IBM RISC/6000 workstations (Models 340, 350, and 360; IBM Corporation, Austin, TX) and on a cluster of SGI Origin-200 workstations (Silicon Graphics Inc., Mountainview, CA). The alanine shielding surfaces were constructed by choosing 358 ϕ/ψ points in Ramachandran space, with a more dense placement of points in the allowed regions. The valine and leucine surfaces were created using a strategic placement of 100 ϕ/ψ points in Ramachandran space. Separate surfaces were created for each conformationally allowed rotomer of leucine and valine. Z-surfaces for the chemical-shift tensors were created using a Gaussian equation:

$$(5.1) \quad Z_{\delta_{nn}}(\phi, \psi) = \exp\left[-\frac{(\delta_{nn}^{ecs} - \delta_{nn}(\phi, \psi))^2}{\omega^2}\right]$$

where δ_{nn}^{ecs} is the experimental chemical-shift tensor, $\delta_{nn}(\phi, \psi)$ is the chemical-shift tensor surface, and ω is the root-mean-square deviation between experimentally measured and predicted chemical-shift tensors (for all Z-surfaces in this chapter, $\omega = 2.42$ ppm).

5.4. Results and Discussion

There are two possible ways in which the CSAs of amino acids can be used to determine local structure. One can either use chemical-shift tensors to provide torsional restraints in a simulated annealing program such as X-PLOR[102,114], or one can use probabilistic methods to actually predict dihedral angles based on measured chemical-shift tensors[103,105]. In either case, the complex dependence of chemical-shift tensors on their local environment must first be understood for such techniques to be possible. This can be accomplished in two ways. First, one can experimentally measure the chemical-shift anisotropies of a group of proteins that have known structures and create

empirical surfaces that describe each chemical-shift tensor (δ_{11} , δ_{22} , and δ_{33}) as a function of the dihedral angles ϕ , ψ , and where appropriate χ_1 and χ_2 . Indeed, this approach has already been used to produce empirical surfaces that describe the behavior of isotropic C_α and C_β chemical shifts in proteins as a function of the dihedral angles ϕ and ψ [94]. The second way to correlate C_α chemical-shift tensors with local structure is to use theoretical chemical-shift surfaces obtained by *ab initio* quantum chemical calculations on small amino-acid fragments[100,103,114,115]. The main advantage to using theoretical chemical-shift surfaces for structure prediction and refinement is that they can cover the complete Ramachandran ϕ/ψ space, whereas empirical surfaces are confined to conformations that exist in the subset of proteins that are used to create the surface. This limitation to empirical surfaces can be troublesome since often proteins will sacrifice the local energy of an amino-acid residue by pushing it into a conventionally “unallowed” region in order to satisfy an overall decrease in the energy of a protein. In addition, simulated-annealing programs often stray into unallowed regions of Ramachandran space on a path to determining an overall protein fold, preventing empirical surfaces from constantly providing energy restraints based on measured chemical shifts.

5.4.1. Correlations between Theory and Experiment

Despite the advantages of theoretical chemical-shift surfaces over empirical surfaces, there is one major problem with using theoretical surfaces to predict chemical shifts. Although it has been definitively shown that chemical-shift surfaces can reproduce the behavior C_α and C_β chemical shifts in proteins[38,98], they often do not

fully predict the *range* of chemical shifts—especially surfaces created using Hartree-Fock methods[116] (see fig. 2.2). This means that without correction, no theoretical chemical-shift surface could ever be used to predict structure because, for a given ϕ/ψ pair, the predicted chemical shift would always be wrong. Fortunately, this can easily be remedied by scaling the chemical-shift surfaces based on correlations between measured and predicted chemical-shift values[105]. However, with 20 naturally occurring amino acids, most with a variety of rotamer conformations, scaling each surface based on experimentally measured chemical shifts could potentially be very time consuming. Furthermore, isotropic chemical shifts taken from protein NMR studies are often insufficient to obtain accurate scaling parameters because of the relatively small ~8 to 12 ppm ranges of most C_α and C_β isotropic chemical shifts in proteins[100,116]. One possible way to remedy this situation is to use comparisons between experimentally determined and theoretically predicted C_α chemical-shift *tensors* in peptides. Whereas the isotropic C_α chemical-shift range in proteins may be only 8 to 12 ppm, anisotropic C_α chemical shifts in solid-state peptides can exceed 60 ppm. In principle this should provide a chemical-shift range large enough to accurately scale the theoretical chemical-shift surfaces so that they can be used to predict local structure.

By using the $^{13}C_\alpha$ -labeled peptides described in section 5.2, scaling factors for alanine, leucine, and valine chemical-shift surfaces were determined. The $^{13}C_\alpha$ chemical-shift tensors for nine crystal forms of the six peptides listed in table 5.1 were determined using slow-spinning CPMAS experiments coupled with analysis of spinning-sideband intensities using the Herzfeld-Berger method[5]. Figure 5.1 shows CPMAS spectra of $^{13}C_\alpha$ -labeled A*AA II at spinning speeds of 821 Hz, 928 Hz, 1024 Hz and 10 kHz.

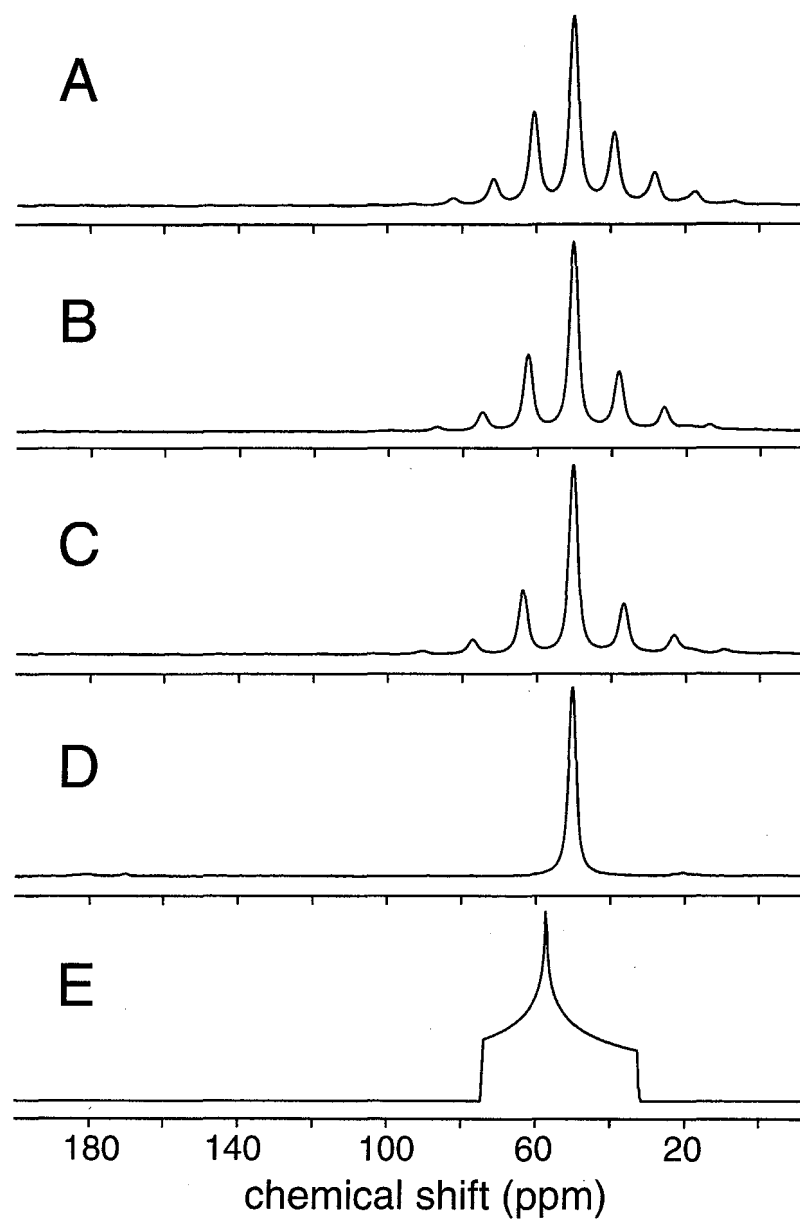


Figure 5.1. CPMAS spectra for crystalline $^{13}\text{C}_{\alpha}$ -labeled A*AA II. For all experiments, the CP contact time was 2.5 ms, the decoupling field strength was 108 kHz, and the recycle delay was 1.5 s. (A) 40,960 scans were acquired, spinning at 821 Hz. (B) 24,576 scans were acquired, spinning at 928 Hz. (C) 28,672 scans were acquired, spinning at 1024 Hz. (D) 2,048 scans were acquired, spinning at 10 kHz. (E) Simulated static spectrum based on the chemical-shift tensors derived from (A-C). Figure adapted from Ref. [105].

Although two molecules with slightly different conformations exist in the unit cells of both forms of A*AA, the resolution of our experiments was not high enough to differentiate between them, and only one line was observed. The chemical-shift tensor values determined for A*AA II and the other eight peptide samples are summarized in table 5.2.

Table 5.2. Experimentally measured $^{13}\text{C}_\alpha$ chemical-shift tensors.

Residue	Compound	δ_{11}	δ_{22}	δ_{33}
Alanine	G*AV	76.7	54.1	27.1
	A*AA I	70.4	53.0	27.2
	A*AA II	69.7	52.4	26.7
	Boc-V*AL-Aib-VAL-OMe I	72.5	54.5	31.3
Leucine	Boc-VA*L-Aib-VAL-OMe I	73.4	57.5	35.5
	Boc-VA*L-Aib-VAL-OMe II	71.6	58.0	36
	L*LVY-OMe	69.3	52.3	32.2
Valine	Boc-VAL-Aib-*VAL-OMe I	79.1	64.0	37.0
	LL*VY-OMe	77.4	58.0	40.7

Using theoretical chemical-shift tensor surfaces that describe the behavior of the three principle values of the CSA (δ_{11} , δ_{22} , and δ_{33}) as a function of ϕ and ψ , theoretical chemical shifts were determined for each peptide sample based on the dihedral angles provided in the crystal structure references listed in table 5.1. Chemical-shift tensor surfaces for alanine are shown in fig. 5.2. For leucine and valine, which both possess multiple rotomer conformations, multiple chemical-shift tensor surfaces exist to account

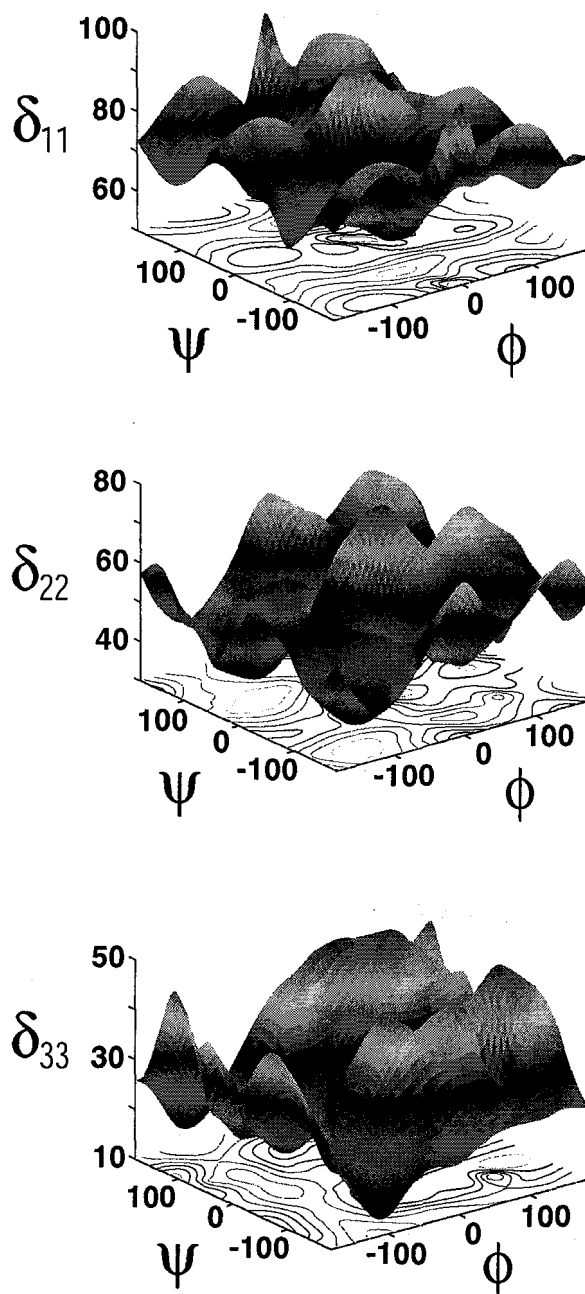


Figure 5.2. Alanine Ramachandran shielding surfaces for C_α sites in *N*-formyl-L-alanine amide. (A) δ_{11} ; (B) δ_{22} ; (C) δ_{33} . Surfaces were approximated using 358 points spread over ϕ/ψ space with a more dense placement of points in allowed regions.

for each of the allowed backbone rotomers. These correspond to $\chi_1 = 180^\circ$, -60° and $+60^\circ$ for valine and $\chi_1 = 180^\circ$, $\chi_2 = -60^\circ$ and $\chi_1 = 180^\circ$, $\chi_2 = +60^\circ$ for leucine.

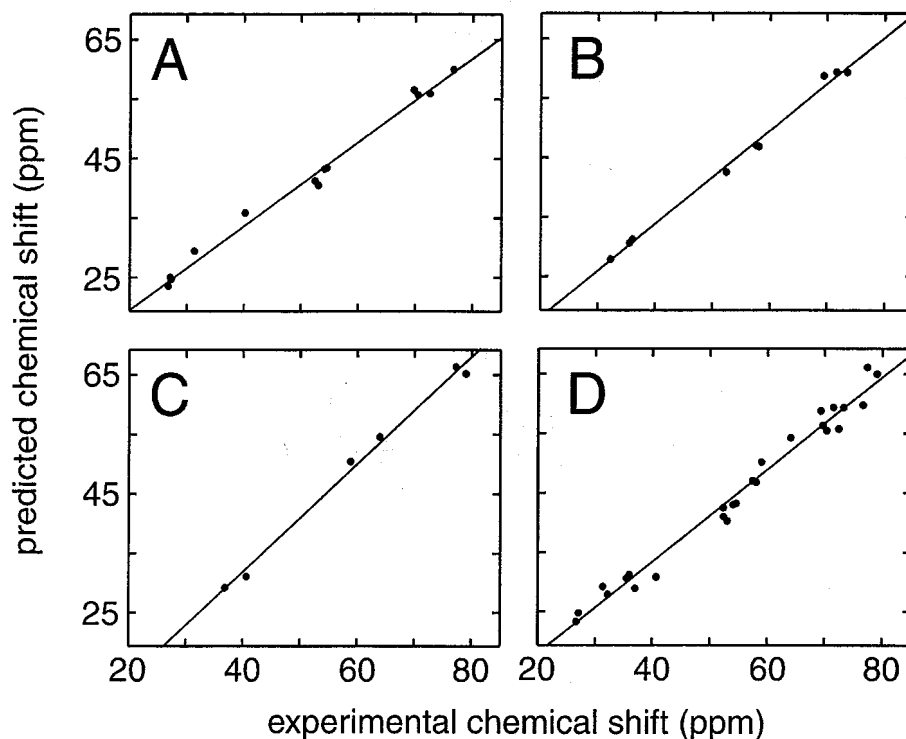


Figure 5.3. Theoretical $^{13}\text{C}_\alpha$ chemical-shift tensor elements for alanine (A), leucine (B), and valine (C) peptides versus the experimentally measured tensors. For (A): slope = 0.71, y-intercept = 4.1 ppm, $R = 1.0$, and rmsd = 1.72. For (B): slope = 0.79, y-intercept = 1.46 ppm, $R = 1.0$, and rmsd = 1.23 ppm. For (C): slope = 0.91, y-intercept = -5.7 ppm, $R = 1.0$, and rmsd = 1.50 ppm. (D) Combination of the data from (A-C). Slope = 0.77, y-intercept = 1.4 ppm, $R = 0.99$, and rmsd = 2.43 ppm.

Figure 5.3 shows plots of the experimentally determined $^{13}\text{C}_\alpha$ chemical-shift tensors versus the predicted values for the alanine (fig. 5.3a), leucine (fig. 5.3b), and valine (fig. 5.3c) residues in the peptides listed above. As can be seen from the three

plots, the slopes and intercepts for all three amino acid residues are comparable, as are the rmsd's (which range from 1.5 to 1.7 ppm). Figure 5.3d shows a compilation of the data for all three amino acids (slope = 0.77, y-intercept = 1.4 ppm). With a total of 27 data points and an overall rmsd of 2.4 ppm, figure 5.3d clearly demonstrates that backbone dihedral angles are the main determinants of the tensor components of the C_{α} chemical shifts in both β -branched and non- β -branched amino acids alike. Using the slope and intercept listed above, all of the surfaces were scaled so that predicted chemical-shift ranges were identical to the experimentally determined ranges. This permitted the use of these chemical-shift tensor surfaces for the prediction of local structure in seven of the nine peptide samples.

5.4.2. Predictions of Dihedral Angles in Solid-State Peptides

As mentioned earlier, there are two ways in which chemical-shift tensor surfaces can be used to help determine structure in peptides and proteins. The first is as a restraint in simulated annealing programs. Since the chemical shift can mathematically be described as the 2nd-derivative of the energy of a nucleus with respect to the external magnetic field, B_0 , and the nuclear magnetic moment, μ [32]

$$(5.2) \quad \sigma_{\alpha\beta} = \frac{\partial^2 E}{\partial \mu_{\alpha} \partial B_{0\beta}},$$

any chemical-shift surface can be converted directly into a local energy restraint[114]. The other way to obtain local structure using chemical-shift tensor surfaces is to use probabilistic methods to predict ϕ and ψ from measured CSAs. One such method is the Z-surface approach[103], which uses Bayesian probability surfaces to define the

probability of any given ϕ/ψ pair describing the correct local geometry. A 1Z -surface is created using the formula in eq. (5.1). Once an experimental chemical-shift tensor is measured, it is compared to every point on the corresponding chemical-shift tensor surface to determine which ϕ/ψ conformations produce a chemical shift close to the measured value. A Gaussian is used to define the probability that a given ϕ/ψ conformation is correct. As can be seen in any of the tensor surfaces shown in fig. 5.2, an infinite number ϕ/ψ conformations correspond to most measured chemical shifts, making a 1Z -surface incapable of predicting structure on its own. However, by taking the product of n 1Z -surfaces, a nZ -surface can be created that ideally possesses only one ϕ/ψ solution.

The Z-surface approach was first used to predict local conformations of proteins in solution based on C_α , C_β , and H_α chemical shifts[103]. In solution, all three chemical shifts are required in order to create a 3Z -surface capable of predicting a unique ϕ/ψ conformation. In solids, additional experiments to determine the C_β and H_α isotropic shifts are not always needed, since the three components of the chemical-shift anisotropy, δ_{11} , δ_{22} , and δ_{33} , provide the necessary three independent parameters. Figure 5.4 shows a series of Z-surfaces for Boc-VA*L-Aib-VAL-OMe I. Figures 5.4a-c show the 1Z -surfaces that correspond to δ_{11} , δ_{22} , and δ_{33} , and fig. 5.4d shows the 3Z -surface that is a product of the 1Z -surfaces in figs. 5.4a-c. As can be seen in fig. 5.4d, the 3Z -surface predicts multiple high-probability ϕ/ψ conformations. Some of these conformations can be eliminated from consideration because they lie in regions of Ramachandran space that are conformationally unallowed. In fig. 5.4e, this is accomplished by zeroing the probability in all unallowed regions of ϕ/ψ space. Figure 5.4f shows an expansion of the highest

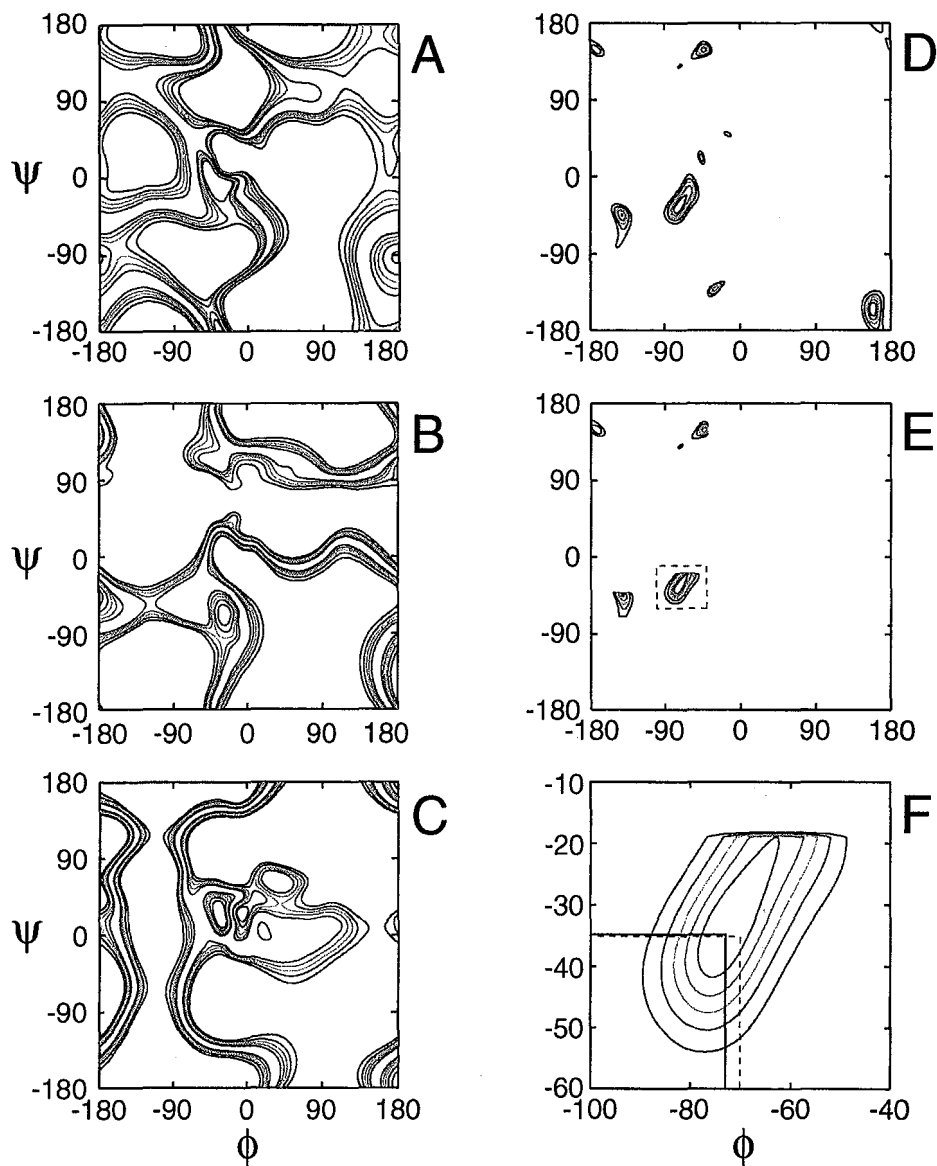


Figure 5.4. Z-surfaces calculated from the experimentally determined CSA of the $^{13}\text{C}_\alpha$ leucine in Boc-VA*L-Aib-VAL-OMe I and theoretical leucine chemical shift surfaces scaled according to the correlation determined in fig. 5.3d. (A) ^1Z -surface for δ_{11} . (B) ^1Z -surface for δ_{22} . (C) ^1Z -surface for δ_{33} . (D) ^3Z -surface showing the intersection of the surfaces from (A-C). (E) As in (D), with all of the conformationally unallowed regions zeroed. The boxed region contains the area of highest probability and is expanded in (F) The predicted dihedral angles are $\phi = -74^\circ$, $\psi = -35^\circ$ (solid lines), while those determined in the crystal structure are $\phi = -71^\circ$, $\psi = -35^\circ$ (dashed lines).

probability region of figs. 5.4d and e. In table 5.3, the predicted leucine dihedral angles for Boc-VA*L-Aib-VAL-OMe I as well as the dihedral angles for the other peptides are compared to values taken from their x-ray structures. Dihedral angles for A*AA I and A*AA II were not predictable because the measured chemical-shift tensors resulted from an average of two structures present in the AAA unit cell. Although an average theoretical chemical-shift tensor can be predicted from two structures, a structure can not be predicted from an average of two chemical-shift tensors.

Table 5.3. Summary of dihedral angles predicted using the CSA/Z approach.

Compound	X-ray		Predicted	
	ϕ	ψ	ϕ	ψ
G*AV	-69	-38	-69	-27
Boc-V*AL-Aib-VAL-OMe I ^a	-61	-45	-52	-31
Boc-VA*L-Aib-VAL-OMe I ^b	-71	-35	-74	-35
Boc-VA*L-Aib-VAL-OMe II ^{a,b}	-62	-29	-67	-31
L*LVY-OMe ^{a,b}	-129	124	-100	111
Boc-VAL-Aib-*VAL-OMe I	-87	-11	-78	149
LL*VY-OMe	-124	120	-152	113

^aThe listed ϕ/ψ solution is the result of a weighted average of two nearby high-probability solution.

^bIn addition to predicting ϕ and ψ the correct χ_2 rotamer was also predicted based on comparisons of the highest probability solutions for each rotamer ³Z surface.

For the ³Z-surfaces obtained for Boc-V*AL-Aib-VAL-OMe I, Boc-VA*L-Aib-VAL-OMe II, and L*LVY-OMe, two solutions were found that were very close to each

other (within $\pm 30^\circ$ in both ϕ and ψ). In each case, it was noticed that the correct ϕ/ψ conformation was between the two close solutions (fig. 5.5). By using an average of the ϕ and ψ angles for each solution (weighted by the probabilities of each solution) a more accurate conformational prediction was made for each of the three peptides. Although this averaging of conformations is unnecessary (the highest-probability solution is still close to the actual conformation), given the repeated success of the weighted average, it appears to be a reasonable procedure to use when two high-probability solutions are in close proximity to each other.

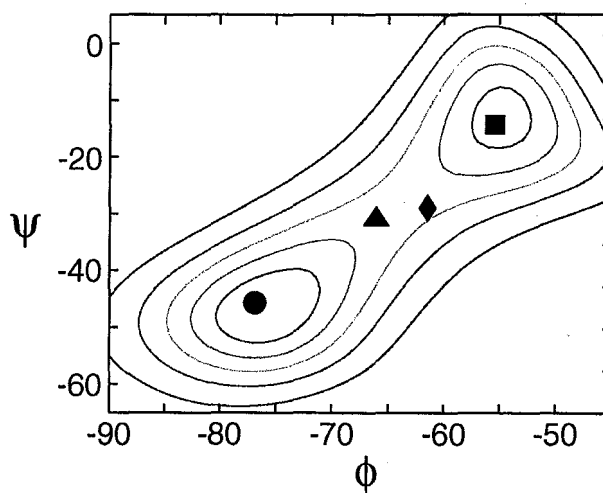


Figure 5.5. Example of the weighted averaging of two close solutions. The points marked by (■) and (●) are the two predicted solutions. The (▲) marks the weighted average of the two solutions. The actual solution (according to the x-ray structure) is marked by the (◆).

Table 5.3 clearly demonstrates the predictive power of the “CSA/Z” method when applied to alanine and leucine residues in solid-state peptides. Overall, predictions of ϕ were

accurate to within $\pm 9.2^\circ$ and predictions of ψ were accurate to within $\pm 7.8^\circ$. It should be noted that for leucine, the predictive power did not stop at just ϕ and ψ ; attempted predictions of ϕ and ψ using the leucine chemical-shift tensor surfaces that corresponded to incorrect χ_2 values (according to the x-ray structures) gave lower probability solutions than predictions using the correct χ_2 surface. This suggests that δ_{11} , δ_{22} , and δ_{33} might also be sufficient to predict χ_2 backbone dihedral angles. This is not surprising given that for certain χ_2 conformations, the α -carbon and the δ -carbon in leucine can be in close proximity (the γ -gauche effect).

Dihedral angle predictions for valine residues were not as successful as those for alanine and leucine. For Boc-VAL-Aib-*VAL-OMe I, the wrong solution was predicted, and for LL*VY-OMe, the highest probability solution was obtained using the wrong χ_1 conformation (although the prediction using the correct χ_1 surface was close to the actual conformation). It is unclear at this point why the valine predictions are not as accurate as those for alanine and leucine. One possibility is that an α -carbon CSA is not sufficient to predict ϕ , ψ , and χ_1 , in which case using 1Z -surfaces for the three $^{13}C_\beta$ chemical-shift tensor elements to determine a 1Z -surface should vastly improve dihedral angle predictions in valine. Currently, $^{13}C_\beta$ chemical-shift surfaces exist for a variety of amino acids.

5.5. Conclusions

Given the need for selective ^{13}C and ^{15}N isotopic labeling in solid-state NMR studies of peptides and proteins, techniques that maximize the information content of each labeled sample are desirable. The CSA/Z method is potentially an excellent source of additional structural constraints in studies of peptides and proteins. For each $^{13}C_\alpha$

label used to measure a distance through dipolar recoupling, a local ϕ/ψ conformation around that $^{13}\text{C}_\alpha$ nucleus can be obtained. With the inclusion of Z-surfaces for $^{13}\text{C}_\beta$ and $^{13}\text{C}_\gamma$ chemical-shift tensors, as well as Z-surfaces which predict the orientation of the CSA, it should be possible to provide additional constraints on both backbone and side-chain dihedral angles, thereby increasing the predictive power of the CSA/Z surface method.

Chapter 6: Spin-Polarization Induced Nuclear Overhauser Effect

6.1. Introduction

Xenon is chemically inert, yet exhibits NMR parameters that are highly sensitive to its chemical environment. Considerable work has therefore capitalized on the utility of ^{129}Xe ($I = 1/2$) as a magnetic resonance probe of molecules, materials, and biological systems[52,117-121]. Much of this work has utilized the highly sensitive chemical shift of ^{129}Xe in order to reveal properties of the xenon environment. Selective polarization transfer from protons to ^{129}Xe has also been used to investigate sites of xenon binding[122] and xenon preferential solvation[123]. Such experiments have the advantage of providing direct microscopic information regarding the xenon surroundings, and should prove useful for the interpretation of experimental ^{129}Xe chemical shifts, but they rely on the weak intermolecular cross-relaxation between ^{129}Xe and nuclear spins in its environment. Furthermore, selective irradiation in complex ^1H spectra can be difficult to achieve, and 2D heteronuclear ^1H - ^{129}Xe NOESY experiments would be enormously time-consuming.

As discussed in chapter 3, the nuclear spin polarization of ^{129}Xe can be increased by 4-5 orders of magnitude through optical pumping. Laser-polarized ^{129}Xe provides significantly enhanced sensitivity for a variety of NMR and MRI experiments[124]. For example, the xenon polarization can be transferred via cross-relaxation to molecules in solution[56,125,126] and to surfaces[57,59,127-131] by a process called the "spin polarization-induced nuclear Overhauser effect" or "SPINOE". This chapter provides a general theoretical framework describing the SPINOE in solution, with emphasis placed on the interpretation of SPINOE results in terms of the interactions between xenon and its environment.

6.2. The Solomon Equations for a Two-Spin System

Cross-relaxation between two spins, I and S, is described by the Solomon equations[132,133]:

$$(6.1a) \quad \frac{dI_z}{dt} = -\rho_I(I_z - I_0) - \sigma_{IS}(S_z - S_0)$$

$$(6.1b) \quad \frac{dI_z}{dt} = -\rho_S(S_z - S_0) - \sigma_{SI}(I_z - I_0)$$

where I_z and S_z are the average values of the z-component of the \bar{I} and \bar{S} nuclear spin operators, and I_0 and S_0 are the equilibrium values, with

$$(6.2) \quad I_0 = \frac{I(I+1)\hbar\gamma_I B_0}{3kT}$$

and similarly for spin S. The values ρ_I , ρ_S and σ_{IS} , σ_{SI} are respectively the auto-relaxation and cross-relaxation rate constants. A full solution to the Solomon equations can be found in the literature[134,135]. If the nuclear spin-lattice relaxation of spin S is much slower than that of spin I (normally the case for dissolved ^{129}Xe), the change in the polarization of spin I is well-approximated by:

$$(6.3) \quad f_I(t) = f_I(0)e^{-\rho_I t} - \frac{S_0}{I_0} f_S(0) \frac{\sigma_{IS}}{\rho_I} (1 - e^{-\rho_I t})$$

where

$$(6.4) \quad f_I(t) = \frac{(I_z(t) - I_0)}{I_0}$$

is the fractional polarization enhancement of spin I (and similarly for spin S). Equation (6.3) is the solution to eq. (6.1.a) given a constant polarization of spin S, and is valid in the short time limit (i.e., for times short relative to the spin-lattice relaxation time

of spin S, $T_1^S = \frac{1}{\rho_S}$) or when the S spin polarization is maintained by continuous flow (fig. 6.1). The second term on the right side of eq. (6.3) describes the time evolution of the polarization of spin I originating from $S \rightarrow I$ polarization transfer. For intermolecular polarization transfer, the magnitude of this term is often small with respect to the equilibrium polarization of spin I[136], requiring an NMR pulse sequence dedicated to the direct measurement of the SPINOE difference. Such a heteronuclear difference NOE pulse sequence is described in section 6.6. Hereafter, an NMR spectrum obtained using this sequence will be referred to as a SPINOE spectrum.

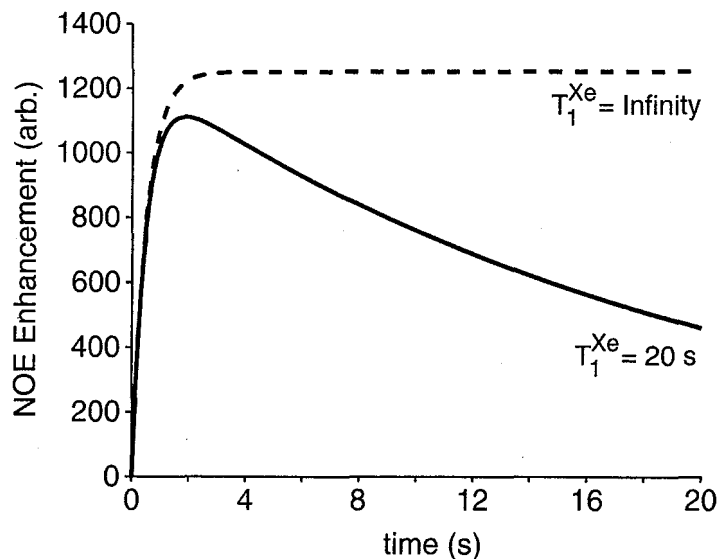


Figure 6.1. Calculated time dependence of the SPINOE signal, including (solid line) and not including (dotted line) the exponential decay caused by the eventual ^{129}Xe spin-lattice relaxation. Curves were calculated with $\rho_I = 2 \text{ s}^{-1}$, $\sigma_{IS} = 0.001 \text{ s}^{-1}$ and $\rho_S = 0.05 \text{ s}^{-1}$ (for the solid curve). Behavior such as that shown with the dotted line may also be seen under conditions of continuous flow of polarized xenon[129]. Figure taken from Ref. [136].

6.3. ^{129}Xe to ^1H Polarization Transfer

In the framework of the dipolar-coupled two-spin model, the auto-relaxation of spin I (^1H) is solely a consequence of dipole-dipole interactions with spin S (^{129}Xe). However, molecules in solution contain many-spin systems, so intermolecular ^1H - ^{129}Xe dipole-dipole interactions are not likely to contribute significantly to the ^1H auto-relaxation rate. For solutes at low concentration in deuterated solvents, when no paramagnetic species are present, intramolecular ^1H - ^1H dipole-dipole interactions are expected to dominate the auto-relaxation of protons in molecules large enough to bind xenon. Therefore, the simplest realistic model for $^{129}\text{Xe} \rightarrow ^1\text{H}$ polarization transfer requires at least a three-spin system: two interacting ^1H 's and one ^{129}Xe in dipolar interaction with one of the ^1H sites. However, for the purpose of interpreting experimental SPINOE spectra, the two-spin model is sufficient, remembering that in eq. (6.3), $\rho_I \approx \frac{1}{T_1^H}$, where T_1^H is the experimental spin-lattice ^1H relaxation time.

Finally, because both ^1H and ^{129}Xe nuclei have a spin quantum number of $I = 1/2$, the ratio $\frac{S_0}{I_0}$ is equal to $\frac{\gamma_{Xe}}{\gamma_H}$ (and is negative, due to the negative value of γ_{Xe}).

Equation (6.3) can then be rewritten as:

$$(6.6) \quad f_H(t) = f_H(0)e^{-t/T_1^H} - \frac{\gamma_{Xe}}{\gamma_H} f_{Xe}(0) \sigma_{HXe} T_1^H (1 - e^{-t/T_1^H}).$$

By using the measured ^1H enhancements, and provided that the ^1H relaxation times and the ^{129}Xe polarization are known, eq. (6.6) may be used to obtain the ^1H - ^{129}Xe cross-relaxation rates, σ_{HXe} . Values of σ_{HXe} for various protons in a sample can then be used

to provide structural information, as will be shown in chapters 10 and 11 for α -cyclodextrin and cryptophane-A, respectively.

6.4. General Considerations for ^1H - ^{129}Xe Cross-Relaxation Rates

The quantity σ_{HXe} largely controls the $^{129}\text{Xe} \rightarrow ^1\text{H}$ polarization transfer. Assuming an exponential decay for the H-Xe dipole-dipole interaction correlation function, the cross-relaxation rate is given by [133]:

$$(6.7) \quad \sigma_{HXe} = \left(\frac{\mu_0}{4\pi} \right)^2 \frac{\hbar^2 \gamma_H^2 \gamma_{Xe}^2}{10} \left\langle \frac{1}{r_{HXe}^6} \right\rangle [6J(\omega_H + \omega_{Xe}) - J(\omega_H - \omega_{Xe})]$$

with

$$(6.8) \quad J(\omega) = \frac{\tau_c}{1 + \omega^2 \tau_c^2},$$

where τ_c is the correlation time associated with the fluctuations of the H-Xe dipole-dipole interactions, r_{HXe} is the H-Xe internuclear distance, and $\langle \rangle$ denotes the ensemble average.

Both $\langle r_{HXe}^{-6} \rangle$ and τ_c control the amplitude and selectivity of the $^{129}\text{Xe} \rightarrow ^1\text{H}$ polarization transfer. The dependence of σ_{HXe} on the correlation time can be understood from fig. 6.2 where $\omega_H [6J(\omega_H + \omega_{Xe}) - J(\omega_H - \omega_{Xe})]$ is displayed as a function of $\omega_H \tau_c$. The function indicates that σ_{HXe} is always positive and has its maximum value at $\omega_H \tau_c \approx 0.68$. An increase in the correlation time from a few ps ($\omega_H \tau_c = 0.01$ - 0.02) to a value corresponding to the maximum (τ_c in the range 0.2-0.5 ns) gives rise to a ~ 20 -fold increase in σ_{HXe} . However, this increase does not necessarily translate into an increase

in the observed SPINOE enhancement. Indeed, in real systems an increase in the correlation time characterizing the H-Xe dipole-dipole interactions is most frequently accompanied by a corresponding increase in the correlation time characterizing the H-H dipole-dipole interactions, and a concomitant reduction of T_1^H .

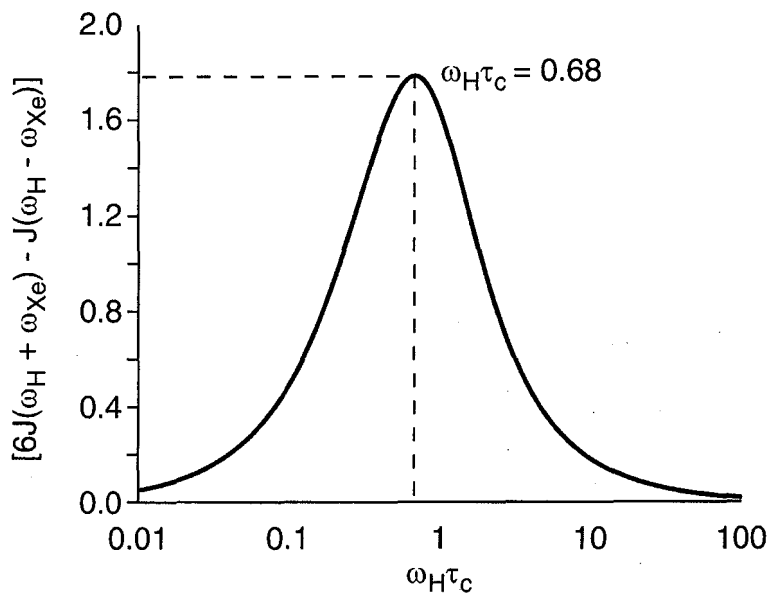


Figure 6.2. Illustration of the dependence of the ^1H - ^{129}Xe cross-relaxation rate, σ_{HXe} , on the correlation time. Figure adapted from Ref. [136].

6.5. Effects of σ_{HXe} and Intermolecular Interactions on the SPINOE

The value of σ_{HXe} depends on H-Xe dipole-dipole interactions which change with the structural and dynamical characteristics of the intermolecular couplings between xenon and its molecular environment. A given molecule, M, may participate in various types of interactions with a xenon atom including non-specific interactions (i.e., diffusive coupling), preferential solvation, and xenon binding (the formation of a Xe:M complex).

Exchange phenomena are involved between these various situations, but the exchange is generally rapid with respect to both the ^1H and ^{129}Xe relaxation rates. Furthermore, ^1H chemical shifts are expected to be poorly sensitive to intermolecular interactions with xenon, and therefore fast-exchange conditions with respect to the ^1H chemical-shift NMR time scale are also likely to be fulfilled. This behavior implies that the ^1H spectrum will not be resolved according to the solute-xenon interactions, and that the observed ^1H SPINOE enhancement may originate from a combination of interaction modes. Therefore, the experimental H-Xe cross-relaxation rate is most generally written as:

$$(6.9) \quad \sigma_{HXe} = \sum_i \frac{[M]_i}{[M]_T} \sigma_{HXe}^i$$

where the summation runs over the interaction modes, $[M]_T$ is the total concentration of the solute, $[M]_i$ is the molar concentration of the solute involved in the interaction mode i , and σ_{HXe}^i is the H-Xe cross-relaxation rate associated with that mode.

For a dilute solution of xenon-binding molecules, a simple model considers two modes of interaction: diffusive coupling, σ_{HXe}^d , which exists for any kind of solute molecule, and xenon binding, σ_{HXe}^b , which gives rise to the formation of a 1-to-1 xenon:host complex:

$$(6.10) \quad \sigma_{HXe} = \sigma_{HXe}^d + \frac{[\text{Xe}:M]}{[M]_T} \sigma_{HXe}^b.$$

In eq. (6.10), it is assumed that both "empty" host molecules and molecules with included xenon (hereafter, included xenon is referred to as Xe_{in}) experience identical diffusive coupling with unbound xenon (referred to as Xe_{out}); $[\text{Xe}:M]$ is the equilibrium molar concentration of the xenon:host complex ($[\text{Xe}:M] \equiv [Xe]_{in}$).

6.5.1. Cross-Relaxation Rates in the Diffusive Coupling Regime

A proper description of the intermolecular cross-relaxation originating from diffusive coupling requires a detailed microscopic understanding of the structure and dynamics of solutions. Although molecular dynamics simulations are very helpful for characterizing intermolecular relaxation[137,138], they tend to be computationally demanding. However, simpler models of intermolecular relaxation can be found in the literature that rely on crude assumptions[133], yet provide reasonable qualitative descriptions of the intermolecular dipole-dipole relaxation process. For example, it can be shown that σ_{IS} should be linearly dependent on the concentration of molecules bearing spin S; thus, σ_{HXe}^d is dependent on $[Xe]_{out}$. Such a dependence in fact arises from the ensemble average of r_{HXe}^{-6} . To a good approximation, $\langle r_{HXe}^{-6} \rangle^d$ is proportional to $[Xe]_{out}$, and therefore a concentration-normalized H-Xe cross-relaxation rate, σ_{HXe}^n ($s^{-1} \cdot M^{-1}$), may be defined according to the relation:

$$(6.11) \quad \sigma_{HXe}^d = \sigma_{HXe}^n [Xe]_{out}.$$

Concerning the dynamics of the diffusive coupling, it is clear that an upper bound for the correlation time τ_c^d is provided by the residence time of xenon in the solvation shell of the solute. In common solvents, τ_c^d is in the range of 10^{-12} to 10^{-11} s, and the condition of extreme narrowing is therefore fulfilled. The 1H - ^{129}Xe cross-relaxation rate due to diffusive coupling is then given by:

$$(6.12) \quad \sigma_{HXe} = \left(\frac{\mu_0}{4\pi} \right)^2 \frac{\hbar^2 \gamma_H^2 \gamma_{Xe}^2}{10} \langle r_{HXe}^{-6} \rangle^d 5\tau_c^d.$$

It is worth noting that τ_c^d may be unrelated to the correlation time controlling the 1H

dipole-dipole intramolecular relaxation of the solute molecule. For instance, in circumstances where the molecular mass of the solute significantly exceeds the xenon atomic mass, the tumbling motion of the solute molecules is expected to be slow on the timescale of the residence of xenon atoms in the solvation shell of the solute. As a consequence, the importance of the SPINOE signal originating from diffusive coupling is expected to decrease for increasing solute size, not because σ_{HXe}^d is affected, but because T_1^H is reduced (see eq. (6.6)).

The order of magnitude of σ_{HXe}^n and σ_{HXe}^d can now be estimated by assuming the system is a monatomic fluid and by using the approximation[136]

$$(6.13) \quad \langle r_{HXe}^{-6} \rangle^d \approx (4\pi N_A \times 10^{-27}) \left(\frac{1}{3} r_0^{-3} [Xe]_{out} \right),$$

where r_0 is the proton-xenon minimum approach distance. Using this result and eqs. (6.11) and (6.12), with $\tau_c^d = 5$ ps and r_0 in the range 3.0-3.2 Å, σ_{HXe}^n is estimated to be on the order of $10^{-5} \text{ s}^{-1} \cdot \text{M}^{-1}$, a figure in agreement with experimental results[56,125]. Because the solubility of xenon in organic solvents under standard conditions is on the order of 0.1 M, σ_{HXe}^d is expected to be on the order of 10^{-6} s^{-1} .

6.5.2. Cross-Relaxation Rates in the Binding Regime

Binding of xenon implies that a particular configuration of a xenon-solute pair has a lifetime long enough that it can be considered as a supramolecule. The time scale relevant to $^{129}\text{Xe} \rightarrow ^1\text{H}$ polarization transfer is the correlation time, τ_r , for tumbling motion of the transient Xe-solute pair. Binding implies that the lifetime of the Xe-solute pair is much longer than the correlation time for its overall tumbling motion, and

therefore the latter controls the dynamics of σ_{HXe}^b . Under these circumstances, the description of the Xe-H cross-relaxation rate reduces to the intramolecular case, and eq. (6.7) may be used with $\tau_c^b = \tau_r$ to obtain H-Xe average distances that characterize the structure of the xenon-host complex. Naturally, the validity of such an analysis of experimental σ_{HXe}^b data depends on the importance of internal dynamics. The consequences of internal motions of the host molecule, in addition to the motion of xenon inside the binding site, are $\tau_c^b < \tau_r$ and $\langle r_{HXe}^{-6} \rangle^b$ values which may be difficult to interpret because they correspond to weighted averages over multiple configurations. In such cases, molecular dynamics simulations may be helpful.

An upper bound for σ_{HXe}^b can be estimated from eqs. (6.7) and (6.8) using $\omega_H \tau_c^b = 0.68$ (fig. 6.2) and $\langle r_{HXe}^{-6} \rangle^b = (3.2 \text{ \AA})^{-6}$ (an estimate of the minimum approach distance of Xe and H). For a ^1H resonance frequency of 400 MHz, these numbers correspond to a σ_{HXe}^b value of $3 \times 10^{-3} \text{ s}^{-1}$, a figure three orders of magnitude larger than the value expected for the ^1H - ^{129}Xe cross-relaxation rate due to diffusive coupling. Indeed, σ_{HXe}^b values of this order have been observed for xenon bound to α -cyclodextrin in solution[125].

6.5.3. Dependence of σ_{HXe} on the Xe Concentration

In section 6.5.1, it was shown that σ_{HXe}^d is, to a good approximation, proportional to the concentration of unbound xenon. An additional concentration dependence of the experimental cross-relaxation rate may arise from the effect of the xenon concentration

on the binding equilibrium. Based on the definition of the binding constant, K , for the equilibrium $Xe_{out} + M \leftrightarrow Xe:M$, the following relationships hold:

$$(6.14) \quad \frac{[Xe:M]}{[M]_T} = \frac{K[Xe]_{out}}{1 + K[Xe]_{out}},$$

which reduces for the case of weak binding to

$$(6.15) \quad \frac{[Xe:M]}{[M]_T} \approx K[Xe]_{out},$$

and for the case of strong binding and excess xenon to

$$(6.16) \quad \frac{[Xe:M]}{[M]_T} \approx 1.$$

Equations (6.14) and (6.15) are written in terms of $[Xe]_{out}$, and not as a function of the total concentration in xenon, because for dilute solutions of host molecules, $[Xe]_{out}$ is well approximated by the equilibrium solubility of xenon in the pure solvent. For example, an equilibrium constant of $\sim 2 \text{ M}^{-1}$ has been reported for the binding of xenon to cyclodextrin in DMSO (298 K)[122]. For an equilibrium xenon pressure of 1 atm, the solubility of xenon in DMSO is 0.024 M (298 K). Therefore, eq. (6.15) applies to this system, and a linear increase in the SPINOE originating from binding is expected upon increasing xenon pressures (at least for pressure in the range of 0-3 atm), as shown in fig. 6.3. However, in tetrachloroethane (xenon solubility $\sim 0.1 \text{ M}$), the equilibrium constant for the binding of xenon to cryptophane-A was estimated to be larger than 3000 M^{-1} (278 K)[139], and therefore eq. (6.16) is more appropriate (fig. 6.3). Using eqs. (6.11) and (6.14), eq. (6.10) can now be rewritten taking account of the isotopic abundance in ^{129}Xe , A_{129} as:

$$(6.17) \quad \sigma_{HXe} = A_{129} \left[\sigma_{HXe}^n [Xe]_{out} + \frac{K[Xe]_{out}}{1 + K[Xe]_{out}} \sigma_{HXe}^b \right].$$

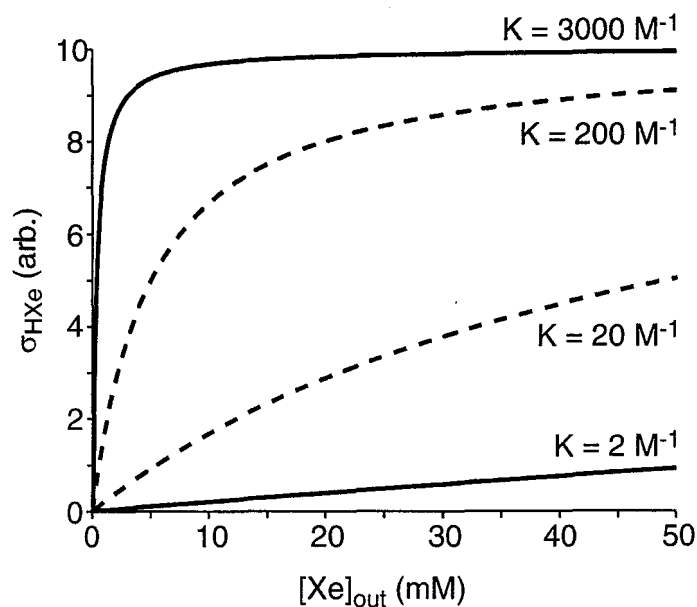


Figure 6.3. Dependence of experimental Xe-H cross-relaxation rate (σ_{HXe}) originating from xenon binding on the equilibrium xenon concentration in the solvent for various association constants, K . Curves with solid lines are for systems that have been studied via SPINOE experiments (Xe:cyclodextrin in DMSO, $K = 2 \text{ M}^{-1}$; Xe:cryptophane-A in $(\text{CDCl}_2)_2$, $K = 3000 \text{ M}^{-1}$). The dotted curves, added for illustrative purposes, correspond to what would be expected for Xe:cyclodextrin in H_2O , $K \approx 20 \text{ M}^{-1}$ [122], and xenon:myoglobin or xenon:hemicarcerand, $K \approx 200 \text{ M}^{-1}$ [140,141]. Figure taken from Ref. [136].

6.6. The DINOE Sequence

For systems in which $\frac{\sigma_{HXe}}{\rho_H} \ll 1$, the enhancement of the ^1H signal is typically

small when compared to the thermal equilibrium signal. In such cases, it is desirable to suppress the equilibrium ^1H signal so all that remains is the signal due to the SPINOE enhancement. Figure 6.4 shows two variants of a difference-SPINOE or “DINOE”

sequence for measuring a SPINOE spectrum in which the equilibrium ^1H signal is efficiently suppressed, thus permitting the direct observation of SPINOE signals as low as $\sim 1 \times 10^{-4}$ times that of the equilibrium signal. In both sequences, the equilibrium ^1H signals are first saturated by 90° and gradient pulses, and the saturation is maintained by a 180° pulse followed immediately by a gradient pulse. A ^{129}Xe 180° pulse allows SPINOE signals to accumulate during the mixing periods τ_1 and τ_2 . The total mixing period, $\tau = \tau_1 + \tau_2$, is in the range of the ^1H T_1 's but is short compared to the ^{129}Xe T_1 . The ratio τ_1/τ_2 is chosen to minimize the overall equilibrium ^1H signal observed in the absence of ^1H - ^{129}Xe cross-relaxation. The 180° ^1H and ^{129}Xe inversion pulses are experimentally optimized BIR-4 adiabatic inversion pulses[142]. Each ^1H SPINOE spectrum is the difference of two acquisitions. The resulting ^1H SPINOE signal is given by the following relation:

$$(6.18) \quad \Delta f_H(\tau) = -\frac{\gamma_{Xe}}{\gamma_{He}} f_{Xe}(0) \sigma_{HXe} T_1^H (1 - e^{-\tau/T_1^H}),$$

where $\Delta f_H(\tau)$ is the observed difference-SPINOE enhancement.

For observation of ^1H - ^{129}Xe SPINOE in strongly bound systems, such as xenon in cryptophane-A, an additional factor must be considered when using the DINOE sequence. Because xenon bound to cryptophane-A is in slow exchange with xenon in the solvent, the ^{129}Xe NMR spectrum has two peaks, separated by over 150 ppm. This makes inversion of all of the xenon spins problematic, even when using an adiabatic pulse like BIR-4. Furthermore, each time the ^{129}Xe magnetization is only partially inverted, magnetization is lost, preventing one from making the assumption that $f_{Xe}(t) \approx f_{Xe}(0)$, even though T_1^{Xe} may be long. Fortunately, two steps can be taken to

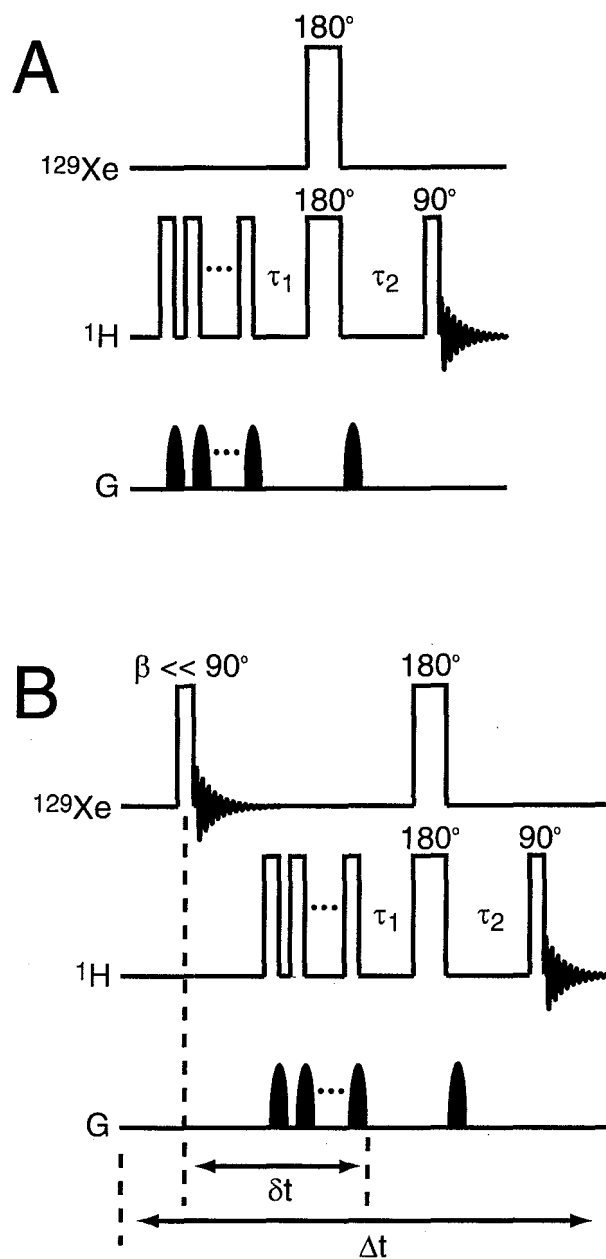


Figure 6.4. Variants of the "DINOE" heteronuclear difference NOE pulse sequence for ^{129}Xe - ^1H SPINOE NMR experiments. The pulse sequence in (B) is identical to the one shown in (A), with the addition of a small pulse to the ^{129}Xe magnetization that allows measurement of the ^{129}Xe polarization.

counter incomplete inversion of the ^{129}Xe magnetization. First, $f_{\text{Xe}}(t)$ can be measured by sampling the ^{129}Xe magnetization at the start of each scan (fig. 6.4b). Second, the loss of magnetization between the τ_1 and τ_2 periods can be accounted for by using an inversion fraction, q , so that eq. (6.18) can be re-written as

$$(6.19) \quad \Delta f_H(\tau) = -\frac{\gamma_{\text{Xe}}}{\gamma_{\text{He}}} f_{\text{Xe}}^{\text{obs}}(0) \cos(\beta) e^{-\delta d / T_1^{\text{Xe}}} \sigma_{\text{HXe}} T_1^{\text{H}} \times \left\{ \left(1 - e^{-\tau_1 / T_1^{\text{H}}}\right) - (1 - q) \left(1 - e^{-\tau_2 / T_1^{\text{H}}}\right) \right\},$$

where $f_{\text{Xe}}^{\text{obs}}(0)$ is the fractional ^{129}Xe polarization observed at the start of each scan, the factor $e^{-\delta d / T_1^{\text{Xe}}}$ accounts for the decay of ^{129}Xe magnetization during the time interval between its measurement and the beginning of the SPINOE measurement (see fig. 6.4b), and the term $(1 - q) \left(1 - e^{-\tau_2 / T_1^{\text{H}}}\right)$ accounts for the smaller SPINOE during the delay τ_2 originating from the loss of ^{129}Xe polarization incurred from inefficient inversion. In practice, the value of q typically varied between ~ 0.5 and ~ 0.8 in experiments involving cryptophane-A when BIR-4 pulses were used to invert the ^{129}Xe magnetization. Although they were never used in the SPINOE experiments reported in this thesis, adiabatic inversion pulses whose amplitude and phase are modulated in the form of a hyperbolic tangent[143] were shown to produce values of q that were >0.95 over a 30 kHz range.

Chapter 7: NMR in Liquid and Supercritical Xenon

7.1. Introduction

Increasing the nuclear spin polarization of molecules in solution could be useful for a variety of liquid-state NMR and MRI experiments, especially in circumstances where the observed nucleus is in low natural abundance or the species in question are short-lived. As shown in the previous chapter, one means of achieving enhanced NMR signals in solution is through polarization transfer from dissolved laser-polarized ^{129}Xe to other solute species via the Spin Polarization-Induced Nuclear Overhauser Effect or SPINOE. However, the enhancement possible through introducing xenon as a solute to enhance the NMR signals of other solute molecules is severely limited, especially when the xenon solubility is low and the xenon T_1 is very short[136]. It has been suggested[125,144] that much larger bulk signal enhancements could be generated by using laser-polarized xenon as a polarizing solvent, due to the dramatic increase of the xenon density in such samples. Indeed, liquid laser-polarized xenon was produced[144-146] and used as a polarizing solvent at $-73\text{ }^\circ\text{C}$ to achieve large signal enhancements for certain solutes[126].

Although liquid xenon is a useful solvent in some circumstances[147,148], the solubility characteristics improve dramatically in the supercritical phase[149,150], and the higher and broader temperature range is more convenient for chemical and biophysical investigations. The single phase of supercritical samples obviates the need for stirring, and the low viscosity leads to narrow solute linewidths, especially for samples containing quadrupolar nuclei[151-153]. Furthermore, the density of supercritical xenon, and hence its physical properties (e.g. solubility, dielectric constant,

etc.), are strongly pressure dependent[154]; the physical properties of the solvent can therefore be manipulated to provide specific solvent environments[149]. For example, by fine-tuning the density and composition of supercritical solvents, the dielectric constant was manipulated as to influence the rate and selectivity of chemical reactions[148]. The enhanced thermal stability of biomolecules in supercritical solvents may also prove advantageous for certain experiments[155,156]. By using supercritical laser-polarized xenon as a solvent for catalytic and kinetic studies via NMR, high sensitivity may be achieved under favorable solvent conditions.

7.2. Experimental

Preliminary experiments involving the production of liquid and supercritical laser-polarized xenon were performed using the batch-mode optical pumping apparatus described in subsection 3.2.1. For these experiments, the xenon was completely recoverable (barring any accidents), and so enriched ^{129}Xe (80 atom %) purchased from Isotec (Miamisburg, OH) was utilized. Later, more successful experiments were performed using the continuous-flow apparatus described in subsection 3.2.2. For these experiments, natural abundance ^{129}Xe was used (26 atom %), also obtained from Isotec.

7.2.1. Design of the High-Pressure NMR Tube

Perhaps the most important and delicate piece of equipment in the high-pressure xenon experiments discussed in this chapter is the high-pressure tube—designed to not only hold xenon at very high pressures, but to also withstand the dramatic temperature changes required to rapidly move from the solid phase to beyond the supercritical point.

In this subsection, two tube designs will be discussed, a thick-walled capillary Pyrex™ tube (0.8 mm inner diameter) and a thin-walled sapphire tube (1.5 mm inner diameter). Because of its extremely small inner diameter (and hence very small volumes), the Pyrex™ tubes were ideal for experiments using the batch-mode optically pumping apparatus. The sapphire tube had a much larger volume, and hence the continuous-flow optical pumping setup was required in order to produce enough polarized xenon to reach the supercritical point.

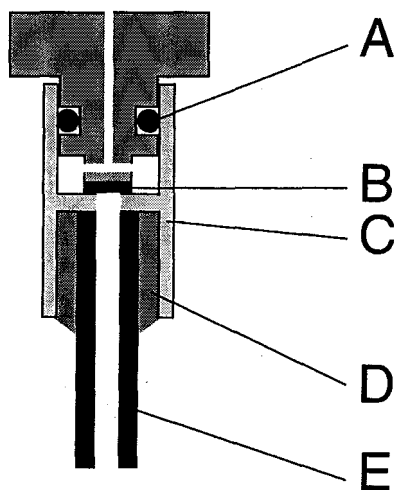


Figure 7.1. Schematic of a high-pressure NMR tube with a BeCu-alloy or titanium valve. A Viton O-ring (A) allows the tube to remain sealed during xenon transfer. A Vespel™ plate (B) at the top of the capillary tube forms a high-pressure seal which prevents any appreciable loss of xenon over many weeks. The valve (C) is glued with Aremco 568 epoxy (D) to either a Pyrex™ capillary tube or a sapphire tube (E). As a precaution, both types of tube were subject to frequent pressure checks of up to 140 atm before experimental use.

A schematic of the high-pressure valve system used for both the PyrexTM and sapphire tubes is shown in fig. 7.1[157,158]. Due to their favorable magnetic properties, the valves were either made of a BeCu-alloy or of titanium. A Viton O-ring (fig. 7.1a) seals the upper and lower components of the valve, preventing xenon from escaping during transfer into the tube. These O-rings are very susceptible to cracks caused by closing the valve tightly, and so have to be replaced after opening and closing the tube more than two or three times. A VespelTM plate (fig. 7.1b) at the top of the capillary tube forms a high-pressure seal which prevents any appreciable loss of xenon over many weeks. The VespelTM plate tended to become unglued after a few closures, and so often had to be replaced or re-glued. The valves were glued to the PyrexTM and sapphire tubes (fig. 7.1e) with Aremco 568 epoxy (fig. 7.1d). The tubes were coated with SurfaSilTM (Pierce Chemical, Rockford, IL) to protect the xenon from paramagnetic centers embedded in the tubes. The valves were coated with polystyrene for the same reason.

7.2.2. Production of Polarized Liquid and Supercritical ¹²⁹Xe

Because they require different optical pumping set-ups, techniques for production of liquid or supercritical laser-polarized xenon differed for the two types of tube (PyrexTM and sapphire). Figure 7.2 shows the phase of the ¹²⁹Xe during different points in the production of supercritical laser-polarized xenon using the batch-mode apparatus/PyrexTM tube. Following optical pumping at ~60 °C (fig. 7.2a), the laser-polarized ¹²⁹Xe gas from the optical pumping cell was frozen with liquid nitrogen into a detachable U-tube sidearm (fig. 7.2b). The sidearm was placed in an external magnetic field provided by a small permanent magnet (1 T) in order to maintain the polarization of

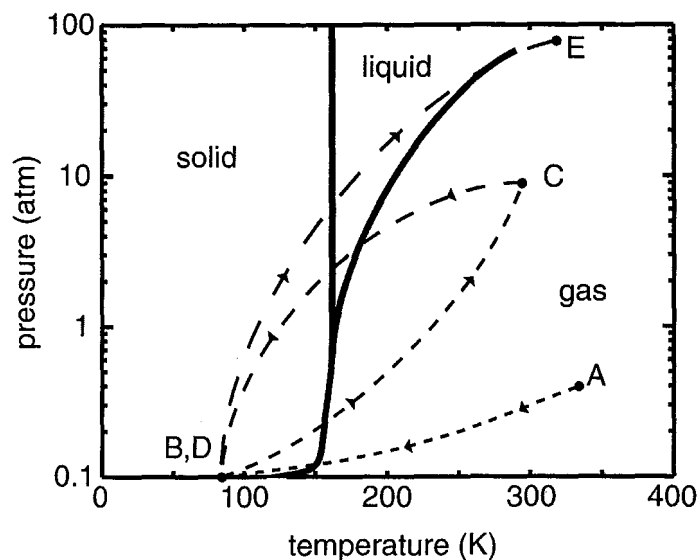


Figure 7.2. Schematic of the phase diagram for xenon[159] which shows the path through which supercritical laser-polarized xenon was produced using the batch-mode apparatus. The dashed lines between the points are estimates of the paths between phases and are meant only to guide the eye. The xenon is first laser-polarized at low-pressure (~ 0.4 atm) and high temperature (~ 60 °C) for 30 minutes (A) and then frozen into a sidearm (B). The sidearm is rapidly warmed producing xenon gas (C) which is then condensed and eventually frozen into the capillary tube (D). Finally, the tube is warmed to 52 °C, reaching the supercritical state (E). Figure taken from Ref. [61].

the solid xenon. Next, the valve separating the sidearm from the optical pumping cell was closed and the solid xenon was sublimed (fig. 7.2c) and then condensed (and eventually frozen) by a liquid-nitrogen bath into the high-pressure capillary tube which was also residing next to a 1 T permanent magnet (fig. 7.2d). This two-step transfer procedure was used to ensure that the xenon condensing in the capillary tube would first pass through the liquid phase, thus preventing solid xenon blockages in the capillary tube during freezing. The transition to the supercritical state (fig. 7.2e) was visually confirmed by the disappearance of first the solid and then liquid xenon phases upon

heating the tube to ~ 60 °C with hot water in the fringe field of the superconducting NMR magnet before lowering the tube into the magnet.

Production of liquid or supercritical laser-polarized xenon was far easier using the continuous-flow optical pumping set-up. After collecting xenon in the U-tube (fig. 3.5) for ~ 20 minutes, the flow was halted and the entire system was pumped down with a diffusion pump. Once the pressure in the U-tube (and surrounding tubing) dropped below ~ 1 millitorr, the pump was closed off and the xenon was warmed inside the U-tube with hot water. A pressure gauge allowed observation of the pressure inside the U-tube. The total volume of the U-tube area was estimated at ~ 100 mL, and a 20 minute pumping run at a flow of 0.5 to 1.0 ft³/min could easily produce xenon pressures in the U-tube of 800 to 1000 torr. When the xenon was frozen from the U-tube into the attached sapphire tube, the pressure in the U-tube would typically drop below ~ 150 torr. Once sealed in the sapphire tube, the xenon was quickly warmed with ~ 60 °C water so that the transition through the liquid phase on the way to the supercritical phase would be rapid. It was hypothesized (but never investigated fully) that slow warming of the tube was responsible for previous problems with relaxation of the xenon.

7.3. Results and Discussion

Figure 7.3a shows a ^{129}Xe spectrum of supercritical laser-polarized xenon obtained using the PyrexTM tube and batch-mode pumping setup. Figure 7.3b shows the corresponding equilibrium spectrum taken several hours later. The magnetization produced is inverted in phase with respect to the equilibrium signal shown owing to the direction of the magnetic field in which the xenon was laser-polarized. The chemical

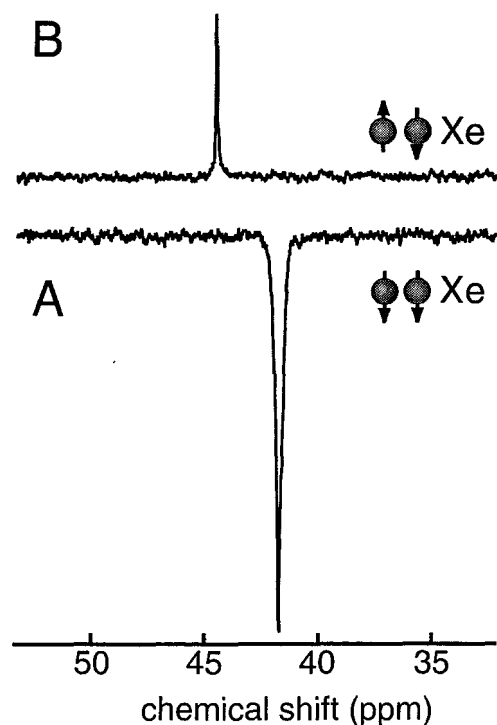


Figure 7.3. (A) Spectrum of supercritical laser-polarized xenon at 52 °C. The spectrum was acquired with one pulse (tipping angle $\approx 3^\circ$). The chemical shift (41.8 ppm) was referenced to that of xenon at zero pressure, indicating a pressure of ~ 65 atm[160]. (B) Spectrum of ^{129}Xe at 22 °C after it had been allowed to reach an equilibrium polarization over several hours. The spectrum was acquired with one pulse ($\approx 90^\circ$). The ^{129}Xe chemical shift (44.5 ppm) indicates a pressure of ~ 54 atm, slightly below the critical pressure (57.6 atm). Figure taken from Ref. [61].

shift of the equilibrium spectrum (44.5 ppm) taken at room temperature (~ 22 °C) corresponds to a xenon density of approximately 81.5 amagats[160] (fig. 7.4a). The difference in chemical shift between the laser-polarized and equilibrium spectra corresponds to a temperature change of ~ 30 C°. Therefore, the chemical shift of 41.8 ppm and temperature of ~ 52 °C indicates that the pressure in the capillary tube immediately after warming the laser-polarized xenon was ~ 65 atm (fig. 7.4b). This

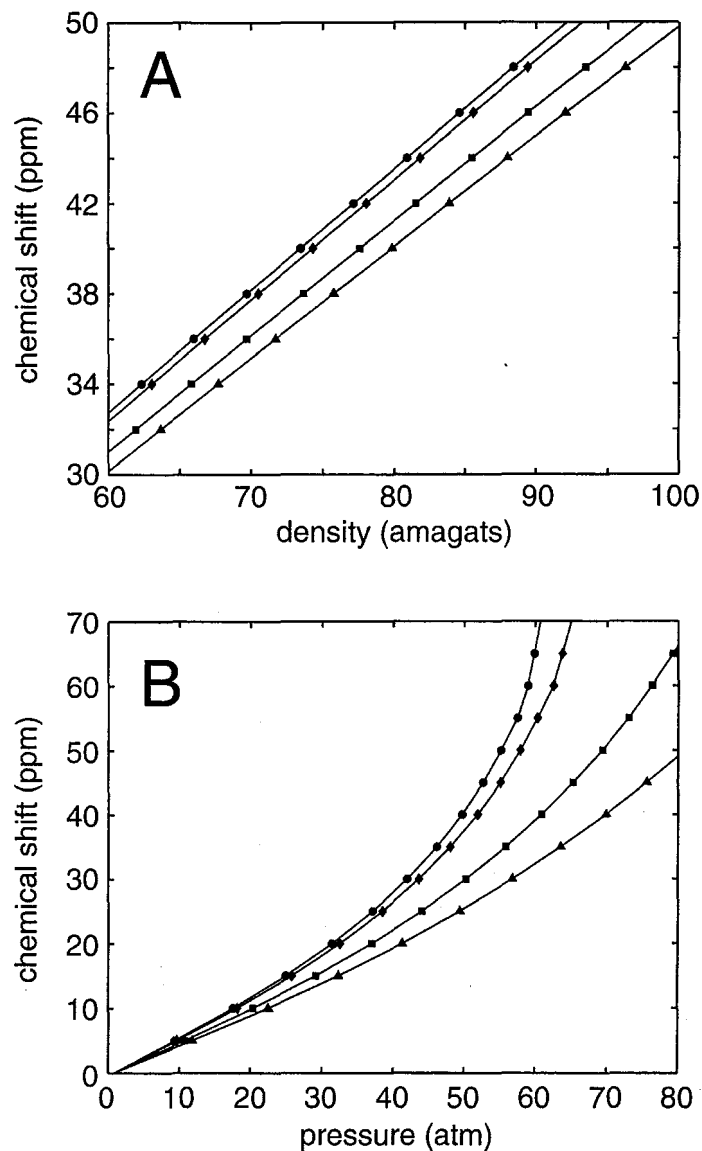


Figure 7.4. ^{129}Xe chemical shift of gaseous xenon as a function of density (A) and pressure (B) at 22 °C (●), 27 °C (◆), 47 °C (■), and 67 °C (▲). The curves were calculated from the temperature and density dependence of the ^{129}Xe chemical shift described by Jameson *et al.*[160]; the xenon pressure was determined from the specific volume, i.e., the inverse density of the xenon which is tabulated as a function of pressure and temperature[161]. The dashed lines in (A) indicate the conditions under which the spectrum in fig. 6.3a was obtained, while the dashed line in (B) shows the critical pressure of xenon. Figure adapted from Ref. [61].

temperature and pressure puts the xenon well beyond the critical point (16.6 °C, 57.6 atm)[159]. The broader linewidth of the spectrum in fig. 7.3a may originate from local density fluctuations in the thermally non-equilibrated sample. Matlab scripts for calculating temperatures, densities and pressures of xenon samples based on the ^{129}Xe chemical shift are available in the “/usr/data/sc_xe” directory on any of the Pines’ group SGI computers.

The laser-polarized ^{129}Xe signal in fig. 7.3 was approximately 140 times that of the equilibrium signal. This enhancement factor represents a loss of almost two orders of magnitude compared to the ^{129}Xe polarization typically prepared by the optical pumping apparatus. It is likely that paramagnetic impurities in the metal valves and tubing were responsible for this loss in polarization, because the T_1 relaxation times of xenon in the solid, liquid, and gas phases are extremely long, and no significant loss of polarization is suffered during transitions between phases[58,144,162,163]. Furthermore, once the supercritical state was achieved, the ^{129}Xe polarization was observed to last for hundreds of seconds.

Given the lack-luster results obtained using batch-mode optical pumping and the tendency for glass tubes to blow-up during heating, we turned to a more robust set-up using a continuous-flow optical pumping setup that offered substantially higher polarizations (2 to 3 times higher than we were getting with the Ti:sapph laser) and sapphire tubes that could sustain much higher pressures. Using the continuous-flow optical pumping setup and sapphire tubes, we were able to substantially increase the polarization to nearly 2000 times that of the equilibrium signal (fig. 7.5). Whereas the

density of the sample in fig. 7.3 was 81.5 amagats, the density of the xenon sample in fig. 7.5 was 135.3 amagats, which at a temperature of 35 °C gives a pressure of 71 atm.

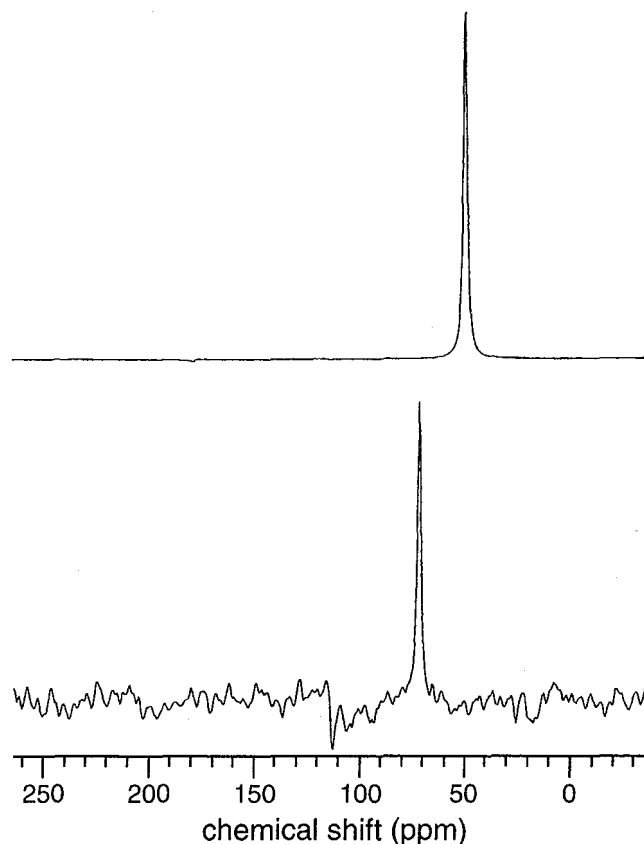


Figure 7.5. (A) Spectrum of supercritical laser-polarized xenon at 35 °C. The spectrum was acquired with one pulse (tipping angle $\approx 3^\circ$). The chemical shift (50.2 ppm) was referenced to that of xenon at zero pressure, indicating a pressure of ~ 72 atm[160] and a density of 135.3 amagats[161]. (B) Spectrum of ^{129}Xe at 20.5 °C after it had been allowed to reach an equilibrium polarization over several hours. The spectrum was acquired with one pulse (tipping angle $\approx 90^\circ$). The ^{129}Xe chemical shift (72.4 ppm) indicates a pressure of ~ 59 atm, which is in excess of critical pressure (57.6 atm).

7.4. Conclusions

These results demonstrate the feasibility of generating supercritical laser-polarized ^{129}Xe for high-resolution NMR studies. Supercritical laser-polarized xenon has the potential to integrate numerous classes of chemistry with the high selectivity of NMR without sacrificing sensitivity. The solubility characteristics of supercritical xenon are favorable for many types of compounds, and can be further improved with the addition of various modifiers[164,165]. Furthermore, since xenon is completely transparent to UV, visible, and mid-IR radiation, it is an attractive solvent for *in situ* spectroscopy, e.g. for organometallic chemistry and photochemistry[165]. The ability to produce supercritical laser-polarized xenon, coupled with a long T_1 and potentially high density (≥ 2 g/mL) make supercritical laser-polarized xenon ideal for increasing the polarization of solute molecules, while the tunable physical characteristics of such a supercritical solvent should permit a wide range of *in situ* studies via NMR.

Chapter 8: Double-Quantum MAS NMR of Spin $I = 1$ Nuclei

8.1. Introduction

Determining the structure of a protein or peptide in the solid-state using NMR is an inherently difficult task. Although dipolar recoupling techniques make it possible to reproduce the same basic set of experiments that liquid-state NMR spectroscopists use to determine protein structures, the inherent lack of resolution in solid-state biological samples (due to broadening from strong ^1H - ^1H dipolar couplings and the magnetic susceptibility anisotropy of most amorphous samples) usually precludes the full assignment of ^{13}C and ^{15}N resonances. This fact led Tycko to suggest that using only conventional ^1H - ^{13}C - ^{15}N correlation experiments, the largest protein that could be fully assigned would be ~30 residues long[85]. Therefore, for full solid-state NMR structures to be determined in unoriented, non-crystalline proteins, novel methods for separating and assigning the ^{13}C and ^{15}N resonances must be developed.

One conceivable method for performing resonance assignments and structural studies in solid-state NMR is to utilize ^{14}N NMR of the backbone amides. ^{14}N is a spin $I = 1$ nucleus with a very low γ ($\approx \frac{1}{15}\gamma_H$) and a very high natural abundance (99.6%). The quadrupolar coupling of ^{14}N is extremely sensitive to its environment, and so has the potential to provide a wealth of structural information about a protein sample[166]. Unfortunately, it is this sensitivity that makes ^{14}N solid-state NMR so difficult—the large 1st-order quadrupolar couplings in the backbone ^{14}N nuclei of amino acids (table 8.1) makes conventional high-field single-quantum NMR impractical. Although techniques have been developed that help to eliminate this broadening, there are certain drawbacks to each of these techniques, as will be discussed below.

In this chapter, the theory behind a potential technique for correlating ^{14}N double-quantum resonances with ^{13}C chemical shifts will be introduced. This technique, dubbed TRDQCP for Triple-Resonance Double-Quantum Cross Polarization, combines fast magic-angle spinning and multi-dimensional NMR with the double-quantum cross-polarization experiment originally performed by Ernst *et. al.*[167]. Although still in the developmental stage, TRDQCP has the potential for providing increased resolution and sensitivity over conventional double-quantum CP or overtone spectroscopy, and could possibly be used to obtain complete backbone ^{13}C assignments in medium-size solid-state proteins.

Table 8.1. ^{14}N quadrupolar coupling strengths and anisotropy parameters for different amino acids at 77 K. Data taken from Ref. [168].

Amino Acid	e^2Qq (MHz)	η
L-Histidine	1.251	0.113
L-Glutamic Acid	1.115	0.154
L-Asparagine·HCl	1.209	0.182
L-Alanine	1.205	0.261
L-Tyrosine	1.078	0.414
Glycine	1.249	0.501
L-Cysteine	1.273	0.640
L-Phenylalanine	1.363	0.597
L-Serine	1.215	0.184
L-Aspartic Acid	1.287	0.149
L-Proline	1.623	0.955

8.2. A Survey of ^{14}N NMR and NQR Techniques

Techniques for obtaining resolvable ^{14}N spectra in the solid-state can be divided into two categories—techniques that utilize high magnetic fields, and those that operate at low magnetic fields. In the ensuing section, both categories of experiment will be discussed, along with their advantages and disadvantages.

8.2.1. Low-Field ^{14}N NMR Techniques

The problem with the 1st-order quadrupolar coupling in solids is not necessarily the strength of the interaction, but rather its orientational dependence. Indeed, in the absence of any anisotropic quadrupolar terms, the isotropic quadrupolar shift can be used to separate resonances that would normally overlap based only on their chemical shifts[167]. However, eliminating the orientationally dependent components of the 1st-order quadrupolar coupling in spin $I = 1$ nuclei is far from trivial. Unlike half-integer quadrupolar nuclei, spin $I = 1$ nuclei do not possess a single-quantum transition that is unaffected to first-order by the quadrupolar Hamiltonian. This renders techniques like DOR and DAS almost useless, since resulting spectra would still be dominated by effects originating from $H_Q^{(1)}$ under MAS. Furthermore, there is no MQMAS experiment that is compatible with the energy levels of a spin $I = 1$ nucleus.

There is another way to eliminate the orientationally dependent terms of any Hamiltonian besides sample rotation. Anisotropic terms in perturbing NMR Hamiltonians (chemical shift, quadrupolar coupling, etc) arise from the truncation that occurs in the presence of a large Zeeman Hamiltonian (i.e., high field). Absent an external magnetic field, the quadrupolar coupling loses any orientational dependence,

and all that remains are the pure quadrupolar energy levels shown in fig. 8.1a. Indeed, the quadrupolar coupling parameters listed in table 8.1 were obtained through the direct observation of quadrupolar transitions at zero-field using nuclear quadrupole resonance (NQR)[168]. There are two main problems with NQR as a tool for studying ^{14}N nuclei. First, the sensitivity of such experiments is extraordinarily low, since the energy splitting in NQR is proportional to the quadrupolar coupling that, as seen in table 8.1, is on the order of a few MHz for amino acids. Problems with low sensitivity in NQR can be obviated to an extent by the use of SQUID detectors[169,170] or probes that shuttle samples between zero and high field[171]. The other disadvantage to zero-field NQR is that one cannot use the sharp ^{14}N resonances to assign neighboring ^{13}C resonances, since the chemical-shift Hamiltonian disappears at zero-field.

8.2.2. High-Field ^{14}N NMR Techniques

As was stated previously, for a spin $I = 1$ nucleus there is no single-quantum transition that is unaffected to first-order by the quadrupolar Hamiltonian. However, as seen in fig. 1.5, the frequency of the double-quantum $m = -1$ to 1 transition is invariant to $H_Q^{(1)}$. Therefore, by measuring the ^{14}N double-quantum spectrum, the large 1st-order quadrupolar coupling can be eliminated, leaving only the 2nd-order quadrupolar coupling, which both broadens and shifts the double-quantum linewidth. Unfortunately, a double-quantum transition is not directly observable in NMR, and so special techniques must be used that allow detection of the $m = -1$ to $m = +1$ transition. Two such techniques are overtone spectroscopy[172] and double-quantum cross polarization[167].

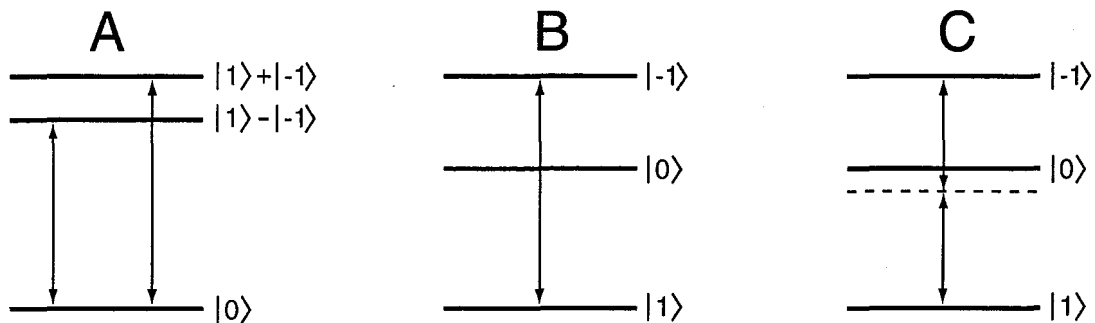


Figure 8.1. (A) ^{14}N NQR energy levels. The presence of a small magnetic field mixes the $m = -1$ and $m = +1$ spin states to create two non-degenerate transitions. (B) The single-photon ^{14}N overtone transition. (C) The two-photon ^{14}N double-quantum transition.

Overtone spectroscopy utilizes the perturbing effect of the quadrupolar interaction to turn a normally unobservable double-quantum transition into an observable single-quantum transition. In the absence of the quadrupolar interaction, the spin states of an ^{14}N nucleus are eigenfunctions of the truncated NMR Hamiltonian. Under such conditions, there is no mixing of the $m = -1$ and $m = +1$ spin states, and so the $m = -1$ and $m = +1$ double-quantum transition is forbidden (and unobservable in a conventional NMR coil). However, in the presence of a strong quadrupolar coupling, the $T_{2\pm 2}$ components of the 2nd-order quadrupolar Hamiltonian (see eq. (1.46)) cause the $m = -1$ and $m = +1$ spin states to mix, creating a weakly-forbidden single-quantum transition at roughly twice the ^{14}N Larmour frequency (fig. 8.1b). This “overtone” transition can then be observed using a conventional NMR coil [166,172]. Although overtone spectroscopy is an excellent tool for performing ^{14}N NMR, it does have one principle drawback. As the external magnetic field is increased, the mixing of the $m = -1$ and $m = +1$ spin states caused by the quadrupolar coupling decreases and the transition becomes harder to excite and observe.

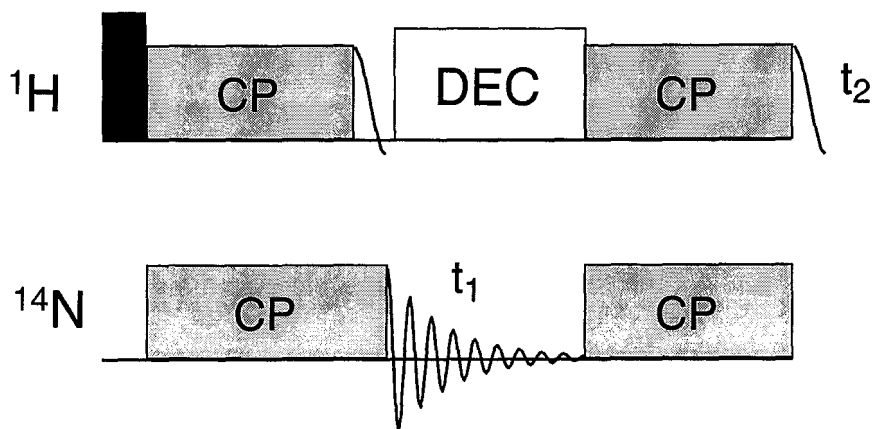


Figure 8.2. Double-quantum cross-polarization pulse sequence. Following CP, the ^1H magnetization is allowed to decay while the ^{14}N double-quantum magnetization remains spin locked. After t_1 , the magnetization is returned to the protons via a second CP step. The ^1H magnetization (often just the first point) is detected in t_2 .

This means that any advantages in sensitivity and lineshape that might be gained by working at high magnetic fields would be negated by a decrease in the sensitivity of the overtone experiment.

Double-quantum cross-polarization (DQCP) works in a slightly different way than overtone spectroscopy. Whereas overtone spectroscopy is based on a directly observable one-photon absorption (fig. 8.1c), DQCP involves a true double-quantum absorption, and so cannot be observed directly. However, because DQCP does not rely on a mixing of the $m = -1$ and $m = +1$ spin states, it has no restrictions based on field strength. The pulse sequence for DQCP is shown in fig. 8.2. In a standard cross-polarization experiment, the Rabi frequencies of the ^1H and ^{14}N nuclei would be matched according to the Hartmann-Hahn condition, so that

$$(8.1) \quad \Omega_H = \Omega_N.$$

This would lead to a polarization of the two single-quantum ^{14}N transitions. However, by setting the ^{14}N Rabi frequency to twice that of protons,

$$(8.2) \quad \Omega_H = 2 \times \Omega_N,$$

a two-photon absorption process occurs and the double-quantum ^{14}N transition is excited. Since the double-quantum transition is not directly observable, the ^{14}N polarization must be detected indirectly, and so a second CP period is used to return magnetization to the neighboring protons for detection.

Unfortunately, there are two major drawbacks to DQCP that prevent its use in solid-state NMR studies of biological molecules. First, although ^1H - ^{14}N cross-polarization results in a seven-fold enhancement of ^{14}N double-quantum polarization, this enhancement is exactly cancelled by the reverse CP to the protons. Second, it is very difficult to obtain perfect subtraction of the residual ^1H signal that is present because of the spin-locking fields and decoupling. This makes observing the influence of the ^{14}N magnetization on the ^1H signal very difficult. However, through the incorporation of high-speed MAS and multidimensional NMR, double-quantum CP may yet be a viable tool for studying solid-state biological samples.

8.3. Triple-Resonance Double-Quantum Cross Polarization

Figure 8.3 shows the proposed pulse sequence for triple-resonance double-quantum cross-polarization or TRDQCP. As with DQCP, magnetization originates from the abundant proton spins and is transferred to the ^{14}N double-quantum transition via CP at twice the ^{14}N Rabi frequency. However, in TRDQCP the magnetization is then transferred to ^{13}C nuclei instead of back to the protons. This alternate implementation of

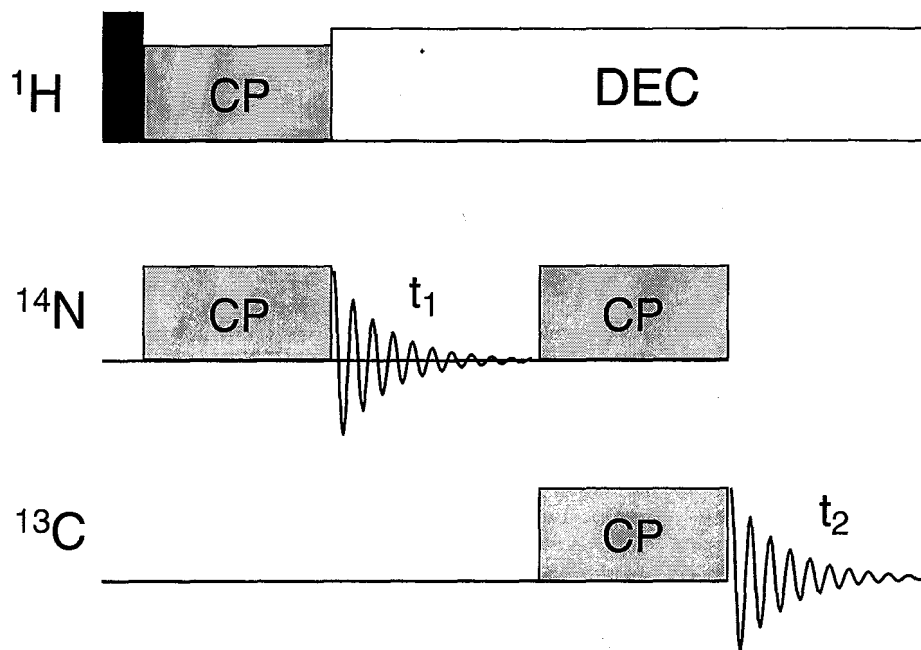


Figure 8.3. Triple-resonance double-quantum cross-polarization pulse sequence. The sequence is essentially the same as the DQCP pulse sequence (fig. 8.2), except the magnetization is transferred to ^{13}C nuclei as opposed to returning it to ^1H nuclei for detection in t_2 .

DQCP has two major advantages. First, cross-polarization from ^{14}N nuclei to ^{13}C nuclei is preferable to cross-polarization from ^{14}N nuclei to ^1H nuclei because the enhancement of the ^{13}C magnetization is greater than it would be for protons. Second, the ^{13}C magnetization detected during t_2 can be used to create $\text{C}'\text{-N-C}_\alpha$ correlations, whereas the ^1H magnetization in DQCP is simply discarded because it is not resolvable.

In addition to using ^{13}C NMR to indirectly detect the ^{14}N double-quantum FID, another improvement over the conventional DQCP experiment may be possible. Assuming the successful excitation and detection of the double-quantum transition, the

only remaining limitation to the TRDQCP technique would be the broad 2nd-order quadrupolar lineshape of the double-quantum transition. Ideally, a multiple-angle spinning technique like DOR or DAS could be employed to remove the 2nd-order quadrupolar broadening. However, it is unlikely that a triple-resonance DAS or DOR probe will ever be built that would be sensitive enough to implement the TRDQCP technique. In reality, the only way to achieve any sort of line narrowing would be to use high-field magnets and to spin very fast at the magic angle (to remove at least part of $H_Q^{(2)}$). Although cross-polarization to quadrupolar nuclei under MAS is problematic (owing to changes in the ^{14}N nutation frequency as the rotor turns), it is believed that either low-power spin-locking or linear ramps of the spin-locking power[173] (see fig. 1.12) should make CP to the double-quantum ^{14}N transition possible, even at very high spinning speeds.

III. Applications of NMR to the Study of Macromolecules

Chapter 9: Solid-State NMR Studies of PrP 89-143

9.1. Introduction

Despite the great progress that has been made in the last 20 years toward understanding the nature and origin of prion diseases[67], a number of important questions have yet to be answered. For instance, little is known about the structure of the scrapie form of the prion protein because *in vitro* conversions of PrP^c to PrP^{sc} are currently not possible. Furthermore, structural studies of PrP^c have yet to shed any light on how or why PrP^c undergoes a structural transformation to PrP^{sc}. Lacking the ability to perform an *in vitro* conversion of PrP^c to PrP^{sc}, Kaneko and coworkers began studying synthesized fragments of the prion protein that they believed might carry the infectious features of PrP^{sc}. Of particular interest was the fragment consisting of residues 89 through 143 of the prion protein that, as shown in chapter 4, contains a disproportionate number of the mutations that cause familial prion diseases. In addition, previous NMR studies of the PrP 108-121 region (which makes up the center of PrP 89-143) showed that it could easily convert between α -helical and β -sheet conformations[87].

PrP 89-143 lies in a generally unstructured area of PrP^c, with a four-residue sheet (S1) providing the only secondary structure in the region. In aqueous solution, PrP 89-143 has been shown by NMR to be devoid of any structure, but rather exists as a random coil. However, Kaneko *et al.* showed that upon sitting in an acetonitrile:water solution for a few weeks, certain mutants of PrP 89-143 form long fibrils that are believed to assemble from peptides possessing a regular structure[74]. Indeed, circular dichroism and infrared studies suggest the presence of β -sheet structure in aggregated PrP 89-143.

In this chapter, preliminary studies of the secondary structure in four variants of the PrP 89-143 peptide are described. These correspond to the wild-type and 3AV mutant (A112V, A114V, and A117V) of Syrian hamster PrP 89-143 and the wild-type and P101L mutant of mouse PrP 89-143. For the Syrian hamster peptides (hPrP 89-143), it will be shown by analysis of ^{13}C chemical shifts that the wild-type peptide adopts an α -helical conformation in the solid-state, whereas the 3AV mutant consists of a mixture of α -helical and β -sheet structures. For the mouse sequence (mPrP 89-143), ^{13}C NMR studies show that both the wild-type and P101L peptides consist of a mixture of α -helical and β -sheet conformations. Upon conversion to an aggregated form, both the 3AV and P101L mutants shift to an entirely β -sheet structure, while the wild-type peptides resist the conversion process. These results suggest that the fibrils formed by the 3AV and P101L aggregated peptides may be similar in form to the β -amyloid fibrils reported for other protein systems[174,175].

9.2. Experimental

To monitor the structure along the length of each PrP 89-143 peptide, ^{13}C labels were placed in multiple sites in the amino-acid sequence. Labels were selected on the basis of their isotropic chemical-shift ranges[96] so that all of the ^{13}C sites would be resolvable in a 1D NMR spectrum. The following section contains a brief description of the synthesis of the PrP 89-143 peptides, the process by which they are converted to an aggregated form, and the parameters of the solid-state NMR experiments used for their study.

9.2.1. Peptide Synthesis

All peptides were synthesized using optimized Fmoc chemistry on an Applied Biosystems 433 peptide synthesizer. Fmoc amino acid derivatives were pre-activated by reaction with 2-(1H-benzotriazol-1-yl)-1,1,3,3-tetramethyluronium hexafluorophosphate (HBTU) and diisopropylethylamine (DIEA). After the coupling of each amino acid, a capping step was performed using N-(2-chlorobenzoyloxycarbonyloxy) succinimide (Novabiochem, La Jolla, CA). Labeled residues were coupled manually using a 1.5 fold excess of amino acid and coupling efficiency was monitored using the quantitative ninhydrin test. Peptides were cleaved from the resin with 1% TFA in dichloromethane (CH_2Cl_2), and the cleaved peptide solution was collected in a round-bottomed flask containing pyridine. The peptidyl-resin was treated with additional aliquots of cleavage mixture and the filtrates were combined. CH_2Cl_2 was eliminated using a rotary evaporator and the residue taken up in 20% acetic acid. The crude peptides were purified by reversed-phase HPLC on a Rainin (Emeryville, CA) liquid chromatography system using a Vydac C-18 semi-preparative column (250×10 mm). The identity of the purified peptides was confirmed by electrospray mass spectrometry using a Perkin Elmer-Sciex API-300 instrument.

9.2.2. Conversion of PrP 89-143 to the Aggregated State

To convert the 3AV and P101L PrP 89-143 peptides to an aggregated state, they were dissolved in a 50:50 (v/v) mixture of acetonitrile and acetate buffered saline (100 mM NaCl, 20 mM NaOAc, and pH = 5.0). The solution was then allowed to sit undisturbed for ~3 weeks. After ~2 weeks, the solution grew cloudy due to the formation of an insoluble aggregate. Aggregation was judged complete at ~3 weeks, after which

the aggregate suspension was spun in an ultracentrifuge to remove the solid material. The supernatant was poured off and the gelatinous pellet was dried overnight by blowing $N_2(g)$ over the sample.

9.2.3. Solid-State NMR

All ^{13}C NMR spectra were obtained either at 7.07 Tesla (corresponding to a ^{13}C Larmour frequency of 75.74 MHz) on a home-built spectrometer based on a Tecmag (Houston, Texas) pulse programmer with a Chemagnetics (Fort Collins, CO) 4-mm double-resonance MAS probe, or at 11.72 Tesla (corresponding to a ^{13}C Larmour frequency of 125.75 MHz) on a triple-resonance Varian/Chemagnetics Infinity spectrometer with a 4-mm T3 triple-resonance MAS probe. For spectra obtained at 7.07 Tesla, the CP contact time was 2.0 ms, the 1H decoupling field strength was 91 kHz, and the recycle delay was 1.0 second. For spectra obtained at 11.72 Tesla, the CP contact time was 2.0 ms, the 1H decoupling field strength was 114 kHz, and the recycle delay was 1.0 second. Isotropic shift values were measured relative to the carbonyl carbon of glycine at 176.04 ppm.

9.3. Results and Discussion

In chapter 5, a technique was introduced through which the $^{13}C_{\alpha}$ chemical-shift tensors could be used to predict dihedral angles in peptides and proteins. Given that the chemical-shift anisotropy of a ^{13}C nucleus is strongly coupled to the surrounding local structure, it is not surprising that isotropic ^{13}C chemical shifts can also be used to analyze secondary structure in proteins. Indeed, for many years isotropic chemical shifts have been used to map secondary structure in both liquid-state[94,95] and solid-state[96,176]

peptides and proteins. Using a series of $^{13}\text{C}_\alpha$, $^{13}\text{C}_\beta$, and $^{13}\text{C}_0$ labels, the secondary structure of PrP 89-143 both before and after aggregation was studied via solid-state NMR. The ^{13}C labels used for both the hPrP and mPrP peptides are summarized in table 9.1. Different amino-acid labels were utilized to minimize spectral overlap and simplify assignment of the different resonances. The expected chemical-shift ranges for each label are also shown in table 9.1.

Table 9.1. ^{13}C labels used to study the secondary structures of hPrP 89-143 and mPrP 89-143.

hPrP 89-143		mPrP 89-143	
Label	Shift Range (ppm) ^a	Label	Shift Range (ppm) ^a
G93 C_α	43 – 44	G93 C_α	43 – 44
G113 C_0	168 – 172	A114 C_α	46 – 54
V114 C_α	56 – 66	V120 C_α	56 – 66
A119 C_α	46 – 54	A132 C_β	14 – 22
A132 C_β	14 – 22	M128 C_0	170 – 176
M128 C_0	170 – 176	G141 C_0	168 – 172

^aShift ranges were approximated on the basis of data from Refs. [94] and [96].

9.3.1. NMR Studies of the 3AV Mutant of PrP 89-143

Figure 9.1 shows a ^{13}C CPMAS spectrum of the wild-type PrP 89-143 peptide using the Syrian hamster sequence (hPrP 89-143). Resonance assignments were based on published ^{13}C solid-state chemical-shift ranges[96]. All of the chemical shifts of the wild-type spectrum are consistent with an α -helical conformation for the peptide (table 9.2).

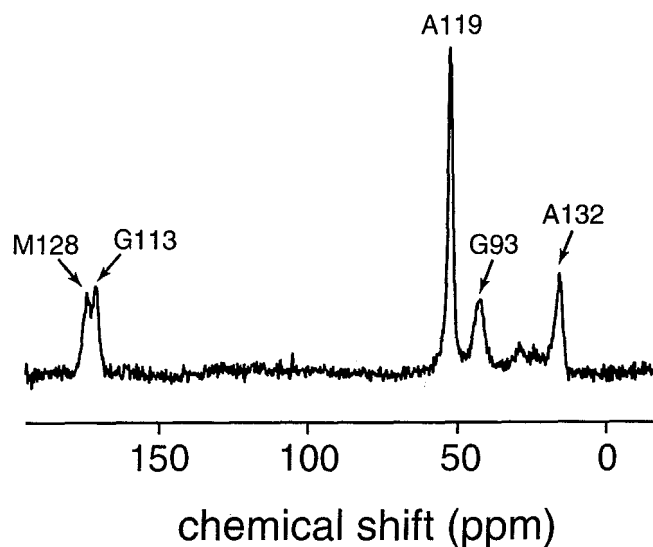


Figure 9.1. Solid-state ^{13}C NMR spectrum of wild-type hPrP 89-143. Resonance assignments are based on the chemical shift ranges shown in table 9.1.

Table 9.2. Comparison of measured chemical shifts in hPrP 89-143 with typical α -helical and β -sheet chemical shifts in solid-state peptides. All chemical shifts are reported in ppm and are referenced to TMS via the $^{13}\text{C}_0$ resonance in glycine (176.04 ppm).

Label	Expected Chemical Shifts ^a		Experimental Chemical Shifts	
	α -Helix	β -Sheet	Wild-type	3AV (converted)
G93 C_α	Unknown	43.2	43.0	42.8
G113 C_0	171.8	168.5	172.6	169.5
V114 C_α	65.5	58.3	N/A	57.6
A119 C_α	52.5	48.7	52.9	49.2
A132 C_β	15.1	20.1	16.2	20.6
M128 C_0	175.1	170.6	175.6	170.8

^aValues taken from Ref. [96].

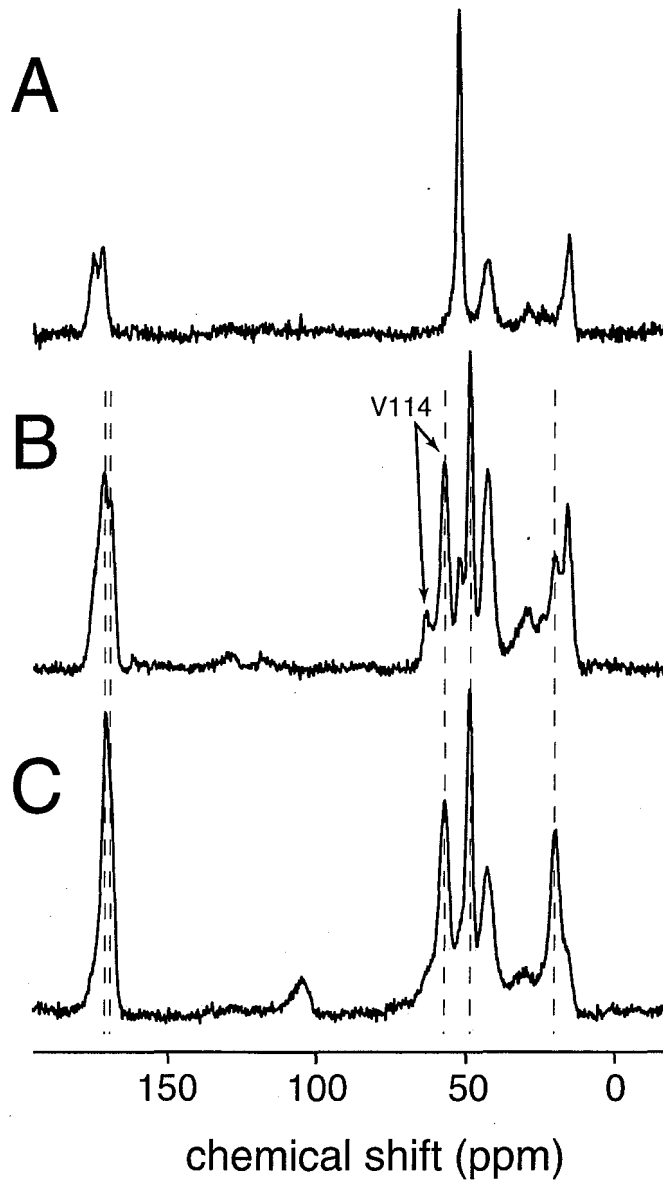


Figure 9.2. Solid-state ^{13}C NMR spectra of hPrP 89-143. (A) ^{13}C NMR spectrum of wild-type hPrP 89-143. (B) ^{13}C NMR spectrum of the 3AV mutant of hPrP 89-143. (C) ^{13}C NMR spectrum of aggregated hPrP 89-143 3AV. The dashed lines show the correspondence between β -sheet resonances in both the unconverted and converted 3AV peptides. The chemical shifts for the spectra in (A) and (C) can be found in table 9.2.

In fig. 9.2, the wild-type ^{13}C NMR spectrum (fig. 9.2a) is compared with spectra of the 3AV mutant of hPrP 89-143, both before (fig. 9.2b) and after (fig. 9.2c) conversion to the aggregated state. Unlike the wild-type sample, which appears to be almost exclusively α -helical in the solid-state, the unconverted 3AV peptide spectrum shows a mixture of α -helical and β -sheet conformations (table 9.2). The differences between the wild-type and 3AV spectra were not unexpected; the 3AV mutation was chosen with the intention of driving the peptide into a β -sheet structure in an attempt to mimic the structure of PrP^{Sc}. As seen in fig. 9.2c, the aggregated form of the 3AV mutant peptide appears to be exclusively β -sheet. This complete conversion to a β -sheet conformation is consistent with the observation by negative stain electron microscopy and infrared spectroscopy that aggregated PrP 89-143 peptides form small β -rich fibrils[74]. Indeed, amyloid fibrils consisting of proteins or peptides in a β -sheet conformation have been found for a variety of other protein systems[174,175].

9.3.2. NMR Studies of the P101L Mutant of PrP 89-143

Figure 9.3 shows the ^{13}C NMR spectrum of wild-type mPrP 89-143. The ^{13}C labels in the mPrP 89-143 samples were slightly altered so that a valine $^{13}\text{C}_\alpha$ label would appear in both the wild-type and P101L peptides. In addition, the $^{13}\text{C}_0$ label at G113 in hPrP 89-143 was moved to G141 in mPrP 89-143. Figure 9.3 clearly shows a mixture of α -helical and β -sheet conformations for the wild-type mPrP 89-143 peptide that is similar to that observed for the 3AV mutant of hPrP 89-143 (table 9.3). Given that the Syrian hamster and mouse amino-acid sequences are nearly identical (see fig. 4.2), this change is somewhat perplexing.

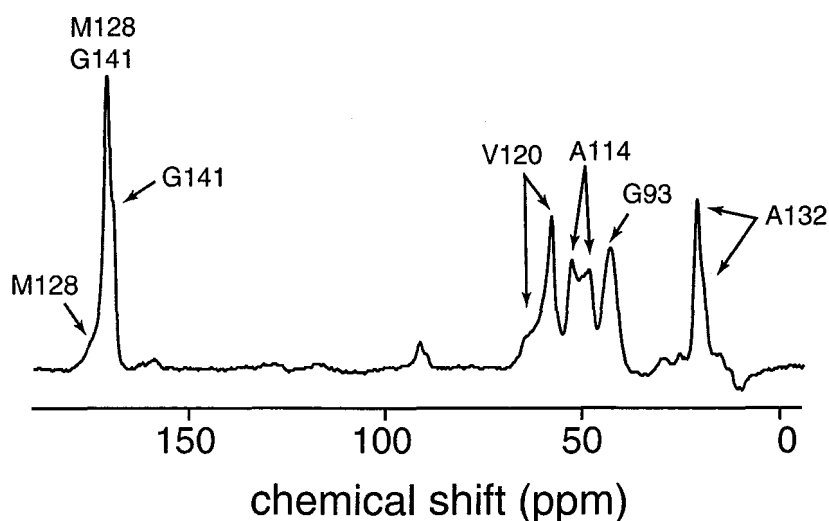


Figure 9.3. Solid-state ^{13}C NMR spectrum of wild-type mPrP 89-143. Resonance assignments are based on the chemical shift ranges shown in table 9.1.

Table 9.3. Comparison of measured chemical shifts in mPrP 89-143 with typical α -helical and β -sheet chemical shifts in solid-state peptides. All chemical shifts are reported in ppm and are referenced to TMS via the $^{13}\text{C}_0$ resonance in glycine (176.04 ppm).

Label	Expected Chemical Shifts ^a		Experimental Chemical Shifts	
	α -Helix	β -Sheet	Wild-type ^b	P101L (converted)
G93 C_α	Unknown	43.2	42.8	42.3
A114 C_α	65.5	58.3	52.6; 48.3	48.4
V120 C_α	52.5	48.7	64.1; 57.8	58.1
A132 C_β	15.1	20.1	15.05; 20.88	20.6
M128 C_0	175.1	170.6	174.9; 170.6 ^c	170.4
G141 C_0	171.8	168.5	170.6 ^c ; 169.3	168.9

^aValues taken from Ref. [96].

^bTwo conformations were present in the wild-type peptide. Chemical shifts for both conformations are listed, with the α -helical chemical shifts listed first.

^cThe M128 $^{13}\text{C}_0$ β -sheet resonance overlaps with the G141 $^{13}\text{C}_0$ α -helix resonance, and so the two are indistinguishable.

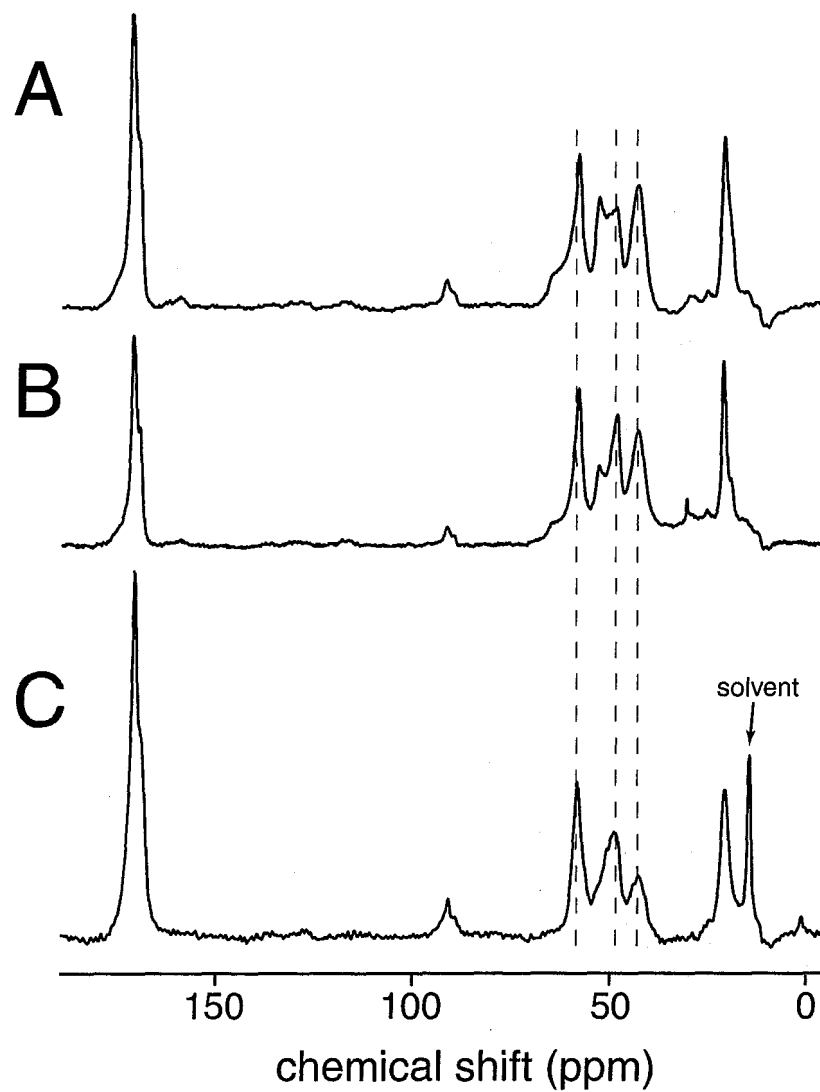


Figure 9.5. Solid-state ^{13}C NMR spectra of mPrP 89-143. (A) ^{13}C NMR spectrum of wild-type mPrP 89-143. (B) ^{13}C NMR spectrum of the P101L mutant of mPrP 89-143. (C) ^{13}C NMR spectrum of aggregated mPrP 89-143 P101L. The dashed lines show the correspondence between β -sheet resonances in both the unconverted and converted P101L peptides. The chemical shifts for the spectra in (A) and (C) can be found in table 9.3.

Figure 9.4 shows a comparison between the ^{13}C NMR spectra of the wild-type (fig. 9.4a) and P101L (figs. 9.4b-c) variants of mPrP 89-143. The same set of resonances is observed in both the wild-type and unconverted P101L spectra, although the intensities of the α -helical resonances in the mutant spectrum are approximately half that of the wild-type. This suggests that the P101L mutation supports the formation of a β -sheet conformation, although perhaps not as much so as the 3AV mutation in hPrP 89-143. Upon aggregation, the P101L mutant converts to a β -sheet form just as the 3AV mutant does (table 9.3). However, the resonances in the converted P101L spectrum appear to be broader than the unconverted P101L spectrum. One possible explanation for this change is a difference in the spectrometer setup that could have occurred during the ~ 1 month between when the two spectra were obtained. Another possibility is that two β -sheet conformations are present, which would account for what appear to be shoulders on the A114 C_α and G93 C_α peaks. This is supported to some extent by the observation of Kaneko *et al.* that not all of the aggregated material is present in fibril form[74], and that different fibril lengths were present in the aggregated P101L sample that was used for this study.

9.3.3. Comparisons between hPrP 89-143 and mPrP 89-143

As can be seen in figs. 9.2 and 9.4 and tables 9.2 and 9.3, the ^{13}C NMR spectra of hPrP 89-143 and mPrP 89-143 are very similar. The only noticeable differences between the two compounds is the mixture of conformations seen in the wild-type mPrP 89-143 spectrum, and the line broadening observed in the converted P101L spectrum. This is somewhat troublesome, given that the P101L mutant has been shown to be infectious

while the 3AV mutant is not. Both compounds form fibrils, and both have what appears to be β -rich secondary structures, so it is unclear from these studies what differentiates the functionality of the two peptides.

One possible explanation for the infectivity of the P101L mutant could be a subtle change in the tertiary structure of the peptide that would not be visible in the observed ^{13}C isotropic chemical shifts. L-Proline residues are conformationally limited[177], and so the mutation of P101 to a leucine might allow the P101L peptides to pack together into a fibril that is capable of binding to PrP^c . Indeed, this hypothesis is supported by the fact that only the aggregated form of mPrP 89-143 P101L is infectious, and by the fact that P104L is also a mutation that causes the onset of a familial prion disease.

9.4. Conclusions

Using solid-state ^{13}C NMR, the secondary structures of two fragments of the prion protein, hPrP 89-143 and mPrP 89-143, have been studied. In both cases it has been shown that in the solid state, these peptides have a propensity to form both α -helical and β -sheet structures. However, upon conversion to an aggregated form, both the mouse and Syrian hamster mutants (P101L and 3AV, respectively) convert to a β -sheet conformation. Although it is currently unknown whether these converted β -sheet peptides form a regular structure in the aggregated form, the fact that they form long fibrils suggests some degree of long range order. If a regular structure does exist, future solid-state NMR studies using heteronuclear and homonuclear dipolar recoupling to measure internuclear distances and the CSA/Z method to measure dihedral angles should provide enough structural constraints to determine the structure of mPrP 89-143 P101L.

Chapter 10: SPINOE Studies of α -Cyclodextrin

10.1. Introduction

As seen in chapter 6, in systems where the auto-relaxation rate of protons (ρ_H) is much faster than the ^1H - ^{129}Xe cross-relaxation rate (σ_{HXe}), the signal enhancement produce by the SPINOE will typically be small compared to the equilibrium ^1H signal. This has the effect of severely limiting the utility of the SPINOE for bulk ^1H signal enhancement in a sample, unless the density of polarized xenon atoms is very high (as it would be if polarized xenon were used as a solvent) or the xenon polarization is very high (which is difficult to achieve). However, the power of the SPINOE technique lies not in a brute-force polarization of all spins, but rather in the ability of polarized xenon atoms in solution to selectively enhance the polarization of atoms in areas of a molecule where the xenon atoms may preferentially reside. For instance, it is hoped that SPINOE may some day be used to “light-up” hydrophobic pockets of proteins and possibly provide dynamics information regarding the cooperative motions in proteins that allow atoms and molecules (such as benzene) access to these hydrophobic pockets.

An excellent model of a hydrophobic binding pocket in a protein is α -cyclodextrin (α -CD), an cyclic oligosaccharide (fig. 10.1) that forms a hydrophobic pocket known to bind xenon[122,178]. In this chapter, experiments to probe the interaction of xenon with α -CD will be discussed. Using SPINOE experiments, the ^1H - ^{129}Xe cross-relaxation rates between xenon and the nine different proton sites in α -CD were measured. The distance dependencies of the measured ^1H - ^{129}Xe cross-relaxation rates were then incorporated into a simple model for determining the preferred location of bound xenon in α -CD.

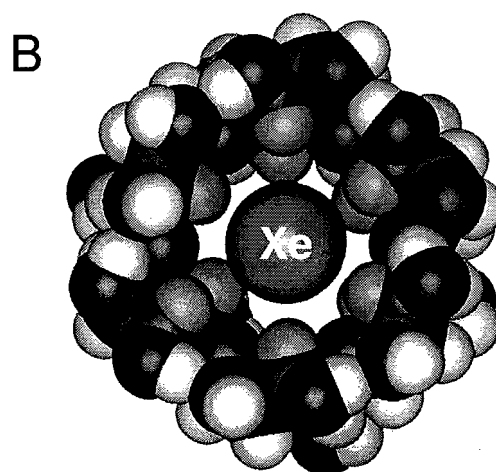
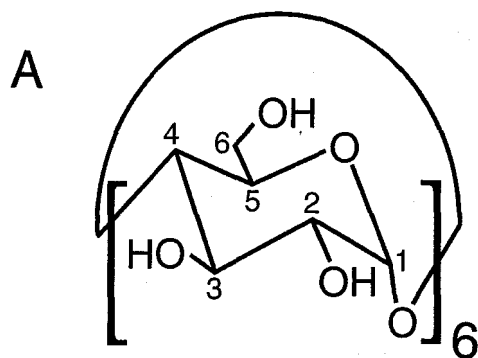


Figure 10.1. (A) Structural formula of α -cyclodextrin. (B) CPK model of α -cyclodextrin[179] in which a xenon atom is placed within the hydrophobic pocket. Figure taken from Ref. [125].

10.2. Experimental

All NMR experiments were performed on dehydrated α -cyclodextrin. Dehydration was accomplished by heating hydrated α -cyclodextrin (Sigma-Aldrich, St. Louis, MO) to 100 °C under vacuum for a period of ~24 hours. Deuterated DMSO was obtained from Isotec (Miamisburg, OH) and used without further purification.

Approximately 2 mL of a 0.05 M solution of dehydrated α -CD in d_6 -DMSO were placed in an NMR tube equipped with a sidearm and Teflon stopcocks to isolate the different sections of the tube from each other and the atmosphere (fig. 3.4). The sample was then degassed repeatedly using a freeze-pump-thaw cycle to remove any dissolved oxygen.

The optical pumping apparatus as well as the optical pumping procedure used for the experiments described in this chapter can be found in subsection 3.2.1. In all α -CD SPINOE experiments, enriched ^{129}Xe obtained from Isotec was used. ^1H and ^{129}Xe NMR spectra were obtained using a Varian/Chemagnetics CMX-400 Infinity spectrometer operating at a ^1H frequency of 400.15 MHz and a Bruker 10 mm double resonance liquids probe. SPINOE measurements were made using the pulse sequence shown in fig. 6.4a, and ^1H T_1 's were measured via a standard inversion-recovery experiment.

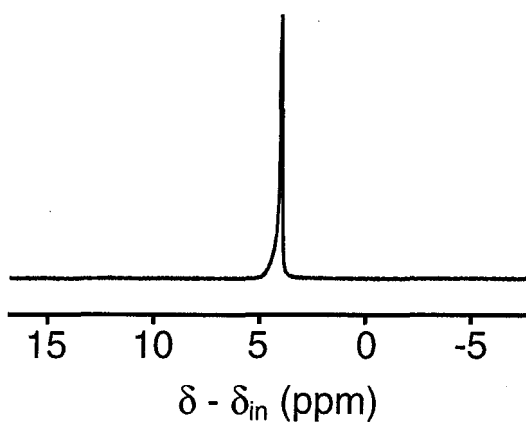


Figure 10.2. ^{129}Xe NMR spectrum of laser-polarized xenon dissolved in a 0.05 M solution of α -cyclodextrin in d_6 -DMSO.

10.3. Results and Discussion

A ^{129}Xe NMR spectrum of laser-polarized xenon in a 0.05 M solution of dehydrated α -cyclodextrin in d_6 -DMSO is shown in fig. 10.2. Because of the low xenon binding constant ($K \approx 2 \text{ M}^{-1}$) for xenon in an α -CD:DMSO solution, there exists a fast exchange between xenon bound to α -CD and xenon in solution, resulting in the single peak in fig. 10.2. The equilibrium ^1H NMR spectrum of a 0.05 M solution of dehydrated α -cyclodextrin in d_6 -DMSO is shown in fig. 10.3a, with labels corresponding to the nine proton sites designated in fig. 10.1a. Figures 10.3b and 10.3d show ^1H - ^{129}Xe SPINOE spectra of α -CD obtained with negatively and positively polarized ^{129}Xe , respectively. Of the nine proton sites in α -CD, the H3 and H5 protons had the largest SPINOE enhancement, which is expected because of their proximity to the xenon binding site in α -CD. Since the ^1H - ^{129}Xe cross-relaxation rate, σ_{HXe} , is proportional to $\langle r_{\text{HXe}}^{-6} \rangle$ (see eq. (6.7)), protons that reside close to the binding site of the xenon atom will be enhanced by the bound xenon more than protons that reside outside the binding pocket. Indeed, whereas the other seven protons point the outside of the molecule, the H3 and H5 protons point toward the center of the hydrophobic pocket.

Because the binding of xenon to α -CD in DMSO falls in the weak binding limit (eq. (6.15)), it is possible to rewrite eq. (6.17) as follows:

$$(10.1) \quad \sigma_{\text{HXe}} = A_{129} [\sigma_{\text{HXe}}^n [\text{Xe}]_{\text{out}} + \sigma_{\text{HXe}}^b [\text{Xe}]_{\text{out}}].$$

Since σ_{HXe} is linearly dependent on $[\text{Xe}]_{\text{out}}$, it can be written in terms of a normalized “molar” cross-relaxation rate, σ_{HXe}^m , where $\sigma_{\text{HXe}} = \sigma_{\text{HXe}}^m [\text{Xe}]_{\text{out}}$, so that

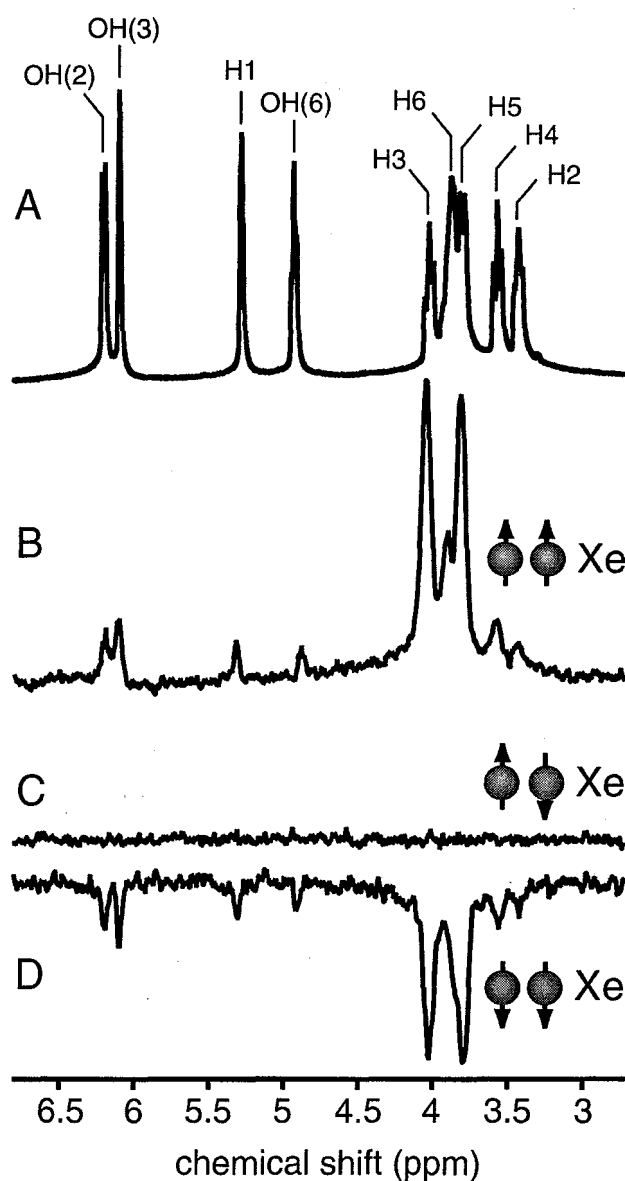


Figure 10.3. (A) ^1H NMR spectrum of 0.05 M α -cyclodextrin in d_6 -DMSO. (B) ^1H SPINOE spectrum of α -CD acquired with the pulse sequence in fig. 6.4a ($\tau_1 = 0.63$ s and $\tau_2 = 0.37$ s) after introduction of negatively polarized ^{129}Xe . (C) as in (B), but in the absence of a xenon 180° pulse. (D) ^1H SPINOE spectrum of α -CD acquired after introduction of negatively polarized ^{129}Xe . Figure adapted from Ref. [125].

$$(10.2) \quad \sigma_{HXe}^m = \frac{\sigma_{HXe}}{[Xe]_{out}}$$

Values for σ_{HXe}^m can then be found using eq. (6.18) and ^1H T_1 's measured with an inversion-recovery experiment. Table 10.1 lists the measured ^1H - ^{129}Xe molar cross-relaxation rates for all nine protons in α -CD. As expected from the spectrum in fig. 10.3b, the highest cross-relaxation rates belong to the H3 and H5 protons; the cross-relaxation rates of the other seven "outer" protons are between 5 and 10 times smaller than those of the H3 and H5 protons. However, the ^1H - ^{129}Xe cross-relaxation rates for the outer protons are still at least an order of magnitude greater than those of *p*-nitrotoluene[125], suggesting that σ_{HXe} is still dominated by σ_{HXe}^b for these protons. Therefore, one can expect that the ensemble average of possible H-Xe distances for each proton, $\langle r_{HXe}^{-6} \rangle$, reflects the distance from the proton to the preferential location of a xenon atom within the binding pocket of α -CD.

Table 10.1. ^1H - ^{129}Xe molar cross-relaxation rates, σ_{HXe}^m , and ^1H spin-lattice relaxation times, T_1^H .

Proton	σ_{HXe}^m ($10^{-3} \text{ s}^{-1} \cdot \text{M}^{-1}$)	T_1^H (s)
H1	0.44 ± 0.14	1.1
H2	1.3 ± 0.5	1.1
H3	4.1 ± 0.8	1.2
H4	1.6 ± 0.3	1.1
H5	4.9 ± 1.2	0.87
H6	1.2 ± 0.4	0.78
OH(2)	0.70 ± 0.22	1.2
OH(3)	0.86 ± 0.18	1.0
OH(6)	0.36 ± 0.14	1.1

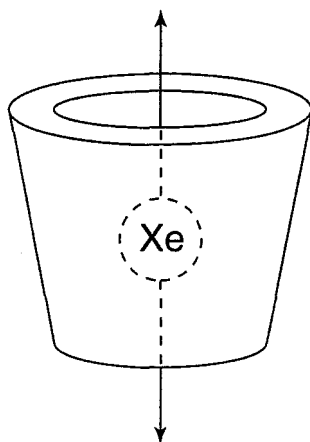


Figure 10.4. Schematic of a model for determining the preferred location of xenon atoms bound to a cyclodextrin molecule. By calculating H-Xe distances at a variety of xenon positions inside the cavity and comparing them to relative distances obtained from cross-relaxation rates, a range of possible xenon locations was determined.

Using an x-ray structure of α -cyclodextrin[179], a simple model was created to translate measured ^1H - ^{129}Xe cross-relaxation rates into structural information about the preferred location of xenon inside the α -CD hydrophobic pocket. In the model, a xenon atom was moved in a straight line through the α -CD hydrophobic pocket (fig. 10.4), and at regular intervals, the distances between the xenon atom and all of the surrounding protons were calculated. For each xenon location, an ensemble average of distances was obtained by averaging over all of the distances for a particular proton site (i.e. H1, H2, etc.). Since σ_{HXe} is proportional to r_{HXe}^{-6} , it was possible to determine ratios of Xe-H distances, based on measured cross-relaxation rates, that could then be compared to Xe-H distance ratios taken from the model. For instance, based on the cross-relaxation rates reported in table 10.1, a ratio of 1:1.5 can be obtained for the Xe-H1 and Xe-H5 distances. According to the model, a ratio between 1:1.2 and 1:2 corresponds to Xe-H5

distances of about 3 to 6 Å and Xe-H1 distances of about 6 to 8 Å. This is consistent with a distribution of xenon locations within the hydrophobic pocket.

10.4. Conclusions

These results show the potential of ^{129}Xe - ^1H SPINOE experiments for probing the structure and dynamics of molecules in solution. Through the measurement of ^1H - ^{129}Xe cross-relaxation rates using the SPINOE, it is possible to derive structural and dynamical information about the nature of hydrophobic pockets that bind xenon. This may have implications for future NMR studies of systems involved in hydrophobic binding including, for example, inclusion compounds, membranes, and proteins.

Chapter 11: SPINOE Studies of Cryptophane-A

11.1. Introduction

Cryptophane-A (MW = 895.02 g/mol) is a nearly spherical cage molecule composed of two cyclotrimeratrylene bowls connected by three OCH₂CH₂O spacer bridges (fig. 11.1). In a recent study, it was shown that the complex of xenon and cryptophane-A in 1,1,2,2-tetrachloroethane exhibits particularly strong binding, with a reported binding constant (K) greater than 3000 M⁻¹ at 278 K[139]. Unlike the complexes of xenon and hemicarcerands (which exhibit K 's on the order of ~200 M⁻¹)[141], the Xe:cryptophane-A complex is formed without a high degree of constrictive binding (i.e., trapped xenon is not required to overcome large steric constraints of the portals of cryptophane-A in order to escape confinement), giving xenon residence times on the order of milliseconds instead of hours[139]. Although cryptophane-A possesses high intramolecular connectivity and three short spacer bridges linking the two cyclotrimeratrylene subunits (making it a somewhat rigid molecule), the internal degrees of freedom associated with the spacer bridges allow the molecule to adopt various conformations. These conformations involve changes in the dihedral angle O-CH₂-CH₂-O and, referring to the oxygen atoms, are either *gauche*-like or *anti*-like in nature.

In this chapter, a detailed study of the xenon:cryptophane-A complex is presented. Through SPINOE experiments, ¹H-¹²⁹Xe cross-relaxation rates between bound xenon and the proton sites in cryptophane-A were measured. These relaxation rates were then used to determine the preferred conformation of the spacer bridges in cryptophane-A upon binding of xenon.

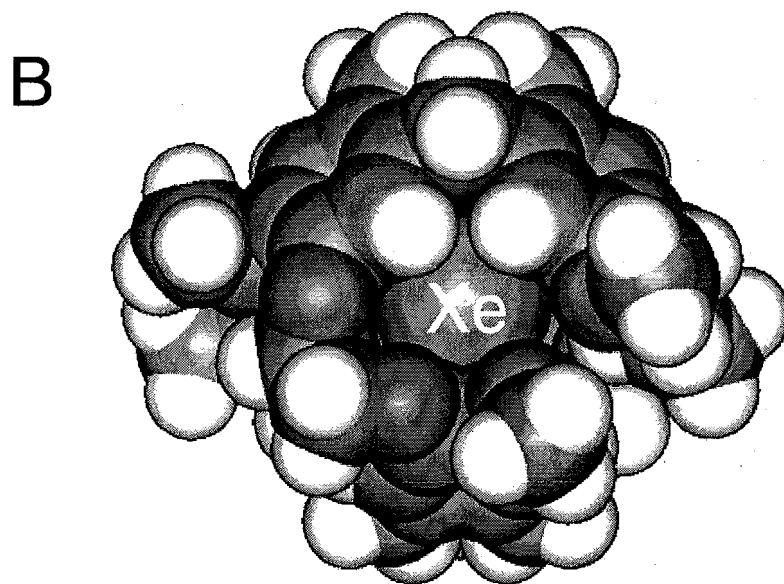
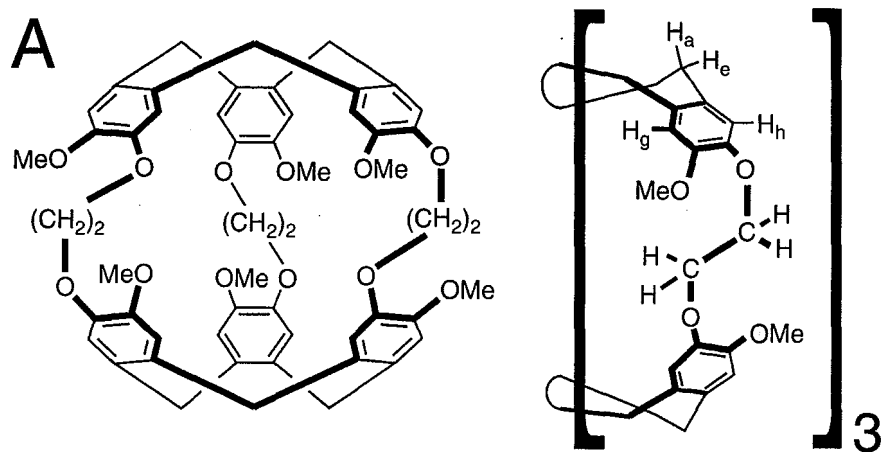


Figure 11.1. (A) Chemical formula of cryptophane-A and atom labeling used in the ¹H spectrum (the assignment of the ¹H signals of the spacer bridges is discussed later). (B) CPK model of one possible conformation of cryptophane-A with a xenon atom placed within the binding pocket. Figure adapted from Ref. [136].

11.2. Experimental

Cryptophane-A, synthesized according to a procedure described elsewhere[180], was provided by A. Collet and coworkers. Deuterated 1,1,2,2-tetrachloroethane, $(\text{CDCl}_2)_2$, was purchased from Sigma-Aldrich (St. Louis, MO) and used without further purification. Approximately 2 mL of a ~ 0.05 M solution of cryptophane-A in $(\text{CDCl}_2)_2$ was placed in a 10 mm NMR tube equipped with a sidearm and Teflon stopcocks used to isolate the sample and the sidearm from each other and from the atmosphere. Helium gas was gently bubbled through the solution for 5 to 10 minutes in order to displace any other gases complexed by cryptophane-A. The sample was then degassed by several freeze-pump-thaw cycles on a vacuum line.

The optical pumping apparatus as well as the optical pumping procedure used for the experiments described in this chapter can be found in subsection 3.2.1. The ^{129}Xe polarization for these experiments was typically in the range of 1-10%. Quantities of $\sim 3 \times 10^{-4}$ mol of isotopically enriched xenon gas (80% ^{129}Xe , Isotec) were used in each experiment. Following optical pumping, laser-polarized ^{129}Xe was frozen into the sidearm of the NMR tube, transported to the spectrometer, and sublimated in the fringe field of the NMR magnet. After opening the xenon reservoir, shaking the sample tube, and inserting it into the magnet, the NMR experiment was immediately performed. Generally, additional experiments could be performed by administering fresh polarized xenon to the solution by simply re-shaking the sample tube.

^1H and ^{129}Xe NMR spectra were recorded at room temperature (~ 22 C $^\circ$) on a Varian/Chemagnetics CMX-400 Infinity NMR spectrometer operating at a ^1H frequency of 400.15 MHz. ^1H - ^{129}Xe SPINOE spectra were obtained using the pulse sequence

shown in fig. 6.4b. Measurements of ^1H T_1 's were made using the inversion-recovery technique and determined using a 3-parameter non-linear least-square-fitting procedure.

Computer modeling of the Xe:cryptophane-A complex was carried out using the Chem3D Plus™ software from CambridgeSoft (Cambridge, MA). The interaction parameters for xenon were user-defined, and correspond to a Xe-Xe Lennard-Jones interaction potential with $\sigma = 3.90 \text{ \AA}$ and $\varepsilon = 251.5 \text{ K}$ [181].

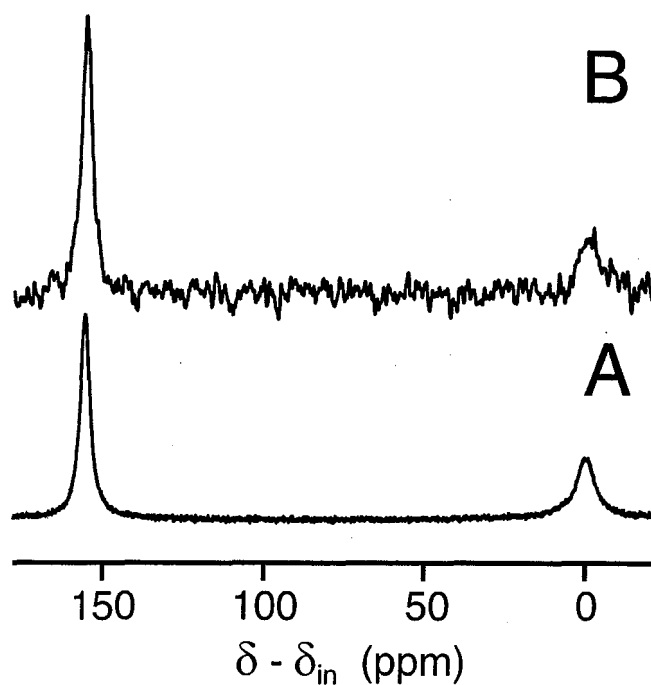


Figure 11.2. Typical ^{129}Xe NMR spectra for xenon dissolved in a cryptophane-A/ $(\text{CDCl}_2)_2$ solution, with (A) and without (B) laser-polarization. Spectrum (A) was acquired with one scan using a pulse of small tipping angle ($\sim 2.5^\circ$). Spectrum (B) was acquired with 8 scans using 90° pulses with a delay of 60 s between acquisitions. The ^{129}Xe spectra are referenced to the signal corresponding to xenon bound to cryptophane-A (Xe_{in}). A second signal can be seen roughly 160 ppm downfield from that of Xe_{in} , corresponding to unbound xenon residing in the $(\text{CDCl}_2)_2$ solvent (Xe_{out}). Figure taken from Ref. [136].

11.3. Results and Discussion

Figure 11.2 shows ^{129}Xe NMR spectra of xenon dissolved in the cryptophane-A solution, with (fig. 11.2a) and without (fig. 11.2b) laser-polarization. The ^{129}Xe spectrum exhibits two lines separated by ~ 160 ppm and considerably broadened due to chemical exchange. The higher-field signal corresponds to xenon trapped in the cryptophane-A cavity, Xe_{in} , with a chemical shift ~ 60 ppm downfield with respect to xenon gas resonance extrapolated to zero pressure. The trapping of xenon by cryptophane-A has been thoroughly studied by Reisse and coworkers[139]. The spectrum in fig. 11.2a was obtained with one scan using a RF pulse of small tipping angle ($\sim 2.5^\circ$). Using thermally polarized ^{129}Xe , a comparable spectrum requires hours of signal averaging.

As shown in fig. 11.3, the integrated intensities of both Xe_{in} and Xe_{out} decrease with the same time evolution, indicating that the relaxation of ^{129}Xe is a slow process compared to xenon exchange. The average T_1 of ^{129}Xe , T_1^{ave} , was found to be 22.1 s when the molar fraction of Xe_{in} was 0.74. The relaxation time of unbound ^{129}Xe is very long (hundreds of seconds in pure $(\text{CDCl}_2)_2$) and does not contribute significantly to the average relaxation time. Based on the molar fraction of Xe_{in} , the relaxation time of included ^{129}Xe , $T_1^{ave} [Xe_{in} / (Xe_{in} + Xe_{out})]$, was estimated to be 16.4 s. From a second experiment with a Xe_{in} molar fraction of 0.92, the relaxation time of trapped ^{129}Xe was estimated to be 16.2 s. The ^1H T_1 values for cryptophane-A are listed in table 11.1. The longest relaxation times, ~ 0.8 s, are those of the methoxy and aromatic hydrogens. Thus, relaxation of ^{129}Xe in this system is slow with respect to ^1H relaxation and so eq. (6.19) can be used when considering $^{129}\text{Xe} \rightarrow ^1\text{H}$ SPINOE polarization transfer.

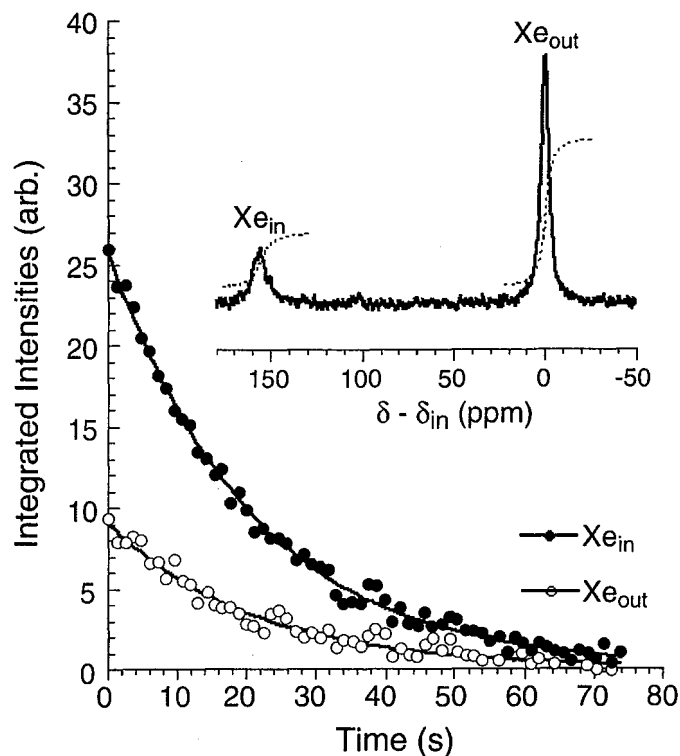


Figure 11.3. ^{129}Xe NMR spectrum of laser-polarized xenon dissolved in a ~ 0.05 M solution of cryptophane-A in $(\text{CDCl}_2)_2$ and time evolution of the integrated intensities. The small amount of xenon used is reflected in the fact that $[\text{Xe}]_{\text{in}} > [\text{Xe}]_{\text{out}}$. Figure adapted from Ref. [136].

Table 11.1. Spin-lattice relaxation times, SPINOE enhancements, relative ^1H - ^{129}Xe cross-relaxation rates, and calculated relative $\langle r_{\text{HXe}}^{-6} \rangle^b$ values in *gauche* conformations for the various protons of cryptophane-A.

proton	type	T_1^H (s)	SPINOE (%)	$\sigma_{\text{HXe}}^b / \sigma_{\text{H}_{g,h}\text{Xe}}^b$	$\langle r_{\text{HXe}}^{-6} \rangle^b / \langle r_{\text{H}_{g,h}\text{Xe}}^{-6} \rangle^b$
aromatic	H_g, H_h	0.80	11.0	(1.00)	(1.00)
axial	H_a	0.27	3.0	0.47	0.3–0.4
linker	H_j, H_j'	0.36	5.2	0.67	0.3
linker	H_k, H_k'	0.41	13.0	1.55	1.5–1.8
methoxy	Me	0.83	2.6	0.23	0.1–0.3
equatorial	H_e	0.35	2.7	0.35	0.3–0.4

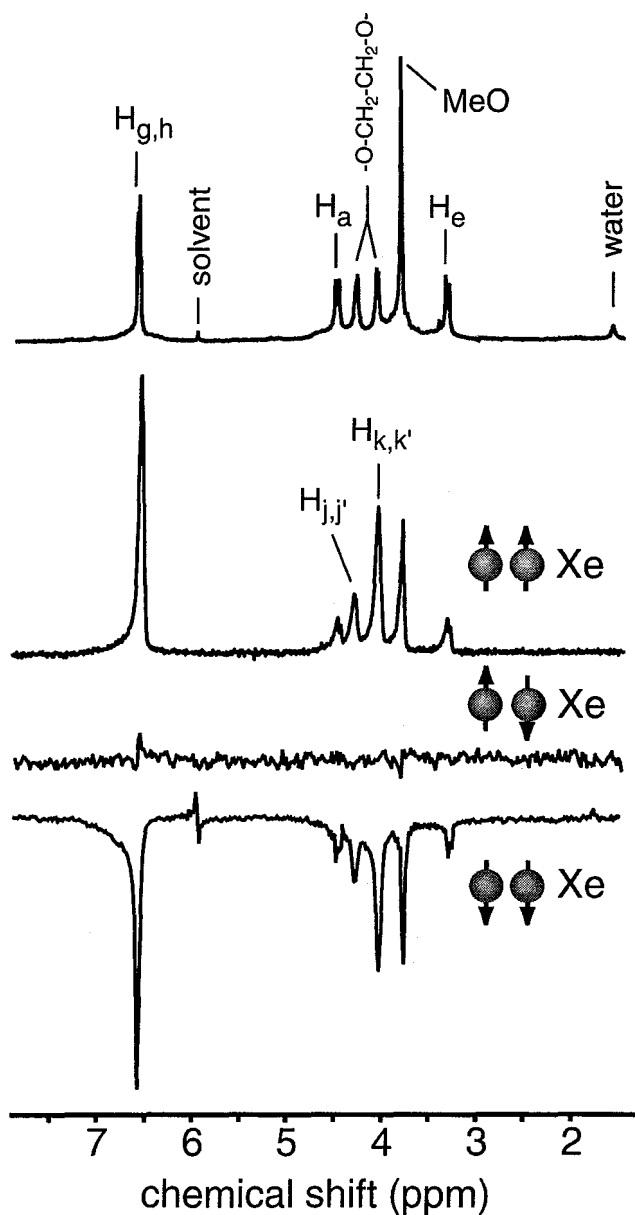


Figure 11.4. (A) ^1H NMR equilibrium spectrum of ~ 0.05 M cryptophane-A in $(\text{CDCl}_2)_2$ with chemical shift assignments. (B) ^1H SPINOE spectrum acquired with the pulse sequence shown in fig. 6.4b following introduction of positively polarized ^{129}Xe to the solution. (C) As in (B), but with ^{129}Xe at thermal equilibrium, demonstrating virtually complete suppression of all contributions to the ^1H NMR signal. (D) ^1H SPINOE spectrum with negatively polarized ^{129}Xe (prepared by inverting the direction of the magnetic field in which the ^{129}Xe is laser-polarized). Values of $\tau_1 = 315$ ms and $\tau_2 = 185$ ms were used for the SPINOE experiments shown. Figure taken from Ref. [136].

The equilibrium ^1H NMR spectrum of the cryptophane-A solution is shown in fig. 11.4a. The assignment of the cryptophane-A signals can be found elsewhere[139]; the proton NMR signals of the spacer bridges (which comprise an AA'BB' spin system) are discussed below. Figures 11.4b-d respectively show SPINOE spectra obtained with positively laser-polarized ^{129}Xe , with ^{129}Xe at equilibrium, and with negatively laser-polarized ^{129}Xe . Whereas the equilibrium spectrum is dominated by the signal of the methoxy group, in the SPINOE spectra the signal from the aromatic protons is the most intense. The observed ^1H enhancements in fig. 11.4b range between 3% and 13% (see table 11.1). In addition, it is clear that the selectivity of the SPINOE is not primarily a consequence of unequal ^1H relaxation times, since the T_1^H 's for the methoxy and aromatic protons are similar.

The determination of the H-Xe cross-relaxation rates requires the value of the ^{129}Xe polarization enhancement. $f_{\text{Xe}}^{\text{obs}}(0)$ is estimated from the quantitative comparison of the integrated intensities of the laser-polarized and equilibrium ^{129}Xe NMR spectra. These spectra need to be recorded in very different conditions (e.g., duration and amplitude of the RF observation pulse, receiver gain, etc.), and so the estimation of $f_{\text{Xe}}^{\text{obs}}(0)$ may be prone to errors. In the case of cryptophane-A, broadening of the ^{129}Xe NMR signals originating from exchange (yielding line widths greater than 500 Hz) and the long ^{129}Xe relaxation times (estimated to be in the range of 50 to 90 s in the samples used for SPINOE experiments) are responsible for low signal-to-noise ratios in the equilibrium spectrum. From the experimental data given in table 11.1, and using a

$f_{\text{Xe}}^{\text{obs}}(0)$ value measured to be $\sim 1.3 \times 10^4$ (with uncertainty on the order of 50%), $\frac{\sigma_{\text{HXe}}}{A_{129}}$

was estimated to be $\sim 1.2 \times 10^{-4} \text{ s}^{-1}$ for the aromatic protons (see eqs. (6.17) and (6.19)).

From multiple experiments, $\frac{\sigma_{HXe}}{A_{129}}$ values in the range 1×10^{-4} to $4 \times 10^{-4} \text{ s}^{-1}$ were found

for the aromatic protons. This figure is two orders of magnitude larger than the value expected for ^1H - ^{129}Xe cross-relaxation rates originating from diffusive coupling. The observed SPINOE enhancements can therefore be considered as originating entirely from the binding of xenon. Furthermore, the SPINOE spectra were obtained with a dissolved xenon concentration in excess of the cryptophane-A concentration. Under these

circumstances, eq. (6.16) is valid, giving $\frac{\sigma_{HXe}}{A_{129}} = \sigma_{HXe}^b$.

The largest σ_{HXe}^b values characterizing the binding of xenon to cryptophane-A are found to be 5 to 10 times smaller than the largest values observed when xenon binds to α -cyclodextrin (table 10.1). Such a discrepancy is unlikely to originate from differences in the dynamics of the $^{129}\text{Xe} \rightarrow ^1\text{H}$ polarization transfer. Indeed, it has been shown that for the binding of xenon to cryptophane-A in $(\text{CDCl}_2)_2$ at room temperature, σ_{HXe}^b is expected to reach 70% of its maximum value. Instead, the discrepancy in the σ_{HXe}^b values suggests differences in the structure of these xenon complexes. Given $\tau_c^b = 0.6 \text{ ns}$ and $\sigma_{HXe}^b \approx 1-4 \times 10^{-4} \text{ s}^{-1}$, eq. (6.7) leads to a $\langle r_{HXe}^{-6} \rangle^b$ value in the range $0.5-2 \times 10^{-4} \text{ \AA}^{-6}$, thus the average distance between the aromatic protons and the xenon atom is 4.1-5.2 \AA . These results are in good agreement with computer modeling, which gives values of 4.5-4.8 \AA (from minimum energy structures of xenon included in the cavity of cryptophane-A, see below). Based on the model introduced in chapter 10, the r_{HXe} values between a

xenon atom positioned at the center of the cavity in α -CD and the nearest protons are found to be in the range of 3.2-3.8 Å. These calculated ranges of proton-to-xenon distances translate into a 4 to 8-fold increase in the cross-relaxation rates (neglecting dynamical effects) over those found for cryptophane-A, in agreement with the experimental observations.

For xenon in an α -cyclodextrin solution, it is possible to define a normalized molar cross-relaxation rate, since in the weak binding limit, $\sigma_{HXe} \propto [Xe]_{out}$. With a binding constant of $\sim 3000 \text{ M}^{-1}$, xenon in cryptophane-A falls within the strong binding regime, and so it is impossible to determine concentration-independent coupling constants. However, it is possible to derive *relative* ^1H - ^{129}Xe cross-relaxation rates. Detailed information regarding the structure of the complex can be obtained in the absence of information about the absolute values of σ_{HXe}^b ; furthermore, the use of relative ^1H - ^{129}Xe cross-relaxation rates avoids the uncertainty attached to the determination of $f_{Xe}^{obs}(0)$. Table 11.1 gives the σ_{HXe}^b values of the cryptophane-A protons relative to the value for the aromatic protons. Assuming that internal dynamics do not cause significant fluctuations in the intermolecular dipole-dipole interactions, the relative σ_{HXe}^b values listed in table 11.1 reveal structural information regarding the Xe: cryptophane-A complex. Of particular interest are the results obtained for the protons belonging to the $\text{OCH}_2\text{CH}_2\text{O}$ spacer bridges (or linkers). Indeed, one pair of these protons (labeled H_k and $\text{H}_{k'}$) experiences, in the presence of ^{129}Xe , a dipolar-coupling constant more than twice as large as that between ^{129}Xe and the other pair of protons (H_j and $\text{H}_{j'}$). Because the dynamics of both pairs of protons is most likely similar, these results indicate that H_k and $\text{H}_{k'}$ are, on average, closer to the xenon atom than H_j and $\text{H}_{j'}$.

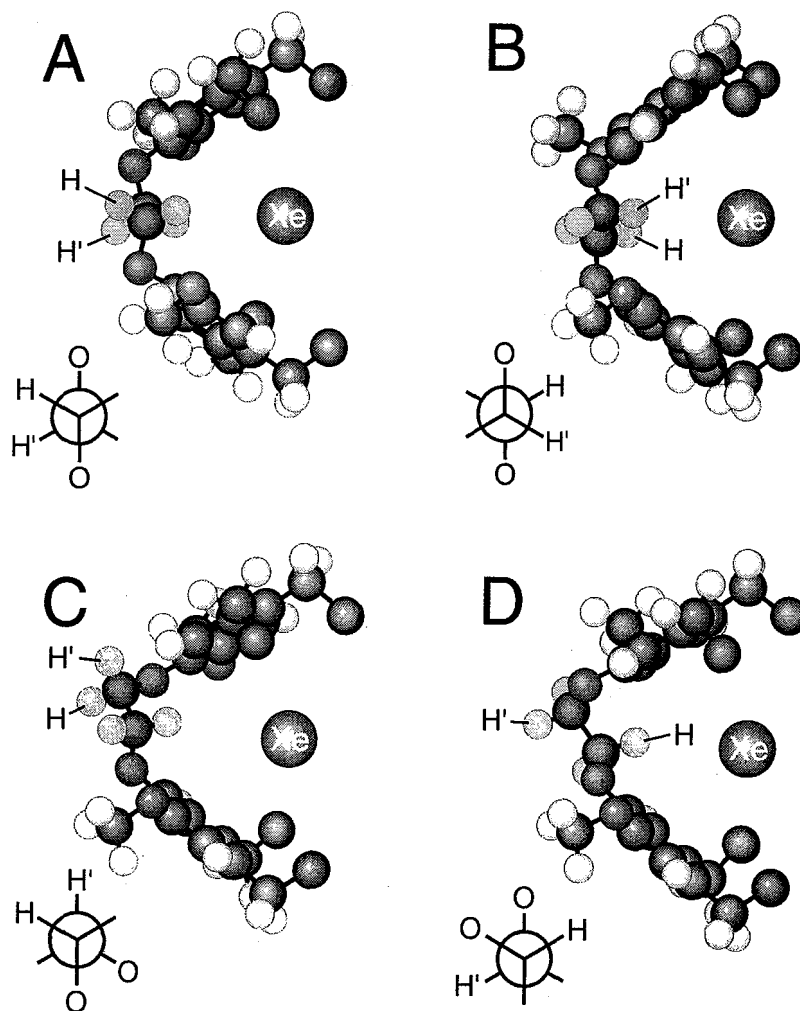


Figure 11.5. Minimum energy structures of cryptophane-A with included xenon for the various conformations of the displayed spacer bridge. The atoms of the cyclotrimerethylene subunits are at similar positions in each view; the molecule is slightly rotated such that the spacer bridge is clearly visible. In (A) and (B), the linkers are in an *anti* conformation. In (C) and (D), the linkers are in a *gauche* conformation. Figure courtesy of Boyd M. Goodson.

Computer modeling was used to generate minimum energy structures of cryptophane-A with included xenon. Structures are shown in fig. 11.5 for the various conformations of the displayed spacer bridge. In figs. 11.5a and 11.5b, the linkers are in an *anti* conformation. These conformations possess C_2 symmetry axes which bisect the C-C bond of the linkers and intercept at the center of the cavity where the xenon atom is found. Therefore, in fig. 11.5a the protons labeled H and H' have the same chemical shift which, *a priori*, is different from the chemical shift of the other pair of protons. The structures shown in figs. 11.5b-d were obtained from the structure in fig. 11.5a, where the labels were left unchanged; the H and H', which were remote with respect to the xenon atom in fig. 11.5a, are the proximal protons in fig. 11.5b. In both of these *anti* conformations, the proton-xenon distances are similar and lead to similar relative $\langle r_{HXe}^{-6} \rangle^b$ values. From table 11.2 it can be seen that the calculated values for the proximal H's in the *anti* conformations are significantly different from the corresponding experimental result. Even if it were considered that both *anti* structures are present simultaneously, the experimental results could not be explained. In figs. 11.5c and 11.5d, the linkers are in a *gauche* conformation. These structures do not possess C_2 symmetry axes, but for each of them an equivalent structure exists in which the position of protons H and H' are interchanged. Therefore, for each pair of protons, $\langle r_{HXe}^{-6} \rangle^b$ must be calculated as the average between the two protons. It is worth noting that in both of these *gauche* structures, the partner of the proton which is the nearest to xenon is the farthest proton; in table 11.2, this pair is referred to as the "proximal" H's because it leads to the largest $\langle r_{HXe}^{-6} \rangle^b$ value. Thus the H and H' which are "remote" with respect to the xenon

atom in fig. 11.5c become the "proximal" H's in fig. 11.5d. From table 11.2, it can be seen that both *gauche* structures lead to relative $\langle r_{HXe}^{-6} \rangle^b$ values in good agreement with the experimental results. Both of these *gauche* structures might be present simultaneously, but if this is the case, one conformation must be in considerable excess in order to explain the observed difference in cross-relaxation rates between the proton pairs.

Table 11.2. Experimental ^1H - ^{129}Xe cross-relaxation rates for the protons of the spacer bridges of cryptophane-A relative to the value for the aromatic protons, and relative $\langle r_{HXe}^{-6} \rangle^b$ values calculated using the structures in fig. 11.5 (see text).

	proximal H's	remote H's
experimental	1.55	0.67
<i>anti</i> 11.5a	5.2	0.5
<i>anti</i> 11.5b	4.4	0.5
<i>gauche</i> 11.5c	1.8	0.3
<i>gauche</i> 11.5d	1.5	0.3

In the last column of table 11.1 are listed the relative $\langle r_{HXe}^{-6} \rangle^b$ values for the various protons of cryptophane-A calculated using the *gauche* structures. For the methoxy group, the calculation was carried out for various positions of these protons; the calculation leads to values in agreement with the experimental relative cross-relaxation rates despite the fact that the dynamics of the polarization transfer might be somewhat different in this case. A more rigorous treatment of the expected cross-relaxation rates

could be performed using molecular dynamics simulations, and in such calculations the three spacer bridges of cryptophane-A should not be considered independently. Furthermore, these calculations neglect the effects of relayed SPINOEs, which in the present system might be on the order of 10-15% between geminal protons. Despite these simplifications, it can be concluded on the basis of the experimental SPINOE enhancements that the most probable conformation of the spacer bridges of cryptophane-A when the molecule complexes xenon (in $(\text{CDCl}_2)_2$ at room temperature) is a *gauche* conformation. This is in agreement with the simulation of resolution-enhanced ^1H NMR signals performed elsewhere[139]. Additionally, the chemical shifts of $\text{H}_{\text{k},\text{k}'}$ and $\text{H}_{\text{j},\text{j}'}$ characterize the protons of the spacer bridges of cryptophane-A which are, respectively, *gauche* and *anti* with respect to the vicinal oxygen atom.

11.4. Conclusions

In this chapter SPINOE studies of the xenon: cryptophane-A complex were described. Selective ^1H enhancements were observed, permitting the preferred conformations adopted by cryptophane-A to be determined, and a more complete assignment of the ^1H spectrum to be obtained. By using laser-polarized xenon and SPINOE experiments, detailed microscopic information can be obtained, demonstrating the utility of such methods to directly probe of molecular structure and dynamics in solution.

IV. References

- [1] C. P. Slichter, *Principles of Nuclear Magnetic Resonance*; 3rd ed.; Springer-Verlag: New York, 1990.
- [2] L. Emsley, D. D. Laws, and A. Pines, in *Proceedings of the International School of Physics "Enrico Fermi"*; B. Maraviglia, Ed.; IOS Press: Amsterdam, 1999; Vol. CXXXIX, pp 45-210.
- [3] S. Wang, *Two-Dimensional Nuclear Magnetic Resonance of Quadrupolar Systems.*; Ph.D. Thesis, University of California, Berkeley, 1997.
- [4] A. Abragam, *Principles of Nuclear Magnetism*; Clarendon Press: Oxford, 1961.
- [5] J. Herzfeld, and A. E. Berger. "Sideband intensities in NMR spectra of samples spinning at the magic angle." *J. Chem. Phys.*, 73, 6021-6030 (1980).
- [6] A. C. Olivieri. "Rigorous statistical analysis of errors in chemical-shift-tensor components obtained from spinning sidebands in solid-state NMR." *J. Magn. Reson. A*, 123, 207-210 (1996).
- [7] P. Hodgkinson, and L. Emsley. "The reliability of the determination of tensor parameters by solid-state nuclear magnetic resonance." *J. Chem. Phys.*, 107, 4808-4816 (1997).
- [8] A. Pines, M. G. Gibby, and J. S. Waugh. "Proton-enhanced NMR of dilute spins in solids." *J. Chem. Phys.*, 59, 569-590 (1973).
- [9] N. F. Ramsey, and R. V. Pound. "Nuclear audiofrequency spectroscopy by resonant heating of the nuclear spin system." *Phys. Rev.*, 81, 278-279 (1951).
- [10] S. R. Hartmann, and E. L. Hahn. "Nuclear double resonance in rotating frame." *Phys. Rev.*, 128, 2042-2045 (1962).
- [11] M. Mehring, *High Resolution NMR in Solids*; Springer-Verlag: New York, 1983.

- [44] M. A. Bouchiat, T. R. Carver, and C. M. Varnum. "Nuclear polarizations in ^3He gas induced by optical pumping and dipolar exchange." *Phys. Rev. Lett.*, 5, 373-375 (1960).
- [45] W. Happer, E. Miron, S. Schaefer, D. Schreiber, W. A. van Wijngaarden, and X. Zeng. "Polarization of the nuclear spins of noble-gas atoms by spin exchange with optically pumped alkali-metal atoms." *Phys. Rev.*, A29, 3092-3110 (1984).
- [46] T. G. Walker, and W. Happer. "Spin-exchange optical pumping of noble-gas nuclei." *Rev. Mod. Phys.*, 69, 629-642 (1997).
- [47] D. Raftery, H. Long, T. Meersmann, P. J. Grandinetti, L. Reven, and A. Pines. "High-field NMR of adsorbed xenon polarized by laser pumping." *Phys. Rev. Lett.*, 66, 584-587 (1991).
- [48] M. S. Albert, G. D. Cates, B. Driehuys, W. Happer, B. Saam, C. S. Springer Jr., and A. Wishnia. "Biological magnetic resonance imaging using laser polarized Xe-129." *Nature*, 370, 199-201 (1994).
- [49] Y.-Q. Song, H. C. Gaede, T. Pietraß, G. A. Barrall, G. C. Chingas, M. R. Ayers, and A. Pines. "Spin-polarized Xe-129 gas imaging of materials." *J. Magn. Reson. A*, 115, 127-130 (1995).
- [50] J. P. Mugler III, B. Driehuys, J. R. Brookeman, G. D. Cates, S. S. Berr, R. G. Bryant, T. M. Daniel, E. E. de Lange, J. H. Downs III, C. J. Erikson, W. Happer, D. P. Hinton, N. F. Kassel, T. Maier, D. Phillips, B. T. Saam, K. L. Sauer, and M. E. Wagshul. "MR imaging and spectroscopy using hyperpolarized Xe-129 gas: preliminary human results." *Magn. Reson. Med.*, 37, 809-815 (1997).

- [51] A. K. Jameson, C. J. Jameson, and H. S. Gutowsky. "Density dependence of Xe-129 chemical shifts in mixtures of xenon and other gases." *J. Chem. Phys.*, 53, 2310-2320 (1970).
- [52] J. Fraissard, and T. Ito. "Xe-129 NMR study of adsorbed xenon: a new method for studying zeolites and metal-zeolites." *Zeolites*, 8, 350-361 (1988).
- [53] A. Bifone, Y.-Q. Song, R. Seydoux, R. E. Taylor, B. M. Goodson, T. Pietraß, T. F. Budinger, G. Navon, and A. Pines. "NMR of laser-polarized xenon in human blood." *Proc. Natl. Acad. Sci. USA*, 93, 12932-12936 (1996).
- [54] H. W. Long, H. C. Gaede, J. Shore, L. Reven, C. R. Bowers, J. Kritzenberger, T. Pietraß, A. Pines, P. Tang, and J. A. Reimer. "High field cross polarization NMR from laser-polarized xenon to a polymer surface." *J. Am. Chem. Soc.*, 115, 8491-8492 (1993).
- [55] C. R. Bowers, H. W. Long, T. Pietraß, H. C. Gaede, and A. Pines. "Cross polarization from laser polarized solid xenon $^{13}\text{CO}_2$ by low-field thermal mixing." *Chem. Phys. Lett.*, 205, 168-170 (1993).
- [56] G. Navon, Y.-Q. Song, T. Rõöm, S. Appelt, R. E. Taylor, and A. Pines. "Enhancement of solution NMR and MRI with laser-polarized xenon." *Science*, 271, 1848-1851 (1996).
- [57] E. Brunner, R. Seydoux, M. Haake, A. Pines, and J. A. Reimer. "Surface NMR using laser-polarized ^{129}Xe under magic angle spinning conditions." *J. Magn. Reson.*, 130, 145-148 (1998).

- [58] M. Gatzke, G. D. Cates, B. Driehuys, D. Fox, W. Happer, and B. Saam. "Extraordinarily slow nuclear spin relaxation in frozen laser-polarized ^{129}Xe ." *Phys. Rev. Lett.*, 70, 690-693 (1993).
- [59] H. J. Jansch, T. Hof, U. Ruth, J. Schmidt, D. Stahl, and D. Fick. "NMR of surfaces: sub-monolayer sensitivity with hyperpolarized ^{129}Xe ." *Chem. Phys. Lett.*, 296, 146-150 (1998).
- [60] T. K. Hitchens, and R. G. Bryant. "Noble-gas relaxation agents." *J. Magn. Reson.*, 124, 227 (1997).
- [61] M. Haake, B. M. Goodson, D. D. Laws, E. Brunner, M. C. Cyrier, R. H. Havlin, and A. Pines. "NMR of supercritical laser-polarized xenon." *Chem. Phys. Lett.*, 292, 686-690 (1998).
- [62] B. Sigurdsson, P. A. Palsson, and H. Grimsson. "Visna, a demyelinating transmissible disease of sheep." *J. Neuropath. Exp. Neur.*, 16, 389-403 (1957).
- [63] T. Alper, D. A. Haig, and M. C. Clarke. "Exceptionally small size of scrapie agent." *Biochim. Biophys. Res. Commun.*, 22, 278-284 (1966).
- [64] G. A. H. Wells, A. C. Scott, C. T. Johnson, R. F. Gunning, R. D. Hancock, M. Jeffrey, M. Dawson, and R. Bradley. "A novel progressive spongiform encephalopathy in cattle." *Vet. Rec.*, 121, 419-420 (1987).
- [65] R. F. Marsh, R. A. Bessen, S. Lehmann, and G. R. Hartsough. "Epidemiology and experimental studies of a new incident of transmissible mink encephalopathy." *J. Gen. Virol.*, 72, (1991).
- [66] D. Westaway, V. Zuliani, C. Mirenda-Cooper, M. Da Costa, S. Neuman, A. L. Jenny, L. Detweiler, and S. B. Prusiner. "Homozygosity for prion protein alleles

- encoding glutamine-171 renders sheep susceptible to natural scrapie." *Genes Dev.*, 8, (1994).
- [67] S. B. Prusiner. "Prions" *Proc. Natl. Acad. Sci. USA*, 95, 13363-13383 (1998).
- [68] S. B. Prusiner. "Novel proteinaceous infectious particles cause scrapie." *Science*, 216, 136-144 (1982).
- [69] D. C. Bolton, M. P. McKinley, and S. B. Prusiner. "Identification of a protein that purifies with the scrapie prion." *Science*, 218, 1309-1311 (1982).
- [70] R. K. Meyer, M. P. McKinley, K. A. Bowman, M. B. Braunfeld, R. A. Barry, and S. B. Prusiner. "Separation and properties of cellular and scrapie prion proteins." *Proc. Natl. Acad. Sci. USA*, 83, 2310-2314 (1986).
- [71] S. B. Prusiner, D. Groth, D. C. Bolton, S. B. Kent, and L. E. Hood. "Purification and structural studies of a major scrapie prion protein." *Cell*, 38, (1984).
- [72] S. B. Prusiner, D. Groth, A. Serban, N. Stahl, and R. Gabizon. "Attempts to restore scrapie prion infectivity after exposure to protein denaturants." *Proc. Natl. Acad. Sci. USA*, 90, 2793-2797 (1993).
- [73] H. Büeler, A. Aguzzi, A. Sailer, R.-A. Greiner, P. Autenried, M. Aguet, and C. Weissmann. "Mice devoid of PrP are resistant to scrapie." *Cell*, 73, 1339-1347 (1993).
- [74] K. Kaneko, H. L. Ball, H. Wille, H. Zhang, D. Groth, M. Torchia, P. Trembley, J. Safar, S. B. Prusiner, S. J. De Armond, M. A. Baldwin, and F. E. Cohen. "A synthetic peptide initiates Gerstmann-Sträussler-Scheinker (GSS) disease in transgenic mice." *J. Mol. Biol.*, 295, 997-1007 (2000).

- [75] N. Nathanson, J. Wilesmith, and C. Griot. "Bovine spongiform encephalopathy (BSE): causes and consequences of a common source epidemic." *Am. J. Epidemiol.*, 145, (1997).
- [76] D. Bateman, D. Hilton, S. Love, Z. M., J. Beck, and J. Collinge. "Sporadic Creutzfeld-Jakob disease in a 18-year-old in he U.K." *Lancet*, 347, (1995).
- [77] P. Brown, M. A. Preece, and R. G. Will. "Friendly fire in medicine - hormones, homografts, and Creutzfeld-Jakob disease." *Lancet*, 340, 24-27 (1992).
- [78] T. B. de Villemeur, J.-P. Deslys, A. Pradel, C. Soubrié, A. Apérovitch, M. Tardieu, J.-L. Chaussian, J.-J. Hauw, D. Dormont, M. Ruberg, and Y. Agid. "Creutzfeld-Jakob disease from contaminated growth hormone extracts in France." *Neurology*, 47, 690-695 (1996).
- [79] T. Esmonde, C. J. Lueck, L. Symon, L. W. Duchon, and R. G. Will. "Creutzfeld-Jakob disease and lyophilized dura mater grafts - report of 2 cases." *J. Neurol. Neurosurg. Psychiatry*, 56, 999-1000 (1993).
- [80] J. Hope, L. J. Morton, C. F. Farquhar, G. Multhaup, K. Beyreuther, and R. H. Kimberlin. "The major polypeptide of scrapie-associated fibrils (SAF) has the same size, charge-distribution and N-terminal protein sequence as predicted for the normal brain protein (PrP)." *EMBO J.*, 5, 2591-2597 (1986).
- [81] J. Stöckel, J. Safar, A. C. Wallace, F. E. Cohen, and S. B. Prusiner. "Prion protein selectively binds copper(II) ions." *Biochemistry*, 37, 7185-7193 (1998).
- [82] R. Riek, S. Hornemann, G. Wider, R. Glockshuber, and K. Wütrich. "NMR characterization of the full-length recombinant murine prion protein, mPrP(23-231)." *FEBS Lett.*, 413, 282-288 (1997).

- [83] H. Liu, S. Farr-Jones, N. B. Ulyanov, M. Llinas, S. Marqusee, D. Groth, F. E. Cohen, S. B. Prusiner, and T. L. James. "Solution structure of Syrian hamster prion protein rPrP(90-231)." *Biochemistry*, 38, 5362-5377 (1999).
- [84] B. W. Caughey, A. Dong, K. S. Bhat, D. Ernst, S. F. Hayes, and W. S. Caughey. "Secondary structure analysis of the scrapie-associated protein PrP 27-30 in water by infrared spectroscopy." *Biochemistry*, 30, 7672-7680 (1991).
- [85] R. Tycko. "Prospects for resonance assignments in multidimensional solid-state NMR spectra of uniformly labeled proteins." *J. Biomol. NMR*, 8, 239-251 (1996).
- [86] G. C. Telling, M. Scott, J. Mastrianni, R. Gabizon, M. Torchia, F. E. Cohen, S. J. De Armond, and S. B. Prusiner. "Prion propagation in mice expressing human and chimeric PrP transgenes implicates the interaction of cellular PrP with another protein." *Cell*, 83, 79-90 (1995).
- [87] J. Heller, A. C. Kolbert, R. Larsen, M. Ernst, T. Bekker, M. Baldwin, S. B. Prusiner, A. Pines, and D. E. Wemmer. "Solid-state NMR studies of the prion protein H1 fragment." *Protein Science*, 5, 1655-1661 (1996).
- [88] Y. Ishii, and T. Terao. "Determination of internuclear distances by observation of the Pake-doublet patterns using the MLEV-8 sequences with composite pulses." *J. Magn. Reson. A*, 115, 116-118 (1995).
- [89] Y. Tomita, E. J. O'Connor, and A. McDermott. "A method for dihedral angle measurement in solids: rotational resonance NMR of a transition-state inhibitor of triose phosphate isomerase." *J. Am. Chem. Soc.*, 116, 8766-8771 (1994).
- [90] K. Schmidt-Rohr. "A double-quantum solid-state NMR technique for determining torsion angles in polymers." *Macromolecules*, 29, 3975-3981 (1996).

- [91] X. Feng, Y. K. Lee, D. Sandstrom, M. Eden, H. Maisel, A. Sebald, and M. H. Levitt. "Direct determination of a molecular torsion angle by solid-state NMR." *Chem. Phys. Lett.*, 257, 314-320 (1996).
- [92] R. Tycko, D. P. Weliky, and A. E. Berger. "Investigation of molecular structure in solids by two-dimensional NMR exchange spectroscopy with magic angle spinning." *J. Chem. Phys.*, 105, 7915-7930 (1996).
- [93] M. Mehta, P. Bower, D. Gregory, H. Zebroski, and G. Drobny, "Direct determination of protein backbone conformation using double-quantum solid-state NMR." *Experimental NMR Conference*, Asilomar, CA, 1996.
- [94] S. Spera, and A. Bax. "Empirical correlation between protein backbone conformations and C_{α} and C_{β} ^{13}C nuclear magnetic resonance chemical shifts." *J. Am. Chem. Soc.*, 113, 5490-5492 (1991).
- [95] D. S. Wishart, and B. D. Sykes. "The ^{13}C chemical-shift index: a simple method for the identification of protein secondary structure using ^{13}C chemical shift data." *J. Biomol. NMR*, 4, 171-180 (1994).
- [96] H. Saito. "Conformation-dependent ^{13}C chemical shifts: new means of conformational characterization as obtained by high-resolution solid-state ^{13}C NMR." *Magn. Reson. Chem.*, 24, 835-852 (1986).
- [97] H. Saito, and I. Ando. "High-resolution solid-state NMR studies of synthetic and biological macromolecules." *Annu. Rep. NMR Spectrosc.*, 21, 209-290 (1989).
- [98] A. C. de Dios, J. G. Pearson, and E. Oldfield. "Secondary and tertiary structural effects on protein NMR chemical shifts: an *ab initio* approach." *Science*, 260, 1491-1496 (1993).

- [99] A. C. de Dios, and E. Oldfield. "Ab initio study of the effects of torsion angles on carbon-13 nuclear magnetic resonance chemical shielding in N-formyl-L-alanine amide, N-formyl-L-valine amide, and some simple model compounds: applications to protein NMR spectroscopy." *J. Am. Chem. Soc.*, 116, 5307-5314 (1994).
- [100] D. D. Laws, H. Le, A. C. de Dios, R. H. Havlin, and E. Oldfield. "A basis size dependence study of carbon-13 nuclear magnetic resonance spectroscopic shielding in alanyl and valyl fragments: toward protein shielding hypersurfaces." *J. Am. Chem. Soc.*, 117, 9542-9546 (1995).
- [101] N. Asakawa, H. Kurosu, I. Ando, A. Shoji, and T. Ozaki. "A structural study of peptides and proteins containing L-alanine residues by C-13 NMR spectroscopy combined with ab initio chemical shift calculations." *J. Mol. Struct.*, 317, 119-129 (1994).
- [102] J. Kuszewski, J. Qin, A. M. Gronenborn, and G. M. Clore. "The impact of direct refinement against $^{13}\text{C}_\alpha$ and $^{13}\text{C}_\beta$ chemical shifts on protein structure determination by NMR." *J. Magn. Reson. B*, 106, 92-96 (1995).
- [103] H. Le, J. G. Pearson, A. C. de Dios, and E. Oldfield. "Protein structure refinement and prediction via NMR chemical shifts and quantum chemistry." *J. Am. Chem. Soc.*, 117, 3800-3807 (1995).
- [104] P. Luginbühl, T. Szyperski, and K. Wüthrich. "Statistical basis for the use of $^{13}\text{C}_\alpha$ chemical shifts in protein structure determination." *J. Magn. Reson. B*, 109, 229-233 (1995).

- [105] J. Heller, D. D. Laws, M. Tomaselli, D. S. King, D. E. Wemmer, A. Pines, R. H. Havlin, and E. Oldfield. "Determination of dihedral angles in peptides through experimental and theoretical studies of α -carbon chemical shift tensors." *J. Am. Chem. Soc.*, 119, 7827-7831 (1997).
- [106] S. Chaturvedi, G. Kuantee, and R. Parthasarathy. "A sequence preference for nucleation of α -helix crystal structures of Gly-L-Ala-L-Val and Gly-L-Ala-L-Leu: Some comments on the geometry of leucine zippers." *Biopolymers*, 31, 397-407 (1991).
- [107] J. K. Fawcett, N. Camerman, and A. Camerman. "The structure of the tripeptide alanyl-L-alanyl-L-alanine." *Acta Crystallographica B*, 31, 658-665 (1975).
- [108] A. Hempel, N. Camerman, and A. Camerman. "L-Alanyl-L-Alanyl-L-Alanine: parallel pleated sheet arrangement in unhydrated crystal structure, and comparisons with the antiparallel sheet structure." *Biopolymers*, 31, 187-192 (1991).
- [109] I. L. Karle, J. L. Flippen-Anderson, K. Uma, and P. Balaram. "Unfolding an α -helix in peptide crystals by solvation: conformational fragility in a heptapeptide." *Biopolymers*, 33, 827-837 (1993).
- [110] I. L. Karle, J. L. Flippen-Anderson, K. Uma, and P. Balaram. "Apolar peptide models for conformational heterogeneity, hydration, and packing of polypeptide helices: crystal structure of hepta- and octapeptides containing α -aminoisobutyric acid." *Prot. Struct. Funct. Gen.*, 7, 62-73 (1990).

- [111] G. Precigoux, C. Courseille, S. Geoffre, and F. Leroy. "Crystal structure of the 10-13 sequence of angiotensinogen L-leucyl-L-leucyl-L-valyl-L-tyrosyl methyl ester." *J. Am. Chem. Soc.*, 109, 7463-7465 (1987).
- [112] P. B. W. Ten Kortenaar, B. G. Van Dijk, J. M. Peeters, B. J. Raaben, P. J. H. M. Adam, and G. I. Tesser. "Rapid and efficient method for the preparation of Fmoc-amino acids starting from 9-fluorenylmethanol." *Int. J. Peptide Protein Res.*, 27, 398-400 (1986).
- [113] F. London. "Gauge-including atomic orbitals." *J. Phys. Radium*, 8, 397-409 (1937).
- [114] J. G. Pearson, J. F. Wang, J. L. Markley, H. Le, and E. Oldfield. "Protein structure refinement using carbon-13 nuclear magnetic resonance spectroscopic chemical shifts and quantum chemistry." *J. Am. Chem. Soc.*, 117, 8823-8829 (1995).
- [115] R. H. Havlin, H. Le, D. D. Laws, A. C. de Dios, and E. Oldfield. "Ab initio quantum chemical investigation of carbon-13 NMR shielding tensors in glycine, alanine, valine, isoleucine, serine, and threonine: comparisons between helical and sheet tensors, and the effects of χ_1 on shielding." *J. Am. Chem. Soc.*, 119, 11951-11958 (1997).
- [116] J. G. Pearson, H. Le, L. K. Sanders, N. Godbout, and E. Oldfield. "Predicting chemical shifts in proteins: Structure refinement of valine residues by using ab initio and empirical geometry optimizations." *J. Am. Chem. Soc.*, 119, 11941-11950 (1997).

- [117] P. J. Barrie, and J. Klinowski. "¹²⁹Xe NMR as a probe for the study of microporous solids: a critical review." *Prog. NMR Spectrosc.*, 24, 91-108 (1992).
- [118] J. Jokisaari. "NMR of noble gases dissolved in isotropic and anisotropic liquids." *Prog. NMR Spectrosc.*, 26, 1-25 (1994).
- [119] D. Raftery, and B. F. Chmelka, in *NMR Basic Principles and Progress*; B. Blümich, Ed.; Springer-Verlag: Berlin, Heidelberg, 1994; Vol. 30, pp 111-158.
- [120] T. Pietraß, and H. Gaede. "Optically polarized Xe-129 in NMR spectroscopy." *Adv. Mater.*, 7, 826-838 (1995).
- [121] M. S. Albert, and D. Balamore. "Development of hyperpolarized noble gas MRI." *Nucl. Instr. and Meth. in Phys. Res. A*, 402, 441-453 (1998).
- [122] K. Bartik, M. Luhmer, S. J. Heyes, R. Ottinger, and J. Reisse. "Probing molecular cavities in alpha-cyclodextrin solutions by xenon NMR." *J. Magn. Reson. B*, 109, 164-168 (1995).
- [123] Y. Xu, and P. Tang. "Amphiphilic sites for general anesthetic action? Evidence from ¹²⁹Xe-¹H intermolecular Overhauser effects." *Biochim. Biophys. Acta*, 1323, 154-162 (1997).
- [124] B. M. Goodson, *Nuclear Magnetic Resonance of Laser-Polarized Noble Gases in Molecules, Materials, and Organisms*; Ph.D. Thesis, University of California, 1999.
- [125] Y.-Q. Song, B. M. Goodson, R. E. Taylor, D. D. Laws, G. Navon, and A. Pines. "Selective enhancement of NMR signals for α -cyclodextrin with laser-polarized xenon." *Angew. Chem., Int. Ed. Engl.*, 36, 2368-2370 (1997).

- [126] R. J. Fitzgerald, K. L. Sauer, and W. Happer. "Cross-relaxation in laser-polarized liquid xenon." *Chem. Phys. Lett.*, 284, 87-92 (1998).
- [127] T. Rööm, S. Appelt, R. Seydoux, A. Pines, and E. L. Hahn. "Enhancement of surface NMR by laser-polarized noble gases." *Phys. Rev. B*, 55, 11604-11610 (1997).
- [128] D. Raftery, E. MacNamara, G. Fisher, C. V. Rice, and J. Smith. "Optical pumping and magic angle spinning: sensitivity and resolution enhancement for surface NMR obtained with laser-polarized xenon." *J. Am. Chem. Soc.*, 119, 8746-8747. (1997).
- [129] M. Haake, A. Pines, J. A. Reimer, and R. Seydoux. "Surface-enhanced NMR using continuous-flow laser-polarized xenon." *J. Am. Chem. Soc.*, 119, 11711-11712 (1997).
- [130] T. Pietraß, R. Seydoux, and A. Pines. "Surface ^{29}Si NMR by SPINOE-CP from LPX" *J. Magn. Reson.*, 133, 299-303 (1998).
- [131] E. Brunner, M. Haake, A. Pines, J. A. Reimer, and R. Seydoux. "Enhancement of ^{13}C NMR signals in solid C_{60} and C_{70} using laser-polarized xenon." *Chem. Phys. Lett.*, 290, 112-116 (1998).
- [132] I. Solomon. "Relaxation processes in a system of two spins." *Phys. Rev.*, 99, 559-565 (1955).
- [133] J. H. Noggle, and R. E. Schirmer, *The Nuclear Overhauser Effect: Chemical Applications*; Academic Press: New York, London, 1971.
- [134] J. Cavanagh, W. J. Fairbrother, A. G. Palmer, and N. J. Skelton, *Protein NMR Spectroscopy: Principles and Practice.*; Academic Press: San Diego, 1996.

- [135] Y.-Q. Song. "Spin polarization-induced nuclear Overhauser effect: An application of spin-polarized xenon and helium." *Concepts Magn. Res.*, 12, 6-20 (2000).
- [136] M. Luhmer, B. M. Goodson, Y.-Q. Song, D. D. Laws, L. Kaiser, M. C. Cyrier, and A. Pines. "Study of xenon binding in cryptophane-A using laser-induced NMR polarization enhancement." *J. Am. Chem. Soc.*, 121, 3502-3512 (1999).
- [137] M. Luhmer, A. Moschos, and J. Reisse. "Intermolecular dipole-dipole spin relaxation of xenon-129 dissolved in benzene. A molecular-dynamics simulation study." *J. Magn. Reson. A*, 113, 164-168 (1995).
- [138] M. Luhmer, and J. Reisse. "Quadrupole NMR relaxation of the noble gases dissolved in simple liquids and solutions. A critical review of experimental data in the light of computer simulation results." *Prog. NMR Spectrosc.*, 33, 57-76 (1998).
- [139] K. Bartik, M. Luhmer, J.-P. Dutasta, A. Collet, and J. Reisse. "Xe-129 and H-1 NMR study of the reversible trapping of xenon by cryptophane-A in organic solution." *J. Am. Chem. Soc.*, 120, 784-791 (1998).
- [140] R. F. Tilton Jr., and I. D. Kuntz Jr. "Nuclear magnetic resonance studies of xenon-129 with myoglobin and hemoglobin." *Biochemistry*, 21, 6850-6857 (1982).
- [141] D. J. Cram, M. E. Tanner, and C. B. Knobler. "Host-guest complexation. 58. Guest release and capture by hemicarcerands introduces the phenomenon of constrictive binding." *J. Am. Chem. Soc.*, 113, 7717-7727 (1991).

- [142] M. Garwood, and K. Yong. "Symmetric pulses to induce arbitrary flip angles with compensation for RF inhomogeneity and resonance offsets." *J. Magn. Reson.*, 94, 511-525 (1991).
- [143] T. L. Hwang, P. C. M. van Zijl, and M. Garwood. "Fast broadband inversion by adiabatic pulses." *J. Magn. Reson.*, 133, 200-203 (1998).
- [144] K. L. Sauer, R. J. Fitzgerald, and W. Happer. "Laser-polarized liquid xenon." *Chem. Phys. Lett.*, 277, 153-158 (1997).
- [145] C. H. Tseng, G. P. Wong, V. R. Pomeroy, R. W. Mair, D. P. Hinton, D. Hoffmann, R. E. Stoner, F. W. Hersman, D. G. Cory, and R. L. Walsworth. "Low-Field MRI of Laser Polarized Noble Gas" *Phys. Rev. Lett.*, 81, 3785-3788 (1998).
- [146] C. H. Tseng, R. W. Mair, G. Wong, D. Williamson, D. G. Cory, and R. L. Walsworth. "Magnetic resonance imaging of laser polarized liquid xenon." *Phys. Rev. E*, 59, 1785-1788 (1999).
- [147] P. M. Rentzepis, and D. C. Douglass. "Xenon as a solvent." *Nature*, 10, 165-166 (1981).
- [148] P. E. Savage, S. Gopalan, T. I. Mizan, C. J. Martino, and E. E. Brock. "Reactions at supercritical conditions - applications and fundamentals." *AIChE J.*, 41, 1723-1778 (1995).
- [149] S. Ikawa, and Y. Fujita. "Intramolecular and intermolecular hydrogen bonds of 4-hydroxy-4-methylpentan-2-one in supercritical xenon." *J. Phys. Chem.*, 97, 10607-10612 (1993).

- [150] E. Castillo, A. Marty, D. Combes, and J. S. Condoret. "Polar substrates for enzymatic reactions in supercritical CO₂." *Biotech. Lett.*, 16, 169-174 (1994).
- [151] I. T. Horváth, and J. M. Millar. "NMR under high gas pressure." *Chem. Rev.*, 91, 1339-1351 (1991).
- [152] J. W. Rathke, R. J. Klingler, and T. R. Krause. "Propylene hydroformylation in supercritical carbon dioxide." *Organometallics*, 10, 1350-1355 (1991).
- [153] J. W. Rathke, R. J. Klingler, and T. R. Krause. "Thermodynamics for the hydrogenation of dicobalt octacarbonyl insupercritical carbon dioxide." *Organometallics*, 11, 585-588 (1992).
- [154] F. Okada, and V. A. Apkarian. "Electronic relaxation of Xe₂Cl in gaseous and supercritical fluid xenon." *J. Chem. Phys.*, 94, 133-144 (1991).
- [155] S. V. Kamat, E. J. Beckman, and A. J. Russell. "Enzyme activity in supercritical fluids." *Crit. Rev. Biotech.*, 15, 41-71 (1995).
- [156] N. Fontes, E. Nogueiro, A. M. Elvas, T. C. deSampaio, and S. Barreiros. "Effect of pressure on the catalytic activity of subtilisin Carlsberg suspended in compressed gases." *Biochim. Biophys. Acta*, 1383, 165-174 (1998).
- [157] D. C. Roe. "Sapphire NMR tube for high-resolution studies at elevated pressure." *J. Magn. Reson.*, 63, 388-391 (1985).
- [158] I. T. Horváth, and E. C. Ponce. "New valve design for high-pressure sapphire tubes for NMR measurements." *Rev. Sci. Instrum.*, 62, 1104-1105 (1991).
- [159] D. R. Lide, Ed. *CRC Handbook of Chemistry and Physics 1990-1991*; 71 ed.; CRC Press: Boca Raton, 1990.

- [160] C. J. Jameson, A. K. Jameson, and S. M. Cohen. "Temperature and density dependence of Xe-129 chemical shift in xenon gas." *J. Chem. Phys.*, 59, 4540-4546 (1973).
- [161] V. A. Rabinovich, A. A. Vasserman, V. E. Nedostup, and L. S. Veksler, *Thermophysical properties of neon, argon, krypton, and xenon (English translation)*.; Hemisphere Publishing: Washington, D.C., 1988.
- [162] E. R. Hunt, and H. Y. Carr. "Nuclear magnetic resonance of Xe-129 in natural xenon." *Phys. Rev.*, 130, 2302-2305 (1963).
- [163] G. D. Cates, D. R. Benton, M. Gatzke, W. Happer, K. C. Hasson, and N. R. Newbury. "Laser production of large nuclear-spin polarization in frozen xenon." *Phys. Rev. Lett.*, 65, 1591-2594 (1990).
- [164] H. Destailats, and R. Fernández-Prini. "Solubility of I₂(s) and equilibrium concentration of the (I₂+C₆H₆) charge transfer complex in supercritical xenon with added C₆H₆." *J. Chem. Thermod.*, 29, 1209-1221 (1997).
- [165] S. M. Howdle, M. Jobling, and M. Poliakoff. "Spectroscopic investigations of organometallic photochemistry in supercritical fluids." *ACS Symposium Ser.*, 488, 121-131 (1992).
- [166] N. Chandrakumar, *Spin-1 NMR*; Springer-Verlag: Berlin, 1996; Vol. 34.
- [167] P. Brunner, M. Reinhold, and R. R. Ernst. "Double-quantum cross polarisation. Heteronuclear excitation and detection of NMR double-quantum transitions in solids." *J. Phys. Chem.*, 73, 1086 (1980).

- [168] M. J. Hunt. "The symmetry of the electric field gradient in tetrahedral environments and its application to ^{14}N pure quadrupole resonance in amino acids." *J. Magn. Reson.*, 15, 113-121 (1974).
- [169] M. D. Hurliman, C. H. Pennington, N. Q. Fan, J. Clarke, A. Pines, and E. L. Hahn. "Pulsed ^{14}N Fourier Transform NQR with a dc SQUID." *Phys. Rev. Lett.*, 69, 684 (1992).
- [170] U. Werner, B. Black, M. Ziegeweld, and A. Pines. "SQUID-NQR of nitrogen-14 in amino acids and small peptides." *Chem. Phys. Lett.*, 209, 17-21 (1993).
- [171] J. M. Millar, A. M. Thayer, A. Bielecki, D. B. Zax, and A. Pines. "Zero field NMR and NQR with selective pulses and indirect detection." *J. Chem. Phys.*, 83, 934-938 (1985).
- [172] R. Tycko, P. L. Stewart, and S. J. Opella. "Peptide plane orientations determined by fundamental and overtone ^{14}N NMR." *J. Am. Chem. Soc.*, 108, 5419-5425 (1986).
- [173] S. M. De Paul, M. Ernst, J. S. Shore, J. F. Stebbins, and A. Pines. "Cross Polarization from Quadrupolar Nuclei to Silicon" *J. Phys. Chem. B.*, 101, 3240-3249 (1997).
- [174] N. Schormann, J. R. Murrell, J. J. Liepnieks, and M. D. Benson. "Tertiary structure of an amyloid immunoglobulin light chain A: proposed model for amyloid fibril formation." *Proc. Natl. Acad. Sci. USA*, 92, 9490-9494 (1995).
- [175] J. W. Kelly. "Amyloid fibril formation and protein misassembly: A structural quest for insights into amyloid and prion diseases." *Structure*, 5, 595-600 (1997).

- [176] H. Saito, R. Tabeta, A. Shoji, and T. Ozaki. "Conformational characterization of polypeptides in the solid state as viewed from the conformation dependent ^{13}C chemical shifts determined by the ^{13}C cross polarization/magic angle spinning method: oligo(L-alanine), poly(L-alanine), copolymers of L- and D-alanine, and copolymers of L-alanine with N-methyl or N-benzyl-L-alanine." *Macromolecules*, 16, 1050-1057 (1983).
- [177] T. E. Creighton, *Proteins: Structure and Molecular Properties*; W.H. Freeman and Company: New York, 1993.
- [178] J. A. Ripmeester, C. I. Ratcliffe, and J. S. Tse. "The nuclear magnetic resonance of Xe-129 trapped in clathrates and some other solids." *J. Chem. Soc. Faraday Trans. 1*, 84, 3731-3745 (1988).
- [179] W. Saenger, and M. Noltenmeyer. "X-Ray structure of α -cyclodextrin." *Angew. Chem. Int. Ed. Engl.*, 13, 552-553 (1974).
- [180] J. Canceill, and A. Collet. "2-Step synthesis of D3 and C3H cryptophanes." *J. Chem. Soc., Chem. Commun.*, 582-584 (1988).
- [181] A. A. Clifford, P. Gray, and N. Platts. "Lennard-Jones 12-6 parameters for 10 small molecules." *J. Chem. Soc. Faraday. Trans. 1*, 73, 381-382 (1977).

V. Appendix A: Simulations and Programs

A.1. Matlab Script for Calculating CSA lineshapes

```
% Matlab CSA Pattern Script
% written by David Laws and Yung-ya Lin

% Based on equations from Ref. [11].

% === Input Parameters ===

w33=-22.; % PAS values
w22=-47.;
w11=-56.;

nbeta=5000; % # of sampling pts in beta angle
ngama=10000; % # of sampling pts in gamma angle

% === Powder Average ===

betalst=[0:180/(nbeta-1):180]/180*pi;
freq=[-130:1:0];
spec=zeros(size(freq));

for ii=1:nbeta
    [num2str(round(ii/nbeta*100))' % done']
    beta=betalst(ii);
    alpha=(0:360/(ngama-1):360)/180*pi.';
    wzz=w11*(cos(alpha).^2)*(sin(beta)^2) + ...
        w22*(sin(alpha).^2)*(sin(beta)^2) + w33*(cos(beta)^2);
    temp=hist(wzz,freq);
    spec=spec+temp*sin(beta);
end

save csa_spec.mat
plot(freq,spec);grid;
xlabel('Frequency (ppm)')
```

A.2. REDOR Decay Least-Squares Fitting Function (Matlab)

```
function dc=fit_redor(data,points,range_min, range_max)

t_list = data(:,1);

rmsd_min = 1000000000;
dc_best = 0;

for dc_temp=range_min:5:range_max+10

    dc_temp

    diff = 0;
    rmsd = 0;
    rmsd_min

    for i = 1:points
        S(i) = 1 - sqrt(2)*pi*besselj(.25,t_list(i)*dc_temp)*besselj(-.25,t_list(i)*dc_temp)/4;
        diff = diff + (S(i)-data(i,2))^2;
    end

    rmsd = sqrt(diff/(points-1));

    if (rmsd < rmsd_min)
        rmsd_min = rmsd;
        dc_best = dc_temp;
    end
end

for dc_temp=dc_best-50:dc_best+50

    diff = 0;
    dc_temp

    for i = 1:points
        S(i) = 1 - sqrt(2)*pi*besselj(.25,t_list(i)*dc_temp)*besselj(-.25,t_list(i)*dc_temp)/4;
        diff = diff + (S(i)-data(i,2))^2;
    end

    rmsd = sqrt(diff/(points-1));

    if (rmsd < rmsd_min)
        rmsd_min = rmsd;
        dc_best = dc_temp;
    end
end

x=.001:max(t_list(:))/1000:max(t_list(:));
S1 = 1 - sqrt(2)*pi*besselj(.25,x*dc_best).*besselj(-.25,x*dc_best)/4;
figure(1)
plot(x,S1,data(:,1),data(:,2),'x')
dc = dc_best
```

A.3 ^1H - ^{13}C CPMAS Simulation with Build-Up Curve (GAMMA)

```

// David Laws
// UC-Berkeley
//
// Based on cpecho4.cc by Marco Tomaselli
//
#include "gamma.h"
#include "floq2_op.h"
#include "floq_op.h"
#include "nmr_floq_acq.h"

main(int argc, char *argv[])
{
    int cheng; // Index for cheng1 and cheng2
    String outFile_name; // Spectrum data file
    String bufile; // Build-up curve data file
    int p=1;
    double mm; // CP match condition
    double roto=0; // Rotor speed
    double omegarf; // Nutation frequency
    double dij; // Dipolar coupling constant
    double Dwcp; // Dwell time in the CP period
    double Dw=0; // Dwell time in the spectrum
    double phstep=0; // Number of rotor phases
    int NP=0; // Number of points in the spectrum
    int NPcp=0; // Number of points in CP
    double theta; // Euler angle
    double phi; // Euler angle
    double phidel2=0; // A rotation angle
    double blength; // H-X bond length
    double gam0, gam1; // Nuclear gyromagnetic ratios
    double CPmix; // CP mixing time
    const double MA=54.7356; // The MAGIC angle
    double s11, s22, s33; // Carbon CSA
    double larmor=0; // Converts ppm to Hz
    double maxFreq, minFreq, SR; // Spectral range
    int N; // Floquet dimension

    query_parameter (argc,argv,p++, "output-name", outFile_name);
    query_parameter (argc,argv,p++, "build-up-name", bufile);
    query_parameter (argc,argv,p++, "Larmor Frequency", larmor);
    query_parameter (argc,argv,p++, "Spectral Range (+/-)", SR);
    query_parameter (argc,argv,p++, "Number of Points", NP);
    query_parameter (argc,argv,p++, "omega-rot [Hz]", roto);
    query_parameter (argc,argv,p++, "omega-rot [kHz]", omegarf);
    query_parameter (argc,argv,p++, "step in rot. phase", phstep);
    query_parameter (argc,argv,p++, "CP mix time [ms]", CPmix);
    query_parameter (argc,argv,p++, "NP in CP", NPcp);
    query_parameter (argc,argv,p++, "CP match condition", mm);
    query_parameter (argc,argv,p++, "cheng-no.", cheng);
    query_parameter (argc,argv,p++, "Floquet dimension", N);
    query_parameter (argc,argv,p++, "Bond length", blength);
    query_parameter (argc,argv,p++, "S11", s11);
    query_parameter (argc,argv,p++, "S22", s22);
    query_parameter (argc,argv,p++, "S33", s33);
}

```

```

// Defining the spin system
spin_system AB(2); // 2-spin-system
AB.isotope(0,"1H");
AB.isotope(1,"13C");
gam0 = AB.gamma(0);
gam1 = AB.gamma(1);

// Defining the cheng rotation numbers
int cheng1[] = { 2, 3, 5, 8, 13, 21, 34, 55, 89, 144, 233, 377, 616, 987, 1597, 2584, 4181,
6765, 10946, 17711};
int cheng2[] = { 1, 1, 2, 3, 5, 8, 13, 21, 34, 55, 89, 144, 233, 377, 616, 987, 1597, 2584,
4181, 6765};

// Extraneous variable assignments
double time_axis[NPcp];
maxFreq = SR;
minFreq = -1.*SR;
Dw = double(1./(2*SR));
Dwcp = double(CPmix/(1000*NPcp));
String outstar = outFile+".dat";
String bstar = bufile+".dat";
ofstream os (outstar);
ofstream bs (bstar);
coord B (0,0,1); // Defines orientation along +z direction

// Calculate dipolar coupling constant
dij = (122000.)*(gam1/gam0)/((blength)*(blength)*(blength));

// Set the dipolar coupling space tensor
matrix dc1(3,3);
dc1.put_h(-dij/2.,0,0); dc1.put_h(0.,0,1); dc1.put_h(0.,0,2);
dc1.put_h(-dij/2.,1,1); dc1.put_h(0.,1,2);
dc1.put_h(dij,2,2);

space_T DIP1(A2(dc1)); // eigenbasis
space_T DIPR1; // powder loop

// Set the X CSA space tensor
matrix s1(3,3);
s1.put_h(s11,0,0); s1.put_h(0,0,1); s1.put_h(0,0,2);
s1.put_h(s22,1,1); s1.put_h(0,1,2);
s1.put_h(s33,2,2);

s1 *= (complex)larmor; // Converts ppm into Hz
space_T CS2 (A2(s1)); // eigenbasis

// Set the X CSA spin tensor
spin_T TTS2 = T_CS2(AB,1,B); // Spin CSA Hamiltonian

// Initialize our density matrix
gen_op sigmaZ = sigma_eq(AB); // initial density matrix
gen_op sigma; // evolution density matrix

```

```

// Create a detection matrix
gen_op detect = Fm(AB,1); // Defining a 13C detection operator

// Initialize our spectra
block_1D buspec(NPcp);
block_1D buspecsum1(NPcp);
block_1D buspecsum2(NPcp);
block_1D spect(NP);
block_1D specsum1(NP);
block_1D specsum2(NP);

// Define our dipolar Hamiltonian
gen_op H;
gen_op U;
gen_op H1 = sqrt(1./6.)*(2*Iz(AB,0)*Iz(AB,1));

// Define the CSA Hamiltonian
gen_op H_0; //0th order Hamiltonian
gen_op H_1;
gen_op H_2;
gen_op H_1c; //1st Order Hamiltonian
gen_op H_2c; //2nd Order Hamiltonian
H_0 = T_prod(CS2, TTS2, 0);
floq_op fsigma (N, AB.HS(), roto);

// Begin the powder loop
for (int b=1;b<cheng1[cheng];b++) // eg. cheng1[cheng] = 28657
{
cout<<"b="<<b<<"of"<<cheng1[cheng]<<"\n";
cout.flush();

// calculate the orientation for the current step
// alpha = 360 * cheng1 * ((cheng2*b) mod cheng1)
theta = 180./cheng1[cheng] * b;
phi = 360./cheng1[cheng] * ((cheng2[cheng]*b)%cheng1[cheng]);

// this is the initial position at time zero
DIPR1 = T_rot(DIP1,-phi,-theta,0);

for (double roinit=0;roinit<360.;roinit+=phstep)
{
sigma = Iypuls(AB,sigmaZ,0,90.);

// Do the CP evolution
for (int bb=0; bb < NPcp;bb++)
{
phidel2= double(roto)*double(Dwcp)*double(2*3.141593*bb)+double(roinit/360.);

H=DIPR1.component(2,0)*d2(0,0,MA)*H1+
DIPR1.component(2,1)*d2(1,0,MA)*exp(-complex(0,phidel2))*H1+
DIPR1.component(2,2)*d2(2,0,MA)*exp(-2*complex(0,phidel2))*H1+
DIPR1.component(2,-1)*d2(-1,0,MA)*exp(complex(0,phidel2))*H1+
DIPR1.component(2,-2)*d2(-2,0,MA)*exp(2*complex(0,phidel2))*H1+
omegarf*1000.*Ix(AB,0)+(omegarf*1000.+mm*roto)*Ix(AB,1);

buspec (bb) = trace ( sigma ,Ix(AB,1) );
}
}
}

```

```

        time_axis[bb] = bb*Dwcp;
        U = prop (H,Dwcp);
        sigma= evolve (sigma,U);
    }
    buspecsum1 += buspec;

// Use Floquet to calculate the spectrum
    space_T CS2P;
    CS2P = T_rot(CS2,-phi,-theta, -roinit);
    H_1 = CS2P.component(2,1) * TTS2.component(2,0);
    H_2 = CS2P.component(2,2) * TTS2.component(2,0);
    H_1c = H_1*sqrt(1./3.);
    H_2c = H_2*sqrt(1./6.);
    fsigma.put_block(sigma, 0, 0);
    floq_op HAMFLOQ(N, AB.HS(), roto);

    HAMFLOQ.put_sdiag(adjoint(H_2),-2); // side-diagonal -2
    HAMFLOQ.put_sdiag(adjoint(H_1),-1); // side-diagonal -1
    HAMFLOQ.put_sdiag(H_0,0); // main-diagonal
    HAMFLOQ.put_sdiag(H_1,1); // side-diagonal 1
    HAMFLOQ.put_sdiag(H_2,2); // side-diagonal 2
    HAMFLOQ.add_omega(); // add omegar on diagonal
    spec(fsigma,detect,HAMFLOQ,minFreq,maxFreq,NP,spect);

    specsum1 += spect;
}

for (int l =0;l<NPcp;l++) // weighting for powder loop
{
    buspecsum1(l)*=sin(theta*PI/180);
}
buspecsum2+=buspecsum1;
for (int ll =0;ll<NP;ll++) // weighting for powder loop
{
    specsum1(ll)*=sin(theta*PI/180);
}
specsum2+=specsum1;

}

for (int kk=0; kk<NPcp; kk++)
{
    bs << time_axis[kk] << " " << Re(buspecsum2(kk)) << "\n";
}

specsum2 = IFFT(specsum2);
exponential_multiply(specsum2,-10.);

for (int ii=0; ii<NP;ii++)
{
    os<< Dw*ii << " " <<Re(specsum2(ii)) << " " << Im(specsum2(ii)) << "\n";
}
return 0;
}

```

A.4. ^1H - ^{13}C CPMAS Matching Profile Simulation (GAMMA)

```
// David Laws
// UC Berkeley

#include "gamma.h"
#include "floq2_op.h"
#include "floq_op.h"
#include "nmr_floq_acq.h"

// this program maps the matching profile for static CP
// for a two spin system
// including one  $^{13}\text{C}$  probe-spin (1 protons + 1 carbon)

main(int argc, char *argv[])
{
    int cheng; // Index for cheng1 and cheng2
    int p=1;
    double mm; // CP match condition
    double mmin; // CP match condition
    double mmax; // match scaling
    double roto =0; // Nutation frequency
    double omegarf; // Dipolar coupling constant
    double dij; // Dwell time in the CP period
    double Dwcp; // Number of points in CP
    int NPcp=0; // Euler angle
    double theta; // Euler angle
    double phi; // H-X bond length
    double blength; // Nuclear gyromagnetic ratios
    double gam0, gam1; // CP mixing time
    double CPmix;
    double mstep;
    double temp;

    query_parameter (argc,argv,p++,"match freq scaling [Hz] =",roto);
    query_parameter (argc,argv,p++,"omega-rf [kHz] =",omegarf);
    query_parameter (argc,argv,p++,"CP mix time [ms] =",CPmix);
    query_parameter (argc,argv,p++,"NP in CP =",NPcp);
    query_parameter (argc,argv,p++,"minimum match condition =",mmin);
    query_parameter (argc,argv,p++,"maximum match condition =",mmax);
    query_parameter (argc,argv,p++,"step in match condition =",mstep);
    query_parameter (argc,argv,p++,"cheng-no. =",cheng);
    query_parameter (argc,argv,p++,"Bond length =",blength);

    // Defining the spin system
    spin_system AB(2); // 2-spin-system
    AB.isotope(0," $^1\text{H}$ ");
    AB.isotope(1," $^{13}\text{C}$ ");
    gam0 = AB.gamma(0);
    gam1 = AB.gamma(1);

    /// Defining the cheng rotation numbers
    int cheng1[] = { 2, 3, 5, 8, 13, 21, 34, 55, 89, 144, 233, 377, 616, 987, 1597, 2584, 4181,
        6765, 10946, 17711 };
    int cheng2[] = { 1, 1, 2, 3, 5, 8, 13, 21, 34, 55, 89, 144, 233, 377, 616, 987, 1597, 2584,
        4181, 6765 };
}
```

```

for (mm = mmin; mm <= mmax+mstep; mm=mm+mstep)
{
// Extraneous variable assignments
dij = (122000.)*(gam1/gam0)/((blength)*(blength)*(blength));
Dwcp = double(CPmix/(1000*NPcp));

// Set the dipolar coupling space tensor
matrix dc1(3,3);
dc1.put_h(-dij/2.,0,0);      dc1.put_h(0.,0,1);      dc1.put_h(0.,0,2);
                             dc1.put_h(-dij/2.,1,1);      dc1.put_h(0.,1,2);
                             dc1.put_h(dij,2,2);

space_T DIP1(A2(dc1));      // eigenbasis
space_T DIPR1;              // powder loop

// Initialize our density matrix
gen_op sigmaZ = sigma_eq(AB);      // initial density matrix
gen_op sigma;                  // evolution density matrix

// Initialize our spectra
block_1D buspec(NPcp);
block_1D buspecsum1(NPcp);
block_1D buspecsum2(NPcp);

// Define our dipolar Hamiltonian
gen_op H;
gen_op U;
gen_op H1 = sqrt(1./6.)*(2*Iz(AB,0)*Iz(AB,1)); // heteronuclear

// Begin the powder loop
for (int b=1;b<cheng1[cheng];b++)    // eg. cheng1[cheng] = 28657
{
// calculate the orientation for the current step
// alpha = 360 * cheng1 * ((cheng2*b) mod cheng1)

theta = 180./cheng1[cheng] * b;      // [0,180]
phi = 360./cheng1[cheng] * ((cheng2[cheng]*b)%cheng1[cheng]); // [0,360]

// this is the initial position at time zero
DIPR1 = T_rot(DIP1,-phi,-theta,0);
sigma = Iypuls(AB,sigmaZ,0,90.);

// Do the CP evolution
for (int bb=0; bb < NPcp;bb++)
{
H=DIPR1.component(2,0)*H1+
omegarf*1000.*Ix(AB,0)+(omegarf*1000.+mm*roto)*Ix(AB,1);

buspec (bb) = trace ( sigma ,Ix(AB,1) );
U = prop (H,Dwcp);
sigma= evolve (sigma,U);
}
buspecsum1=buspec;

```

```

for (int l=0;l<NPcp;l++) // weighting for powder loop
{
buspecsum1(l)*=sin(theta*PI/180);
}
buspecsum2+=buspecsum1;
}

temp = Re(buspecsum2(0));

for (int kk=0; kk<NPcp; kk++)
{
if (Re(buspecsum2(kk)) > temp)
{
temp = Re(buspecsum2(kk));
}
}
cout << mm*roto << " " << temp << "\n";
cout.flush();
}
return 0;
}

```

A.5. ^1H - ^{13}C Static CP Simulation with Build-up Curve (GAMMA)

```
// David Laws
// UC Berkeley

#include "gamma.h"

// this program simulates a static-cp transfer for a two spin system
// (1 protons + 1 carbon) using the Cheng powder rotation algorithm

main(int argc, char *argv[])
{
    int cheng; // Index for cheng1 and cheng2
    String outFile; // Spectrum data file
    String bufile; // Build-up curve data file
    int p=1;
    double mm; // CP match offset (Hz)
    double SR; // Spectral Range (+/-)
    double omegarf; // Nutation frequency
    double dij; // Dipolar coupling constant
    double Dwcp; // Dwell time in the CP period
    double Dw = 0; // Dwell time in the spectrum
    int NP=0; // Number of points in the spectrum
    int NPcp=0; // Number of points in CP
    double theta; // Euler angle
    double phi; // Euler angle
    double blength; // H-X bond length
    double gam0, gam1; // Nuclear gyromagnetic ratios
    double Cpmix; // CP mixing time
    double s11, s22, s33; // Carbon CSA
    double larmor=0; // Converts ppm to Hz

    query_parameter (argc,argv,p++, "output-name", outFile);
    query_parameter (argc,argv,p++, "build-up-name", bufile);
    query_parameter (argc,argv,p++, "Larmor Frequency", larmor);
    query_parameter (argc,argv,p++, "Spectral Range (+/-)", SR);
    query_parameter (argc,argv,p++, "Number of Points", NP);
    query_parameter (argc,argv,p++, "omega-rf [kHz]", omegarf);
    query_parameter (argc,argv,p++, "CP mix time [ms]", Cpmix);
    query_parameter (argc,argv,p++, "NP in CP", NPcp);
    query_parameter (argc,argv,p++, "CP match frequency", mm);
    query_parameter (argc,argv,p++, "cheng-no.", cheng);
    query_parameter (argc,argv,p++, "Bond length", blength);
    query_parameter (argc,argv,p++, "S11", s11);
    query_parameter (argc,argv,p++, "S22", s22);
    query_parameter (argc,argv,p++, "S33", s33);

    // Defining the spin system
    spin_system AB(2); // 2-spin-system
    AB.isotope(0, "1H");
    AB.isotope(1, "13C");
    gam0 = AB.gamma(0);
    gam1 = AB.gamma(1);

    // Defining the cheng rotation numbers

```

```

int cheng1[] = { 2, 3, 5, 8, 13, 21, 34, 55, 89, 144, 233, 377, 616, 987, 1597, 2584, 4181,
                6765, 10946, 17711};
int cheng2[] = { 1, 1, 2, 3, 5, 8, 13, 21, 34, 55, 89, 144, 233, 377, 616, 987, 1597, 2584,
                4181, 6765};

// Extraneous variable assignments
double time_axis[NPcp];
dij = (122000.)*(gam1/gam0)/((blength)*(blength)*(blength));
Dw = double(1./(2*SR));
Dwcp = double(CPmix/(1000*NPcp));
String outstar = outFile+".dat";
String bstar = bufile+".dat";
ofstream os (outstar);
ofstream bs (bstar);
coord B (0,0,1); // Defines orientation along +z direction

// Set the dipolar coupling space tensor
matrix dc1(3,3);
dc1.put_h(-dij/2.,0,0);          dc1.put_h(0.,0,1);          dc1.put_h(0.,0,2);
                                dc1.put_h(-dij/2.,1,1);          dc1.put_h(0.,1,2);
                                dc1.put_h(dij,2,2);

space_T DIP1(A2(dc1));          // eigenbasis
space_T DIPR1;                  // powder loop

// Set the X CSA space tensor
matrix s1(3,3);
s1.put_h(s11,0,0);              s1.put_h(0,0,1);          s1.put_h(0,0,2);
                                s1.put_h(s22,1,1);          s1.put_h(0,1,2);
                                s1.put_h(s33,2,2);

s1 *= (complex)larmor;          // Converts ppm into Hz
space_T CS2 (A2(s1));

// Set the X CSA spin tensor
spin_T TTS2 = T_CS2(AB,1,B);    // Spin CSA Hamiltonian

// Initialize our density matrix
gen_op sigmaZ = sigma_eq(AB);   // initial density matrix
gen_op sigma;                    // evolution density matrix

// Create a detection matrix
gen_op detect = Fm(AB,1);       // Defining a 13C detection operator

// Initialize our spectra
block_1D buspec(NPcp);
block_1D buspecsum1(NPcp);
block_1D buspecsum2(NPcp);
block_1D spect(NP);
block_1D specsum1(NP);
block_1D specsum2(NP);

// Define our dipolar Hamiltonian
gen_op H;
gen_op U;
gen_op H1 = sqrt(1./6.)*(2*Iz(AB,0)*Iz(AB,1));

// Define the CSA Hamiltonian

```

```

gen_op H_0; //0th order Hamiltonian
gen_op H_2; //2nd Order Hamiltonian

H_0 = T_prod(CS2, TTS2, 0);
cout << cheng;
cout.flush();

// Begin the powder loop
for (int b=1;b<cheng1[cheng];b++) // eg. cheng1[cheng] = 28657
{
    cout<<"b="<<b<<"of"<<cheng1[cheng]<<"\n";
    cout.flush();

// calculate the orientation for the current step
// alpha = 360 * cheng1 * ((cheng2*b) mod cheng1)

    theta = 180./cheng1[cheng] * b; // [0,180]
    phi = 360./cheng1[cheng] * ((cheng2[cheng]*b)%cheng1[cheng]); // [0,360]

// rotate the dipolar coupling into the powder frame
    DIPR1 = T_rot(DIP1,-phi,-theta,0);
    sigma = Iypuls(AB,sigmaZ,0,90.);

// Do the CP evolution
    for (int bb=0; bb < NPcp;bb++)
    {
        H=DIPR1.component(2,0)*H1+
        omegarf*1000.*Ix(AB,0)+(omegarf*1000.+mm)*Ix(AB,1);
        buspec (bb) = trace ( sigma ,Ix(AB,1) );
        time_axis[bb] = bb*Dwcp;
        U = prop (H,Dwcp);
        sigma= evolve (sigma,U);
    }
    buspecsum1=buspec;

// calculate the spectrum
    space_T CS2P;
    gen_op H_CSA;
    CS2P = T_rot(CS2,-phi,-theta, 0);
    H_2 = CS2P.component(2,0) * TTS2.component(2,0);
    H_CSA = H_0 + H_2;
    FID(sigma,detect,H_CSA,Dw,NP,spect);
    specsum1 = spect;

for (int l =0;l<NPcp;l++) // weighting for powder loop
{
    buspecsum1(l)*=sin(theta*PI/180);
}
buspecsum2+=buspecsum1;

for (int ll =0;ll<NP;ll++) // weighting for powder loop
{
    specsum1(ll)*=sin(theta*PI/180);
}

specsum2+=specsum1;

```

```
}
  for (int kk=0; kk<NPcp; kk++)
  {
    bs << time_axis[kk] << " " << Re(buspecsum2(kk)) << "\n";
  }

  for (int ii=0; ii<NP;ii++)
  {
    os<< Dw*ii << " " <<Re(specsum2(ii)) << " " << Im(specsum2(ii)) << "\n";
  }
  return 0;
}
```

A.6. ^1H - ^{13}C Static CP Matching Profile Simulation (GAMMA)

```
// David Laws
// UC-Berkeley

#include "gamma.h"
#include "floq2_op.h"
#include "floq_op.h"
#include "nmr_floq_acq.h"

// this program maps the matching profile for CPMAS in a two spin system
// including one  $^{13}\text{C}$  probe-spin (1 protons + 1 carbon)

main(int argc, char *argv[])
{ int cheng; // Index for cheng1 and cheng2
  int p=1;
  double mm; // CP match condition
  double mmin; // CP match condition
  double mmax; // Rotor speed
  double roto =0; // Nutation frequency
  double omegarf; // Dipolar coupling constant
  double dij; // Dwell time in the CP period
  double Dwcp; // Number of rotor phases
  double phstep=0; // Number of points in CP
  int NPcp=0; // Euler angle
  double theta; // Euler angle
  double phi; // A rotation angle
  double phidel2=0; // H-X bond length
  double blength; // Nuclear gyromagnetic ratios
  double gam0, gam1; // CP mixing time
  double CPmix; // The MAGIC angle
  const double MA=54.7356;
  double mstep;
  double temp;

  query_parameter (argc,argv,p++, "omega-rot [Hz] =",roto);
  query_parameter (argc,argv,p++, "omega-rf [kHz] =",omegarf);
  query_parameter (argc,argv,p++, "step in rot. phase =",phstep);
  query_parameter (argc,argv,p++, "CP mix time [ms] =",CPmix);
  query_parameter (argc,argv,p++, "NP in CP =",NPcp);
  query_parameter (argc,argv,p++, "minimum match condition =",mmin);
  query_parameter (argc,argv,p++, "maximum match condition =",mmax);
  query_parameter (argc,argv,p++, "step in match condition =",mstep);
  query_parameter (argc,argv,p++, "cheng-no. =",cheng);
  query_parameter (argc,argv,p++, "Bond length =",blength);

  // Defining the spin system
  spin_system AB(2); // 2-spin-system
  AB.isotope(0," $^1\text{H}$ ");
  AB.isotope(1," $^{13}\text{C}$ ");
  gam0 = AB.gamma(0);
  gam1 = AB.gamma(1);

  // Defining the cheng rotation numbers
```

```

int cheng1[] = { 2, 3, 5, 8, 13, 21, 34, 55, 89, 144, 233, 377, 616, 987, 1597, 2584, 4181,
                6765, 10946, 17711};
int cheng2[] = { 1, 1, 2, 3, 5, 8, 13, 21, 34, 55, 89, 144, 233, 377, 616, 987, 1597, 2584,
                4181, 6765};
    for (mm = mmin; mm <= mmax+mstep; mm=mm+mstep)
    {

// Extraneous variable assignments
    dij = (122000.)*(gam1/gam0)/((blength)*(blength)*(blength));
    Dwcp = double(CPmix/(1000*NPcp));

// Set the dipolar coupling space tensor
    matrix dc1(3,3);
    dc1.put_h(-dij/2.,0,0);          dc1.put_h(0.,0,1);          dc1.put_h(0.,0,2);
                                     dc1.put_h(-dij/2.,1,1);        dc1.put_h(0.,1,2);
                                     dc1.put_h(dij,2,2);

    space_T DIP1(A2(dc1));          // eigenbasis
    space_T DIPR1;                  // powder loop

// Initialize our density matrix
    gen_op sigmaZ = sigma_eq(AB);   // initial density matrix
    gen_op sigma;                   // evolution density matrix

// Initialize our spectra
    block_1D buspec(NPcp);
    block_1D buspecsum1(NPcp);
    block_1D buspecsum2(NPcp);

// Define our dipolar Hamiltonian
    gen_op H;
    gen_op U;
    gen_op H1 = sqrt(1./6.)*(2*Iz(AB,0)*Iz(AB,1)); // heteronuclear

// Begin the powder loop
    for (int b=1;b<cheng1[cheng];b++) // eg. cheng1[cheng] = 28657
    {

// calculate the orientation for the current step
// alpha = 360 * cheng1 * ((cheng2*b) mod cheng1)

        theta = 180./cheng1[cheng] * b; // [0,180]
        phi = 360./cheng1[cheng] * ((cheng2[cheng]*b)%cheng1[cheng]); // [0,360]

// this is the initial position at time zero
        DIPR1 = T_rot(DIP1,-phi,-theta,0);

        for (double roinit=0;roinit<360.;roinit+=phstep)
        {
            sigma = Iypuls(AB,sigmaZ,0,90.);
        }

// Do the CP evolution
        for (int bb=0; bb < NPcp;bb++)
        {
            phidel2= double(roto)*double(Dwcp)*double(2*3.141593*bb)+double(roinit/360.);
        }
    }
}

```

```

H=DIPR1.component(2,0)*d2(0,0,MA)*H1+
  DIPR1.component(2,1)*d2(1,0,MA)*exp(-complex(0,phidel2))*H1+
  DIPR1.component(2,2)*d2(2,0,MA)*exp(-2*complex(0,phidel2))*H1+
  DIPR1.component(2,-1)*d2(-1,0,MA)*exp(complex(0,phidel2))*H1+
  DIPR1.component(2,-2)*d2(-2,0,MA)*exp(2*complex(0,phidel2))*H1+
  omegarf*1000.*Ix(AB,0)+(omegarf*1000.+mm*roto)*Ix(AB,1);

buspec (bb) = trace ( sigma ,Ix(AB,1) );
U = prop (H,Dwcp);
sigma= evolve (sigma,U);
}
buspecsum1+=buspec;
}
for (int l =0;l<NPcp;l++) // weighting for powder loop
{
  buspecsum1(l)*=sin(theta*PI/180);
}
buspecsum2+=buspecsum1;
}
temp = Re(buspecsum2(0));

for (int kk=0; kk<NPcp; kk++)
{
  if (Re(buspecsum2(kk)) > temp)
  {
    temp = Re(buspecsum2(kk));
  }
}
cout << mm*roto << " " << temp << "\n";
cout.flush();
}
return 0;
}

```

A.7. Matlab Script for a Graphical Interface 1D Processing Program

```

function process_panel

    global ph0 ph1 piv_num
    global thepiv outname inname
    global lbr spfreq swpw axis_Hz axis_ppm csref
    global tit_line x_line axt pbc axis_pts
    global spectrumHold pbc x_val y_val
    global Start Value pt_array Trace z_yes

    ph0 = 0;
    ph1 = 0;
    piv_num=0;
    z_yes=0;

    %the Figure box
    a = figure('Color',[0.8 0.8 0.8], ...
        'Position',[200 300 872 654], ...
        'Tag','Fig1');

    %the spectrum box
    b = axes('Parent',a, ...
        'Box','on', ...
        'CameraUpVector',[0 1 0], ...
        'Color',[1 1 1], ...
        'Position',[0.129587 0.298165 0.772936
    0.626911], ...
        'Tag','Axes1', ...
        'XColor',[0 0 0], ...
        'YColor',[0 0 0], ...
        'ZColor',[0 0 0]);
    c = line('Parent',b, ...
        'Color',[0 0 1], ...
        'Tag','Line1', ...
        'XData',[], ...
        'YData',[]);
    c = text('Parent',b, ...
        'Color',[0 0 0], ...
        'HandleVisibility','callback', ...
        'HorizontalAlignment','center', ...
        'Position',[0 -666748 0], ...
        'Tag','Text1', ...
        'VerticalAlignment','cap');
    set(get(c,'Parent'),'XLabel',c);

    %Save button
    b = uicontrol('Parent',a, ...
        'Units','points', ...
        'Position',[15 55 50 20], ...

        'Style','Pushbutton', ...
        'Tag','save1',...
        'String','Save',...
        'Callback','prfns save');

    %Save filename
    b = uicontrol('Parent',a, ...
        'Units','points', ...
        'BackgroundColor',[1 1 1], ...
        'Position',[15 30 80 20], ...
        'String',sprintf('%s',outname), ...
        'Style','edit', ...
        'Tag','outbox', ...
        'Value',1,...
        'Callback','prfns save_name');

    %Sum Button
    b = uicontrol('Parent',a, ...
        'Units','points', ...
        'Position',[15 500 50 20], ...
        'Style','Pushbutton', ...
        'Tag','sumfids',...
        'String','Sum Fids',...
        'Callback','prfns Sum_me');

    %Reverse button
    b = uicontrol('Parent',a, ...
        'Units','points', ...
        'Position',[15 475 50 20], ...
        'Style','Pushbutton', ...
        'Tag','rev1',...
        'String','Reverse',...
        'Callback','prfns reverseme');

    %DC Correction button
    b = uicontrol('Parent',a, ...
        'Units','points', ...
        'Position',[15 450 50 20], ...
        'Style','Pushbutton', ...
        'Tag','save1',...
        'String','DC Corr',...
        'Callback','prfns DC_Corr');

    %Exp Multiply button
    b = uicontrol('Parent',a, ...
        'Units','points', ...
        'Position',[10 400 60 20], ...
        'Style','Pushbutton', ...
        'Tag','exmul',...

```

```

'String','Exp Multiply',...
'Callback','prfns EXP_Mul');

%LB Box

b = uicontrol('Parent',a, ...
'Units','points', ...
'BackgroundColor',[1 1 1], ...
'Position',[10 375 60 18] , ...
'String',sprintf('%d',lbr), ...
'Style','edit', ...
'Tag','lbox', ...
'Value',1,...
'CallBack','prfns lbrval');

%Title Box

b = uicontrol('Parent',a, ...
'Units','points', ...
'BackgroundColor',[1 1 1], ...
'Position',[200 490 300 18] , ...
'String',sprintf('%s',tit_line), ...
'Style','edit', ...
'Tag','titlebox', ...
'Value',1,...
'CallBack','prfns Get_Title');

b = uicontrol('Parent',a, ...
'Units','points', ...
'BackgroundColor',[.8 .8 .8] , ...
'Position',[155 485 45 18], ...
'Style','text', ...
'Tag','StaticText6',...
'String','Plot Title');

%Axis Box

b = uicontrol('Parent',a, ...
'Units','points', ...
'BackgroundColor',[1 1 1], ...
'Position',[200 115 300 18] , ...
'String',sprintf('%s',x_line), ...
'Style','edit', ...
'Tag','axisbox', ...
'Value',1,...
'CallBack','prfns Get_Xline');

b = uicontrol('Parent',a, ...
'Units','points', ...
'BackgroundColor',[.8 .8 .8] , ...
'Position',[160 112 40 18], ...
'Style','text', ...
'Tag','StaticText6',...
'String','X Axis');

%FFT button

b = uicontrol('Parent',a, ...
'Units','points', ...
'Position',[15 325 50 20], ...
'Style','Pushbutton', ...
'Tag','ftransform',...
'String','FFT',...
'Callback','prfns Ftrans');

%Spectrometer Frequency Box

b = uicontrol('Parent',a, ...
'Units','points', ...
'BackgroundColor',[1 1 1], ...
'Position',[10 250 60 18] , ...
'String',sprintf('%10.5f',spfreq), ...
'Style','edit', ...
'Tag','freqbox', ...
'Value',1,...
'CallBack','prfns Spec_Freq');

%Normalize button

b = uicontrol('Parent',a, ...
'Units','points', ...
'Position',[15 210 50 20], ...
'Style','Pushbutton', ...
'Tag','norman',...
'String','Nomalize',...
'Callback','prfns Norm_me');

%Sweep Width Box

b = uicontrol('Parent',a, ...
'Units','points', ...
'BackgroundColor',[1 1 1], ...
'Position',[10 285 60 18] , ...
'String',sprintf('%10.2f',swpw), ...
'Style','edit', ...
'Tag','swbox', ...
'Value',1,...
'CallBack','prfns Sweep_Width');

b = uicontrol('Parent',a, ...
'Units','points', ...
'BackgroundColor',[0.8 0.8 0.8], ...
'Position',[10 270 60 12], ...
'Style','text', ...
'Tag','StaticText1',...
'String','Freq in MHz');

b = uicontrol('Parent',a, ...
'Units','points', ...
'BackgroundColor',[0.8 0.8 0.8], ...
'Position',[10 305 60 12], ...
'Style','text', ...

```

```

    'Tag','StaticText2',...
    'String','Swp Width');

%Set BC Points

b = uicontrol('Parent',a, ...
    'Units','points', ...
    'Position',[10 150 60 20], ...
    'Style','Pushbutton', ...
    'Tag','save1',...
    'String','Set BC Pts',...
    'Callback','prfns Set_BC_PTS');

%

b = uicontrol('Parent',a, ...
    'Units','points', ...
    'Position',[10 175 29 20], ...
    'Style','Pushbutton', ...
    'Tag','save1',...
    'String','BC',...
    'Callback','prfns Basc');

b = uicontrol('Parent',a, ...
    'Units','points', ...
    'BackgroundColor',[1 1 1], ...
    'Position',[41 175 29 20], ...
    'String',sprintf('%d',pbc), ...
    'Style','edit', ...
    'Tag','bcpointsbox', ...
    'Value',1,...
    'CallBack','prfns BC_Points');

%Zero Fill button

b = uicontrol('Parent',a, ...
    'Units','points', ...
    'Position',[15 350 50 20], ...
    'Style','Pushbutton', ...
    'Tag','ZF',...
    'String','Zero Fill',...
    'Callback','prfns ZFill');

%Left Shift button

b = uicontrol('Parent',a, ...
    'Units','points', ...
    'Position',[15 425 50 20], ...
    'Style','Pushbutton', ...
    'Tag','lshift',...
    'String','Left Shift',...
    'Callback','prfns LShift');

%Upload button

b = uicontrol('Parent',a, ...
    'Units','points', ...
    'Position',[635 500 55 20], ...
    'Style','Pushbutton', ...
    'Tag','upl',...
    'String','Upload',...
    'Callback','prfns Upload');

%Spec Right Button

b = uicontrol('Parent',a, ...
    'Units','points', ...
    'Position',[664 400 26 20], ...
    'Style','PushButton', ...
    'Tag','specright',...
    'String','-->',...
    'Callback','prfns spec_right');

%Spec Left Button

b = uicontrol('Parent',a, ...
    'Units','points', ...
    'Position',[635 400 26 20], ...
    'Style','PushButton', ...
    'Tag','specleft',...
    'String','<--',...
    'Callback','prfns spec_left');

%Normalize Button

b = uicontrol('Parent',a, ...
    'Units','points', ...
    'Position',[635 425 55 20], ...
    'Style','PushButton', ...
    'Tag','Norm',...
    'String','Normalize',...
    'Callback','prfns Normin');

%Zoomout Button

b = uicontrol('Parent',a, ...
    'Units','points', ...
    'Position',[635 425 55 20], ...
    'Style','PushButton', ...
    'Tag','Zoomin',...
    'String','Zoom Out',...
    'Callback','prfns zoom_out');

%Zoomin Button

b = uicontrol('Parent',a, ...
    'Units','points', ...
    'Position',[635 450 55 20], ...
    'Style','PushButton', ...

```

```

    'Tag','Zoomout',...
    'String','Zoom In',...
    'Callback','prfns zoom_in');

%Set Axis Button

b = uicontrol('Parent',a, ...
    'Units','points', ...
    'Position',[635 350 55 20], ...
    'Style','PushButton', ...
    'Tag','Zoomout',...
    'String','Set Axis',...
    'Callback','prfns Set_Axis');

b = uicontrol('Parent',a, ...
    'Units','points', ...
    'BackgroundColor',[0.8 0.8 0.8], ...
    'Position',[635 305 60 12], ...
    'Style','text', ...
    'Tag','StaticText3',...
    'String','Ref Freq');

b = uicontrol('Parent',a, ...
    'Units','points', ...
    'BackgroundColor',[1 1 1], ...
    'Position',[635 285 60 18], ...
    'String',sprintf('%7.2f,csref), ...
    'Style','edit', ...
    'Tag','CSREF', ...
    'Value',1,...
    'CallBack','prfns Set_Ref');

%Reference Button

b = uicontrol('Parent',a, ...
    'Units','points', ...
    'Position',[635 260 55 20], ...
    'Style','PushButton', ...
    'Tag','setref',...
    'String','Set Ref',...
    'Callback','prfns Reference');

%Cursor Button

b = uicontrol('Parent',a, ...
    'Units','points', ...
    'Position',[635 230 55 20], ...
    'Style','PushButton', ...
    'Tag','curs',...
    'String','Peak Pick',...
    'Callback','prfns Curs_get');

b = uicontrol('Parent',a, ...

```

```

    'Units','points', ...
    'BackgroundColor',[1 1 1], ...
    'Position',[650 205 45 18], ...
    'String',sprintf('%7.2f,x_val), ...
    'Style','edit', ...
    'Tag','Xval', ...
    'Value',1);

b = uicontrol('Parent',a, ...
    'Units','points', ...
    'BackgroundColor',[1 1 1], ...
    'Position',[650 180 45 18], ...
    'String',sprintf('%7.5f,y_val), ...
    'Style','edit', ...
    'Tag','Yval', ...
    'Value',1);

b = uicontrol('Parent',a, ...
    'Units','points', ...
    'BackgroundColor',[.8 .8 .8 ], ...
    'Position',[635 178 12 18], ...
    'Style','text', ...
    'Tag','StaticText20',...
    'String','Y');

b = uicontrol('Parent',a, ...
    'Units','points', ...
    'BackgroundColor',[.8 .8 .8 ], ...
    'Position',[635 203 12 18], ...
    'Style','text', ...
    'Tag','StaticText21',...
    'String','X');

%Print Button

b = uicontrol('Parent',a, ...
    'Units','points', ...
    'Position',[635 150 55 20], ...
    'Style','PushButton', ...
    'Tag','printtag',...
    'String','Print',...
    'Callback','prfns Print_Spec');

%Hz button

b = uicontrol('Parent',a, ...
    'Units','points', ...
    'Position',[635 325 29 20], ...
    'Style','Pushbutton', ...
    'Tag','axHz',...
    'String','Hz',...
    'Callback','prfns axis_to_Hz');

%PPM button

b = uicontrol('Parent',a, ...

```

```

'Units','points', ...
'Position',[666 325 29 20], ...
'Style','Pushbutton', ...
'Tag','axppm1',...
'String','PPM',...
'Callback','prfns axis_to_ppm');

    %Load Button

b = uicontrol('Parent',a, ...
    'Units','points', ...
    'Position',[15 105 50 20], ...
    'Style','PushButton', ...
    'Tag','reset1',...
    'String','Load',...
    'Callback','prfns loadme');

    %Load filename

b = uicontrol('Parent',a, ...
    'Units','points', ...
    'BackgroundColor',[1 1 1], ...
    'Position',[15 80 80 20], ...
    'String',sprintf('%s',inname), ...
    'Style','edit', ...
    'Tag','loadbox', ...
    'Value',1,...
    'CallBack','prfns load_name');

    %Exit button

b = uicontrol('Parent',a, ...
    'Units','points', ...
    'Position',[15 5 50 20], ...
    'Style','PushButton', ...
    'Tag','exit1',...
    'String','Exit',...
    'Callback','prfns exit');

    %Phasing
    %phc0 slider requires maxphc0 global
    %modified in phaseit.m

b = uicontrol('Parent',a, ...
    'Units','points', ...
    'Position',[150 80 420 20], ...
    'Style','slider', ...
    'Tag','phc0slide',...,
    'ButtonDownFcn','prfns phc0',...
    'Callback','prfns phc0');
set(b,'Max',180,'Min',-180)
set(b,'Value',ph0)

b = uicontrol('Parent',a, ...
    'Units','points', ...
    'BackgroundColor',[1 1 1], ...
    'Position',[580 80 40 20], ...
    'String',sprintf('%5.1f',ph0), ...
    'Style','edit', ...
    'Tag','phase0box', ...
    'Value',1,...
    'CallBack','prfns ph0_text');

    %phc1 slider requires maxphc1 global
    %modified in phaseit.m

b = uicontrol('Parent',a, ...
    'Units','points', ...
    'Position',[150 50 420 20], ...
    'Style','slider', ...
    'Tag','phc1slide',...
    'ButtonDownFcn','prfns phc1',...
    'CallBack','prfns phc1');

set(b,'Max',500,'Min',-500)
set(b,'Value',ph1)

b = uicontrol('Parent',a, ...
    'Units','points', ...
    'BackgroundColor',[1 1 1], ...
    'Position',[580 50 40 20], ...
    'String',sprintf('%5.1f',ph1), ...
    'Style','edit', ...
    'Tag','phase1 box', ...
    'Value',1,...
    'CallBack','prfns ph1_text');

b = uicontrol('Parent',a, ...
    'Units','points', ...
    'BackgroundColor',[.8 .8 .8 ], ...
    'Position',[110 78 35 18], ...
    'Style','text', ...
    'Tag','StaticText8',...
    'String','PH 0');

b = uicontrol('Parent',a, ...
    'Units','points', ...
    'BackgroundColor',[.8 .8 .8 ], ...
    'Position',[110 48 35 18], ...
    'Style','text', ...
    'Tag','StaticText9',...
    'String','PH 1');

    %PH0 C Button

b = uicontrol('Parent',a, ...
    'Units','points', ...
    'Position',[625 80 20 20], ...
    'Style','PushButton', ...
    'Tag','180bottom',...
    'String','C',...
    'Callback','prfns ph0_C');

```

%PH0 F Button

```
b = uicontrol('Parent',a, ...
    'Units','points', ...
    'Position',[650 80 20 20], ...
    'Style','PushButton', ...
    'Tag','180bottom',...
    'String','F',...
    'Callback','prfns ph0_F');
```

%PH1 C Button

```
b = uicontrol('Parent',a, ...
    'Units','points', ...
    'Position',[625 50 20 20], ...
    'Style','PushButton', ...
    'Tag','180bottom',...
    'String','C',...
    'Callback','prfns ph1_C');
```

%PH1 F Button

```
b = uicontrol('Parent',a, ...
    'Units','points', ...
    'Position',[650 50 20 20], ...
    'Style','PushButton', ...
    'Tag','180bottom',...
    'String','F',...
    'Callback','prfns ph1_F');
```

%180 Button

```
b = uicontrol('Parent',a, ...
    'Units','points', ...
    'Position',[175 20 55 20], ...
    'Style','PushButton', ...
    'Tag','180bottom',...
    'String','Phase 180',...
    'Callback','prfns Phase_180');
```

%Reset Button

```
b = uicontrol('Parent',a, ...
    'Units','points', ...
    'Position',[490 20 55 20], ...
    'Style','PushButton', ...
    'Tag','resetbutton',...
    'String','Reset PH',...
    'Callback','prfns Reset_Phase');
```

%Set Pivot Button

```
b = uicontrol('Parent',a, ...
    'Units','points', ...
    'Position',[331 20 55 20], ...
    'Style','PushButton', ...
    'Tag','pivset',...
    'String','Set Pivot',...
    'Callback','prfns Set_pivot');
```

return

A.8. Matlab Script Containing 1D NMR Processing Functions

```

function pfrns(action)

global ph0 ph1 piv_num
global outname inname spec specHOLD
global lbr spfreq swpw axis_Hz axis_ppm csref
global tit_line x_line axt pbc axis_pts
global spectrumHold pbc x_val y_val
global Start Value pt_array Trace
global z_yes axmin axmax specmin specmax
global ptmin ptmax

switch action

case 'Norm_me'

    maxi=max(spec);
    spec=spec./maxi;
    specmax=1;
    specmin=0;
    if(axt==0)
        plot(axis_Hz,real(spec));
    elseif(axt==1)
        plot(axis_ppm,real(spec));
    else
        plot(axis_pts,real(spec));
    end
    if(z_yes==1)
    if(axmin<axmax)
        axis([axmin axmax specmin specmax])
    else
        axis([axmax axmin specmin specmax])
    end
    end

case 'Curs_get'

    plot(axis_pts,real(spec));
    if(z_yes==1)
    if(ptmin<ptmax)
        axis([ptmin ptmax specmin specmax])
    else
        axis([ptmin ptmax specmin specmax])
    end
    end

    [a,b]=ginput(1);
    [c,d]=ginput(1);
    a=ceil(a);

    if(a<c)
        c=ceil(c);
        a=floor(a);

        [y_val_min,l]=min(real(spec(1,a:c)));
        [y_val_max,o]=max(real(spec(1,a:c)));
        if(abs(y_val_min)>abs(y_val_max))
            y_val=y_val_min;
            e=1;
        else
            y_val=y_val_max;
            e=0;
        end
        f=a-1+e;
    else
        a=ceil(a);
        c=floor(c);
        [y_val_min,l]=min(real(spec(1,c:a)));
        [y_val_max,o]=max(real(spec(1,a:c)));
        if(abs(y_val_min)>abs(y_val_max))
            y_val=y_val_min;
            e=1;
        else
            y_val=y_val_max;
            e=0;
        end
        f=c-1+e;
    end

    if(axt==0)
        plot(axis_Hz,real(spec));
        x_val=axis_Hz(f);
    elseif(axt==1)
        plot(axis_ppm,real(spec));
        x_val=axis_ppm(f);
    else
        plot(axis_pts,real(spec));
        x_val=f;

    end

    if(z_yes==1)
    if(axmin<axmax)
        axis([axmin axmax specmin specmax])
    else
        axis([axmax axmin specmin specmax])
    end
    end

    xvalget=findobj(gcf,'Tag','Xval');
    set(xvalget,'String',sprintf('%7.2f',x_val
));
    yvalget=findobj(gcf,'Tag','Yval');
    set(yvalget,'String',sprintf('%7.5f',y_val));

    disp(x_val)
    disp(y_val)

```

```

case 'Sum_me'

    [a,b]=size(spec);
    temp=sum(spec(1:a,:));
    spec=temp;
    plot(axis_pts,real(spec));
    if(z_yes==1)
    if(axmin<axmax)
        axis([axmin axmax specmin specmax])
    else
        axis([axmax axmin specmin specmax])
    end
end

case 'Basc'

    Trace=1;
    spectemp=basl_corr(spec);
    spec2=basl_corr(spectemp);
    [a,b]=size(spec2);
    spec=zeros(1,b);
    spec=spec+spec2;
    spectrumHold=spec;
    if(axt==0)
        plot(axis_Hz,real(spec));
    elseif(axt==1)
        plot(axis_ppm,real(spec));
    else
        plot(axis_pts,real(spec));
    end
    if(z_yes==1)
    if(axmin<axmax)
        axis([axmin axmax specmin specmax])
    else
        axis([axmax axmin specmin specmax])
    end
end

case 'Set_BC_PTS'

    plot(axis_pts,real(spec));
    [c,b]=ginput(pbc);
    pt_array=ceil(c);
    if(axt==0)
        plot(axis_Hz,real(spec));
    elseif(axt==1)
        plot(axis_ppm,real(spec));
    else
        plot(axis_pts,real(spec));
    end
    if(z_yes==1)
    if(axmin<axmax)
        axis([axmin axmax specmin specmax])
    else
        axis([axmax axmin specmin specmax])
    end

end

end
end

case 'BC_Points'

    pbc=eval(get(gcf,'String'));

case 'ph1_C'

    a1=findobj(gcf,'Tag','phc1slide');
    set(a1,'Max',500)
    set(a1,'Min',-500)

case 'ph0_C'

    a1=findobj(gcf,'Tag','phc0slide');
    set(a1,'Max',180)
    set(a1,'Min',-180)

case 'ph1_F'

    a1=findobj(gcf,'Tag','phc1slide');
    set(a1,'Max',ph1+25)
    set(a1,'Min',ph1-25)

case 'ph0_F'

    a1=findobj(gcf,'Tag','phc0slide');
    set(a1,'Max',ph0+10)
    set(a1,'Min',ph0-10)

case 'Reset_Phase'

    ph0=0;
    ph1=0;
    piv_num=0;
    spec=spectrumHold;
    if(axt==0)
        plot(axis_Hz,real(spec));
    elseif(axt==1)
        plot(axis_ppm,real(spec));
    else
        plot(axis_pts,real(spec));
    end
    if(z_yes==1)
    if(axmin<axmax)
        axis([axmin axmax specmin specmax])
    else
        axis([axmax axmin specmin specmax])
    end
end

    UpdateDisplay(ph0,ph1);

case 'Phase_180'

```

```

        spectrumHold=spectrumHold.*exp(-
i*(180)/180*pi);
        PhaseMe(ph0,ph1,piv_num);
        if(axt==0)
            plot(axis_Hz,real(spec));
        elseif(axt==1)
            plot(axis_ppm,real(spec));
        else
            plot(axis_pts,real(spec));
        end
        if(z_yes==1)
            if(axmin<axmax)
                axis([axmin axmax specmin specmax])
            else
                axis([axmax axmin specmin specmax])
            end
        end
        UpdateDisplay(ph0,ph1)
    case 'DC_Corr'
        [b,points]=size(spec);
        a=ceil(.12*points);
        ave=0;
        for i=0:a
            ave=ave+spec(1,points-i);
        end
        ave=ave/(a+1);
        arr=ones(1,points)*ave;
        spec=spec-arr;
        plot(axis_pts,real(spec));
    case 'ph0_text'
        ph0=eval(get(gco,'String'));
        PhaseMe(ph0,ph1,piv_num);
    case 'ph1_text'
        ph1=eval(get(gco,'String'));
        PhaseMe(ph0,ph1,piv_num);
    case 'Set_pivot'
        [a,points]=size(spec);
        x = ((0:(points-1))/(points-1))-0.5;
        plot(x,real(spec));
        [piv_num,c]=ginput(1);
        if(axt==0)
            plot(axis_Hz,real(spec));
        elseif(axt==1)
            plot(axis_ppm,real(spec));
        else
            plot(axis_pts,real(spec));
        end
        if(z_yes==1)
            tempmin=1.2*specmin;
            if(axmin<axmax)
                axis([axmin axmax tempmin specmax])
            else
                axis([axmax axmin tempmin specmax])
            end
        end
        title(tit_line)
        xlabel(x_line)
        print
        close figure(50)
    case 'save_name'

```

```

        %getting the name of the export file

        outname=get(gco,'String');

    case 'save'

        %push Save button

        button=questdlg('Save spectrum?');

        if strcmp(button,'Yes')
            if(axt==0)
                s0=sprintf('save %s axis_Hz
%s',outname,outname);
            elseif(axt==1)
                s0=sprintf('save %s axis_ppm
%s',outname,outname);
            else
                s0=sprintf('save %s axis_pts
%s',outname,outname);
            end

            s1=sprintf('%s=spec;',outname);
            eval(s1)
            eval(s0);
        elseif strcmp(button,'No')
            return
        end

    case 'load_name'

        %getting the name of the import file

        inname=get(gco,'String');

    case 'loadme'

        %push Load button

        button=questdlg('Load datafile?');

        if strcmp(button,'Yes')
            s1=sprintf('load %s.mat',inname);
            eval(s1);
            s2=sprintf('spec=%s',inname);
            eval(s2);

            [c,d]=size(spec);
            axis_pts=1:d;

            plot(axis_pts,real(spec));
            axt=2;
            z_yes=0;
            specHOLD=spec;
        elseif strcmp(button,'No')
            return
        end

    case 'spec_left'

        if(axt==0)
            diff=abs(axis_Hz(1)-axis_Hz(2));
        elseif(axt==1)
            diff=abs(axis_ppm(1)-axis_ppm(2));
        else
            diff=1;
        end

        axmin=axmin+diff;
        axmax=axmax+diff;
        if(axt==0)
            plot(axis_Hz,real(spec));
        elseif(axt==1)
            plot(axis_ppm,real(spec));
        else
            plot(axis_pts,real(spec));
        end
        if(z_yes==1)
            if(axmin<axmax)
                axis([axmin axmax specmin specmax])
            else
                axis([axmax axmin specmin specmax])
            end
        end

    case 'spec_right'

        if(axt==0)
            diff=abs(axis_Hz(1)-axis_Hz(2));
        elseif(axt==1)
            diff=abs(axis_ppm(1)-axis_ppm(2));
        else
            diff=1;
        end

        axmin=axmin-diff;
        axmax=axmax-diff;
        if(axt==0)
            plot(axis_Hz,real(spec));
        elseif(axt==1)
            plot(axis_ppm,real(spec));
        else
            plot(axis_pts,real(spec));
        end
        if(z_yes==1)
            if(axmin<axmax)
                axis([axmin axmax specmin specmax])
            else
                axis([axmax axmin specmin specmax])
            end
        end
end

```

```

case 'zoom_in'
    plot(axis_pts,real(spec))
    [axmin,b]=ginput(1);
    [axmax,b]=ginput(1);
    ptmin=ceil(axmin);
    ptmax=ceil(axmax);
    specmax=max(real(spec));
    specmin=min(real(spec))-0.1*specmax;
    specmax=1.1*specmax;

    if(axt==0)
        axmin=axis_Hz(ptmin);
        axmax=axis_Hz(ptmax);
        plot(axis_Hz,real(spec));
    elseif(axt==1)
        axmin=axis_ppm(ptmin);
        axmax=axis_ppm(ptmax);
        plot(axis_ppm,real(spec));
    else
        plot(axis_pts,real(spec));
    end

    if(axmin<axmax)
        axis([axmin axmax specmin specmax])
    else
        axis([axmax axmin specmin specmax])
    end
    z_yes=1;

case 'zoom_out'

    if(axt==0)
        plot(axis_Hz,real(spec));
    elseif(axt==1)
        plot(axis_ppm,real(spec));
    else
        plot(axis_pts,real(spec));
    end
    z_yes=0;

case 'reverseme'

    spectemp=spec;
    [a,points]=size(spec);
    for i=1:points
        spec(1,points-i+1)=spectemp(1,i);
    end
    if(axt==0)
        plot(axis_Hz,real(spec));
    elseif(axt==1)
        plot(axis_ppm,real(spec));
    else
        plot(axis_pts,real(spec));
    end
    if(z_yes==1)

if(axmin<axmax)
    axis([axmin axmax specmin specmax])
else
    axis([axmax axmin specmin specmax])
end

    spectemp=spec;
    [a,b]=size(spec);
    points=b-1;
    for i = 1:points
        spec(1,i) = spectemp(1,i+1);
    end
    spec(1,points)=0;
    plot(axis_pts,real(spec))
    if(z_yes==1)
        if(axmin<axmax)
            axis([axmin axmax specmin specmax])
        else
            axis([axmax axmin specmin specmax])
        end
    end

case 'ZFill'

    spectemp=spec;
    [a,b]=size(spec);
    emp=zeros(1,b);
    spec=zeros(1,2*b);
    spec(1,1:b)=spec(1,1:b)+spectemp(1,:);
    spec(1,(b+1):(2*b))=spec(1,(b+1):(2*b))+emp(1,
:);

    spec=[spectemp emp];
    [c,d]=size(spec);
    axis_pts=1:d;

    plot(axis_pts,real(spec))
    if(z_yes==1)
        if(axmin<axmax)
            axis([axmin axmax specmin specmax])
        else
            axis([axmax axmin specmin specmax])
        end
    end

case 'Upload'

```

```

    ph0=0;
    ph1=0;
    piv_num=0;
    UpdateDisplay(ph0,ph1);
    spec=specHOLD;
    [c,d]=size(spec);
    axis_pts=1:d;

    plot(axis_pts,real(spec))
    z_yes=0;

    case 'lbrval'

        lbr=eval(get(gco,'String'));

    case 'Sweep_Width'

        swpw=eval(get(gco,'String'));

        case 'Spec_Freq'

            spfreq=eval(get(gco,'String'));

    case 'Set_Ref'

        csref=eval(get(gco,'String'));

    case 'Reference'

        if(axt==0)
            plot(axis_Hz,real(spec))
            if(z_yes==1)
                if(axmin<axmax)
                    axis([axmin axmax specmin specmax])
                else
                    axis([axmax axmin specmin specmax])
                end
            end
            [a,b]=ginput(1);
            diff=csref-a;
            [c,points]=size(spec);
            c1=ones(1,points);
            c1=c1.*diff;
            axmin=axmin+diff;
            axmax=axmax+diff;
            axis_Hz=axis_Hz+c1;
            plot(axis_Hz,real(spec))
            if(z_yes==1)
                if(axmin<axmax)
                    axis([axmin axmax specmin specmax])
                else
                    axis([axmax axmin specmin specmax])
                end
            end
        else
            plot(axis_ppm,real(spec))

            if(z_yes==1)
                if(axmin<axmax)
                    axis([axmin axmax specmin specmax])
                else
                    axis([axmax axmin specmin specmax])
                end
            end
        end

        case 'EXP_Mul'

            [a,points]=size(spec);
            dw=swpw.^(-1);
            decay=exp(-lbr*(0:points-1)*dw*pi);
            spec=spec.*decay;
            plot(axis_pts,real(spec));
            if(z_yes==1)
                if(axmin<axmax)
                    axis([axmin axmax specmin specmax])
                else
                    axis([axmax axmin specmin specmax])
                end
            end

        case 'Ftrans'

            spec=fftshift(fft(spec));
            [n,m] = size(spec);
            spectrumHold=spec;
            [a,points]=size(spec);
            axis_pts=1:points;
            %specmax=max(spec);
            %spec=spec/specmax;
            specmax=max(real(spec));
            specmin=min(real(spec));
            plot(axis_pts,real(spec));
            if(z_yes==1)
                if(axmin<axmax)
                    axis([axmin axmax specmin specmax])
                end
            end
        end
    end
end

```

```

else
    axis([axmax axmin specmin specmax])
end
end

axt=2;

case 'Set_Axis'

    [a,points]=size(spec);
    interval=swpw/(points-1);
    axis_Hz=- (swpw/2):interval:(swpw/2);
    axis_ppm=axis_Hz/spfreq;
    plot(axis_Hz,real(spec));
    if(z_yes==1)
axmin=axis_Hz(ptmin);
axmax=axis_Hz(ptmax);
        if(axmin<axmax)
            axis([axmin axmax specmin specmax])
        else
            axis([axmax axmin specmin specmax])
        end
    end

axt=0;

case 'axis_to_Hz'

    plot(axis_Hz,real(spec));
    if(z_yes==1)
axmin=axis_Hz(ptmin);
axmax=axis_Hz(ptmax);
        if(axmin<axmax)
            axis([axmin axmax specmin specmax])
        else
            axis([axmax axmin specmin specmax])
        end
    end

axt=0;

case 'axis_to_ppm'

    plot(axis_ppm,real(spec));
    if(z_yes==1)
axmin=axis_ppm(ptmin);
axmax=axis_ppm(ptmax);
        if(axmin<axmax)
            axis([axmin axmax specmin specmax])
        else
            axis([axmax axmin specmin specmax])
        end
    end

axt=1;

case 'exit'

    button=questdlg('Really
Exit?','mkphase','Yes','No','No');
    if strcmp(button,'Yes')
        close
    elseif strcmp(button,'No')
        return
    end

end
return

%%%%%%%%%%%%%%%%%%%%%%%%%%%%%%%%%%%%%%%%
%
%UPDATEDISPLAY

function UpdateDisplay(ph0,ph1)

    %update phc1 slider and boxes
    %If the slider value is changed, by
    slider or edit

    p1specmax_hnd=findobj(gcf,'Tag','phase1box');
    set(p1specmax_hnd,'String',sprintf('%5.1f',ph1));
    p1s_hnd=findobj(gcf,'Tag','phc1slide');
    set(p1s_hnd,'Value',ph1);

    %update phc0 slider and boxes
    %If the slider value is changed, by
    slider or edit

    p0specmax_hnd=findobj(gcf,'Tag','phase0box');
    set(p0specmax_hnd,'String',sprintf('%5.1f',ph0));
    p0s_hnd=findobj(gcf,'Tag','phc0slide');
    set(p0s_hnd,'Value',ph0);

return

function PhaseMe(ph0,ph1,piv_num)

global spec spectrumHold axis_ppm
global axis_Hz axis_pts axt
global z_yes axmin axmax specmin specmax
global ptmin ptmax

    spectemp=spectrumHold.*exp(-
i*ph0/180*pi);
    [a,points]=size(spec);
    x = ((0:(points-1))/(points-1))-0.5;
    x2=x-piv_num;
    window2 = exp(-i*pi/180*2*x2*ph1);
    spec = spectemp .* window2;
    if(axt==0)
        plot(axis_Hz,real(spec));
    elseif(axt==1)

```

```

    plot(axis_ppm,real(spec));
else
    plot(axis_pts,real(spec));
end
if(z_yes==1)
if(axmin<axmax)
    axis([axmin axmax specmin specmax])
else
    axis([axmax axmin specmin specmax])
end
end
UpdateDisplay(ph0,ph1)

return

function ret=basl_corr(data);
% simple baseline correction with third order
polynomial.
% fit a third order polynomial to the baseline of
the data
% and subtract it.
%
% global Variables:      Value   = value at
the datapoints used for the fit
%                        pt_array = datapoints
for the fit
%                        Start    = starting
value for fit iterations
%                        Trace    = determines
output during fit
%
```

```

x=1:length(data);
global Start Value pt_array Trace count
data=real(data);
count=0;

width=3;

for i=1:length(pt_array);

    Value(i)=sum(data(pt_array(i)-
width:pt_array(i)+width))/(2*width+1);
end
if (prod(size(Start)) ~= 4)
    Start=1e-10*[1 1 1 1];
end
for j=1:2;
    options(14)=3000;
    para=fmins('basl',Start,options);
    Start=para;

plot(pt_array, Value,'o',pt_array,(para(1)+para(2)
*pt_array+ ...

para(3)*pt_array.^2+para(4)*pt_array.^3),'x');
    pause(2);
end
ret=data-
(para(1)+para(2)*x+para(3)*x.^2+para(4)*x.^3);

return
```